UNIVERSITY OF SOUTHERN QUEENSLAND

THE APPLICATION OF MICROWAVE SENSING TO THE MEASUREMENT OF CHEESE CURD MOISTURE

A dissertation submitted by

Brendan Horsfield, BEng (Hons)

for the award of

Doctor of Philosophy

2001

Abstract

There is a need in the dairy industry for instrumentation capable of providing on-line information about the moisture content of cheese during manufacture. Present measurement techniques are usually performed off-line and can be susceptible to human error. It is demonstrated that microwave-based moisture sensing techniques offer a number of potential advantages over conventional methods due to the strong interaction of microwaves with water.

The permittivity of cream cheese curd and low-fat cheddar cheese curd has been measured over a range of frequencies and moisture contents in order to establish the relationship between these variables. A vector reflection coefficient measurement engine based on a six-port reflectometer has been built and tested. A suitable sensing head has been fabricated from a short length of microstrip transmission line. Two sensor characterisation models have been developed and compared with measured data.

A novel algorithm has been developed to resolve the ambiguity inherent in many permittivity measurement techniques. It has been discovered that surface waves can propagate on a grounded dielectric slab covered by a material with a higher dielectric constant, provided the loss factor of the covering medium is greater than zero. It has also been found that the dominant mode of microstrip can radiate when the line is covered by a high-permittivity material, although this can be suppressed if the covering material is sufficiently lossy.

There are three principal conclusions to draw from the investigation in this thesis. Firstly, changes in the moisture content of cheese curd during manufacture produce measurable variations in permittivity. Secondly, these changes can be measured accurately and cheaply using off-the-shelf microwave hardware. Finally, considerable attention must be paid to the charac-

terisation of the sensing head if the instrument is to achieve its full potential. Promising results have been obtained in this area, however certain issues pertaining to the propagation of multiple dominant modes and higher order modes have not been fully resolved and would repay further theoretical analysis.

Certification of Dissertation

I certify that the ideas, experimental work, results, analyses, software and conclusions reported in this dissertation are entirely my own effort, except where otherwise acknowledged. I also certify that the work is original and has not been previously submitted for any other award, except where otherwise acknowledged.

Signature of Candidate | Date

ENDORSEMENT

Signature of Supervisor/s | Date

Date

Acknowledgments

This project has benefited at every stage from the assistance of many people. I wish to express my gratitude to them for their contributions.

Firstly, I would like to thank my supervisors Dr Jim Ball and Dr Nigel Hancock for their support and counsel throughout the course of this project. Both have achieved the difficult task of providing sound guidance while at the same time giving me latitude to exercise my own judgement concerning the scope and direction of the project.

I acknowledge the assistance of the technical support staff of the Faculty of Engineering and Surveying, in particular Keith Fleming, Terry Byrne and Jim Scott. The workshop staff are also owed a debt of thanks for their help in manufacturing the waveguide test cells used in the permittivity survey.

The experimental phases of this project were helped by equipment loans from a number of sources. Thanks are due to: Codan Queensland (formerly Mitec Limited) for the loan of coaxial-to-waveguide adaptors and matched terminations; the Faculty of Applied Science (in particular Ken Mottram and Victor Schultz) for the use of electronic scales and a travelling microscope, and also for the donation of a range of test liquids; Telstra staff at Mt Lofty in Toowoomba for the loan of a microwave frequency counter; and workshop staff in the USQ soil testing laboratory for the loan of a temperature-controlled oven. Thanks also to Dr Marek Bialkowski at the University of Queensland for the use of *Ensemble* and the HP Dielectric Probe Kit.

In the course of this project I have consulted with several people having expert knowledge in certain areas. In particular I wish to thank: Glen Exton from Hewlett Packard and the

personnel at Amberley Air Force Base for their help in verifying the calibration of USQ's HP 8720C Automatic Network Analyser; and Lee McMillan, Nick Shuley and Richard Keam for aiding my understanding of the fundamentals of the spectral domain method.

I wish to express my gratitude to Tony Kilmartin at the Tatura dairy factory and Neil Bredhauer at the Dairy Farmers factory in Toowoomba for their donations of samples of cheese curd. I also appreciate the time they took out of their busy schedules to explain the cheese production process to me and answer my questions.

I gratefully acknowledge the generous financial support provided by the Dairy Research and Development Corporation and the University of Southern Queensland. Also deserving of thanks are Ross Varnes at Codan Queensland for fabricating the microstrip and coplanar waveguide sensors in his own time at no charge, and Dale Press at FasTrack Circuit Boards for etching the frequency stabilisation PCB, also at no charge.

Finally, thanks to my partner Cathy for her love, support and patience throughout this long endeavour.

Contents

List of Figures

List of Tables

Chapter 1

Introduction

1.1 Project Rationale

The moisture content of cheese curd during manufacture is a critical parameter which impacts on both the quality and cost of the final product. At present moisture content is determined by simple weighing and drying methods which, while accurate, are slow and do not lend themselves well to automation. Hence there is a need in the dairy industry for instrumentation which can provide accurate moisture information in real time.

Microwave methods of moisture measurement offer an attractive means of achieving this objective. Due to its polar nature, the water molecule interacts very strongly with electromagnetic waves at microwave frequencies. As a result the dielectric behaviour of moist materials at microwave frequencies should be a strong function of moisture content. In principle it should be possible to design an instrument which exploits this characteristic. However, the practical hurdles to be overcome in designing such an instrument make this a formidable task.

Firstly, measurement hardware is required which can accurately and repeatably measure the reflection and/or transmission properties of a sensor embedded in a sample of cheese curd. Computer control of this hardware is required if the instrument is to be automated.

Secondly, a suitable sensing head is required to interface the instrument to the material under test. The type of sensor chosen must be appropriate for the measurand of interest, and must provide adequate sensitivity to changes in moisture content while not exceeding the dynamic range of the instrument.

Finally, the behaviour of the sensor must be adequately characterised so that measured reflection/transmission data can be mapped to the desired material property.

This thesis presents research progress towards the design of a prototype moisture sensing instrument. It is demonstrated that a future instrument will be based upon the above three functional building blocks, namely a microwave measurement engine, a sensing head and a sensor model.

1.2 Project Background

This work had its genesis as a two-year project funded by the Dairy Research and Development Corporation (DRDC). The objective was to design and build a low-cost microwave-based moisture sensing instrument for the cheese industry. The present author commenced work on the project in mid-1994 at the University of Southern Queensland.

During this two-year period the basic assumptions concerning the theory of operation of the instrument were shown to be valid. Specifically, the dependence of cheese curd permittivity on moisture content was demonstrated experimentally, and the concept of an accurate, low cost instrument to exploit this characteristic was shown to be feasible. However, it also became clear that further, basic research was required in the area of sensor design and characterisation before the instrument could function as hoped.

Thus, at the end of the DRDC-funded phase of the project, the present author commenced work on a model of the instrument's sensing head. Although this work involved a protracted theoretical analysis, it was considered sufficiently important to the accurate operation of the instrument to justify the time and effort. As such, the focus of the second half of the project was directed away from hardware development and towards sensor modelling.

1.3 Aim and Objectives

The broad aim of this project was to demonstrate the feasibility of using microwave sensing to perform online measurement of the moisture content of cheese curd during manufacture.

The specific objectives of this project were then determined as follows:

1. To perform an initial permittivity survey of a variety of cheese types in order to establish the extent to which the dielectric properties of cheese curd are dependent upon moisture content.
2. To design and fabricate low-cost microwave hardware which enables the reflection and/or transmission coefficient of a sensor in contact with a sample of curd to be measured in real time.
3. To develop an accurate theoretical model of a microstrip contact sensor which enables the permittivity of a test material to be deduced from the measured scattering parameters of the sensor.

1.4 Overview of Thesis

The dual emphasis of this project—namely, hardware development and sensor modelling—suggested that a two-part thesis format was appropriate. Consequently, the end of this chapter marks the beginning of Part I, which spans Chapters 2 to 5 and is concerned mainly with an investigation of the dielectric properties of cheese curd, and the development of reflection coefficient measurement hardware. Part II spans Chapters 6 to 10, and describes the development of a theoretical model of the instrument's sensing head. The final chapter of the thesis then draws together the results of Parts I and II, and discusses the significance of these results in the context of the wider body of knowledge in the field.

An overview of each chapter is provided below.

Chapter 1 – Introduction

Chapter 1 introduces the proposition driving this project, namely that it is possible to measure the moisture content of cheese curd accurately and cheaply by microwave sensing, given intelligent instrument design. Chapter 1 also outlines the objectives and scope of the project, and highlights those areas in which original work has been performed.

Chapter 2 – Microwave Sensing

Chapter 2 explains the theoretical background to microwave moisture sensing. Some pertinent examples of previous applications of this theory are reviewed, and the relative merits of microwave-based techniques are summarised.

Chapter 3 – Cheese Curd Permittivity Survey

Chapter 3 is concerned with a survey of the electromagnetic properties of a variety of cheese types. This was designed to establish the extent to which dielectric behaviour is affected by such parameters as frequency, moisture content and salt content.

Chapter 4 – Six-Port Reflectometer

Chapter 4 describes the development and testing of a computer-controlled six-port reflectometer. This instrument was the measurement engine with which the reflection coefficient of cheese curd samples was to be monitored.

Chapter 5 – Microstrip Sensor Structures

Chapter 5 introduces the family of planar sensors which are analysed in detail in later chapters. The strengths and limitations of these structures are explored, and the need for an accurate characterisation algorithm is discussed.

Chapter 6 – The Spectral Domain Method I: Static Approximation

Chapter 6 presents a static analysis of the sensor family introduced in Chapter 5. The analysis technique employed here is a popular one that has been used frequently in the past, however it will be shown in later chapters that this method has some shortcomings which limit its usefulness as a sensor with high permittivity measurands.

Chapter 7 – Surface Waves

Chapter 7 investigates the conditions necessary for surface wave propagation on the sensor structure. The effects of placing the sensor in contact with a high-permittivity, lossy dielectric are investigated, with somewhat surprising and counterintuitive results.

Chapter 8 – The Spectral Domain Method II: Full-Wave Analysis

Chapter 8 follows on from Chapter 7 with a full-wave spectral domain analysis of the sensor structure, taking into account signal loss due to surface wave leakage and radiation. The presence of multiple dominant modes on the sensor structure is also investigated.

Chapter 9 – Simulation of Sensor Scattering Parameters

Chapter 9 brings together the work of previous chapters into a simulation of the scattering parameters of a two-port sensor. While simple in principle, the analysis is made more difficult by the need to account for the capacitance of the launchers at each end of the sensor.

Chapter 10 – Results

Chapter 10 compares and contrasts the theoretical sensor model with experimental results. The superiority of the full-wave analysis over the static analysis is demonstrated, and the limitations of both types of model are discussed.

Chapter 11 – Discussion and Conclusions

Chapter 11 brings together the results of the entire project and highlights their significance to the state of the art. The chapter concludes with some suggestions for future avenues of research in this field.

1.5 Summary of Original Work

In the course of this project original theory and techniques have arisen out of five areas. In two cases the originality resides in the *application* of existing ideas to a new measurement task. The application of existing waveguide-based techniques to the measurement of cheese curd permittivity produced experimental data that was unique at that time. Similarly, the choice of microstrip transmission lines as contact sensors for measuring the S-parameters of cheese curd is also believed to be an original application.

Three novel theoretical results have also been produced. One provides a reliable means of resolving the ambiguity inherent in waveguide permittivity measurement techniques. Another provides an insight into the propagation of surface waves on a dielectric slab covered by a lossy high-permittivity material of infinite extent. Original work has also been carried out in the analysis of radiation leakage from the dominant mode of microstrip immersed in a high-permittivity medium.

The areas of this project in which original work was performed are summarised below.

1. Broadband measurement of cheese curd permittivity.
2. Development of robust algorithm for calculating initial estimate of sample permittivity for waveguide ε_{r} measurements.
3. Use of microstrip transmission line as a contact sensor for cheese curd permittivity measurement.
4. Analysis of surface wave propagation on a grounded dielectric slab immersed in a lossy, high-permittivity medium.

5. Investigation into the conditions necessary for radiation leakage to occur from the dominant mode of microstrip immersed in a lossy, high-permittivity medium.

1.6 Publications

Horsfield, B., Ball, J. A. R., Holmes, W. S., Green, A., Holdem, J. R., and Keam, R. B. (1996). A technique for measuring cheese curd moisture in real time. In *Proceedings of the 1996 Conference on Engineering in Agriculture and Food Processing, Gatton, Australia*. (Paper No. SEAg 96/065).

Ball, J. A. R., Horsfield, B., Holdem, J. R., Keam, R. B., Holmes, W. S., and Green, A. (1996a). Cheese curd permittivity and moisture measurement using a 6-port reflectometer. In *Proceedings of the 1996 Asia-Pacific Microwave Conference, New Delhi, India*. (Session B5, Paper No. INV1).

Ball, J. A. R., Horsfield, B., Holdem, J. R., Keam, R. B., Holmes, W. S., and Green, A. (1996b). On-line moisture measurement during cheese production. In *Proceedings of the 1996 Conference on Scientific and Industrial RF & Microwave Applications, Melbourne, Australia*.

Ball, J. A. R. and Horsfield, B. (1998). Resolving ambiguity in broadband waveguide permittivity measurements on moist materials. *IEEE Transactions on Instrumentation and Measurement*, **47**(2): 390–392.

Ku, H. S., Siores, E., Ball, J. A. R., and Horsfield, B. (1998). An important step in microwave processing of materials: Permittivity measurements of thermoplastic composites at elevated temperatures. In *Proceedings of the 1998 Pacific Conference on Manufacturing, Brisbane, Australia*, pp. 68–73.

Ku, H. S., Ball, J. A. R., Siores, E., and Horsfield, B. (1999). Microwave processing and permittivity measurement of thermoplastic composites at elevated temperature. *Journal of Materials Processing Technology*, **89-90**: 419–424.

Horsfield, B. and Ball, J. A. R. (2000). Surface wave propagation on a grounded dielectric slab covered by a high-permittivity material. *IEEE Microwave and Guided Wave Letters*, **10**(5): 171–173.

Ku, H. S., Horsfield, B., Ball, J. A. R., and Siores, E. (2001). Permittivity measurement of thermoplastic composites at elevated temperature. *Journal of Microwave Power and Electromagnetic Energy*, **36**(2): 101–111.

NOTES:

In the above publications by Ball, Horsfield, Holdem, Keam, Holmes and Green, the candidate's contribution to the reported work was as follows: design of waveguide test cells and dielectric windows; development of software to calculate permittivity of moist materials from measured S-parameters; survey of permittivity and DC conductivity of a variety of cheese curd types over a range of moisture contents; assembly of six-port reflectometer including frequency stabilisation circuit; implementation of six-port reflectometer calibration & control routines in C++; measurement of S_{11} of microstrip knife sensor embedded in samples of cheese curd over a range of moisture contents.

The candidate's contribution to the publications by Ku, Siores, Ball and Horsfield was the design of the WR90 and WR159 waveguide test cells, and the development of software to calculate the permittivity of samples of thermoplastic composites from measured S-parameters.

Part I

Application of Microwave Sensing to Cheese Production

Chapter 2

Microwave Sensing

2.1 Introduction

This chapter introduces the concept of microwave sensing, including theory, implementation strategy, prior art and relative merit in comparison to other techniques.

The first section of this chapter provides an overview of the physical principles which underpin microwave-based sensing techniques. The key mechanisms which determine the dielectric properties of a material are outlined, with particular attention to moist substances. The dielectric behaviour of methanol is also examined, due to its usefulness as a test liquid with a well-understood dielectric spectrum.

The second section identifies the major components which are required in implementing an online, automated moisture sensing instrument. Such components include both the hardware devices like the sensing head, and the software algorithms which perform control and computational functions.

The third section provides a brief review of some relevant past applications of microwave moisture sensing. The relative merits of each approach are examined to assess their suitability for cheese curd moisture measurement.

The final section of this chapter addresses an important implicit assumption in this thesis: namely, that microwave-based approaches offer certain advantages over other, more conventional methods. The benefits of microwave sensing are described, as well as some of the potential limitations.

2.2 Microwave Sensing and the Dielectric Properties of Matter

Microwave measurement techniques exploit the interaction between electromagnetic waves and matter.

The manner in which an electromagnetic field is altered by a material depends on a number of macroscopic factors, including density, temperature, composition, and also upon the microstructure of the material. Strictly speaking, however, the propagation of electromagnetic waves through a substance depends on only two fundamental parameters: the dielectric permittivity ε, and the magnetic permeability μ of the substance.

For the purposes of this project it was assumed that all materials under consideration would be nonmagnetic. This is not an unreasonable assumption. After all, the ultimate aim of the project was to develop a sensor for the dairy industry, where all potential measurands are nonmagnetic. Indeed, most solid and liquid materials in nature are nonmagnetic, so there is no great loss of generality in taking this approach.

Thus, throughout this thesis the term ‘microwave sensing’ refers to the measurement of dielectric properties only. Theoretical models assume a magnetic permeability of $\mu = \mu_0$ for all materials, where μ_0 is the permeability of free space. Additionally, the terms ‘permittivity’ and ‘complex permittivity’ are used interchangeably, while ‘dielectric constant’ and ‘loss factor’ denote the real and imaginary parts of permittivity respectively.

The following sections summarise the physical mechanisms which determine a material’s dielectric behaviour.

2.2.1 Polarisation

The dielectric constant of a material is defined concisely by Hasted (1973, pp. 1–31) as 'a measure of the extent to which the electric charge distribution in the material can be distorted ... by the application of an electric field'. This distortion of charge is referred to as *polarisation*.

All matter can be polarised to a greater or lesser extent, regardless of whether the matter is in a solid, liquid or gaseous state. (In keeping with the theme of the rest of this thesis, the following discussion will apply to dense materials only, i.e. materials in the solid or liquid phase.) Polarisation phenomena can express themselves in four different ways:

Electronic polarisation – Refers to the displacement of electrons in atoms relative to the nucleus, resulting in an uneven distribution of charge in the atom.

Atomic polarisation – Closely related to electronic polarisation, this effect manifests itself as the displacement of atoms within a molecule due to the uneven distribution of charge inherent in the molecule.

Ionic polarisation – Materials containing isolated pools of free charge suspended in a non-conducting background medium can become polarised under the influence of an applied electric field. This phenomenon is also known as the *Maxwell-Wagner* effect (Nyfors and Vainikainen, 1989, pp. 58–62).

Orientation polarisation – The most significant form of polarisation in biological materials at microwave frequencies, this type of polarisation manifests itself as a torque-like force which causes molecules to rotate in line with an applied electric field. This effect is a consequence of uneven distribution of charge in the molecule, which results in the molecule having a permanent dipole moment.

Of the four categories of polarisation, ionic and orientation polarisation are by far the most significant in the microwave band. The dielectric properties of materials subject to these effects can vary dramatically with frequency, temperature, and material composition.

Electronic and atomic polarisation only become significant at infrared and optical frequencies respectively, and will not be discussed further here.

2.2.2 DC Conductivity

If a material possesses a DC conductivity—due for example to the presence of ions—then this will affect the dielectric properties of the material, particularly at low frequencies. The nature of this effect can be predicted from Maxwell's equations, specifically Ampère's law, which states:

$$\nabla \times \mathbf{H} = \mathbf{J} + \frac{\partial \mathbf{D}}{\partial t} \tag{2.1}$$

where $\mathbf{H}$ is the magnetic field intensity, $\mathbf{J}$ is the conduction-current density, and $\mathbf{D}$ is the electric flux density.

Ohm's law at a point states that $\mathbf{J} = \sigma \mathbf{E}$, where σ is the DC conductivity of the medium, and $\mathbf{E}$ denotes the electric field intensity. The constitutive relations state that $\mathbf{D} = \varepsilon_{\mathrm{r}} \varepsilon_0 \mathbf{E}$, where ε_{r} is the permittivity of the medium relative to the free-space permittivity ε_0. It is therefore possible to re-write the right hand side of Equation 2.1 as follows:

$$\mathbf{J} + \frac{\partial \mathbf{D}}{\partial t} = \sigma \mathbf{E} + \frac{\partial \varepsilon_{\mathrm{r}} \varepsilon_0 \mathbf{E}}{\partial t} \tag{2.2}$$

Assuming harmonic time variation, differentiation in time becomes equivalent to multiplication by $j\omega$. Allowing the medium to be lossy (i.e. $\varepsilon_{\mathrm{r}} = \varepsilon'_{\mathrm{r}} - j\varepsilon''_{\mathrm{r}}$), Equation 2.2 becomes

$$\mathbf{J} + \frac{\partial \mathbf{D}}{\partial t} = \sigma \mathbf{E} + j\omega(\varepsilon'_{\mathrm{r}} - j\varepsilon''_{\mathrm{r}})\varepsilon_0 \mathbf{E} \tag{2.3}$$

from which it can be inferred that

$$\varepsilon_{\mathrm{r}} = \varepsilon'_{\mathrm{r}} - j\varepsilon''_{\mathrm{r}} = \varepsilon'_{\mathrm{r}} - j\left(\varepsilon''_{\mathrm{r}} + \frac{\sigma}{\omega \varepsilon_0}\right) \tag{2.4}$$

Thus, from Equation 2.4 it is evident that the impact of non-zero DC conductivity on the permittivity of a material is to introduce an additional loss factor which varies inversely with frequency.

2.2.3 The Debye Behaviour of Polar Materials

As mentioned earlier, the dielectric properties of polar materials can vary considerably with frequency. In the classical case, the permanent dipole moment of the molecule bestows a high value of $\varepsilon'_{\mathrm{r}}$ on the material at DC, decreasing as frequency increases to a much smaller high frequency value. At the same time, the loss factor $\varepsilon''_{\mathrm{r}}$ increases from a low value at DC, to a maximum at the so-called 'relaxation frequency'. The peak value of the loss factor can be relatively high at this frequency, due to the friction between molecules which acts to impede their oscillation with the electric field. Above the relaxation frequency the loss gradually drops to a low value again.

This variation of dielectric properties with frequency can be accurately described by the Debye function, which has the following general form:

$$\varepsilon_{\mathrm{r}} = \varepsilon_{\infty} + \frac{\varepsilon_{\mathrm{s}} - \varepsilon_{\infty}}{1 + j\omega\tau} \tag{2.5}$$

where ε_{r} is the complex dielectric constant of the material, ε_{∞} is the high-frequency permittivity, ε_{s} is the static permittivity, and τ is the relaxation period. All of these parameters have material-specific values, which are usually obtained empirically (Nyfors and Vainikainen, 1989, pp. 41–62).

Equation 2.5 is often separated into real and imaginary components, viz.:

$$\varepsilon'_{\mathrm{r}} = \varepsilon_{\infty} + \frac{\varepsilon_{\mathrm{s}} - \varepsilon_{\infty}}{1 + \omega^2\tau^2} \tag{2.6}$$

$$\varepsilon''_{\mathrm{r}} = \frac{(\varepsilon_{\mathrm{s}} - \varepsilon_{\infty})\omega\tau}{1 + \omega^2\tau^2} \tag{2.7}$$

In some materials, such as mixtures or aqueous solutions, it may not be possible to perfectly describe the properties of the material with only a single relaxation frequency (Hasted, 1973, pp. 1–31). In such situations a number of variations on the classical single-relaxation Debye spectrum are available.

The simplest and most physically meaningful is the multiple component Debye spectrum, which involves the summations of two or more Debye functions with different relaxation times:

$$\varepsilon_{\mathrm{r}} = \varepsilon_{\infty} + \frac{\varepsilon_{\mathrm{s}} - \varepsilon_{H1}}{1 + j\omega\tau_1} + \frac{\varepsilon_{H1} - \varepsilon_{H2}}{1 + j\omega\tau_2} + \ldots + \frac{\varepsilon_{Hn} - \varepsilon_{\infty}}{1 + j\omega\tau_n} \tag{2.8}$$

where τ_n is the relaxation period of the n^{th} component of the mixture, and ε_{Hn} is the height of the n^{th} plateau above the baseline.

Two empirical variations of Equation 2.5 are often used (Nyfors and Vainikainen, 1989, pp. 41–62). The first is known as the *Cole-Cole* equation, given by

$$\varepsilon_{\mathrm{r}} = \varepsilon_{\infty} + \frac{\varepsilon_{\mathrm{s}} - \varepsilon_{\infty}}{1 + (j\omega\tau)^{1-\alpha}} \tag{2.9}$$

The second is known as the *Cole-Davidson* equation, given by

$$\varepsilon_{\mathrm{r}} = \varepsilon_{\infty} + \frac{\varepsilon_{\mathrm{s}} - \varepsilon_{\infty}}{(1 + j\omega\tau)^{\alpha}} \tag{2.10}$$

In both of these equations α is an empirical constant which represents a *distribution* of relaxation times. In Equation 2.9 the distribution is symmetrical, whereas in Equation 2.10 the distribution is asymmetrical (Hasted, 1973, pp. 1–31).

2.2.4 Polar Liquids as Test Dielectrics

An important step in the development of any instrument is experimental verification of correct operation. This requires the use of a test material with known dielectric properties, preferably of the same magnitude as the final measurand. Polar liquids are well suited to this role for several reasons.

Firstly, the fact that polar materials can be well characterised by the Debye equation or one of its variants means that their dielectric behaviour can be determined without the need for independent measurement.

Secondly, the use of polar liquids eliminates many of the problems caused by the non-ideal characteristics of solid and semi-solid materials, such as heterogeneous composition and the presence of air inclusions.

Finally, polar liquids are not biologically active, so their properties do not change with time. They have no special storage requirements beyond those usually required for laboratory chemicals, whereas potential measurands like cheese curd usually require refrigeration.

A range of polar liquids was considered in the course of this project, including formamide, ethanediol, ethanol, methanol and distilled water. The latter two were eventually selected for use as test liquids, the others having the drawbacks of being either too flammable or being emitters of toxic fumes and therefore requiring the use of a fume cupboard.

A plot of the complex permittivity of distilled water at 25°C is shown in Figure 2.1. This data was generated using the classical Debye equation for distilled water with a single relaxation time. Debye parameters were obtained using data from Kaatze (1989).

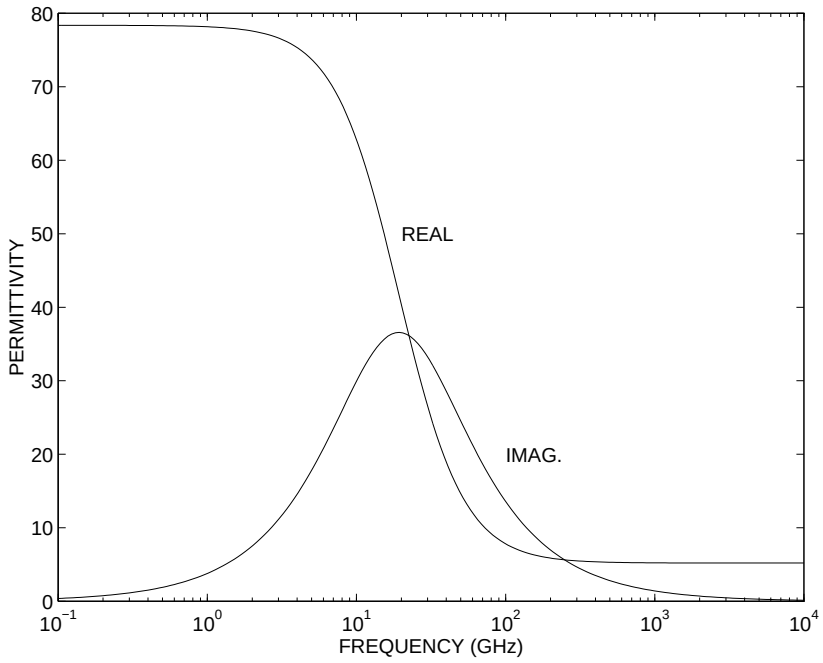

Figure 2.1: Plot of dielectric behaviour of distilled water at 25°C as a function of frequency, with $\varepsilon_s = 78.4$, $\varepsilon_\infty = 5.2$ and $\tau = 8.27$ ps.

A plot of the complex permittivity of methanol at 25°C is shown in Figure 2.2. This data was generated using the Cole-Cole equation with Debye parameters obtained from Jordan et al. (1978).

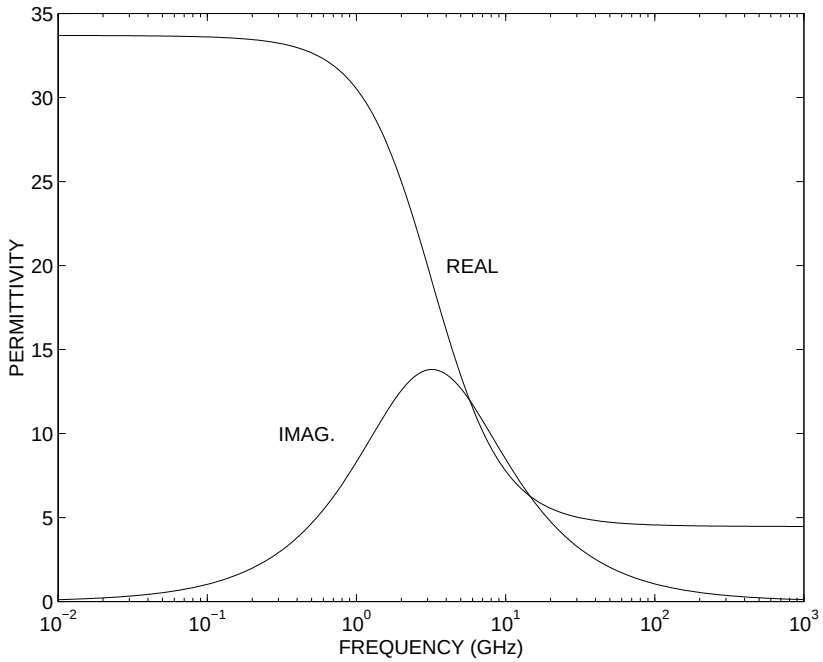

Figure 2.2: Plot of dielectric behaviour of methanol at 25°C as a function of frequency, with $\varepsilon_s = 33.7$, $\varepsilon_\infty = 4.46$, $\tau = 49.69$ ps and $\alpha = 0.036$.

2.3 Key Components of a Microwave Moisture Sensing Instrument

It is envisaged that a successful curd moisture measurement system must consist of the following key subsystems:

Computer Controller – Due to the numerically intensive nature of the software algorithms which estimate curd moisture content, a microprocessor-based controller will be necessary if the instrument is to make measurements in real time.

Microwave Hardware – Consists of a microwave network which is used to measure the reflection or transmission properties of the material under test.

Sensor – Provides an interface between the instrument and the material under test. The sensor transduces the physical properties of cheese curd (such as moisture content, temperature, density etc) into an electrical signature which is dependent upon those properties.

Calibration Algorithm – Before the instrument can be used, it will have to be calibrated against a set of known standards in order to account for imperfections in the microwave hardware.

Sensor Model – A mathematical model which describes the electrical properties of the sensor when it is placed in contact with a sample of curd.

Curd Model – Relates the dielectric properties of cheese curd to moisture content.

Display – Presents results in an appropriate format. This may imply a graphical display to enable monitoring by staff. Alternatively, it may be more desirable to produce an output voltage/current proportional to the moisture content, in order to implement a closed-loop control strategy.

Figure 2.3 depicts the interconnections between these subsystems.

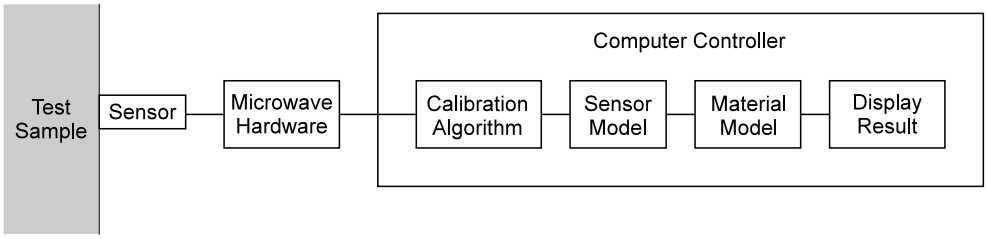

Figure 2.3: Block diagram depicting major components of microwave moisture measurement system.

2.4 Review of Microwave Moisture Sensing Techniques

A large number of microwave moisture sensing methods have been described in the literature. Some pertinent examples are summarised below.

Kudra et al. (1992) have measured the electromagnetic properties of milk at 2.45 GHz using a single-mode active cavity. By measuring the change in the Q-factor of the cavity when samples were placed in it, the permittivity of the samples could be calculated. This enabled the quantities of several constituents of the samples to be estimated. As with all resonant techniques, however, this approach only enables measurements to be made at one frequency.

Kent et al. (1993) have implemented a system which determines the water content of concentrated milk during the manufacture of dried milk products. The method entails the measurement of power lost through a microstrip sensor which is placed in contact with the material under test. Water content is estimated by referring to a family of calibration curves which can be adjusted to compensate for temperature variation. The authors claim that changes in moisture content of $\pm 0.5\%$ may be detected using this system, provided use is restricted to materials with moisture contents below 50%.

Three approaches have been demonstrated by Robinson and Bialkowski (1992) for estimating the moisture content of beach sand by measuring the phase change of a signal transmitted across a sample. Each method makes use of a quadrature mixer, and is contingent upon the density of the sample being known.

Sabburg et al. (1992) have used a waveguide transmission technique to investigate the relationship between permittivity and soil moisture for two Australian soils. A waveguide cell was packed with moistened soil and the transmission coefficient measured using an HP8510 Automatic Network Analyser. This data enabled a transcendental equation relating transmission coefficient to sample permittivity to be solved numerically. The results of this work suggested that the calibration curves built into some commercially available soil moisture measuring instruments are inaccurate.

A density-independent method of moisture determination has been explored by Meyer and Schilz (1980). Transmission measurements were made in a waveguide sample container on a range of materials, including tobacco, feathers and instant coffee. The measured data was used to calculate the complex permittivity, which was then substituted into a function that yielded a result dependent upon moisture content only. This method appeared to work well for materials with low moisture contents (i.e. less than 30%), but became less and less sensitive to any subsequent increases.

2.5 Advantages and Limitations of Microwave Sensing

Before deciding to adopt a microwave-based approach for the measurement of material properties it is helpful to consider the relative merits of this technology.

There are undoubtedly some disadvantages associated with microwave measurement techniques. For example, there is the relatively high expense of microwave sensing to consider, which tends to increase as frequency increases (Nyfors and Vainikainen, 1989, pp. 28–39). There is also the need for very careful, application-specific design of components like sensing heads (Nyfors and Vainikainen, 1989, pp. 28–39). Additionally, the nontrivial problem of instrument calibration must be addressed (Kress-Rogers, 1993, pp. 191–193).

However, in applications such as moisture measurement, microwave sensing has a number of distinct advantages.

Firstly, microwave moisture sensing techniques can be very accurate, often more so than conventional methods. This is because the dielectric permittivity of water at microwave frequencies is much greater than that of biological substances like protein and fat (Kudra et al., 1992). It is therefore the dominant contributor to the overall permittivity of materials like cheese curd, which usually have high moisture contents.

Secondly, microwave sensing is non-hazardous, non-destructive and (depending on the sensor type) non-invasive (Kraszewski, 1996, p. 20).

Thirdly, microwave sensing can be used to measure the bulk properties of a material. Techniques such as infrared sensing only measure the surface properties of the material under test (Kress-Rogers, 1993, pp. 191–193).

Fourthly, microwave measurements can yield information about other constituents besides water. Previous work with milk (Kudra et al., 1992) has demonstrated that it possible to measure protein, salt and fat content in addition to water content.

Finally, if a suitable microprocessor is used to acquire and process data from the microwave instrument, a result can be available within a second or so (Nyfors and Vainikainen, 1989,

pp. 28–39). This real-time measurement capability opens up the possibility of closed loop control, whereby the moisture information from the instrument could be fed back into the manufacturing process, thus providing automatic control of the moisture content of the product.

Chapter 3

Cheese Curd Permittivity Survey

3.1 Introduction

A key phase in the development of a new instrument is gaining an understanding of the measurand of interest. For a microwave moisture sensing instrument this means identifying those parameters which affect the dielectric properties of cheese curd.

This chapter describes a series of experiments that were designed to establish the extent to which curd permittivity is affected by variations in frequency, moisture content and salt content.

The first two sections provide an overview of a waveguide permittivity survey which was conducted on a variety of curd types, including theoretical background, equipment setup and experimental methodology. This is followed by a discussion of a permittivity estimation algorithm which enabled dielectric information to be extracted from measured data. The fourth section presents the results obtained for each curd type, while the fifth section describes the method by which the ionic conductivity of different samples of curd was measured. The chapter concludes with a summary of the findings of the cheese curd measurements and the implications for the development of a moisture sensing instrument.

3.2 Overview of Survey

The technique for measuring cheese curd permittivity was based on work by Ness (1983; 1985) and Sabburg et al. (1992). The method involved filling rectangular waveguide cells with samples of a test material and measuring the transmission coefficient with an Automatic Network Analyser. In order to obtain dielectric information a transcendental equation relating transmission coefficient to permittivity was solved numerically.

A number of waveguide cells of varying sizes were constructed to give coverage of the frequency range 2–12 GHz. Samples of cheese curd were mixed thoroughly prior to being placed into the cells, which were kept in a temperature-stabilised oven at the production temperature. The permittivity was then measured, and the corresponding moisture content determined by weighing and drying the sample.

3.3 Equipment Setup

The equipment setup used for the permittivity survey is depicted in Figure 3.1, the details of which are discussed below.

3.3.1 Automatic Network Analyser

All transmission coefficient measurements were made using a Hewlett Packard 8720C Automatic Network Analyser (hereafter referred to as the 8720C). The frequency range covered by the 8720C extends from 50 MHz to 20.05 GHz with a dynamic range of over 100 dB.

Prior to use the 8720C had to be calibrated to reduce the errors within the instrument, such as source mismatch, imperfect isolation between ports of directional couplers, mismatch due to an internal switch, and mismatch at the reference plane.

Conventional calibration methods for network analysers typically require a number of known calibration standards to be connected to the test ports. The uncalibrated reflection and transmis-

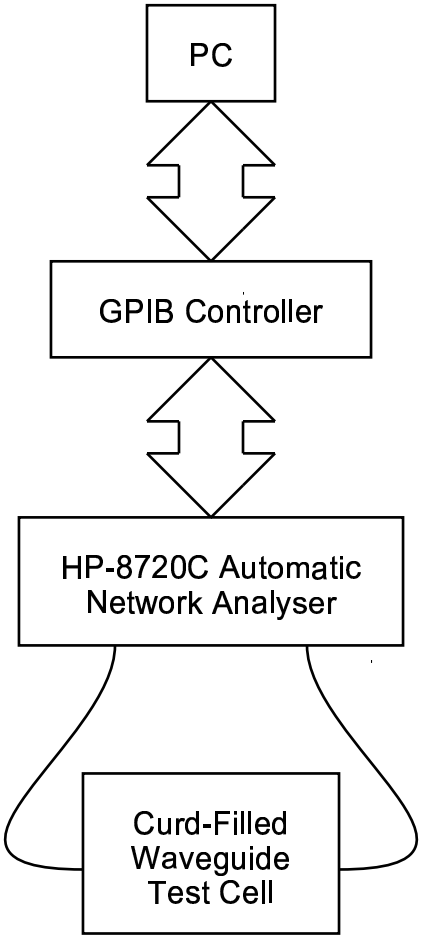

Figure 3.1: Measurement setup used for permittivity survey.

sion coefficients are then measured and entered into an error model of the network analyser. This model is solved for a number of correction coefficients, which enable subsequent measurements to be adjusted such that a much more accurate estimate of the scattering parameters is obtained (Hewlett-Packard Corporation, 1992).

Different error models are possible for a given instrument. In general, the more accurately a model represents the internal mismatches of an instrument, the more calibration standards are required to determine the correction coefficients of the model. For example, the most accurate calibration procedure available on the 8720C is the full two-port calibration. This requires as calibration standards a short circuit termination, an open circuit termination and a matched load. Furthermore, a number of measurements must be made with the two test ports of the instrument connected together directly, or alternatively, connected together via a length of low-loss transmission line.

A less accurate, but simpler, version of this procedure is the through-reflect-line or TRL* (pronounced “TRL-star”) calibration method. This method requires as standards a short circuit OR an open circuit, a low-loss length of line between ports one and two, and a direct connection between the two ports. A variation on this method is the line-reflect-match or LRM* calibration procedure, in which the low-loss transmission line is replaced with a matched termination.

During the course of the cheese curd permittivity survey, both the full two-port and LRM* calibration procedures were evaluated. Due to the greater speed with which LRM* calibrations could be performed, LRM* quickly became the preferred method.

In order to make accurate measurements using waveguide, the above procedures had to be carried out using waveguide calibration standards. A problem arose, however, when trying to implement an open circuited calibration standard. This was because an open waveguide termination radiates energy, resulting in an input reflection coefficient magnitude of less than unity. A phase shift is also induced in the reflected wave due to the effects of the fringing field, which appears as a small terminating reactance (Hewlett-Packard Corporation, 1992). Rather than attempt to account for these effects with a theoretical model, it was far easier to replace the open circuit termination with a short circuit that was offset from the reference plane by a quarter-wave section of waveguide.

All calibration standards except for the matched loads were custom-built at the University of Southern Queensland. Due to the fact that the full two-port and LRM* calibration techniques assumed perfectly conducting short circuit terminations and lossless walls, each calibration standard had to be polished to as smooth a finish as possible, .

3.3.2 Computer and GPIB Controller

Two essential components of the broadband permittivity measurement process were the computer and GPIB controller. These devices facilitated the automation of measurements and the logging of data. When a measurement run was ready to commence the computer would trigger a sweep on the 8720C. The user was then asked to place three markers spaced 90° apart on the network analyser's phase trace; these markers could later be used to calculate a starting estimate of permittivity if one was not already available. The transmission coefficient data and the three marker values were then downloaded to the computer's hard drive, where post-processing could take place to extract permittivity information.

3.3.3 Waveguide Test Cells

Test cells were manufactured in three different sizes of waveguide: WR90, WR159 and WR284. These sizes were chosen because they provided good coverage of the frequency range from 2–12 GHz. Table 3.1 lists the cutoff frequencies for the TE_{10} and TE_{20} modes in each waveguide type.

Table 3.1: Cutoff frequencies for first and second propagating modes in waveguide test cells.

Waveguide Type	f_{co} (GHz)	$2f_{co}$ (GHz)
WR90	6.562	13.123
WR159	3.714	7.428
WR284	2.079	4.159

In practice waveguide is not normally used across the entire bandwidth from f_{co} to $2f_{co}$. This is due to the fact that imperfections and asymmetries in the waveguide can result in propagation

characteristics that depart significantly from the ideal case near these frequencies (Kraus, 1984, pp. 551–560). For example, if the waveguide walls are not perfectly conducting then the attenuation coefficient of the (unfilled) waveguide near f_{co} will be greater than zero, violating one of the assumptions of the permittivity solving software. At the other extreme, as frequency approaches $2f_{co}$ minor imperfections in the waveguide walls can cause coupling to the TE_{20} mode, resulting in errors due to multimoding. In practice it is common to allocate guard bands adjacent to the first and second order cutoff frequencies to reduce the risk of these undesirable effects. For the measurements on cheese curd, however, the full band from f_{co} to $2f_{co}$ was used in an attempt to obtain a continuous permittivity record.

Two cells were manufactured in each waveguide size. This was to eliminate the ambiguity arising from the permittivity solving algorithm, which always produced two possible starting estimates of ε_{r}. Later it was realised that only one cell in each size was required, due to the fact that the larger of the two starting estimates was always the correct one.

Each waveguide test cell had to be made long enough to guarantee that the phase of the transmission coefficient would pass through three consecutive points which were multiples of 90°. Care had to be exercised, however, that the cells were not made so long that the signal emerging from the second port of the cell was outside the dynamic range of the analyser. The lengths of the three most frequently used test cells are listed in Table 3.2.

Table 3.2: Lengths of waveguide test cells used in cheese curd permittivity survey.

Waveguide Type	Length of Test Cell (mm)
WR90	25.0
WR159	30.0
WR284	40.0

Each test cell had a small hole with a screw thread drilled into the centre of the broadwall. This was to allow any excess curd to escape as the samples were heated to the production temperature. It was assumed that the disturbance to the field in the guide due to the screw holes would be negligible. This assumption was later vindicated, when a screw was inserted into the hole such that the end of the screw was flush with the inside wall of the test cell. No measurable difference to the transmission coefficient could be observed.

The basic construction of a waveguide test cell is illustrated in Figure 3.2. The dielectric windows which appear at either end of the cell are discussed in detail in Section 3.3.4.

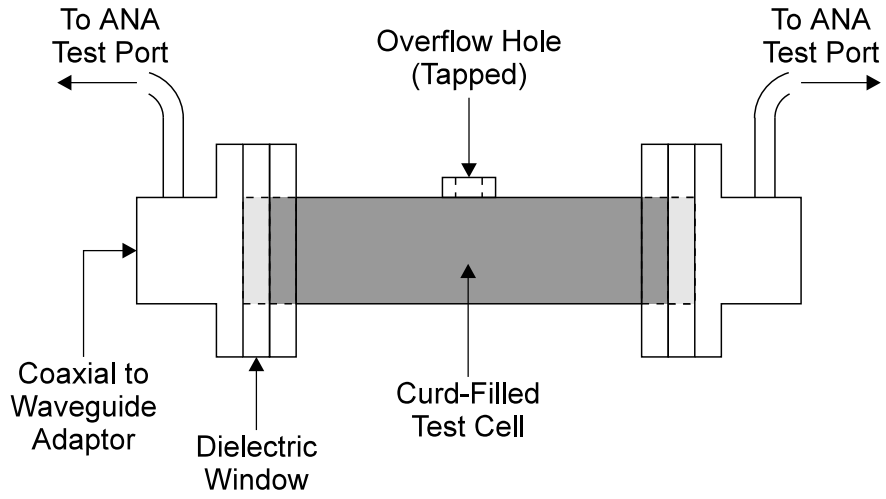

Figure 3.2: Typical waveguide test cell for measuring permittivity of cheese curd.

3.3.4 Dielectric Windows

In order to hold the curd samples in place it was necessary to manufacture dielectric windows for each size of waveguide. By clamping these windows over the end of the test cells, leakage of curd or expressed moisture could be prevented.

The dielectric windows for the smallest sized waveguide type, WR90, consisted simply of a pair of 0.25 inch thick waveguide flanges, with a low-ε_r plug inserted into each flange hole. Machined Teflon blocks were initially used for this purpose, but these proved too difficult to bond securely to the walls of the waveguide flange. This was especially problematic at elevated temperatures, where the different rates of thermal expansion of Teflon and brass would cause the Teflon blocks to drop out of the waveguide flanges under their own weight. Eventually the Teflon blocks were replaced with Araldite. The Araldite was poured into the hole in each flange and allowed to set, before being sanded back flush with the flange faces.

The dielectric windows for the two larger waveguide sizes consisted of 50 mm lengths of waveguide with flanges soldered onto each end. A 0.25 inch thick Teflon block was inserted

into the flange at one end of the waveguide. Persistent problems were again encountered in trying to get the Teflon to bond securely to the wall of the waveguide. The most reliable method was to lay a bead of Araldite around the inside of the waveguide and rest the Teflon block on top. Even this proved at best a temporary fix, as the Araldite would gradually deteriorate at high temperatures.

An advantage of the design of the dielectric windows for the two larger waveguide types was their effect in preventing the coupling of higher-order modes into the test ports of the network analyser. As mentioned earlier, each waveguide type was used between the first and second order cutoff frequencies so that only the TE_{10} mode could propagate. However, the cutoff frequencies of waveguide when filled with a substance other than air are lower than those of air-filled guide. This can be easily shown by examining the equation for the cutoff frequency of waveguide, given below in Equation 3.1:

$$f_c = \frac{1}{2\sqrt{\mu\varepsilon}}\sqrt{\left(\frac{m}{a}\right)^2 + \left(\frac{n}{b}\right)^2} \tag{3.1}$$

For the TE_{10} mode Equation 3.1 reduces to

$$f_c = \frac{1}{2a\sqrt{\mu\varepsilon}} \tag{3.2}$$

From Equation 3.2 it is obvious that if the permittivity ε of the material filling the guide increases, the cutoff frequency f_c decreases. Therefore in the case of the test cells filled with curd, multiple modes could have been excited as the frequency approached $2f_{co}$. If any of these modes had been coupled into the network analyser test ports, later calculations would have been in error, due to the fact that the permittivity solving algorithm assumed that only the dominant mode could propagate.

The dielectric windows of the waveguide sizes WR159 and WR284 reduced the risk of higher order modes being coupled into the test ports by virtue of the 50 mm length of air-filled guide which followed the Teflon blocks. This length of waveguide allowed any higher order modes to decay away such that negligible energy would have remained by the time the signal reached the waveguide-to-coaxial adaptor.

The WR90 dielectric windows did not have a length of air-filled guide between the Teflon/Araldite block and the adaptor, so it is possible that the WR90 measurements suffer from some inaccuracy due to the contributions of higher-order modes.

Another important issue which had to be considered was the effect of the impedance mismatch and nonzero electrical length of each dielectric window on the accuracy of measured results. Some authors have addressed this problem by incorporating the dielectric windows into the mathematical formulation of the S-parameters of the test cell (Bois et al., 1999). This approach requires the permittivity and physical length of the dielectric plugs to be determined in advance, as well as the length of any input and output lines between the reference planes and the dielectric plugs.

For this project, however, it was found that very good results could be obtained by simply calibrating the 8720C at the output planes of the dielectric windows. In this way, the mismatches and phase shifts introduced by the windows were absorbed into the 8720C's own network of systematic errors. The advantages of this approach were threefold:

Firstly, the physical and dielectric parameters of the dielectric windows did not need to be known *a priori* in order to calibrate the 8720C.

Secondly, the mathematical functions for the S-parameters of the samples under test were much simpler to derive, making the permittivity calculation software easier to develop.

Finally, the calibration process was less laborious due to the fact that the dielectric windows did not have to be disconnected and reconnected before and after each calibration.

3.3.5 Temperature Controlled Oven

Different cheese varieties are manufactured at different temperatures. Cream cheese is processed at 80°C, while cheddar and mozzarella cheese are manufactured at about 40°C. Due to the high moisture content of cheese curd, the dielectric behaviour displays a strong temperature dependency.

In order to reproduce the conditions on the production line as closely as possible, a temperature-stabilised oven was used to heat each sample to the production temperature prior to measuring the transmission coefficient. This ensured that the measured dielectric information would be representative of that of the product on the production line.

3.4 Review of Permittivity Measurement Techniques

In order to calculate the permittivity of each curd sample, a suitable algorithm had to be selected to extract dielectric information from the measured S-parameters of the loaded waveguide test cells. A copious number of techniques is available in the literature for this purpose, so the following review is necessarily restricted to a few pertinent examples. While the precise details may vary from method to method, the measurement apparatus is broadly similar in each case. All except one of the reported techniques use test cells that allow both reflection and transmission measurements to be made. The front and back faces of the sample are required to be machined or otherwise formed into a smooth surface such that the incident and reflected waves are normally incident on the sample. Finally, with the exception of the full field approaches, each of the following methods assumes that only one mode of propagation exists within the material under test.

3.4.1 The Transmission/Reflection (T/R) Method

One of the best known techniques for measuring complex permittivity is the Transmission/Reflection (or simply 'T/R') method. Originally suggested by Nicolson and Ross (1970) for TEM-mode fixtures, and subsequently extended by Weir (1974) to cover waveguide, a large number of workers have since developed many variants of this method. Network Analyser manufacturer Agilent (formerly Hewlett-Packard) even offers an Application Note describing how to implement the T/R method using one of their instruments (Hewlett-Packard Corporation, 1985).

As the name implies, the T/R method uses measurements of both S_{11} and S_{21} to infer the relative permittivity ε_{r} and permeability μ_{r} of the material under test. The measured scattering

parameters are related to ε_{r} and μ_{r} via a pair of equations obtained from a signal flow graph analysis of the loaded test cell.

A disadvantage of the conventional T/R method is that the set of equations to be solved becomes ill-conditioned for low-loss samples at frequencies where the length of the sample is an integer multiple of a half-wavelength. This causes gross inaccuracies in the calculated value of permittivity, if indeed it is possible to obtain a solution at all. Baker-Jarvis et al. (1990) have attempted to eliminate this problem by introducing a semi-empirical weighting factor to the set of equations to be solved, which can be used to strengthen or weaken the contributions of S_{11} and S_{22} relative to S_{12} and S_{21}. Using this approach the authors were able to obtain increased accuracy while retaining the relative simplicity which made the original T/R method so attractive.

Boughriet et al. (1997) have also developed a modified version of the T/R method which eliminates the pathological behaviour of the original. Assuming the material under test is nonmagnetic (i.e. $\mu_{\mathrm{r}} = 1$), and presupposing a TEM mode of propagation in the test cell, the authors solve for the effective complex permittivity of the sample. The result is then substituted into an expression which relates the effective permittivity to the true permittivity. In the process, the terms in the original equations which are responsible for causing the instability in the method are eliminated, thereby providing much improved accuracy.

3.4.2 Multiple-Sample/Multiple-Position Methods

Numerous permittivity measurement techniques have been reported in the literature involving the use of several different-length samples and/or several sample locations within the test cell. Each of these methods has been derived by modelling the experimental setup as a cascade of a sample *ABCD* matrix (or in some cases, a wave cascading matrix) between two error matrices. In this way it is possible to mathematically account for the systematic errors introduced by the Network Analyser and the unfilled sections of the test cell. Interestingly, this approach enables the sample permittivity to be calculated from uncalibrated S-parameter measurements. Indeed, some authors claim that calibrating the Network Analyser actually *degrades* the accuracy of their method (Baek et al., 1995).

Enders (1989) has described an iterative method for determining the dielectric and magnetic properties of a material using three samples of different lengths. The reference planes of the measurement system are assumed to coincide with the front and back faces of the sample. Consequently, three different-length test cells are required for this method.

A novel method has been reported by Baek et al. (1995) for determining the permittivity of a material from the S-parameters of a loaded test cell. Again, three sets of measurements must be made, this time with the sample at a different location in the test cell in each case. The complex permittivity of the sample is obtained by iterative solution of a transcendental equation which is derived from an *ABCD* matrix representation of the measurement system. This method requires an accurate starting estimate of permittivity in order to converge to the correct solution.

Two similar methods have recently been presented by Wan et al. (1998) involving four sets of S-parameter measurements. For the first method, two measurements are made on a single sample at two different locations in the test cell. The other two measurements are made on a pair of samples, with the location of one of the samples altered between measurements. In each case it is necessary to record all four S-parameters of the loaded test cell. The second method presented by Wan et al. is similar to the first, except that one of the measurements on the pair of samples is replaced by a measurement on the test cell when empty. Both of these methods enable sample permittivity to be calculated explicitly, provided that a prior estimate of permittivity is available to resolve a sign ambiguity.

Janezic and Jargon (1999) have developed a multiline technique which is slightly less labour-intensive than those described above, requiring only two samples of different lengths to be measured. Using a wave cascading matrix representation of the measurement setup, the authors have shown that it is possible to calculate the propagation coefficient of the sample explicitly. If the test cell is built from a type of transmission line where the relationship between propagation coefficient and permittivity is well understood (e.g. coaxial line or rectangular waveguide), then it only requires one further calculation to determine the complex permittivity.

3.4.3 Full Field Methods

The continuing evolution of fast and cheap desktop computers is gradually making it possible to measure permittivity by direct electromagnetic analysis of the fields in the test cell. This approach typically involves the use of processor- and memory-intensive techniques like the Finite Element method (FEM) or the Finite Difference Time Domain (FDTD) method. Quasi-analytic formulations such as the Method of Moments—which involve a significant amount of algebraic pre-processing but still require a computer to evaluate the final equations—may also be used. Until recently, the time required for these 'full field' solutions to produce a result was prohibitive. However, a number of workers have recently published methods which enable complex permittivity to be calculated from measured S-parameters in a reasonable amount of time.

Jarem et al. (1995) have used a Method of Moments analysis to estimate the complex permittivity and permeability of a partially filled waveguide. This is achieved in two stages. Firstly, the S-parameters of the partially filled waveguide are measured experimentally over a range of sample lengths and heights. Secondly, the simulated S-parameters of the partially filled waveguide—using the same sample lengths and heights as the experimental measurements—are computed repeatedly using the Method of Moments, until values of relative permittivity and permeability are found which minimise a suitably chosen error function.

Abdulnour et al. (1995) have developed an elegant non-iterative method for calculating the permittivity of a discontinuity embedded in a rectangular waveguide or a microstrip line. Using a theoretical formulation based on a combination of the boundary integral equation technique with a modal expansion approach, the authors have generated a family of simulated curves showing the S_{21} of the waveguide or microstrip line as a function of the complex permittivity of the discontinuity. It has then been observed that the curves for $\varepsilon' = \text{constant}$ and $\varepsilon'' = \text{constant}$ can both be described by a relatively simple expression. This allows the complex permittivity of the discontinuity to be calculated explicitly from two sets of S_{21} measurements: one with the sample holder empty, one with the sample holder filled.

In a similar fashion, Huang et al. (1996) have used a technique called the frequency-domain transmission line matrix (FDTLM) method to generate a set of generic curves for a composite

coaxial cell. In contrast to the method of Abdulnour et al. described above, this analysis did not yield a simple explicit expression interrelating S_{21} and ε_{r}. Nevertheless, the authors have shown that it is still possible to estimate the permittivity of the sample in the coaxial cell with an accuracy of better than 1% by simply using the generic curves as a 'lookup table'.

A finite element-based approach has been reported by Deshpande et al. (1997) for samples in a short-circuited waveguide test cell. The solution process involves the use of the Newton-Raphson method to find a value of complex permittivity for which the simulated value of reflection coefficient is equal to the measured value. While simple in principle, this is a very computationally demanding exercise, due to the fact that each iteration of the solution algorithm requires the finite element model to be solved five times in order to calculate the new value of the error function and its partial derivatives.

3.5 Calculation of Permittivity from Transmission Coefficient

The review of permittivity measurement techniques in Section 3.4 has demonstrated that there are many ways to calculate the permittivity of a material embedded in a transmission line test cell. Each approach offers varying degrees of accuracy, speed, versatility and ease of implementation.

For this project, however, a simpler method was chosen. Only one sample was required, of which only the transmission coefficient of the loaded test cell needed to be measured. None of the spurious behaviour associated with the T/R method was encountered, nor was there any need to develop complicated electromagnetic models of the test cell. Furthermore, the method has been shown to work with moist materials (Sabburg et al., 1992), unlike the majority of the methods reviewed in Section 3.4, which were apparently verified solely with low-ε_{r}, low-loss materials such as PTFE.

In essence, the 'transmission coefficient method' enables the permittivity of the sample to be determined by solving the following equation at each frequency of interest:

$$S_{21} = \frac{4\Gamma_1\Gamma_0}{(\Gamma_1+\Gamma_0)^2 e^{\Gamma_1 \mathrm{L}} - (\Gamma_1-\Gamma_0)^2 e^{-\Gamma_1 \mathrm{L}}} \tag{3.3}$$

Equation 3.3 relates the transmission coefficient S_{21} of a filled waveguide test cell of length L to the propagation coefficient Γ_1 of the cell. The term Γ_0 denotes the propagation coefficient of the test cell when empty. This expression has been used by many workers in recent decades. Pertinent examples include Nicolson and Ross (1970), Ness (1985), Hallikainen et al. (1985) and Sabburg et al. (1992).

In practice S_{21} can be measured using an Automatic Network Analyser. Since L and Γ_0 are known in advance, in principle it is possible to solve for Γ_1. The permittivity of the sample in the test cell can be calculated from Γ_1 ($= \alpha_1 + j\beta_1$) using the following relations from Sabburg et al. (1992):

$$\varepsilon'_r = \left(\frac{c}{2af}\right)^2 \left[1 + (\beta_1^2 - \alpha_1^2)\left(\frac{a}{\pi}\right)^2\right] \tag{3.4}$$

$$\tan\delta = \frac{\alpha_1\beta_1 c^2}{2(\pi f)^2 \varepsilon'_r} \tag{3.5}$$

The transcendental nature of Equation 3.3 implies that it has infinitely many solutions, only one of which is physically meaningful. The only way to solve such an equation is via a numerical method. An initial estimate of permittivity is necessary to provide a starting point for the solution process. This can be obtained using a technique which will be described in Section 3.6.

The method used by Ness (1983; 1985) and later by Sabburg et al. (1992) involved the adjustment of ε'_r until the phase angles of the measured and calculated values of S_{21} agreed. Next $\tan\delta$ was adjusted until the magnitudes agreed. This cycle was repeated until the difference between the measured and calculated values of S_{21} was within the required tolerance.

The problem with this approach is that it can be slow to converge. It was eventually rejected in favour of the Newton-Raphson Method, which converges extremely rapidly provided that the initial estimate of ε_{r} is accurate. The only difficulty encountered in using the Newton-Raphson Method in this case was that the function and its derivative were both complex. This was not a serious problem, however, as the Borland C++ compiler offered a complex data type as one of its extensions, making the permittivity solver program quite straightforward to develop.

3.6 Initial Estimate

The technique used to obtain an initial estimate of permittivity was similar to that used by Sabburg et al. (1992), which in turn was based on a method suggested by Ness (1983; 1985).

The idea as originally conceived by Ness involved the estimation of the number of half-wavelengths in a sample. Once this is determined it is a simple matter to calculate the permittivity of the sample. An estimate of the number of half-wavelengths in the sample can be obtained by measuring the frequency at which the phase of S_{21} is a multiple of 90°. At this frequency the phase shift through the sample is given approximately by

$$\beta \mathrm{L} \approx n\pi, \qquad n = \tfrac{1}{2},\ 1,\ 1\tfrac{1}{2},\ \ldots \tag{3.6}$$

where L is the length of the sample and n is the number of half wavelengths in the sample. Mismatches at each end of the sample means the true phase shift will fluctuate around the value predicted by Equation 3.6. However, in practice it was found to be an adequate approximation, which improved as the loss factor of the sample increased due to the greater attenuation experienced by the internally reflected waves.

For a filled length of rectangular waveguide, Ness (1985) has derived the following approximation for the $\varepsilon'_{\mathrm{r}}$ of the material in the waveguide:

$$\varepsilon'_r(f) = \left[1 + \left(\frac{an}{\mathrm{L}}\right)^2\right]\left(\frac{150}{af}\right)^2 \tag{3.7}$$

Using this result, Sabburg et al. (1992) have shown that if two consecutive frequencies are known at which the phase of S_{21} is a multiple of 90°, then Equations 3.8 and 3.9 are obtained:

$$\varepsilon'_r(f_1) = \left[1 + \left(\frac{an_1}{\mathrm{L}}\right)^2\right]\left(\frac{150}{af_1}\right)^2 \tag{3.8}$$

$$\varepsilon'_r(f_2) = \left[1 + \left(\frac{an_2}{\mathrm{L}}\right)^2\right]\left(\frac{150}{af_2}\right)^2 \tag{3.9}$$

If it is assumed that ε'_r is not changing significantly with frequency, it follows that

$$\varepsilon'_r(f_1) = \varepsilon'_r(f_2)$$

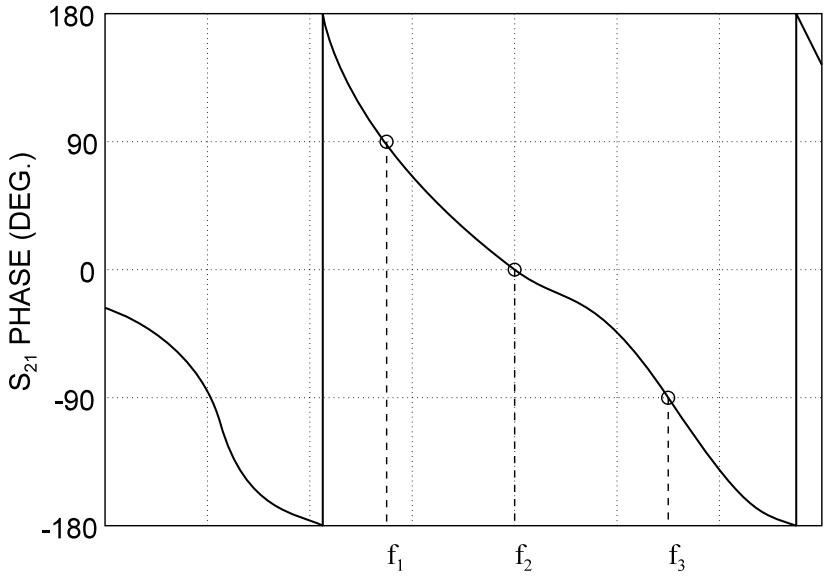

Figure 3.3: Three marker points used to obtain initial estimate of ε_r' from phase of S_{21}.

Equations 3.8 and 3.9 can then be equated to obtain a single equation in n_1 and n_2. By recognising that $n_2 = n_1 + \frac{1}{2}$ for two consecutive frequencies for which the phase of S_{21} differs by 90°, an equation in either n_1 or n_2 is obtained. The quadratic nature of this equation means that two values of n_1 or n_2 are obtained, only one of which is physically valid. Ness resolved this ambiguity by making measurements on two samples of different lengths.

Unfortunately problems arise when attempting to use this technique with highly dispersive materials, where ε_r' may change significantly from one marker to the next. To account for this variation a third point must be measured, also separated by 90° from the other points, as shown in Figure 3.3. This produces the following set of equations to be solved:

$$f = f_1: \qquad \varepsilon_r' + \frac{\partial \varepsilon_r'}{\partial f}(f_1 - f_2) = \left[1 + \left(\frac{a(n_2 - \frac{1}{2})}{\mathrm{L}}\right)^2\right]\left(\frac{150}{af_1}\right)^2 \tag{3.10}$$

$$f = f_2: \qquad \varepsilon_r' = \left[1 + \left(\frac{an_2}{\mathrm{L}}\right)^2\right]\left(\frac{150}{af_2}\right)^2 \tag{3.11}$$

$$f = f_3: \qquad \varepsilon_r' + \frac{\partial \varepsilon_r'}{\partial f}(f_3 - f_2) = \left[1 + \left(\frac{a(n_2 + \frac{1}{2})}{\mathrm{L}}\right)^2\right]\left(\frac{150}{af_3}\right)^2 \tag{3.12}$$

where ε_r' and $\frac{\partial \varepsilon_r'}{\partial f}$ denote the real part of permittivity and its derivative respectively at the middle frequency point f_2.

Solving Equations 3.10 and 3.12 for ε'_r:

$$\begin{bmatrix} 1 & (f_1 - f_2) \\ 1 & (f_3 - f_2) \end{bmatrix} \begin{bmatrix} \varepsilon'_r(f_2) \\ \frac{\partial \varepsilon'_r}{\partial f} \end{bmatrix} = \begin{bmatrix} A \\ B \end{bmatrix}$$

$$\begin{bmatrix} \varepsilon'_r \\ \frac{\partial \varepsilon'_r}{\partial f} \end{bmatrix} = \frac{1}{(f_3 - f_1)} \begin{bmatrix} (f_3 - f_2) & (f_2 - f_1) \\ -1 & 1 \end{bmatrix} \begin{bmatrix} A \\ B \end{bmatrix} \tag{3.13}$$

where

$$\begin{aligned} A &= \left[1 + \left(\frac{a(n_2 - \frac{1}{2})}{\mathrm{L}}\right)^2\right] \left(\frac{150}{af_1}\right)^2 \\ B &= \left[1 + \left(\frac{a(n_2 + \frac{1}{2})}{\mathrm{L}}\right)^2\right] \left(\frac{150}{af_3}\right)^2 \end{aligned}$$

From Equation 3.13 we obtain the following expression for ε'_r:

$$\varepsilon'_r = A\left(\frac{f_3 - f_2}{f_3 - f_1}\right) + B\left(\frac{f_2 - f_1}{f_3 - f_1}\right) \tag{3.14}$$

Equating expressions 3.11 and 3.14 yields:

$$\left[1 + \left(\frac{an_2}{\mathrm{L}}\right)^2\right] \left(\frac{150}{af_2}\right)^2 = A\left(\frac{f_3 - f_2}{f_3 - f_1}\right) + B\left(\frac{f_2 - f_1}{f_3 - f_1}\right) \tag{3.15}$$

Equation 3.15 then reduces to

$$K_1 n_2^2 + K_2 n_2 + K_3 = 0 \tag{3.16}$$

where

$$
\begin{aligned}
K_1 &= \left(\frac{a}{\mathrm{L}}\right)^2 \left[\frac{1}{f_2^2} - \frac{(f_3 - f_2)}{f_1^2(f_3 - f_1)} - \frac{(f_2 - f_1)}{f_3^2(f_3 - f_1)}\right] \\
K_2 &= \left(\frac{a}{\mathrm{L}}\right)^2 \left[\frac{(f_3 - f_2)}{f_1^2(f_3 - f_1)} - \frac{(f_2 - f_1)}{f_3^2(f_3 - f_1)}\right] \\
K_3 &= \frac{1}{f_2^2} - \left[1 + \left(\frac{a}{2\mathrm{L}}\right)^2\right] \left[\frac{(f_3 - f_2)}{f_1^2(f_3 - f_1)} + \frac{(f_2 - f_1)}{f_3^2(f_3 - f_1)}\right]
\end{aligned}
$$

Equation 3.16 is a quadratic equation in n_2, where n_2 is the number of half-wavelengths in the sample at the frequency f_2. Solving this equation for n_2 yields two possible solutions, of which only one is physically valid. One way of resolving this ambiguity is to use the method of Ness which was outlined above, whereby measurements are performed on samples of two different lengths. However, while this approach is reliable, it has the disadvantage of being more expensive to implement, as two test cells are required for each waveguide type. Furthermore, two sets of measurements must be made for each sample, making this approach much more time consuming. This can be a serious drawback if measurements are being made at elevated temperatures, where delays are already incurred in waiting for the temperature of the test sample to equilibrate.

Fortunately, a more efficient means of choosing the correct value of n_2 was found. It was observed that for polar dielectrics, such as distilled water or cheese curd, the larger value of n_2 always corresponded to a negative value of $\frac{\partial \varepsilon_r'}{\partial f}$. Similarly, the smaller value of n_2 always corresponded to a positive value of $\frac{\partial \varepsilon_r'}{\partial f}$. Given that polar materials exhibit a decrease in ε_r' as frequency increases, it is clear that the larger value of n_2, which always produces $\frac{\partial \varepsilon_r'}{\partial f} < 0$, must be the physically valid solution. Obviously this technique could only be applied in situations where qualitative information about the dielectric properties of the material under test was available *a priori*.

Having chosen the correct value of n_2, this estimate had to be rounded off before being used to calculate an initial estimate of permittivity. The rounded value of n_2 depended on the phase of the centre marker. Due to the fact that the phase detection circuit of the Automatic Network Analyser wrapped around from -180° to $+180^\circ$ as phase lag increased, the centre marker could only have four possible phases: 0°, $+90^\circ$, -90°, and $\pm 180^\circ$. A phase shift of 0° was

only possible if there were an even number of half wavelengths in the sample. Therefore, n_2 should be rounded to the nearest even integer. Similarly, a phase shift of $\pm 180^\circ$ could only result from an odd number of half wavelengths in the sample. Hence n_2 should be rounded to the nearest odd integer. Markers with phases of 90° or -90° should be rounded to the nearest odd integer plus $\frac{1}{2}$ or even integer plus $\frac{1}{2}$ respectively. These guidelines are summarised in Table 3.3.

Table 3.3: Guidelines for rounding off n_2 for all possible S_{21} marker phases.

S_{21} Phase	Rounded Value of n_2
0°	Nearest Even Integer
-90°	Nearest Even Integer $+\frac{1}{2}$
$\pm 180^\circ$	Nearest Odd Integer
$+90^\circ$	Nearest Odd Integer $+\frac{1}{2}$

The rounded value of n_2 could then be substituted into either Equation 3.11 or Equation 3.14 to calculate the initial estimate of the permittivity of the sample. Some typical results obtained using this method are presented in Table 3.4.

Table 3.4: Initial estimates of the permittivity of several moist materials as calculated by permittivity estimation algorithm. More accurate values of permittivity obtained using Newton's Method are included for comparison.

Material (% moisture g/g)	Freq. (GHz)	$\lvert S_{21}\rvert$ (dB)	$\angle S_{21}$ (deg.)	n_2 (initial)	n_2 (rounded)	ε' (initial)	$\varepsilon' - j\varepsilon''$ (calculated)
Water	6.1944	-52.76	-90	11.73	11	71.668	$70.456 - j22.362$
	6.5071	-56.78	-180				
	6.8244	-60.80	90				
Mozzarella Cheese Curd (43.4%)	2.7066	-35.08	90	3.72	4	23.574	$22.592 - j12.743$
	3.1168	-36.52	0				
	3.5286	-38.74	-90				
Cream Cheese Curd (50.1%)	9.2958	-31.23	180	7.65	7.5	20.772	$20.581 - j5.383$
	9.9710	-33.23	90				
	10.6530	-35.59	0				

This work was the subject of a journal article which was published in *IEEE Transactions on Instrumentation and Measurement* (Ball and Horsfield, 1998). The article describes the permittivity estimation algorithm in essentially the same way as that given here, with the exception that the journal article is couched in terms of quarter wavelengths in the sample. As a result the rounded estimates of n_2 produced by the algorithm are double those produced when working in terms of half wavelengths. However, the calculated value of permittivity is identical.

In practice this algorithm was found to produce the correct result every time for aqueous dielectrics. However, for non-dispersive dielectrics (i.e. materials for which $\frac{\partial \varepsilon_r'}{\partial f} = 0$) the reliability of this technique deteriorated, displaying a strong dependence on the loss factor of the dielectric. For example, when measuring PTFE, for which $\varepsilon_r' = 2.08$ and $\tan\delta = 0.0004$, the correct value of n_2 was produced. However, for a similar measurement on a sample of acrylic, which has $\varepsilon_r' = 2.6$ and $\tan\delta = 0.015$, no real-number values of n_2 exist which satisfy Equation 3.16. This appears to be a direct consequence of the higher loss in acrylic compared to PTFE.

Ku et al. (1998; 1999; 2001) encountered this problem when attempting to use the same software to measure the dielectric properties of thermoplastic composites at elevated temperatures. In such situations it was necessary to obtain a starting estimate for ε_r from another source, bypassing the aforementioned procedure entirely.

3.7 Verification of Technique

In order to verify that the permittivity calculation software was working correctly, the permittivity of a known substance was measured. Distilled water was chosen for this purpose due to its well understood dielectric properties.

As discussed in Chapter 2, water exhibits strong variation in dielectric behaviour with frequency. The permittivity of water is also sensitive to temperature. Due to its polar nature, water obeys a Debye characteristic, which is repeated here in Equation 3.17:

$$\varepsilon^* = \varepsilon_\infty + \frac{\varepsilon_s - \varepsilon_\infty}{1 + j\omega\tau} \tag{3.17}$$

The parameters ε_∞, ε_s and τ are usually obtained empirically, due to the difficulties which are encountered in analysing the water molecule theoretically (Nyfors and Vainikainen, 1989).

The measured results for distilled water are shown in Figure 3.4, with the Debye curve superimposed for comparison. The agreement for the real parts is within 1%, while for the imaginary parts the agreement is within 3.7%. Due to the extremely high level of attenuation which was experienced in the WR90 band, a shorter test cell (10 mm in length) had to be fabricated to ensure that the signal emerging from the second port of the test cell was within the dynamic range of the 8720C.

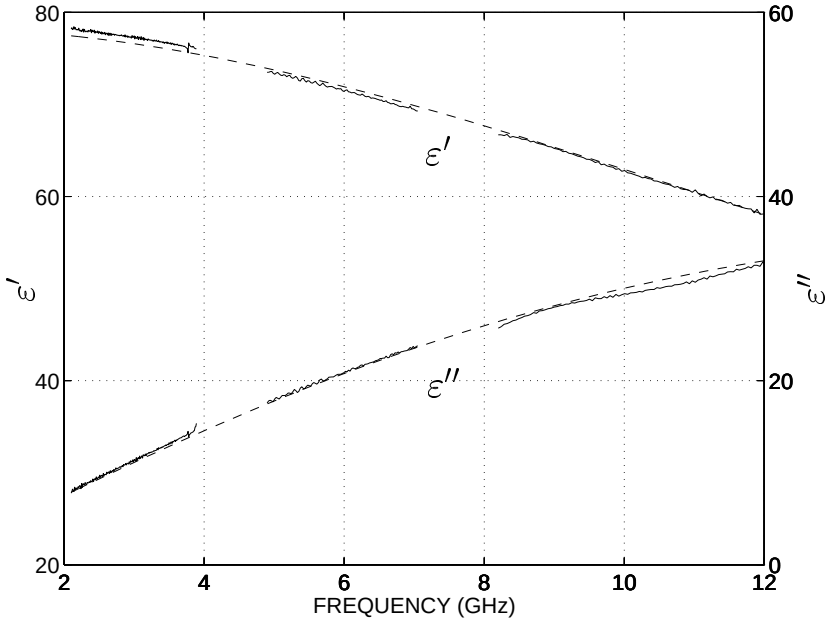

Figure 3.4: Measured and simulated permittivity of distilled water at 25°C.

3.8 Results of Measurements on Cheese Curd

Detailed permittivity measurements were carried out for two different cheese types. The moisture content of each test sample was obtained by conventional weighing and drying. The results of these measurements are presented in the following sections.

This work was the subject of three conference papers. Refer to Horsfield et al. (1996) and Ball et al. (1996a; 1996b) for details.

3.8.1 Cream Cheese Permittivity Measurements

Samples of cream cheese curd were obtained from Tatura Milk Industries in Victoria. Tatura staff placed each sample of curd in a plastic bag in a refrigerated container, which was then shipped to USQ in Toowoomba.

On receipt of the curd samples it was often observed that moisture had pooled at the bottom of the plastic bags, suggesting that the distribution of water through the sample was no longer homogeneous. In order to make the moisture distribution more even, each sample was stirred thoroughly before being loaded into the waveguide test cell.

As cream cheese curd is processed at 80°C, loaded waveguide test cells were placed in the temperature-controlled oven for several hours prior to measuring S_{21} with the Automatic Network Analyser. This ensured that all measurements were made under conditions similar to those of the production environment. The exact temperature of each sample was determined by inserting a small thermocouple-based probe connected to a digital thermometer into the overflow hole at the top of the cell. A typical plot of the measured S_{21} for cream cheese curd is given in Figure 3.5.

Three markers were recorded with S_{21} in order to calculate an initial estimate of permittivity. These markers are plotted on the graphs in Figure 3.5 as circles. The exact values are listed in Table 3.5.

Table 3.5: S_{21} marker values for cream cheese curd sample with 50.1% moisture content.

Frequency (GHz)	S_{21} Magnitude (dB)	S_{21} Phase (deg.)
9.2958	−31.23	180
9.9710	−33.23	90
10.6530	−35.59	0

Using the algorithm described in Section 3.6, the following estimates are obtained for the number of half-wavelengths in the sample and the corresponding value of $\frac{\partial \varepsilon_r'}{\partial f}$:

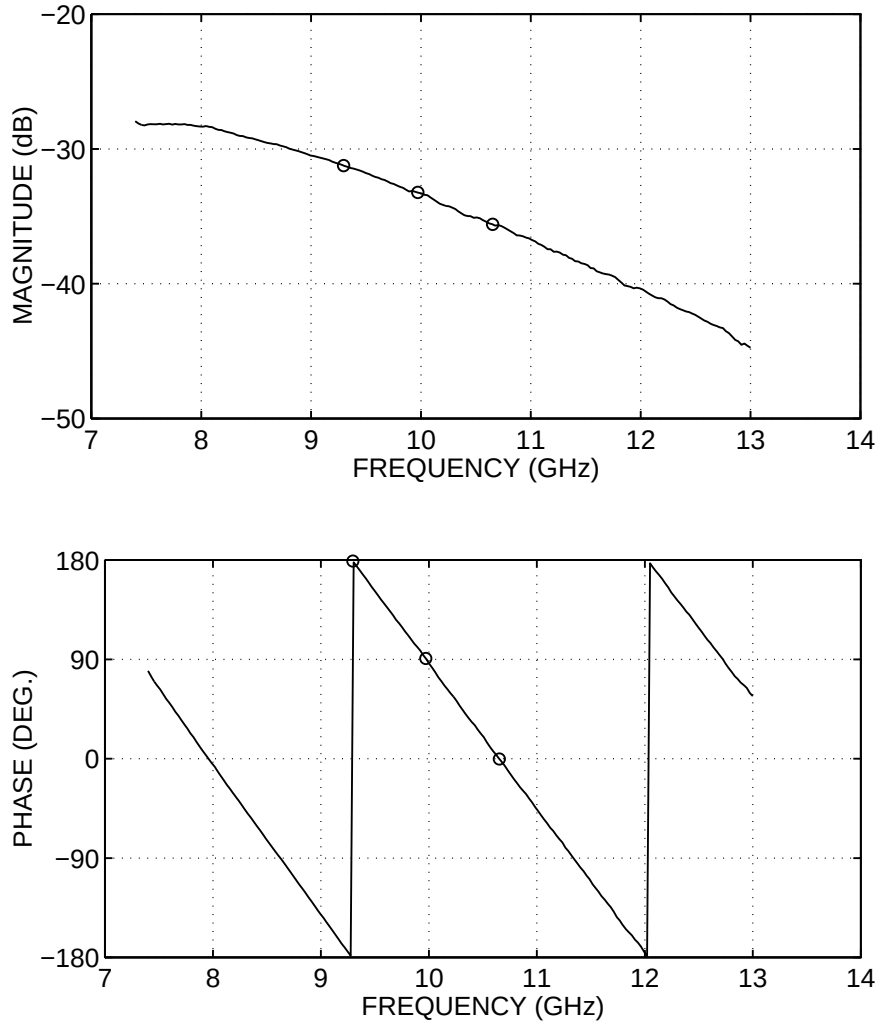

Figure 3.5: Measured transmission coefficient S_{21} of Tatura cream cheese curd sample with 50.1% moisture content at a temperature of 79.4°C. Markers used to obtain permittivity estimate are shown as circles. Test cell is comprised of a 25 mm length of WR90 waveguide.

$$\text{Estimate 1:} \quad n_2 = 3.5, \quad \frac{\partial \varepsilon_r'}{\partial f} = +0.4368 \text{ GHz}^{-1}$$

$$\text{Estimate 2:} \quad n_2 = 7.5, \quad \frac{\partial \varepsilon_r'}{\partial f} = -0.0670 \text{ GHz}^{-1}$$

Given that cream cheese is an aqueous dielectric, Estimate 1 above is obviously the nonphysical solution as it corresponds to a positive value of $\frac{\partial \varepsilon_r'}{\partial f}$. Therefore Estimate 2 is the correct solution (it is also the larger value of n_2, which as discussed in Section 3.6 was always found to correspond to the physical solution).

Substituting n_2 into either Equation 3.11 or Equation 3.14 produces an initial estimate of permittivity of $\varepsilon_r' = 20.7723 - j0$. Using this value as a starting estimate for Newton's method enables the permittivity of the sample to be calculated across the entire frequency band.

The results of these calculations, along with a selection of results from each waveguide size for a range of moisture contents, are presented in Figure 3.6. A number of features in this Figure are worth highlighting.

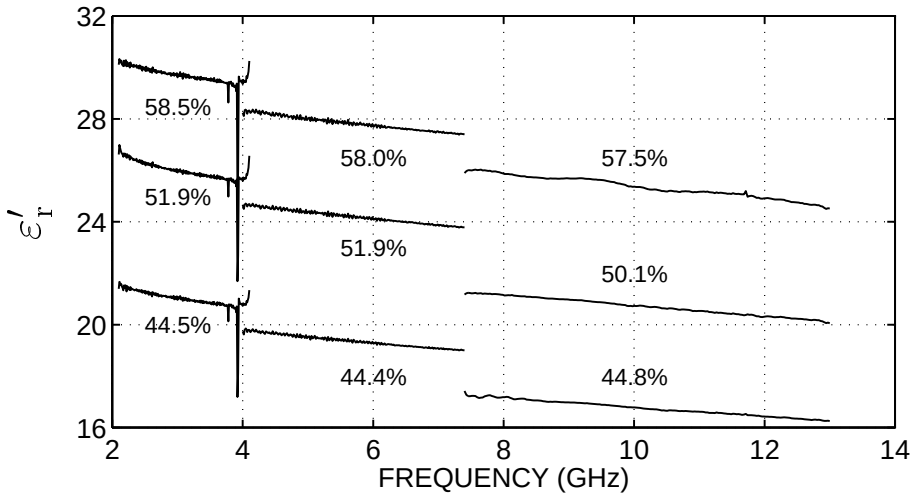

(a) Real part.

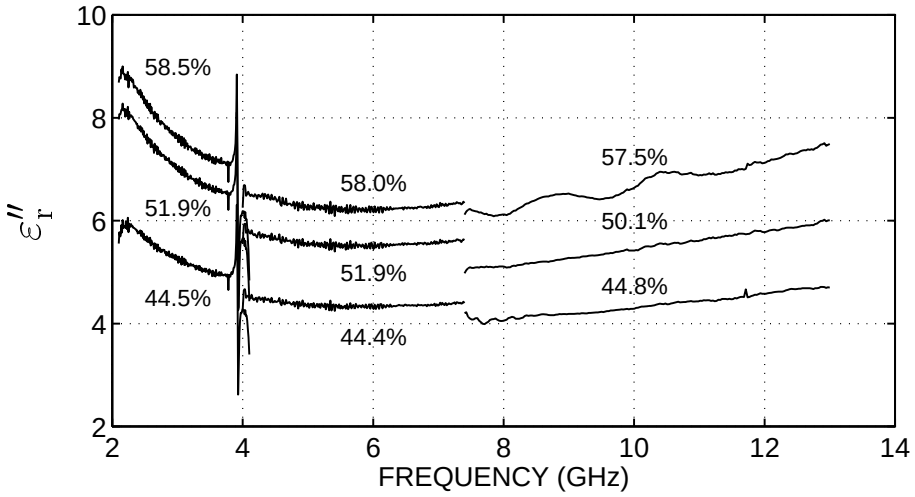

(b) Imaginary part.

Figure 3.6: Permittivity of Tatura cream cheese curd samples for a range of moisture contents.

Firstly, the graph of the real part of permittivity ε_r' has a negative slope, as would be expected for a material with a high moisture content.

Secondly, it is obvious from the graph of the imaginary part of permittivity ε_r'' that each curd sample contained salt. This is revealed by the increased loss factor at low frequencies, a characteristic typical of dielectrics with nonzero conductivity. The impact of free charge on the loss factor of a dielectric was examined in Section 2.2.2, where it was noted that a material with conductivity σ will have an additional loss factor given by

$$\varepsilon_\sigma'' = \frac{\sigma}{\omega\varepsilon_0} \tag{3.18}$$

where ε_σ'' is the loss resulting from the conductivity σ of the material, and ω is radian frequency. As ω increases the value of ε_σ'' becomes asymptotic to zero, and the loss factor is dominated by the polar loss of the water in the material.

Thirdly, the measurements made with WR284 waveguide exhibit some dramatic fluctuations about the mean as the frequency approaches 4 GHz. This spurious behaviour may have been the result of multimoding, an issue which was addressed in Sections 3.3.3 and 3.3.4. Certainly the practice of using each type of waveguide beyond the conventional cutoff frequency would have increased the risk of multimoding occurring. It is also possible that the measured results were adversely affected by impedance mismatches in the waveguide to coaxial transitions. This is not uncommon in practical transitions, which are usually designed to provide a good match within a given waveguide band, but may have significantly poorer return loss at the upper and lower limits of the band. This would have degraded the accuracy of transmission coefficient measurements around these frequencies, contributing to the spurious results observed near 4 GHz.

Fourthly, in Figure 3.6(b) the oscillations in the results for the curd sample with 57.5% moisture content suggest that the integrity of the measurement setup was compromised during this measurement. Most likely to be at fault were one of the solder joints between the semirigid coaxial cable and the SMA adaptors which connect the waveguide adaptors to the 8720C. This was a recurring problem which was exacerbated by the high temperature at which the measurements were performed, and the mechanical stresses caused by the inflexibility of the semirigid cable.

Finally, it is clear in both parts of Figure 3.6 that the permittivity plots for curd samples with the same moisture content do not line up properly from one waveguide band to the next. This discrepancy can almost certainly be attributed to slippage of the dielectric windows, which was discussed in Section 3.3.4. The impact of this problem can be visualised (to a first approximation) as a lengthening of the test cell. As the Teflon shim moves back into the waveguide which contains it, the curd in the test cell moulds itself into the volume previously occupied by the shim. Thus, the effective value of L in Equation 3.3 will be greater than the length of the waveguide test cell itself. (In reality the situation is somewhat more complicated than this, as the shift in the position of the Teflon window invalidates the calibration data stored in the Network Analyser.)

The effect on the calculated value of permittivity is demonstrated in Figure 3.7. The same measured S_{21} data was analysed three times to calculate the permittivity, with a slightly different value of L each time. It is obvious from the displayed results that Equation 3.3 is highly sensitive to small perturbations in the value of L. Indeed, at the upper extreme of the frequency band, where the end of the WR159 graph should line up with the start of the WR90 graph, it can be seen that a slip of 1 mm in the position of one of the dielectric windows (or a slip of 0.5 mm in both windows) results in relative errors of 6.7% and 5.8% in the real and imaginary parts respectively of the calculated permittivity.

Notwithstanding the error introduced by the dielectric windows, a clear correlation can be seen to exist between curd permittivity and moisture content. This is better illustrated by plotting permittivity against moisture content at a single frequency point, as shown in Figure 3.8. The relationship between moisture content and permittivity over the measured range appears to be reasonably linear, as indicated by the least-squares lines of best fit in Figure 3.8. The correlation coefficients for the real and imaginary parts of permittivity are 0.9927 and 0.9897 respectively.

3.8.2 Cheddar Cheese Permittivity Measurements

A substantial number of permittivity measurements were performed on samples of cheddar cheese curd. The same experimental methodology was used as for the cream cheese measure-

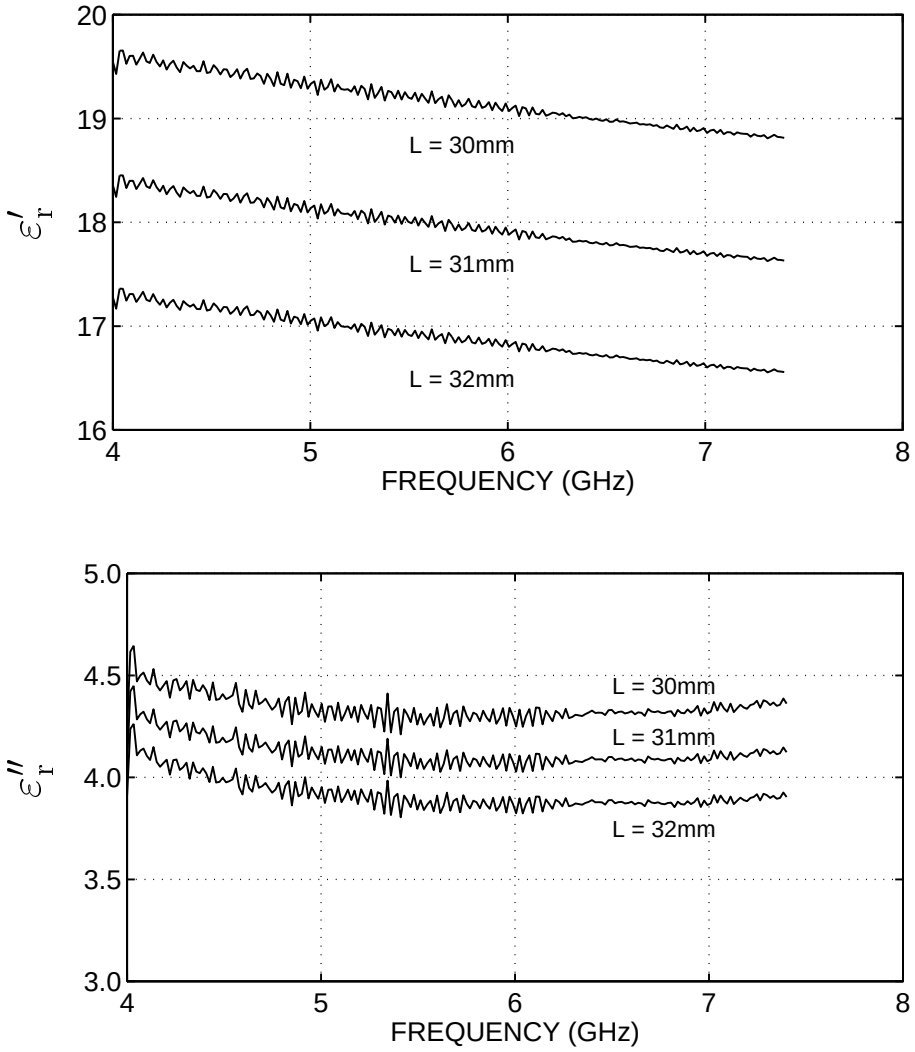

Figure 3.7: Graphs demonstrating sensitivity of calculated permittivity to perturbations in length of test cell (waveguide type = WR159, moisture content = 44.4%, temperature = 79.4°C). The true length of the test cell is 30 mm.

ments, with the exception that the oven temperature was lowered to the production temperature for cheddar cheese (approximately 40°C). The other difference was that the cheddar samples had a much firmer consistency than the cream cheese samples, requiring greater care to be exercised in molding each sample into the waveguide test cells to avoid air gaps.

The results obtained for cheddar cheese curd demonstrated many of the same characteristics as the cream cheese measurements. As such, they are not presented here, but are included in Appendix B for reference.

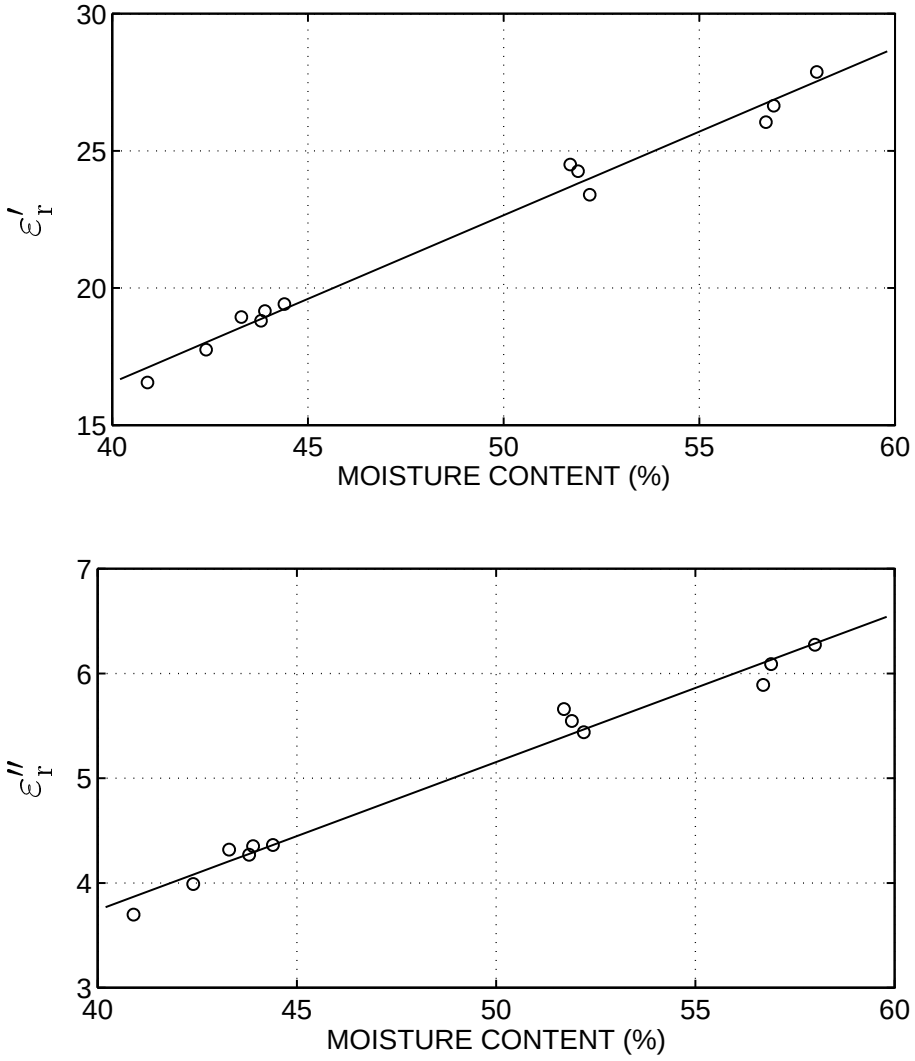

Figure 3.8: Complex permittivity vs moisture content for Tatura cream cheese curd at a frequency of 5.7 GHz (waveguide type = WR159, temperature $\approx 80°C$). Measured data is represented by small circles. The solid lines are the least-squares lines of best fit to this data.

3.9 Conductivity Measurements

In Section 3.8.1 it was shown that the loss factor of cheese curd at lower frequencies was strongly affected by ionic conductivity. In order to quantify this parameter the test cell shown in Figure 3.9 was fabricated.

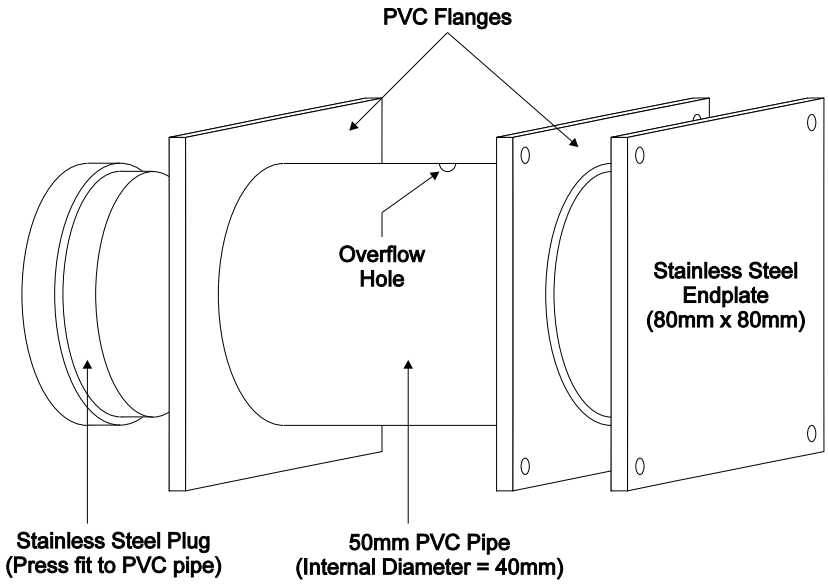

Figure 3.9: Exploded view of test cell used to measure ionic conductivity of cheese curd.

The test cell consisted of 50 mm length of PVC pipe of internal diameter 40 mm, with a PVC flange glued onto each end. A stainless steel plug was inserted into one end of the pipe to hold the curd sample in place. Not visible on Figure 3.9 is a short stainless steel lug which was brazed onto the exterior face of the plug, to enable the test cell to be connected into an electrical circuit. Upon filling the test cell with a sample of curd, a plate was bolted over the end of the pipe. Any excess curd was expressed through a small bleeder hole drilled into the top of the pipe. The conductivity cell was then placed in the oven to be heated to the production temperature. When the temperature of the curd sample stabilised, the test cell was placed into the measurement circuit depicted in Figure 3.10.

A 50 Hz sinusoidal source was connected in series with the curd-filled test cell. (An AC source was used in order to minimise the effects of polarisation.) The r.m.s. values of the volt drop

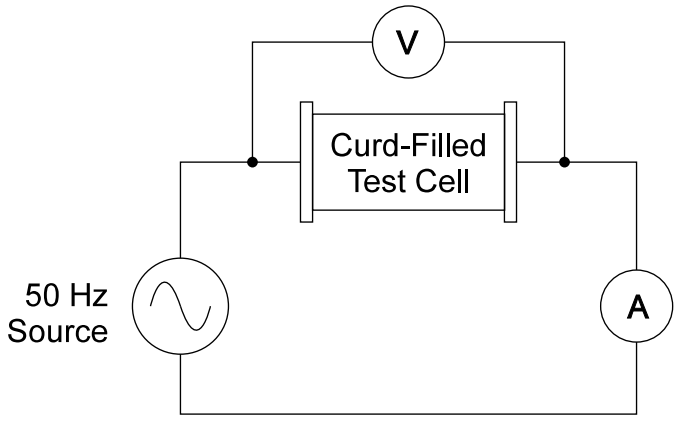

Figure 3.10: Equipment setup used to measure ionic conductivity of curd sample in PVC test cell.

across the cell and the current flowing through it were then measured, and the conductivity σ calculated as follows:

$$\sigma = \frac{I_{\mathrm{rms}} l}{V_{\mathrm{rms}} A} \qquad \text{S/m} \tag{3.19}$$

where V_{rms} and I_{rms} are the r.m.s. voltage and current across and through the cell respectively, l is the length of the cell, and A is its cross-sectional area.

Like permittivity, the conductivity of cheese curd was also found to depend upon moisture content, as shown in Figure 3.11. This begs the question as to why this parameter was not used as the basis for a moisture sensing instrument, instead of permittivity.

The answer is that the conductivity of an aqueous dielectric does not depend on moisture content per se. On the contrary, deionised distilled water has a conductivity of zero. The correlation between conductivity and moisture content observed in Figure 3.11 is actually a consequence of the dissolved salts in the milk from which the cheese is manufactured. Depending on the source of the milk, the proportion of dissolved salt will vary from batch to batch. As such, an instrument which relied upon conductivity to measure moisture content would really be a ‘salt meter’, not a moisture meter.

This can be demonstrated by comparing conductivity measurements on mozzarella cheese at four different points in the manufacturing process. These results are shown in Figure 3.12.

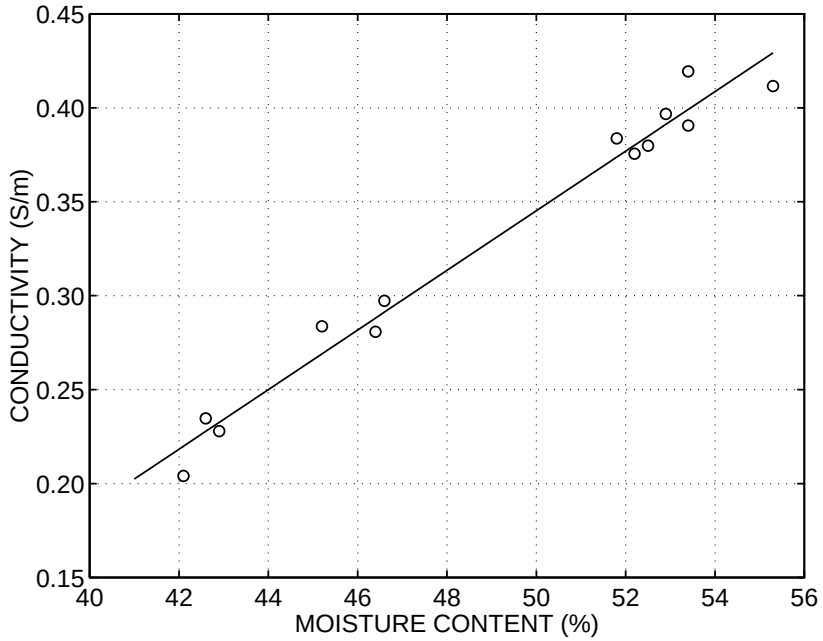

Figure 3.11: Conductivity vs moisture content for Tatura cream cheese curd at a temperature of 80°C. Measured data is represented by small circles. Solid line is the least-squares regression curve of conductivity on moisture content.

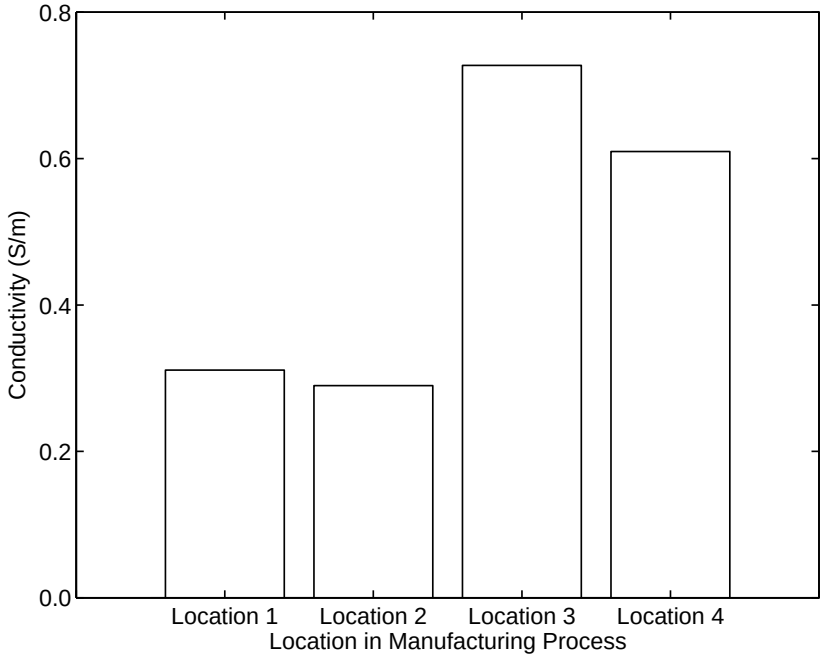

Figure 3.12: Conductivity of mozzarella curd measured at different stages in the manufacturing process.

The first two measurements were made at Locations 1 and 2, where the curd is still very wet and the only salt in the curd is that which was present in the milk. The second two measurements were made at Locations 3 and 4, where the curd is a few percent dryer and salt has been added. Due to the lower moisture content of the curd at the latter two locations, it would intuitively seem fair to assume that the conductivity should also be lower. However, it is clear from Figure 3.12 that the conductivity is significantly higher at these locations, despite the lower moisture content. The only parameter which has changed apart from moisture content is the salt content. The conclusion to be drawn from these results is that conductivity does not necessarily provide a reliable indication of the moisture content of cheese curd.

3.10 Conclusion

This chapter has described a series of measurements on the electromagnetic properties of cheese curd as a function of moisture content and frequency.

Using an Automatic Network Analyser to measure the transmission coefficient of a variety of cheese curd types, the complex permittivity of each sample was calculated. It was observed that the permittivity of all curd samples was a strong function of frequency. The behaviour of curd permittivity was consistent with a Debye characteristic, however there was also evidence of a contribution to the loss factor at low frequencies. This was attributed to ionic conductivity caused by the presence of dissolved salts.

Measurements performed on a number of curd samples indicated that there is a clear correlation between moisture content and permittivity. Within the range of measured values the real part of permittivity was found to be more sensitive to changes in moisture content than the imaginary part. Both values increased approximately linearly with increasing moisture content.

In the process of conducting this work a novel means has been developed of resolving the ambiguity inherent in waveguide permittivity measurements. This algorithm was found to be highly reliable when measuring dispersive materials. It was less reliable when the measurand had a constant permittivity and a large loss factor.

A purpose-built test cell has been fabricated to measure the conductivity of different types of curd over a range of moisture contents. It was found that while conductivity increased as moisture content increased, this parameter was also strongly affected by the salt content of the curd. This suggests that conductivity-based moisture sensing techniques are likely to be unreliable unless the salt content of the ingredients can be normalised prior to their addition to the production process.

Chapter 4

Six-Port Reflectometer

4.1 Introduction

One of the main propositions of this thesis is that accurate measurement of material properties can be achieved at relatively low cost using microwave-based techniques. To demonstrate the validity of this proposition, a laboratory prototype of a microwave moisture meter was implemented. The following chapter describes the development of this instrument from concept to realisation.

The first section introduces the six-port reflectometer, which forms the core hardware of the moisture sensing instrument. Indeed, nearly all of the other components in the instrument can be regarded as support hardware for this device. The theory of operation of six-ports is summarised, and a geometrical interpretation of the six-port power ratio equations is presented.

The second section is concerned with instrument calibration. Topics of discussion include the calibration algorithm which was used, and the choice of standard terminations.

The third section explains how the the six-port concept can be extended to enable transmission measurements to be made.

The fourth section reviews some pertinent examples from the literature of previous six-port

implementations. This provides evidence to support the assertion that a six-port was an appropriate choice of measurement engine for the instrument.

The next eight sections describe how the laboratory prototype was constructed. Each of the main building blocks are discussed in turn, including the six-port network, oscillator, frequency stabilisation circuit, sensor, data acquisition and control hardware, and computer controller. Also discussed is the means by which the diode detectors were characterised, providing improved accuracy and dynamic range.

Finally, the overall performance of the instrument is evaluated, including strengths, limitations and areas where future efforts should be directed.

4.2 Six-Port Fundamentals

The device at the heart of the prototype moisture sensing instrument was a microwave six-port reflectometer. The concept of using a six-port network for measuring vector impedances has been around since at least 1966 (Labaar, 1984). Intensive development work on six-ports was later undertaken by such workers as Engen and Hoer (Engen and Hoer, 1972; Engen, 1976; Engen, 1978b).

A highly attractive feature of the six-port reflectometer is that it enables accurate vector reflection measurements to be made using only scalar (i.e. power sensing) components. No frequency conversion or phase sensing circuitry is required, making the six-port a comparatively simple and cheap alternative to conventional instruments like the Automatic Network Analyser.

4.2.1 Theory of Operation

A schematic representation of a six-port system is shown in Figure 4.1. The basic elements are a microwave signal source, a six-port network and a sensing interface to the material under test. Four diode detectors P_3–P_6 are used to make power measurements at different points in the circuit, from which the vector reflection coefficient Γ of the test material can be calculated explicitly. This result can then be used to determine the permittivity and/or moisture content of the sample, provided a suitable sensor model or calibration curve is available.

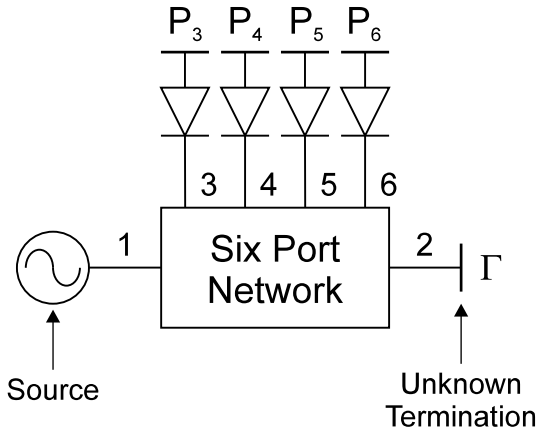

Figure 4.1: Block diagram of a six-port reflectometer. Γ represents the vector reflection coefficient of the unknown termination on Port 2.

Generally speaking the six-port network depicted in Figure 4.1 can be comprised of any linear junction with six connections to the 'outside world'. Indeed, a range of six-port topologies has been described in the literature, and it is clear that performance characteristics can vary markedly between designs. Consequently, the decision as to which six-port network to use for a given application is an important one.

A concise derivation of the theory of operation of the six-port reflectometer has been presented by Somlo and Hunter (1985, pp. 183–198), the salient points of which are summarised here for completeness.

Firstly, the impedances of power meters P_3–P_6 are assumed to be matched to Ports 3–6 of the six-port. This simplifies the problem greatly, as the power measured at P_3–P_6 then depends only on the incident and reflected waves at Port 2. It can be shown (Somlo and Hunter, 1985, pp. 184–185) that the signals b_3–b_6 emergent at Ports 3–6 can be written

$$b_i = M_i a_2 + N_i b_2 \qquad i = 3,\ 4,\ 5,\ 6 \tag{4.1}$$

where M_i and N_i are complex constants, and a_2 and b_2 are the incident and reflected waves respectively at Port 2. This implies that the power P_i measured at the i^{th} port will be proportional to $|b_i|^2$, i.e.

$$P_i = |M_i a_2 + N_i b_2|^2 \qquad i = 3,\ 4,\ 5,\ 6 \tag{4.2}$$

In practice, of course, the assumption of perfectly matched detectors will not be true. A finite mismatch will exist at each port of the six-port network, requiring a calibration procedure to be performed in order to correct for these effects. This issue is discussed in more detail in Section 4.3.

The next step is to select one of the measurement ports as a reference port, and normalise the other three ports to it. If the reference port is chosen to be Port 6, then the power ratios p_i at the other three ports are

$$p_i = q_i \left| \frac{1 + A_i\Gamma}{1 + A_6\Gamma} \right|^2 \qquad i = 3,\ 4,\ 5 \tag{4.3}$$

where

$$\begin{aligned} p_i &= \frac{P_i}{P_6} \\ q_i &= K_i \left| \frac{N_i}{N_6} \right|^2 = K_i \frac{|S_{i1}|^2}{|S_{61}|^2} \\ K_i &= \text{real constants of proportionality} \\ A_i &= \frac{M_i}{N_i} = \frac{S_{i2}S_{21}}{S_{i1}} - S_{22} \end{aligned}$$

The three nonlinear equations represented by Equation 4.3 can be solved explicitly for the vector reflection coefficient Γ of the unknown termination on Port 2 (Somlo and Hunter, 1985, pp. 186–188):

$$\Gamma = \frac{\sum_{i=3}^{6}(F_i + jG_i)p_i}{1 + \sum_{i=3}^{5} H_i p_i} \tag{4.4}$$

where F_i, G_i and H_i are real constants which must be determined through calibration.

4.2.2 Graphical Interpretation of Six-Port Operation

A more intuitive understanding of how six-ports work can be gained from a graphical representation of the power ratio expressions in Equation 4.3. Each of these expressions represents a cir-

cle in the complex Γ-plane. If an unknown load is attached to Port 2 of the six-port, the reflection coefficient is given by the point of intersection between the three circles (Engen, 1978b). This is illustrated in Figure 4.2.

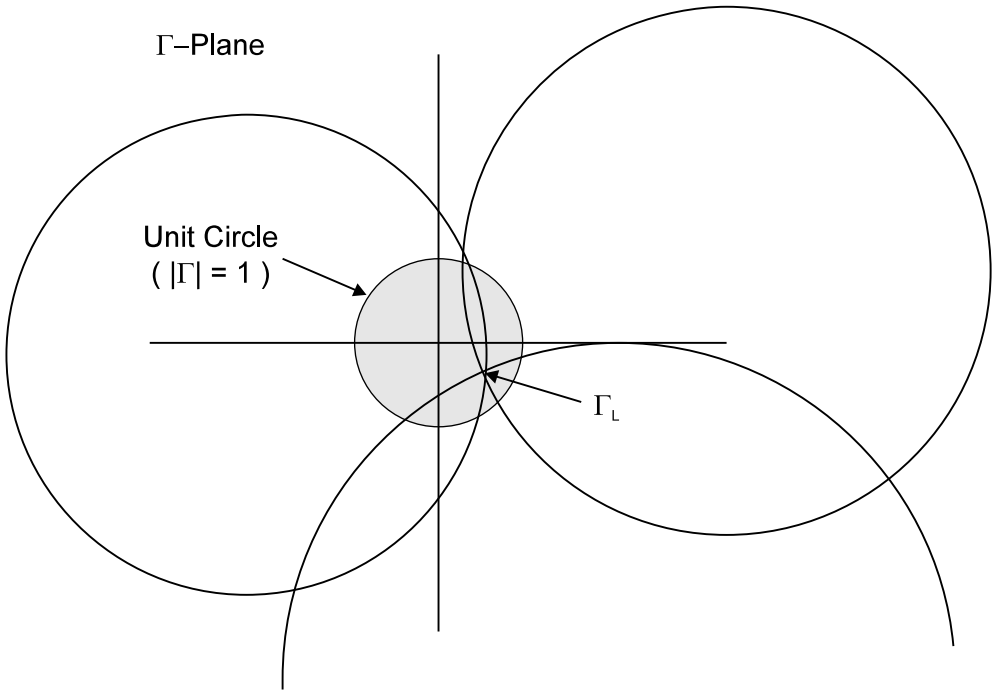

Figure 4.2: Plot of six-port power ratio equations in the complex Γ-plane. Point of intersection yields reflection coefficient Γ_L of load on Port 2.

Expressions for the centre and radius of each circle can be derived by rearranging Equation 4.3. Dividing both sides by q_i we obtain

$$\left|\frac{1+A_i\Gamma}{1+A_6\Gamma}\right|^2 = e_i \tag{4.5}$$

where $e_i = p_i/q_i$.

Expanding the numerator and denominator of the left hand side of Equation 4.5 into products of complex conjugate factors yields

$$\frac{(1+A_i\Gamma)(1+A_i^*\Gamma^*)}{(1+A_6\Gamma)(1+A_6^*\Gamma^*)} = e_i \tag{4.6}$$

$$(1+A_i\Gamma)(1+A_i^*\Gamma^*) = (1+A_6\Gamma)(1+A_6^*\Gamma^*)e_i \tag{4.7}$$

Expanding Equation 4.7 and collecting like terms:

$$|\Gamma|^2 + \Gamma\frac{(e_iA_6 - A_i)}{(e_i|A_6|^2 - |A_i|^2)} + \Gamma^*\frac{(e_iA_6^* - A_i^*)}{(e_i|A_6|^2 - |A_i|^2)} = \frac{(1 - e_i)}{(e_i|A_6|^2 - |A_i|^2)} \tag{4.8}$$

Completing the square:

$$\begin{aligned} |\Gamma|^2 + \Gamma\frac{(e_iA_6 - A_i)}{(e_i|A_6|^2 - |A_i|^2)} + \Gamma^*\frac{(e_iA_6^* - A_i^*)}{(e_i|A_6|^2 - |A_i|^2)} \\ + \frac{|e_iA_6 - A_i|^2}{(e_i|A_6|^2 - |A_i|^2)^2} = \frac{(1 - e_i)}{(e_i|A_6|^2 - |A_i|^2)} + \frac{|e_iA_6 - A_i|^2}{(e_i|A_6|^2 - |A_i|^2)^2} \end{aligned} \tag{4.9}$$

Factorising Equation 4.9 and taking the square root of both sides completes the transformation:

$$\left|\Gamma + \frac{(e_iA_6^* - A_i^*)}{(e_i|A_6|^2 - |A_i|^2)}\right| = \frac{\sqrt{(1 - e_i)(e_i|A_6|^2 - |A_i|^2) + |e_iA_6 - A_i|^2}}{(e_i|A_6|^2 - |A_i|^2)} \tag{4.10}$$

Equation 4.10 represents a circle with centre C_i and radius R_i given by

$$C_i = \frac{-(e_iA_6^* - A_i^*)}{(e_i|A_6|^2 - |A_i|^2)} \tag{4.11}$$

$$R_i = \frac{\sqrt{(1 - e_i)(e_i|A_6|^2 - |A_i|^2) + |e_iA_6 - A_i|^2}}{(e_i|A_6|^2 - |A_i|^2)} \tag{4.12}$$

The measurement of the unknown reflection coefficient has thus been reduced to a geometrical problem which entails the determination of a point common to all three six-port circles.

4.2.3 Impact of Circle Locations on Performance

Apart from the assumption of matched power meters, the six-port equations derived in Sections 4.2.1 and 4.2.2 are totally general. A significant feature of these equations is that the centres of the six-port circles are functions of reflection coefficient. This is clear from Equation 4.11, which shows that C_i is a function of e_i, where

$$e_i = \left|\frac{1 + A_i\Gamma}{1 + A_6\Gamma}\right|^2$$

The variable nature of C_i can cause problems in practical six-ports. For example, the situation may arise where all three circle centres lie close together in the complex plane. As a result the three circles will be almost concentric, making the point of intersection very sensitive to noise or residual calibration errors. Another problem can occur if any of the circle centres lie inside the perimeter of the Smith chart. In the event that the unknown reflection coefficient is in close proximity to one of the circle centres, the radius of the corresponding circle will be relatively small. As a result the signal-to-noise ratio may be very small in this region of the Smith chart, adversely affecting measurement accuracy (Berman et al., 1987).

A well-known solution to the problem of wandering circle centres is to design the six-port network such that the reference port responds only to the forward signal. This is usually achieved using a directional coupler. From Equation 4.2 we know that the power measured at Port 6 of the six-port network is

$$P_6 = |M_6 a_2 + N_6 b_2|^2$$

If the six-port network is designed such that only the forward signal b_2 is monitored at this port, then M_6 must equal zero. Since $A_6 = M_6/N_6$ this implies $A_6 = 0$ as well. It is then easy to show that Equations 4.11 and 4.12 reduce to

$$C_i = -\frac{1}{A_i} \tag{4.13}$$

$$R_i = \left|\Gamma + \frac{1}{A_i}\right| \tag{4.14}$$

The above expression for the circle centres C_i is dependent only upon the complex constants A_i, which are fixed for a given six-port design. Thus, as the reflection coefficient of the unknown termination varies, only the radius of each circle will change.

Having demonstrated that it is possible to fix the locations of the six-port circles in the complex plane, the next question is where these locations should be. Intuitively it seems reasonable to assume that the three circles should be roughly equispaced around the perimeter of the Smith chart. As for the distance of the circle centres from the origin, Engen (1977b) has suggested that a value of approximately 1.5 provides a favourable tradeoff between the dynamic range and resolution required of the power sensing circuitry.

4.2.4 Impact of Noise and Calibration Errors on Performance

In practice the presence of noise and imperfections in the calibration data may result in the three circles not intersecting at a single point. Instead, a small quasi-triangular region may be defined, with the true reflection coefficient residing either in or near this region (Somlo and Hunter, 1985, p. 190). Alternatively, the three circles may not intersect at all. Either way, a level of uncertainty will surround the calculated value of reflection coefficient.

Some workers have attempted to mitigate against the effects of noise by calculating statistically based 'best guesses' of reflection coefficient (Brunetti, 1991). Such techniques enable confidence levels to be assigned to measurements, and can even provide an indication of how the noise sensitivity of the six-port varies for different values of reflection coefficient (Berman et al., 1987).

However, for the purposes of this project such measures were not employed. The measured reflection coefficient was calculated using Equation 4.4, even though this formulation may not necessarily produce an optimal estimate of Γ (Berman et al., 1987). It was believed that the first and best line of defence against noise and calibration errors was to optimise those components most susceptible to such problems. This implies the use of low-noise power meters, a frequency-stabilised oscillator (preferably with low phase noise) and high quality calibration standards. Further improvements in robustness were sought through the use of a six-port network having circle centres at sensible locations in the complex plane, as discussed in Section 4.2.3.

4.3 Calibration Procedure

Prior to use a six-port reflectometer must be calibrated against a set of known standards. The calibration procedure enables the constant terms F_i, G_i and H_i in Equation 4.4 to be determined, thereby making calculation of reflection coefficient possible.

A wide range of calibration algorithms has been suggested in the literature; see for example work by Engen (1978a), Woods (1979), Somlo and Hunter (1982), Neumayer (1990), and

Yakabe et al. (1994). Most of these are algebraically complicated in their derivation, and labour-intensive in their execution due to the (typically) large number of calibration standards required.

One of the more efficient six-port calibration algorithms which has been reported is that of Hunter and Somlo (1985). This technique requires five standards with more or less arbitrary impedances. The only restrictions are that the impedances may not all have the same magnitude nor the same phase, and it is preferable for one of the standards to be a near-match. This technique has a number of advantages over other calibration algorithms.

Firstly, as mentioned above only five calibration standards are required. This is in contrast to other approaches (e.g. Somlo and Hunter, 1982) which can require six or more calibration standards. Indeed, Ghannouchi and Bosisio (1991) have reported a method requiring *thirteen* calibration standards to be connected to the six-port before useful measurements can be made. Obviously the less standards that are required, the faster the instrument can be calibrated. This is desirable if the six-port is to be installed in a factory environment, where it may require periodic recalibration by non-specialist staff.

Secondly, the algorithm of Hunter and Somlo is explicit. Iterative methods such as that described in (Somlo and Hunter, 1982) were avoided as they often require more sophisticated programming to ensure that spurious (i.e. non-physical) solutions are rejected. This is especially the case when noise is present, as the solution procedure then involves the minimisation of an error function. This can be more difficult than the noise-free case, which usually entails the solution of an equation via an established numerical technique such as Newton's method.

Finally, the calibration algorithm in question only requires simple reflective standards and a matched load. Other techniques, such as that of Tarr (1983), involve the use of sliding loads and/or sliding shorts. Such devices are relatively expensive and, unlike simple fixed shorts, cannot usually be custom-built to save money.

Clearly the favourable combination of features offered by the Hunter and Somlo algorithm made it a sensible choice. The specific details of this technique have been well documented by Somlo and Hunter (1985, pp. 193–198), and will not be repeated here.

4.4 Transmission Measurements: The Dual Six-Port

The preceding sections, and indeed the remainder of this chapter, are concerned solely with reflection-based tools and techniques. However, it will be shown in Part II of this thesis that reflection-based techniques are often inferior to those based on transmission measurements. This is largely due to the fact that transmission-based techniques sample a larger volume of the material under test, and therefore tend to be less sensitive to localised variations in composition and microstructure.

It is possible to extend the six-port principles described in Section 4.2 to enable transmission measurements to be made. This requires a duplicate set of six-port hardware, a power divider and a variable phase shifter (Labaar, 1984). Some techniques also require two variable attenuators (Engen, 1978b). The resulting configuration is commonly referred to as a Dual Six-Port, and enables all the scattering parameters of a two-port network to be determined.

Not surprisingly, the calibration of a dual six-port is somewhat more complicated than that of a conventional six-port reflectometer, and the extra hardware which is required more than doubles the cost. For these reasons no attempt was made to incorporate a dual six-port into this project. However, as mentioned above, there is compelling evidence favouring transmission-based techniques over reflection-based techniques, and future work in this area would be well spent adapting the dual six-port for use in microwave sensing.

4.5 Review of Six-Port Applications

Six-ports can be used for virtually any application involving vector impedance measurements to be made. Many examples of practical six-port applications have been reported in the literature, a selection of which is presented below.

Holdem and Tuck (1992) have applied the six-port principle to the problem of measuring the thickness of surface fat on animal carcasses. By irradiating part of the carcass with microwave energy and measuring the amplitude and phase of the resulting standing wave pattern, the reflection coefficient of the carcass can be measured. The reflection coefficient is then transformed to fat depth via a neural network program.

Moreau et al. (1994) have devised a six-port-based method of detecting changes in the permittivity of a test sample while it is being heated in an intense microwave field. The six-port configuration used here is similar to that employed by Holdem and Tuck (1992).

Ghannouchi and Bosisio (1989) have made broadband permittivity measurements on high-loss dielectric liquids using an automatic six-port reflectometer with an open-ended coaxial test probe as the sensing head. The test probe was immersed in each liquid and the reflection coefficient measured. Permittivity information was then extracted from the reflection coefficient data using a model of the fringing field at the end of the test probe.

A six-port network analyser with a real-time display has been implemented by Bialkowski and Dimitrios (1993) for the purpose of making transmission measurements. A somewhat unconventional calibration scheme was used, involving a phase shifter and an attenuator. The complex transmission coefficient was obtained from measured voltages via an iterative algorithm. Reasonably accurate transmission measurements could be made using this system, the uncertainty being $\pm 1^\circ$ for phase and ± 0.5 dB for magnitude. A dynamic range of 40 dB was claimed for the instrument.

From these examples it is obvious that the six-port reflectometer is a versatile instrument which can be used in a diverse range of applications. It therefore seems reasonable to conclude that a six-port is an appropriate measurement engine to use for sensing cheese curd moisture.

4.6 Overview of Prototype Six-Port

In implementing a six-port-based moisture sensing instrument, a number of subsystems were required to provide support functions to the six-port network. Such functions included frequency control, power measurement, data processing, and results display.

A schematic of the prototype instrument is shown in Figure 4.3. An oscillator provides a stimulus signal to the six-port network. A sensor is attached to the test port of the six-port to provide an interface to the material under test. The power at the remaining four ports is measured using diode detectors and a PC with a 12-bit analogue-to-digital converter. The frequency of the test signal is monitored by tracking standing wave nulls on a short-circuited

length of microstrip transmission line. If necessary the frequency of the test signal can be adjusted via a control pin on the oscillator, which is connected to one of the channels of a digital-to-analogue converter.

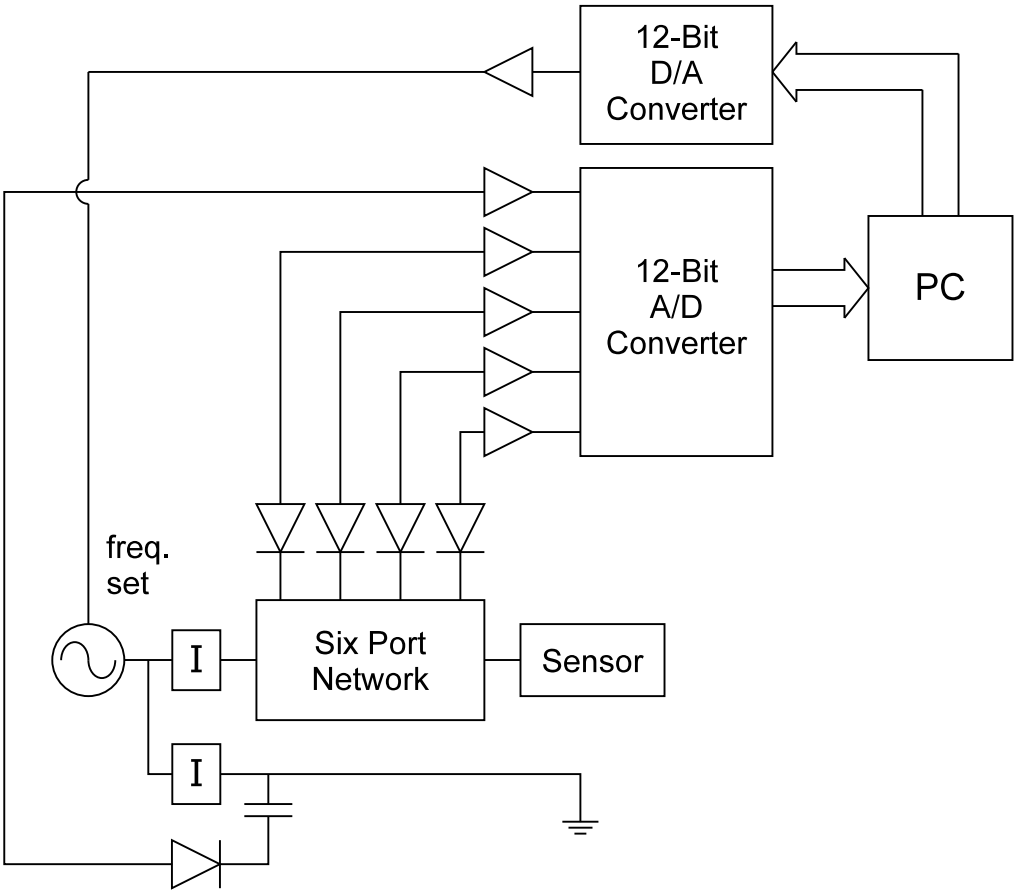

Figure 4.3: Practical implementation of a six-port reflectometer, including oscillator, frequency stabilisation circuit, six-port network, sensor, I/O subsystem, and PC.

The following sections discuss the design and construction of the above subsystems excluding the sensing head, which is covered in detail in later chapters.

4.7 Six-Port Reflectometer Hardware

4.7.1 Circuit Topology and Performance Characteristics

The six-port network chosen for this project was based on the well-known configuration proposed by Engen (1977a). As shown in Figure 4.4, this simple circuit requires only a 6 dB directional coupler, a power divider, three quadrature hybrids and a matched termination.

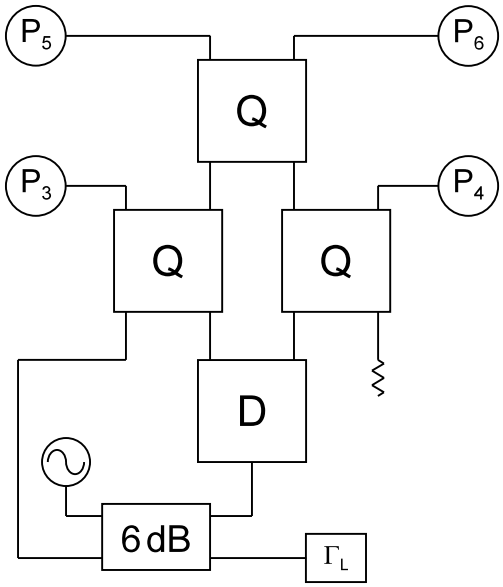

Figure 4.4: Schematic of six-port circuit used in prototype moisture sensing instrument.

The approximate performance characteristics of this six-port can be determined by assuming that all components are ideal. Thus, detectors are assumed perfectly matched, and the power divider, couplers and interconnects are assumed to have zero electrical length. Under these conditions, if the test signal generated by the oscillator has amplitude $2b$ then it is easy to show that:

$$b_3 = \frac{\sqrt{3}b}{2\sqrt{2}}(\Gamma_L + j\sqrt{2}) \tag{4.15}$$

$$b_4 = \frac{j\sqrt{3}b}{2} \tag{4.16}$$

$$b_5 = \frac{-\sqrt{3}b}{4}\left[\Gamma_L - \sqrt{2}(1+j)\right] \tag{4.17}$$

$$b_6 = \frac{j\sqrt{3}b}{4}\left[\Gamma_L + \sqrt{2}(1-j)\right] \tag{4.18}$$

where b_3–b_6 are the amplitudes of the waves incident on the power meters P_3–P_6 in Figure 4.4. The measured power at the i^{th} port is then given by $P_i = |b_i|^2$. Taking Port 4 as the reference port and normalising the other three ports to it yields the following power ratios:

$$\frac{P_3}{P_4} = \frac{1}{2}\left|\Gamma_L + j\sqrt{2}\right|^2 \tag{4.19}$$

$$\frac{P_5}{P_4} = \frac{1}{4}\left|\Gamma_L - \sqrt{2}(1+j)\right|^2 \tag{4.20}$$

$$\frac{P_6}{P_4} = \frac{1}{4}\left|\Gamma_L + \sqrt{2}(1-j)\right|^2 \tag{4.21}$$

Further rearrangement of Equations 4.19, 4.20 and 4.21 produces three circle equations having centres C_i and radii R_i given by:

$$\begin{aligned} C_1 &= -j\sqrt{2} & R_1 &= \sqrt{\tfrac{2P_3}{P_4}} \\ C_2 &= \sqrt{2} + j\sqrt{2} & R_2 &= 2\sqrt{\tfrac{P_5}{P_4}} \\ C_3 &= -\sqrt{2} + j\sqrt{2} & R_3 &= 2\sqrt{\tfrac{P_6}{P_4}} \end{aligned} \tag{4.22}$$

The distance of the circle centres from the origin can be obtained by simply calculating the magnitudes of C_1, C_2 and C_3, which in this case evaluate to $\sqrt{2}$, 2, and 2 respectively. Each of these values satisfies the criterion of Engen (1977b) discussed in Section 4.2.3, which stipulates that circle centres should be a distance of approximately 1.5 from the origin.

In reality there will exist a number of impedance mismatches throughout the six-port network which will cause the above parameters to depart from the ideal case. Furthermore, the non-zero

electrical lengths of real components and interconnects will cause the locations of the three circles to rotate around the Smith chart as frequency varies (although it should be stressed that the *distances* of these locations from the origin will not change). Consequently, there is still a need for the six-port to be calibrated prior to use.

4.7.2 Six-Port Implementation

The six-port network described above was constructed out of stripline-based devices, which have the advantages of low weight and size, and lower cost compared to other technologies such as waveguide or coaxial.

The 6 dB coupler was a Merrimac Industries CTM-6M-5G directional coupler with a bandwidth of 2.0–8.0 GHz. Each of the three quadrature hybrids was a Merrimac Industries QHM-3M-5G 90° Power Divider/Combiner, also having a bandwidth of 2.0–8.0 GHz. The power divider was a Merrimac Industries HJM-4R-10G 180° Power Divider/Combiner. An SMA matched load was attached to the isolated port of the power divider to prevent noise being coupled into the network through this port.

The above devices were interconnected by short purpose-built lengths of RG402U semirigid coaxial cable with SMA adaptors soldered to each end.

The power meters P_3–P_6 shown in Figure 4.4 were comprised of four Wiltron 73N50 diode detectors connected to an amplifier board. These components are discussed in greater detail in Sections 4.10 and 4.12.

4.7.3 Calibration Standards

The five standards used to calibrate the six-port were comprised of four offset short circuits and one matched load. The offset shorts were purpose-built from coaxial connectors and short lengths of RG402U semirigid coax. Small pieces of tinfoil were soldered over the end of the semirigid coax to provide the short circuit termination. The electrical lengths of these standards are listed in Table 4.1.

Table 4.1: Electrical lengths of offset short circuit calibration standards as measured by HP-8720C Automatic Network Analyser.

Standard	Electrical Length (mm)
1	51.797
2	40.921
3	27.128
4	12.418

The matched termination was a broadband load with an N-type connector. An SMA-to-N adaptor enabled the load to be attached to the test port of the six-port.

To accurately characterise the five calibration standards, the reflection coefficients of each were measured with an Automatic Network Analyser across the 2–4 GHz frequency range. As a result it was not necessary for the offset shorts to be perfectly realised, nor was it important for the matched load to be of a high quality.

A minor problem was encountered whereby the reflection coefficients of some standards were very similar at certain frequencies. Indeed, at 3.81 GHz Standards 1 and 4 were almost identical, as shown in the plot of reflection coefficient phase in Figure 4.5. (Reflection coefficient magnitudes are the same for all four standards, as $|\rho| = 1$ for offset short circuit terminations, irrespective of frequency or electrical length.)

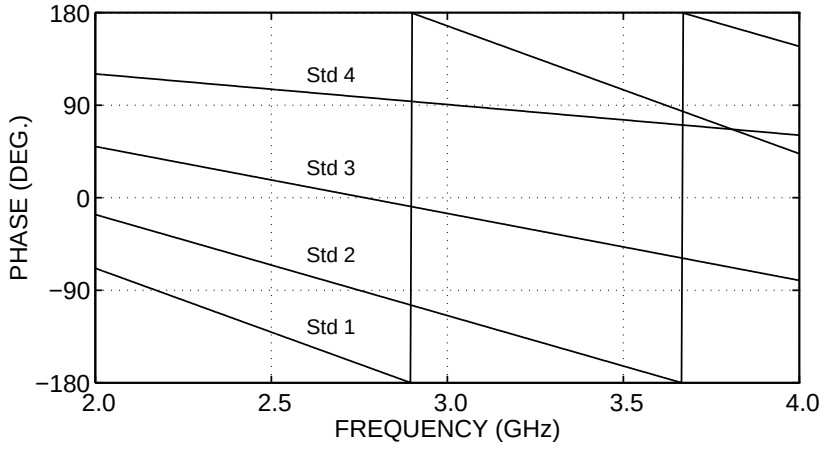

Figure 4.5: Phase of reflection coefficients of six-port calibration standards vs frequency.

The frequency dependent nature of the reflection coefficients was a consequence of the different electrical length of each standard; the rate of change of reflection coefficient phase with frequency is greater for standards with long electrical lengths than for standards with short electrical lengths. If two or more standards have similar reflection coefficients, as is the case at 3.81 GHz, the six-port calibration algorithm becomes poorly conditioned and the instrument becomes much more sensitive to noise and other disturbances. Conversely, if the four offset short circuits are equispaced around the perimeter of the Smith chart, the accuracy of the six-port is maximised (Hunter and Somlo, 1985).

Ideally it would be preferable to use calibration standards whose properties are frequency invariant. However, such standards are difficult to realise in practice and are likely to be expensive. An alternative solution is to measure more than five standards during instrument calibration. The 'best' five standards can then be chosen at each measurement frequency, and the calibration constants calculated accordingly. This approach would be somewhat inconvenient if discrete short circuit terminations were used, however a sliding short or a sliding load would reduce the workload considerably. Unfortunately this is also a relatively high-cost solution.

Ultimately it was decided that for the purposes of laboratory testing it would be easier to simply avoid those frequencies at which the calibration standards had less-than-optimal reflection coefficients.

4.8 YIG-Tuned Oscillator

The test signal for the six-port was provided by an Avantek AV7224-9 YIG-tuned oscillator. This oscillator can generate 100 mW (+20 dBm) of RF output power over a bandwidth of 2.0–4.0 GHz.

One of the defining features of a YIG-tuned oscillator is its highly linear tuning characteristic. The AV7224-9 used for this project has a tuning curve in which $\mathrm{I_{tune}}$ vs $\mathrm{f_{out}}$ deviates from the ideal straight line by less than $\pm 0.2\%$.

The AV7224-9 oscillator is powered by two DC supply rails: a +15 V rail, and a -5 V rail. Additionally, a 20–28 V DC supply is required to power an on-board heater, which mitigates against the effects of ambient temperature fluctuations.

The oscillator output frequency can be changed by varying the current in the main tuning coil. Two control pins are provided on the exterior of the oscillator package for this purpose. As will be discussed in Section 4.12, a D/A converter driving an operational amplifier was used to sweep the oscillator output frequency over the 2–4 GHz band of interest.

An FM tuning coil is included within the oscillator packaging for the purposes of fine-tuning the frequency of the output signal, or for modulation. Neither of these features were required for this project, so the two FM coil pins were tied to the oscillator ground pin.

The oscillator output signal is emitted from an SMA connector on the top of the package.

4.9 Frequency Stabilisation Circuit

4.9.1 Oscillator Performance Limitations

A significant obstacle to the use of the AV7224-9 YIG-tuned oscillator was the need for a means of setting the output frequency accurately and repeatably. This problem was made more difficult by two undesirable performance characteristics.

The first was that the output frequency of the oscillator was affected by variations in ambient temperature, despite the presence of an on-board heater. This problem was most severe at start-up, when the oscillator had not yet reached its operating temperature. This temperature was never precisely established, but it was noted that the oscillator package always became hot to the touch. It is therefore estimated that temperature of the oscillator at equilibrium was close to 50°C. The period of time required for the oscillator to reach its equilibrium temperature was typically about 15 minutes. On cooler days, when the temperature in the laboratory was lower than usual, this time period could be as long as half an hour.

The temperature-sensitive nature of the oscillator can be clearly seen in Figure 4.6, which displays the output frequency of the oscillator as measured by a frequency counter at both start-up and after a period of one hour. The horizontal scale is calibrated against the 12-bit demand word that is sent to the D/A converter, which in turn drives the main tuning coil. This

12-bit word is therefore directly proportional to the coil current. These results indicate that the output frequency for a given coil current can change by anywhere from 85 MHz to 226 MHz as the oscillator heats up.

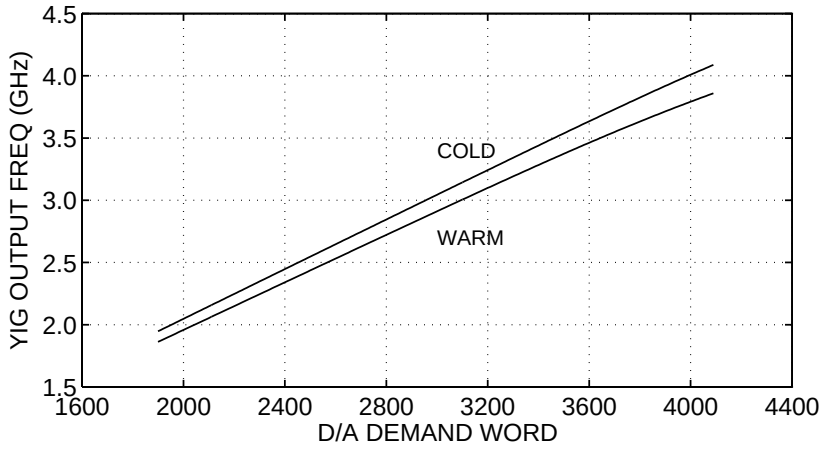

Figure 4.6: Measured tuning characteristic of AV7224-9 YIG-tuned oscillator at two operating temperatures. 'COLD' denotes the temperature of the oscillator at start-up. 'WARM' denotes the temperature of the oscillator at equilibrium (approx 50°C).

The second performance defect to be taken into account was the presence of hysteresis in the tuning characteristic of the oscillator. This was not entirely unexpected; the manufacturer's specifications cite a hysteresis value of the order of 3 MHz for the AV7224-9 oscillator. Thus, ramping up the current in the main tuning coil from a minimum to a maximum would produce a different range of output frequencies to that produced by ramping the current down from maximum to minimum. Obviously the 'highly linear' tuning characteristic described in Section 4.8 is only so when the frequency is swept in one direction.

4.9.2 Prototype Stabilisation Circuit

The net effect of the aforementioned nonlinearities in the transfer function of the oscillator was to create a one-to-many mapping between control current and output frequency. It was therefore necessary to find another means of determining the output frequency which was less sensitive to environmental factors but at the same time simple and economical.

The solution which was eventually adopted consisted simply of a short-circuited length of microstrip transmission line connected to the output of the oscillator by a tee-piece, as shown in Figure 4.7. The magnitude of the resulting standing wave was then measured by a diode detector which was coupled to the line by a surface mount capacitor.

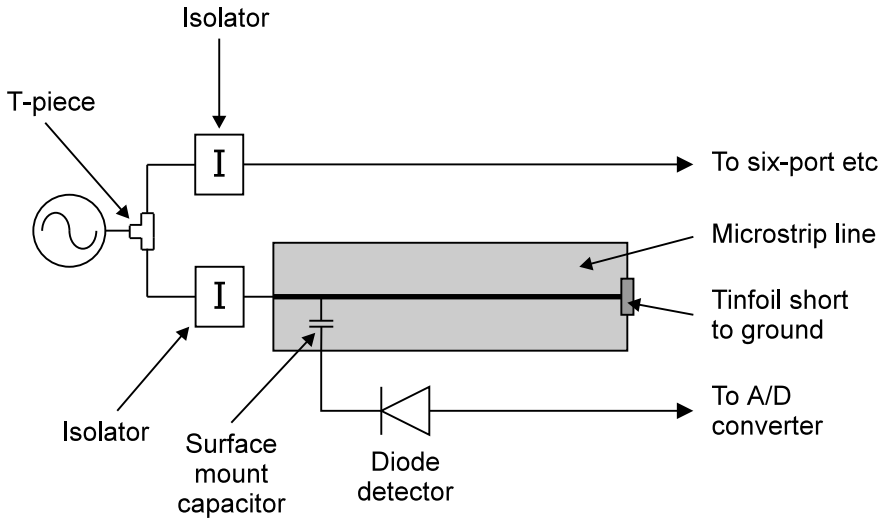

Figure 4.7: Schematic of frequency stabilisation circuit.

The use of this technique required two isolators, as shown in Figure 4.7. This prevented reflected signals from the frequency stabilisation circuit from entering the six-port, and vice versa.

The exact frequencies at which nulls appeared at the diode detector were determined in advance with a frequency counter, and assumed to be constant thereafter. A typical plot of the variation in the standing wave magnitude with frequency as measured by the diode detector is shown in Figure 4.8. Results are shown for both startup and at equilibrium. While the peaks of each set of results show some differences, the nulls are in excellent agreement.

In order to set the oscillator to a given frequency, it is first necessary to locate the two nulls known to occur at frequencies above and below the demand frequency. Linear interpolation is then used to calculate the 12-bit D/A word corresponding to the demand frequency.

To take an example, assume that the user wants to set the oscillator frequency to 2.7 GHz upon startup. The standing wave nulls on either side of this frequency are known to occur at

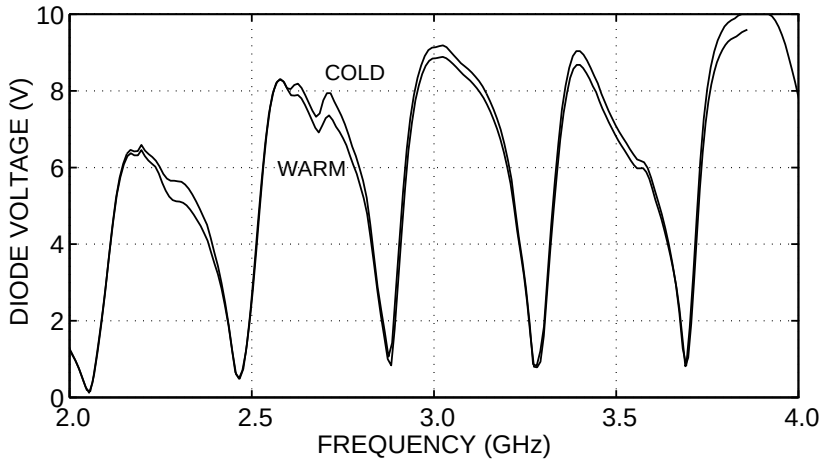

Figure 4.8: Standing wave magnitude vs frequency as measured by frequency stabilisation circuit. 'COLD' denotes the temperature of the oscillator at start-up. 'WARM' denotes the temperature of the oscillator at equilibrium (approx 50°C).

2.4645 GHz and 2.8826 GHz, when the D/A is set to 2530 and 2970 respectively. By linear interpolation, the D/A setting which will produce a signal of 2.7 GHz is **2778**.

Due to dependency of the oscillator's tuning characteristic on temperature, all nulls occurring within the 2–4 GHz band must be tracked continuously, and the D/A output voltage adjusted if necessary to keep the frequency locked to the required value. This can be highlighted by re-plotting the standing wave data in Figure 4.8 against the D/A word instead of frequency. It is clear from Figure 4.9 that the relationship between the output of the D/A converter and the minima in the standing wave on the microstrip transmission line is a strong function of temperature.

The printed circuit board layout of the frequency stabilisation circuit can be found in Appendix C.2.

4.9.3 Performance of Frequency Stabilisation Circuit

In order to evaluate the performance of the frequency stabilisation circuit, the six-port reflectometer was replaced by a frequency counter under GPIB control. The D/A converter output was then swept over a range of voltages, and the predicted and actual oscillator frequencies recorded to a file for comparison.

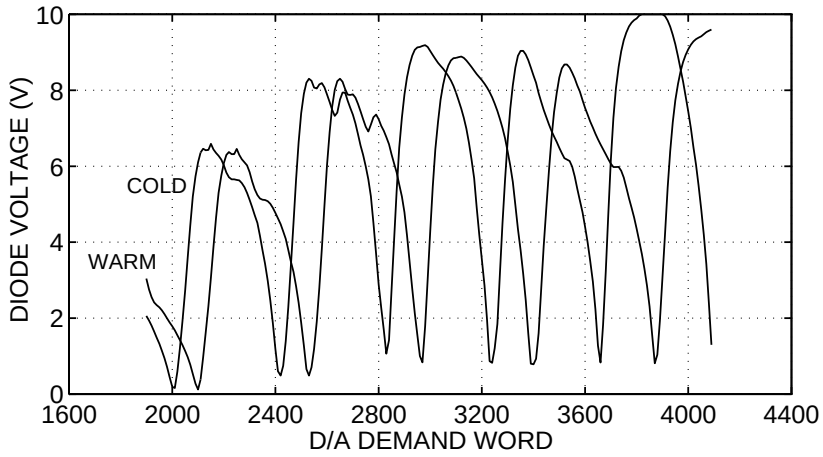

Figure 4.9: Standing wave magnitude vs D/A output word as measured by frequency stabilisation circuit. 'COLD' denotes the temperature of the oscillator at start-up. 'WARM' denotes the temperature of the oscillator at equilibrium (approx 50°C).

To minimise the error due to the drift-prone nature of the oscillator, the location of each null on the standing wave was determined immediately before the test was performed. The results of this test are shown in Figure 4.10. Between 2 GHz and 3.63 GHz the relative error is typically 0.1% or better. Above 3.63 GHz the relative error climbs rapidly for reasons that remain unclear.

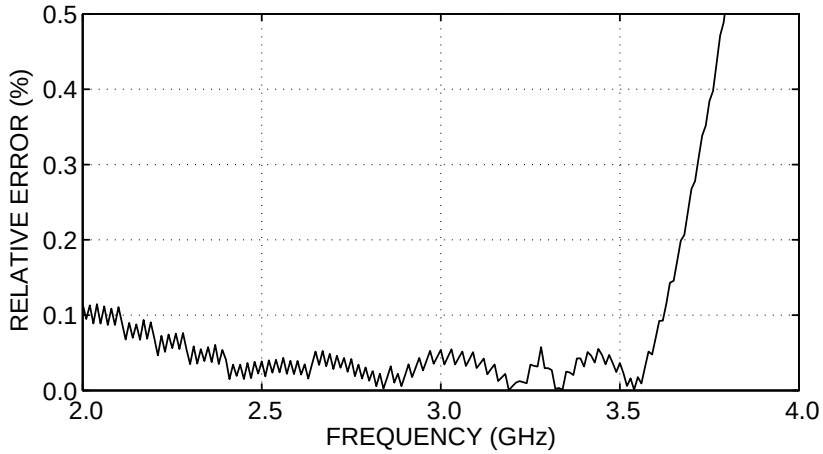

Figure 4.10: Relative error of frequency stabilisation circuit vs frequency.

To examine the effect of the drift in the oscillator tuning characteristic, the frequency error across the 2–4 GHz band was measured four times over a one hour period. The standing wave

nulls were checked only once, at the beginning of the test. The results—shown in Figure 4.11—suggest that the error in the source frequency can be kept to 0.25% or better for frequencies below 3.6 GHz, provided the D/A output values corresponding to each standing wave null are updated at one hour intervals.

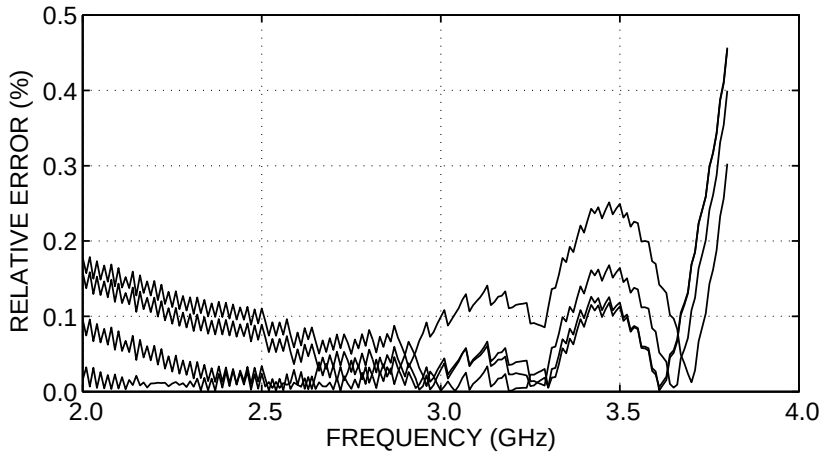

Figure 4.11: Relative error of frequency stabilisation circuit vs frequency measured at regular intervals over a one hour period.

4.10 Diode Characterisation

4.10.1 Benefits of Software Linearisation

Diode detectors are inherently nonlinear devices. While designed to provide a linear power-to-voltage response within specified limits, diodes can be driven into nonlinear regions of operation if the input power level is too large or small.

Therefore in order to improve the dynamic range of the six-port reflectometer, each diode detector was characterised in advance. This involved measuring the output voltage for a range of input power levels, and fitting a suitable function to the measured data. As a result the diodes were able to be used outside their linear regions, making possible the measurement of a wider range of power levels.

It should be noted that this approach does not provide any significant accuracy enhancements to the six-port if the detectors are only used in their linear regions. This is because six-ports do not require accurate measurements of absolute power levels, only power *ratios* (Somlo, 1996).

4.10.2 Linearisation Procedure

In order to characterise the Wiltron 73N50 diode detectors, a Marconi signal generator—under computer control via GPIB— provided an RF signal to each of the diodes in turn. The signal generator was set to the frequency of interest, and the power level automatically swept from -20 dBm to $+13$ dBm in increments of 0.1 dBm. At each power level the output voltage of the detector was measured by the A/D converter and stored to a file.

It then remained to find a convenient function which would enable the input power to the diode to be calculated from the output voltage. This involved fitting a curve to a data set like that shown in Figure 4.12. In practice it proved difficult to find a single function to fulfill this

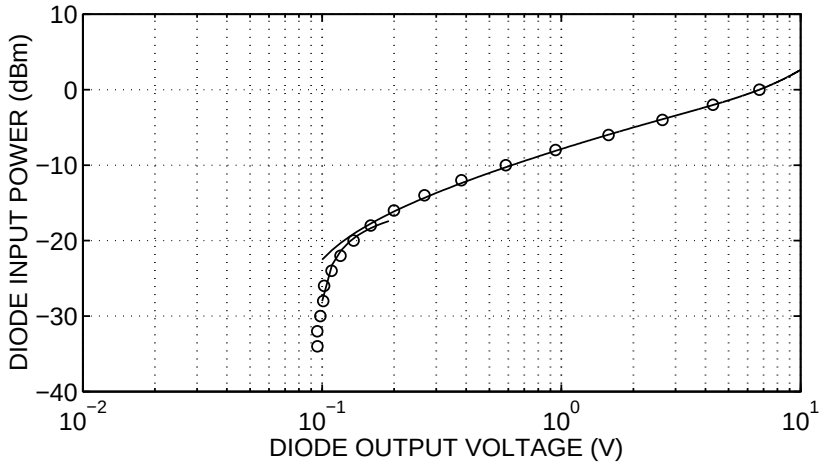

Figure 4.12: Plot of the relationship between input power and output voltage for a Wiltron 73N50 diode detector. Solid lines represent curves of best fit to measured data.

requirement, and attempts were made to fit different functions to different sections of the data set. In the case of the data set in Figure 4.12, a third order polynomial provides a good fit to points above 0.16 V output voltage. Below 0.16 V the diode moves out of its square-law region, and a hyperbolic function provides a better fit to the measured data.

Ultimately, however, such techniques proved unwieldy, and were discarded in favour of simple linear interpolation between measured data points. This was feasible due to the large number of power levels which could be output by the Marconi signal generator; around 330 levels could be dialled up between -20 dBm to $+13$ dBm. Consequently, the error introduced by using linear interpolation to estimate the values of intermediate points was small.

4.10.3 Error Sources

Despite the implementation of the above linearisation procedure, the use of diode detectors in the prototype six-port reflectometer introduced several potential sources of error into the system.

Firstly, during laboratory trials of the six-port the characterisation procedure was performed at only one frequency. This data was then used to make measurements over a range of different frequencies, the assumption being that the Wiltron detectors would not exhibit any significant performance variations between 2 GHz and 4 GHz. Obviously it would have been preferable to characterise the diodes at every frequency of interest, but this would have been very time consuming and labour intensive, even with a partly automated measurement procedure. Thus, any frequency dependency exhibited by the diode detectors was not captured by the linearisation algorithm, leading to an error in the measured reflection coefficient.

Secondly, there is the issue of diode sensitivity to consider. In its linear region a diode should exhibit a constant sensitivity, i.e.

$$\frac{dV_{\mathrm{out}}}{dP_{\mathrm{in}}} = K \tag{4.23}$$

where V_{out} is the diode output voltage, P_{in} is the input power to the diode, and K is a real constant. However, as the diode moves into its nonlinear region, sensitivity becomes a function of input power, i.e.

$$\frac{dV_{\mathrm{out}}}{dP_{\mathrm{in}}} = f(P_{\mathrm{in}}) \tag{4.24}$$

This is illustrated in Figure 4.13, which shows the relationship between input power and output voltage for one of the Wiltron 73N50 diode detectors. (Note that the axes in Figure 4.13 have been transposed in comparison with Figure 4.12.) At the extremes of the plot the curve flattens visibly, indicating a decrease in sensitivity.

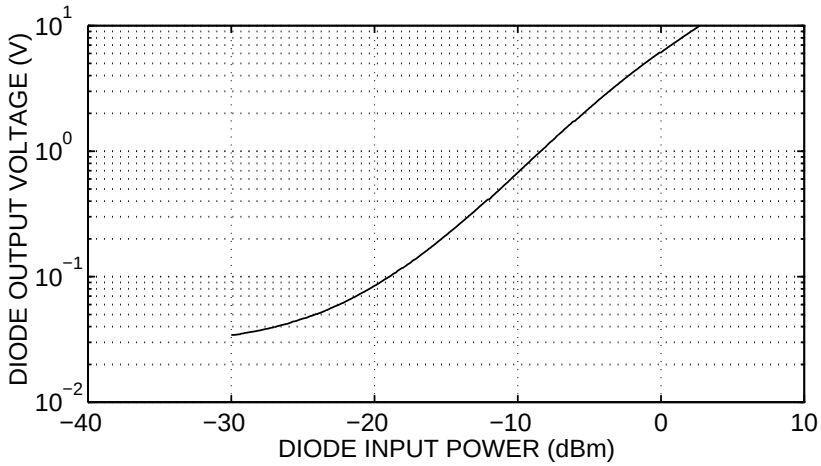

Figure 4.13: Output voltage vs input power for a Wiltron 73N50 diode detector.

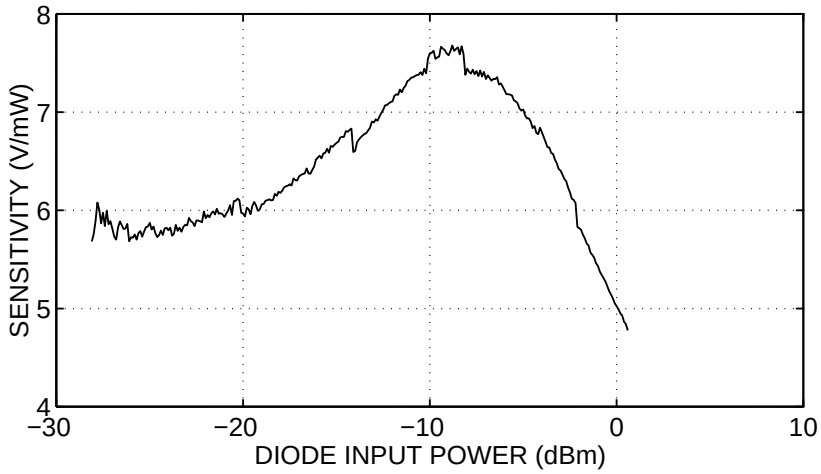

Figure 4.14: Sensitivity of Wiltron 73N50 diode detector vs input power.

Taking the numerical derivative of this data set produces the sensitivity plot in Figure 4.14. (Due to the presence of noise it was necessary to apply a smoothing function to the voltage data prior to calculation of the derivative.) The peak near -10 dBm corresponds approximately to the point of inflection in Figure 4.13. At the edges of the plot the sensitivity drops considerably.

The consequences of using the diode detectors in their less sensitive areas of operation is that power cannot be measured as accurately. This is due to the finite resolution of the A/D converter: as $dV_{\mathrm{out}}/dP_{\mathrm{in}}$ decreases, the relative effect of quantisation noise increases, as does the level of uncertainty surrounding measurements made by the six-port.

The final source of error which is introduced by diode detectors is thermal drift. Some authors have cited this as reason enough to reject diodes in favour of thermistor power meters (Somlo, 1996). The options available in mitigating against thermal drift are somewhat limited, and all add to the expense and complexity of the instrument and its control software.

One option is to install the diodes in a temperature-stabilised housing. This would require a heating element to raise the temperature inside the housing above that of the external environment. A thermal switch controlling power to the heater would also be necessary, to maintain the temperature inside the enclosure to a constant level.

Another option is to recalibrate the detectors before every measurement. This would be extremely cumbersome if performed manually, however several workers have shown how this procedure can be automated. For example, Colef et al. (1990) have inserted a variable attenuator between the oscillator and the six-port network. By sweeping the attenuator over a range of settings and measuring the output voltage from each of the four detectors, it is possible to calculate a performance graph for each diode.

However, for the purposes of this project it was decided that such refinements could be safely neglected, at least during the laboratory testing phase. Besides the time required to develop a strategy to solve the drift problem, there was also the expense of the extra components to consider. As a result, both of these resources were saved for use in other areas, and each diode was recalibrated manually at regular intervals.

4.11 Sensor

To enable the six-port to measure the reflection properties of samples of cheese curd, a suitable sensor had to be developed. The sensor would be attached to the test port of the six-port after calibration, and immersed in the material of interest. The measured reflection coefficient could

then be used to infer the dielectric properties of the curd, assuming an accurate model of the sensor was available.

The range of possible sensor configurations is large, and no single sensor is suitable in every instance. Furthermore, the development of a characterisation algorithm is not a trivial matter. For these reasons a thorough discussion of sensor design is saved for later chapters. The issue of which sensor type to use for measuring cheese curd moisture is discussed in Chapter 5. Sensor characterisation is an issue of such importance that it is the dominant topic of Part II of this thesis.

4.12 Data Acquisition Hardware

Measurement of diode voltages and control of the oscillator frequency was achieved using a custom-built amplifier board and an off-the-shelf data acquisition card. These are discussed below.

4.12.1 Amplifier Board

The amplifier board was a simple printed circuit card, populated with op amps and power conditioning circuitry. Connection to the computer controller was via a ribbon cable terminated with a 50-pin connector, which was soldered to the amplifier board.

Power to the amplifier board was obtained from the PC via the same ribbon cable. The 50-pin connector provided a $+12$ V pin, a -12 V pin and a ground connection. This obviated the need for a separate power supply, reducing the expense and complexity of the system.

An NFC10-12D12 DC-DC converter chip was used to convert the $+12$ V rail to $+24$ V, in order to drive the oscillator's on-board heater. The same $+24$ V rail, in conjunction with two voltage regulator ICs, powered the diode detector preamps and the $+15$ V rail of the oscillator biasing circuit. The -5 V rail of the oscillator biasing circuit was powered from the -12 V rail of the amplifier board via an LM79L05-ACZ voltage regulator.

The output voltages from all five diode detectors were amplified by LTC1150-CN8 chopper stabilised op amps. While more expensive than linear op amps, chopper stabilised amplifiers have virtually zero input offset voltage. This makes them ideal for amplifying small DC signals like diode output voltages, which can reach sub-millivolt levels. The gain of the chopper amplifiers could be varied by using rotary potentiometers as feedback resistors. This enabled the range of output voltages from the amplifiers to be matched to the range of allowable inputs to the A/D converter board.

An LM759 power op amp was employed to drive the main tuning coil of the oscillator. This IC was powered by the $+12$ V and -12 V rails of the amplifier board. Like the chopper amplifiers, a rotary potentiometer was used to set the gain of the LM539 such that the whole 2–4 GHz range of oscillator output frequencies could be produced by incrementing the 12-bit D/A demand word from 0 to 4095.

A schematic of the amplifier board is given in Appendix C.1. The PCB artwork for this circuit can be found in Appendix C.2.

4.12.2 Data Acquisition Card

Monitoring and control of the six-port reflectometer was facilitated by a PC30AT Data Acquisition Card from Amplicon Liveline. Designed to plug into an ISA slot in an IBM-compatible PC, the PC30AT contains a 16 channel 12-bit A/D converter, two D/A converters and three 8-bit digital I/O ports. As mentioned in the previous section, the PC30AT also provides power and ground rails for use by external devices.

To connect the PC30AT to the outside world, a ribbon cable is provided which plugs into a D-type connector at the backplane of the PC. The other end of the ribbon cable terminates in a 50-pin connector, which for this project was soldered to the external amplifier board.

Once the PC30AT board has been installed in the PC and the device drivers loaded, it only remains to calibrate the A/D converter. This entails running a manufacturer-supplied diagnostic program and adjusting several trimpots until the program deems the performance of the A/D to be within acceptable limits.

To make measurements with the PC30AT, the manufacturer has provided a library of interface subroutines. Sample programs in several popular languages are also supplied. (The programming language of choice for this project was Borland C++.) It is then a straightforward matter to incorporate analogue I/O operations into a master control program.

4.13 Computer Controller

An IBM-compatible 386DX PC with 8 MB of RAM carried out all control and computational functions. Software was developed using Borland Turbo C++ for DOS.

During the development and testing phase the system software consisted of several small programs. For example, setting the YIG-tuned oscillator to the desired output frequency was achieved with one program. The measurement of the diode output voltages (and the calculation of the corresponding input power levels) with each calibration standard in place was achieved with another program. A third program calculated the calibration constants, while a fourth calculated the reflection coefficient at the test port of the six-port, and displayed the results on the computer screen.

As the prototype instrument reached a mature stage of development it became desirable to combine these programs together. Rather than write new software, it was more convenient to write a short batch file which would automatically invoke the existing programs in the correct sequence.

A screen dump of a typical results window is shown in Figure 4.15. The the values of the circle centres and radii are printed at the top of the screen, while the calculated value of reflection coefficient is printed at the bottom. If known, the true value of reflection coefficient can also be printed, along with the magnitude and phase errors. This feature enables the quality of the instrument calibration to be checked by comparing the measured value of each standard after calibration to the known value. The three six-port circles and the estimated & true values of reflection coefficient are plotted on a Smith chart in the middle of the screen.

The results in Figure 4.15 were calculated from power readings obtained from a *simulated* six-port based on the classical configuration described in Section 4.7.1. Hence, the circle centres

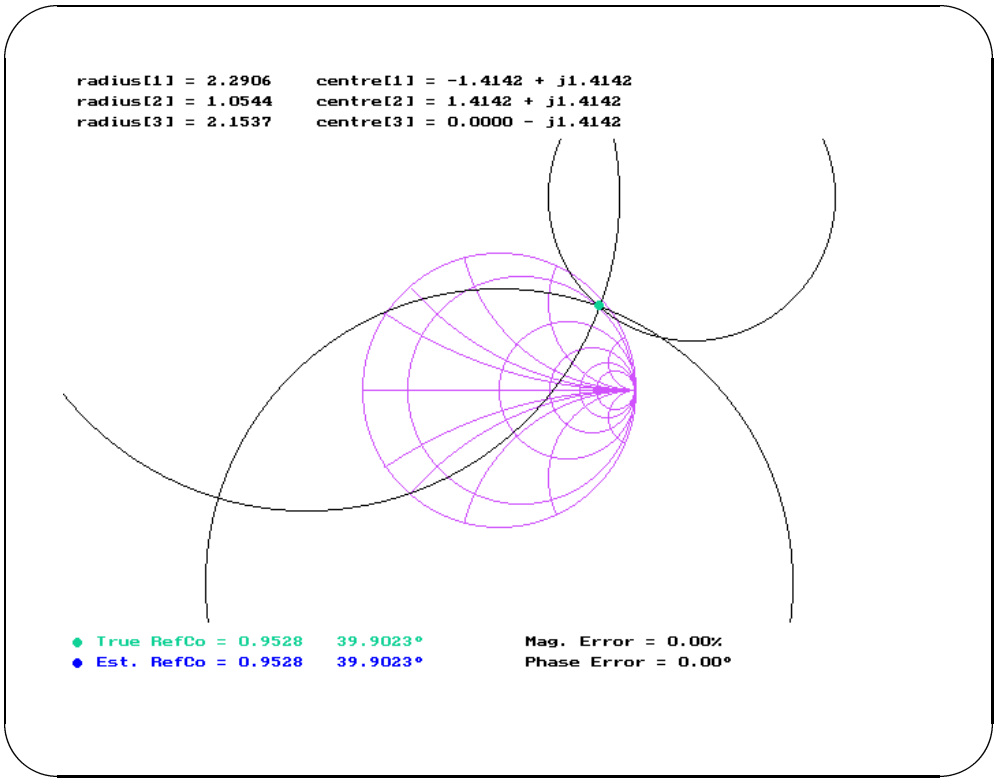

Figure 4.15: Output screen comparing true and estimated values of reflection coefficient as measured by a simulated six-port.

listed at the top of the output screen are the same as those given in Equation 4.22, and the point of intersection is clear and well-defined. However, as discussed in previous sections, the six-port built for this project contained a number of error sources which caused its performance to depart from the ideal case.

4.14 Evaluation of System Performance

The performance of the prototype six-port reflectometer was evaluated by measuring the calibration standards after the calibration process was complete, and comparing with the known values. In the course of the evaluation process it was observed that several factors could adversely affect the accuracy of the instrument.

Firstly, the stability of the source frequency was a critical parameter. Using a Marconi signal generator—which contains a frequency synthesised phase-locked source—the six-port could consistently reproduce its calibration standards with an accuracy of better than 1% magnitude error and 1° phase error. However, when the Marconi was replaced by the YIG-tuned oscillator, magnitude and phase errors were initially of the order of 6–10% and 5° respectively. It was later discovered that the hysteresis in the oscillator's transfer function was causing errors in the frequency-setting algorithm. Further refinements to this software improved the accuracy of the six-port to a level approaching that achievable with the Marconi.

Secondly, as predicted in Section 4.7.3, if the instrument was calibrated at a frequency at which two standards had similar reflection coefficients, measurement accuracy was significantly poorer. For example, at frequencies above 3.5 GHz, two standards had reflection coefficients within 45° of each other. When these standards were re-measured after calibration, the magnitude and phase errors were of the order of 5% and 5° respectively. By contrast, measurements made after the six-port was calibrated at 2.5 GHz—when the four reflective standards were approximately equispaced around the perimeter of the Smith chart—showed greatly improved accuracy.

Another recurring problem was drift in the diode detectors. Over the course of a week the characterisation data for these devices would become less and less representative of the true

diode characteristics. This phenomenon was attributed to ambient temperature variations in the testing laboratory. Provided the diodes were used in their square-law regions this was not a serious concern. Nevertheless, for maximum accuracy a periodic recalibration schedule was implemented.

4.15 Future Directions

It is clear that the prototype six-port described in this chapter would need to be significantly re-engineered before it could be used in a factory environment. The following subsections summarise the areas needing attention.

4.15.1 Improvements to Microwave Hardware

As discussed in Section 4.14, the issues of frequency stability, errors due to similarities between calibration standards, and thermal drift in the diode detectors would need to be revisited. While these problems have been resolved adequately for the purposes of laboratory testing, longer-term solutions would have to be sought in order to minimise the amount of maintenance needed to keep the instrument functioning at peak accuracy.

4.15.2 Sensitivity to RFI/EMI

Electronic components like the amplifier board and computer controller would need to be shielded against electromagnetic interference. A filtered power supply for the PC would also be necessary to suppress mains-induced disturbances caused by large electrical loads being switched in and out of the local distribution network (a common feature of factory environments).

4.15.3 Calibration Issues

Another problem is the amount of time and skill required to calibrate the six-port. Even using the efficient algorithm outlined in Section 4.3, the operator is still required to attach five standards to the six-port in the correct sequence, before re-attaching the sensing head. While the computer controller could make this process easier for the user by providing step-by-step instructions, there is still scope for operator-induced errors in the way each standard is attached—different operators will tighten the connectors to different torques, subtly changing the input reflection coefficient seen by the six-port each time the instrument is calibrated. There is also the issue of maintenance to consider; calibration standards need to be cleaned periodically with isopropyl alcohol to ensure their performance does not degrade over time.

These undesirable aspects could be eliminated if the six-port were self-calibrating. Previous implementations of this idea include the Marconi 6210 Reflection Analyser (Potter, n.d.). This instrument employs a patented Automatic Termination Generator to create a range of test impedances inside the machine, from which the six-port calibration coefficients can be deduced. This technique has the advantages of being fast, broadband and transparent to the user.

Note that the Marconi 6210 is not completely self-calibrating. Like a conventional Network Analyser it is still necessary to measure three external calibration standards to account for directivity, source match and frequency response errors. However, this process could be dispensed with in the six-port built for this project if the circuit were reconfigured in the manner shown in Figure 4.16. While this would add to the internal complexity of the instrument, it would give it a ‘plug and play’ capability that is lacking in conventional six-ports.

4.15.4 Protection Against Environmental Conditions

One of the more prosaic (but nevertheless important) factors to consider in preparing the instrument for use in a cheese factory is protection against local environmental conditions. The humidity in cheese factories can be very high, and equipment is cleaned regularly with large amounts of water and caustic cleaning agents. Obviously any electronic components would need to be installed in a hermetically sealed enclosure in order to operate in such a hostile environment.

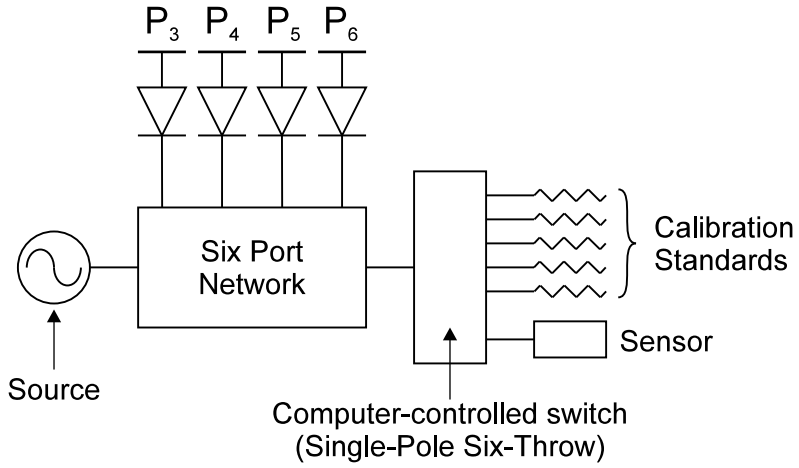

Figure 4.16: Schematic for proposed self-calibrating six-port reflectometer.

4.15.5 Summary

The enhancements which have been described above would all need to be implemented in order to transform the six-port from a laboratory prototype to an instrument suited to commercial use. However, this would have been beyond the scope and resources of this project, where the intention was primarily to demonstrate the feasibility of a concept: namely, that vector impedance measurements can be achieved with relatively simple, low-cost hardware which nevertheless offers a high degree of accuracy.

4.16 Conclusion

This chapter has described the development and testing of a computer-controlled six-port reflectometer suitable for use in a microwave moisture meter.

The operating principles of six-ports have been introduced, including the need for a carefully implemented calibration technique. The advantages offered by six-ports have been discussed, including high accuracy, simplicity and low cost.

A graphical interpretation of the six-port equations has been presented, whereby the unknown reflection coefficient can be represented as the point of intersection between three circles in the

complex plane. This interpretation has provided the basis for a discussion of how to mitigate against the effects of noise and calibration errors. Furthermore, design parameters for the six-port network have been established which provide a tradeoff between the required dynamic range of the power sensors and the resolution of the data acquisition system.

A brief mention of the dual six-port principle has been made. Due to the added expense and complexity involved, this concept has not been explored in depth as part of this project. However, the potential benefits offered by transmission-based measurement systems would justify future investigation of the dual six-port configuration.

Pertinent examples have been provided from the literature of previous six-port implementations. These examples have indicated that six-ports can be used in a diverse range of 'real world' applications, and are not restricted merely to the laboratory environment. As such, the six-port reflectometer has been shown to be a reasonable choice of measurement engine for a microwave moisture sensing instrument.

A detailed description of the design and construction of a prototype six-port has been presented. A six-port topology has been chosen with performance characteristics as near as possible to the ideal. An octave-band oscillator covering 2–4 GHz has been chosen, and a strategy for stabilising the output frequency has been implemented. A power measurement subsystem has been developed, comprising software-linearised diode detectors, chopper stabilised amplifiers and a 12-bit A/D converter. Instrument control and post-processing of measured data is performed by an IBM-compatible PC, which produces a graphical display of the measured reflection coefficient on the screen.

The performance of the completed prototype has been evaluated. It has been found that the six-port can reproduce its calibration standards with an accuracy of better than 1% magnitude error and 1° phase error. However, this level of accuracy requires a test signal with high frequency stability, and reflective calibration standards which are evenly distributed around the Smith chart.

Finally, some strategies to factory-harden the prototype have been suggested. This work was beyond the scope of the original project, but would be a prerequisite of any commercial realisation of the moisture sensing instrument.

Chapter 5

Microstrip Sensor Structures

5.1 Introduction

In designing a microwave-based moisture sensing instrument, the importance of selecting a sensing head which is appropriate for the application of interest cannot be overstated. As the sole interface between the electronic hardware and the material under test, the sensor directly influences the sensitivity and operating limits of the instrument. Furthermore, the complexity of the model required to characterise the sensor impacts on the speed at which an estimate of moisture content can be made available to the user.

The sensor of choice in this project consisted of a short length of microstrip transmission line. This simple structure was designed to be placed in direct contact with samples of cheese curd, thereby altering the propagation characteristics of the microstrip line in a way dependent upon the dielectric properties of the curd. This chapter explains the rationale behind this choice of sensor.

The first section is a review of different sensor types, with examples from the literature, covering the operating principles, strengths and limitations of these devices.

The second section introduces the planar transmission line family of sensors, of which microstrip is a member. The relative merits of this type of sensor are discussed, especially in the

context of high moisture content measurands like cheese curd.

The third section is concerned with the issue of sensor characterisation. Three different characterisation philosophies are compared and contrasted in order to justify the approach that was eventually adopted.

5.2 Review of Alternative Sensor Types

A huge variety of microwave sensors are described in the literature, and in fact entire books are available on that topic alone (e.g. Nyfors and Vainikainen, 1989). Consequently the following review has been restricted to a few pertinent examples of each type of sensor.

The microwave sensors described below have been placed into the following categories:

- Reflection Sensors
- Transmission Sensors
- Resonant Sensors

The definition of a sensor used here includes *any* device in which the properties of an interrogating signal can be altered by the presence of a measurand. Under this definition the waveguide test cells described in Chapter 3 can also be regarded as sensors, due to the fact that the filled cells cause attenuation and phase shifts in the test signal. (A more precise term for this type of sensor is *modifier* (Sydenham et al., 1989, p. 181). This is distinct from the *transducer* style of sensor, whereby energy is changed from one form to another as part of the sensing process.)

5.2.1 Reflection Sensors

Reflection-based microwave sensors are one-port devices which enable material properties to be inferred from changes in the input impedance of the sensor. Often it is convenient to measure the input reflection coefficient of the sensor and then determine the input impedance from the

following relation:

$$Z_T = Z_0 \left(\frac{1 + \rho_T}{1 - \rho_T} \right) \tag{5.1}$$

where Z_T is the input impedance of the sensor, Z_0 is the characteristic impedance of the line feeding the sensor, and ρ_T is the measured input reflection coefficient of the sensor in contact with the test material. Material properties like moisture content can then be deduced from a model of the sensor or from an empirical calibration curve.

5.2.1.1 Open-Ended Coaxial Probes

An example of a reflection-based sensor is the open-ended coaxial probe. As the name suggests, this type of sensor consists of a coaxial transmission line which is unterminated at one end. Measurements are performed by placing the open end in contact with the test material, which then appears as a shunt capacitance and conductance across the end of the line.

This type of sensor was used by Marsland and Evans (1987) to measure the permittivity of a range of lossy, high-permittivity liquids, including methanol, ethanediol, propan-1-ol and saline solution. The uncertainty of the results was better than 10% across the frequency range 50 MHz to 2.6 GHz.

A similar sensor has been used by Stuchly et al. (1982) to measure the dielectric properties of distilled water at 2 GHz, 3 GHz and 3.8 GHz. The errors in the real and imaginary parts respectively were about 0.5% and 5.3%.

Stuchly and Stuchly (1980) have investigated a variety of open-ended probes in applications involving biological materials like muscle and fat. Besides simple open-ended coaxial lines, the authors have analysed configurations where the centre conductor protrudes into the test sample, essentially becoming a monopole antenna. Other sensor types involved the extension of the outer shield past the end of the coaxial line, thereby creating a small chamber for the test sample to be stored in. In total, eleven different probe configurations were examined and assessed.

Finally, commercial products are available based on the open-ended coaxial line concept, e.g. the HP85070M Dielectric Probe Kit from Hewlett-Packard. Included with the kit are the sensing head, calibration standards and software for estimating permittivity from the measured reflection coefficient. The accuracy claimed by the manufacturer is $\pm 5\%$ for the real part of ε_{r} and ± 0.05 for the imaginary part. The sensor can be operated over a nominal frequency range of 200 MHz to 20 GHz, although the upper limit is less for high-permittivity materials.

An advantage of open-ended coaxial probes is that little or no sample preparation is required, allowing non-destructive measurements to be made *in situ*. Furthermore, the geometry of this type of sensor is good for semi-solid materials (Marsland and Evans, 1987). The broadband nature of these devices is another attractive feature.

However, a major limitation with this type of sensor is the need for good contact between the sensor face and the test sample. While this problem is by no means unique to coaxial sensors, their small apertures make them particularly sensitive to contacting errors.

A related problem is that the fringing field across the probe aperture only penetrates a small volume of the test sample. In the case of the HP85070M Dielectric Probe, the sample is required to be only 20 mm wide and $\frac{20}{\sqrt{\varepsilon_r}}$ mm thick (Hewlett-Packard Corporation, 1993). For a sample with $\varepsilon_r = 30 - j0$, this corresponds to a thickness of 3.65 mm. Not surprisingly, the sensitivity of these sensors to air inclusions or other inhomogeneities is high.

Finally, there is the disadvantage that high frequency phenomena, such as higher-order modes and radiation, can be difficult to account for. As frequency increases, the accuracy of simple equivalent circuit models assuming TEM propagation declines, and more sophisticated models are needed to accurately characterise the behaviour of the sensing head.

5.2.1.2 Free-Space Reflection Sensors

Free-space sensors are structures which are designed to radiate microwave energy into the test material as effectively as possible, much like an antenna is designed to radiate into air. By measuring the reflection coefficient of the antenna when it is directed at a sheet of the material under test, it is theoretically possible to infer the permittivity of the material.

In principle this type of sensor offers some significant advantages over other reflection sensors. For example, free-space sensors are non-contacting, non-destructive, and insensitive to the presence of smoke or steam.

In practice, however, there are some considerable obstacles to overcome in implementing an antenna-based reflection sensor. In the case of waveguide horns, fabrication costs can be high. The footprint of antenna sensors may require large sample areas. Conversely, antennae with narrow beam widths can be physically large and occupy a lot of space. Samples must be sufficiently thick to minimise the amplitude of reflections off the back face of the sample. Overly large side lobes may cause spurious reflections to be picked up by the receiver. Broadband measurement of material properties may not be possible for many antenna types. For systems involving vector reflection coefficient measurement, very tight control of the distance between the antenna and the material being measured is required.

For all of the above reasons, free-space reflection sensors were not the preferred choice for this application.

5.2.2 Transmission Sensors

Transmission sensors are two-port devices which enable material properties to be inferred from changes in the transmission coefficient of the sample. One type of transmission sensor has already been discussed in detail in Chapter 3, where waveguide test cells were used to measure the permittivity of samples of cheese curd.

A range of implementation strategies are available with the transmission-based approach. The simplest is the attenuation method, which involves simply measuring the power dissipated in the sample. More complicated is the phase method, which entails the measurement of the phase shift through the sample. The most sophisticated and expensive approach is the vector transmission coefficient measurement method. All three techniques have strengths and weaknesses, which shall be discussed in the following examples.

5.2.2.1 Waveguide Transmission Sensors

The waveguide transmission method of permittivity measurement was discussed in Chapter 3. It involves loading waveguide test cells with samples of the material to be measured. The vector transmission coefficient of the cell is measured using an Automatic Network Analyser and downloaded to an IBM PC. The complex permittivity of the sample can then be determined by solving a transcendental equation.

This technique provides a relatively high level of accuracy across a band of frequencies. It is suitable for liquids and semi-solids, and can also be used for solid materials provided each sample can be molded or machined to fit snugly into the waveguide test cell. Like many transmission methods, the waveguide-based approach is more tolerant of minor variations in the structure of the sample. Discontinuities such as (small) air inclusions or non-uniform moisture distributions can be averaged out somewhat. This is in direct contrast to the reflection-based sensors discussed in Section 5.2.1, some of which were only capable of measuring a sample volume a few millimetres thick.

Unfortunately there are a number of shortcomings with this type of sensor which precludes its use in cheese production, at least for online measurements.

Firstly there is the issue of sample preparation. When loading the waveguide cells it is important to ensure that the samples are homogeneous in texture and that air gaps are kept to a minimum. This can be difficult and time consuming for semisolid materials like cheddar or mozzarella curd.

Secondly, the sampling process itself can introduce uncertainty into the results, due to the difficulty in standardising the method by which curd samples are obtained.

Thirdly, a calibration procedure must be carried out before measurements can be made. In addition to being a specialised and labour-intensive procedure, the calibration standards themselves are expensive and ill-suited to hostile factory environments.

For these reasons the waveguide transmission technique was not a serious contender in the search for a suitable sensing head.

5.2.2.2 Free-Space Transmission Sensors

Free-space sensors were introduced in Section 5.2.1.2. The principles used in designing free-space reflection sensors can also be applied to create a transmission-based measurement system. Two antennae are required, one to transmit and one to receive. By mounting one antenna on either side of the sample it is possible to determine permittivity from the amount of signal that penetrates from the transmitter to the receiver.

The strengths and limitations of free-space transmission sensors are very similar to those based on reflectance measurements. While offering the potential for non-contact sensing, there remain the requirements for large sample sizes and/or physically large antennae. This is evident from the results of workers such as Hallikainen et al. (1986), who used free-space methods to measure the permittivity of snow. In this case, typical sample diameters were of the order of 30 cm, with the separation between the antennae being 23–37 cm. Another source of error with free-space transmission sensors is standing waves in low-loss materials. This can be accounted for by making samples thick enough to ensure there is at least 10 dB of attenuation through the material under test (Nyfors and Vainikainen, 1989, p. 107).

Ultimately the expense and practical difficulty of implementing a free-space transmission sensor ruled out this approach.

5.2.3 Resonant Sensors

Microwave resonators enable permittivity to be measured with potentially the highest level of accuracy of any family of microwave sensors. Essentially a type of tuned circuit, resonant sensors allow dielectric properties of materials to be gleaned from the change in the Q-factor and resonant frequency caused by the presence of samples of the material.

Microwave resonant sensors can be implemented in a variety of ways. Generally speaking, however, this type of sensor consists of a short length of transmission line with a large impedance mismatch at one or both ends. A signal is coupled onto the transmission line, and a standing wave is created by the impedance mismatch(es) at either end.

5.2.3.1 Cavity Resonators and the Perturbation Method

A well known type of resonant sensor is the waveguide cavity. This can be regarded as a length of waveguide transmission line terminated at either end by a short circuit. The test signal is coupled into the cavity via a small probe or loop.

A technique known as the perturbation method is commonly used to infer the dielectric properties of a test material. The material to be measured is prepared as a rectangular shim which is then placed either on the floor of the cavity (longitudinal sample), or upright in the centre of the cavity (transverse sample). If the thickness of the sample is small, then the field pattern in the loaded cavity can be assumed to be approximately equal to that of the empty cavity (Altman, 1964, pp. 409–416). It is then possible to derive equations which express permittivity in terms of the dimensions of the sample and the resonant frequency and Q-factor of the cavity with and without the sample in place. Naturally these expressions are only approximations, but are generally considered sufficiently accurate for measurements in an industrial application (Nyfors and Vainikainen, 1989, pp. 141–145).

Recent implementations of cavity-based measurement systems have been reported in a series of papers by Kraszewski, Nelson and You. In a 1989 paper (Kraszewski, You and Nelson, 1989) the authors describe a system for determining the dielectric properties of soybean seeds. After measuring the permittivity of each seed, the moisture content was determined by standard weighing and drying methods, and the results plotted on a calibration curve. The authors were subsequently able to use these results to measure the moisture content of soybean seeds with a mean error of 0.15% and a standard deviation of 0.51%.

The above procedure has been repeated for corn kernels (Kraszewski, Nelson and You, 1989; Kraszewski et al., 1990), which have a highly irregular shape in comparison to soybean seeds. For this reason the authors found it necessary to measure the permittivity of each corn kernel several times with the kernel oriented differently for each measurement, and record the average permittivity. After establishing a calibration curve relating permittivity to moisture content, the authors were able to measure corn kernel moisture content with a mean error of 0.02% and a standard deviation of 0.62%.

Finally, Kraszewski and Nelson (1992; 1993; 1994) have extended this method to enable seed *mass* to be measured as well as moisture content. The reported accuracy was better than 3%.

Clearly an impressive level of accuracy can be obtained using cavity resonators. Nevertheless, there are several negative aspects to consider when attempting to adapt this technique for the purpose of real-time instrumentation.

Firstly there is the issue of sample preparation to take into account. Solid materials must be machined precisely to ensure a snug fit into the cavity. Liquid or semi-solid materials must be poured to a known depth, and the cavity sealed to avoid leakage. These procedures are likely to be time consuming and require specialist skills. While this may not be a problem in the laboratory, an instrument destined for use in a dairy factory should be more 'user-friendly'.

Secondly, the cost of cavity resonators is relatively high. This is largely because the raw waveguide used to make the cavity is very expensive. Furthermore, due to the fine tolerances which must be satisfied when fabricating cavity resonators, manufacturing costs tend to be higher.

Finally, the high Q-factor of waveguide cavities, often touted as one of the strengths of these devices, is potentially a weakness when attempting to integrate the cavity into a moisture sensing instrument. In order to locate the resonant frequency of the cavity with a test sample in place, the system oscillator must be capable of sweeping over a range of frequencies. However, the high Q-factor of the cavity means that the resonant 'dip' in the magnitude of the measured input reflection coefficient will be extremely narrow-band. In order to locate the minimum value of this dip with any accuracy, the oscillator must be able to sweep in very small frequency increments and its spectral purity must be high. As a result the digital control circuitry must be designed so that a wide range of demand frequencies can be 'dialled up' in sufficiently small steps, i.e. a high-resolution D/A converter will be required. These requirements all drive up the cost and complexity of an instrument based on a waveguide cavity sensor.

5.2.3.2 Quasioptical Resonators

Another type of resonant circuit which can be used to sense material properties is the quasioptical resonator (also known as a *Fabry-Perot* resonator). This device consists of two parallel

mirrors, one or both of which may be parabolic or spherical in shape. Small coupling loops in the middle of the mirrors are used to excite the resonator, producing a standing wave pattern between the mirrors.

A quasioptical resonator can be made into a sensor by placing a thin slab of the test material between the two mirrors. The permittivity of this slab can then be calculated from the parameters of the resonator (Cullen and Yu, 1971).

However, once again the issue of sample preparation must be confronted. Samples must be machined to a precise geometry, and must be carefully oriented relative to the planes of the mirrors.

Another requirement of quasioptical resonators is that components must be manufactured to very strict tolerances. The mirrors must be very smooth, and need to be carefully aligned with respect to each other. The separation between the mirrors is another critical parameter, as is the stability of the frequency source. These factors all act to drive up the cost of the system.

Finally, much of the work reported in the literature appears to have been tailored for low-loss dielectrics like polystyrene, perspex and PTFE (Cook et al., 1974; Lynch, 1983; Chan and Chambers, 1987). This suggests that quasioptical resonators are ill-suited to making measurements on lossy materials such as cheese curd.

5.3 Planar Moisture Sensors

The type of sensors which were investigated as candidates for the moisture sensing instrument all belonged to the family of planar sensors. Such sensors consist simply of a thin substrate material with copper tracks etched on one side, and a ground plane on the other. A typical example is shown in Figure 5.1.

As electromagnetic waves propagate along the sensor, some of the field fringes into the medium above the sensor. This affects the wavelength of the propagating wave, and can also result in signal loss. The combination of these two factors means that the reflection or transmission properties of planar sensors are a function of the material covering the sensor, as well as the

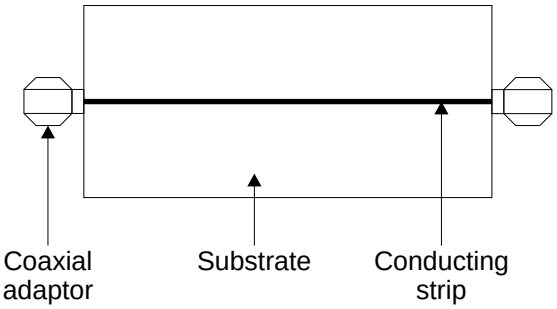

Figure 5.1: Example of a planar transmission sensor.

other parameters like substrate permittivity, substrate thickness, frequency, and the configuration of the copper tracks on the top layer.

These sensors have several advantages compared to other devices.

Firstly, planar sensors are mechanically simple. They do not usually require any specialised manufacturing techniques, and can often be fabricated using standard circuit board etching techniques.

Secondly, due to their simplicity planar sensors are generally very cheap to produce, even in one-off prototyping situations.

Thirdly, sensors with widely varying properties may be fabricated with equal ease, due to the fact that for a given substrate, the only parameter that need be altered to obtain different performance is the pattern of copper on the substrate surface. Consequently it is possible to implement transmission sensors, reflection sensors, radiative sensors, resonant sensors, and sensors which couple either strongly or weakly to the covering layer, depending on the amount of signal loss which can be tolerated (which in turn depends on the dynamic range of the instrument).

Finally, planar sensors can be designed to operate over a wide frequency range, making it possible to perform broadband measurements.

Despite the large number of possible sensor types available, only two main types of planar sensors were investigated due to time constraints. These sensors were microstrip and coplanar waveguide.

5.3.1 Microstrip

Microstrip sensors are perhaps the simplest sensor type of all. Microstrip sensors consist of a single strip (or possibly a number of coupled strips) on a substrate above a ground plane. A typical microstrip transmission line is depicted in Figure 5.2.

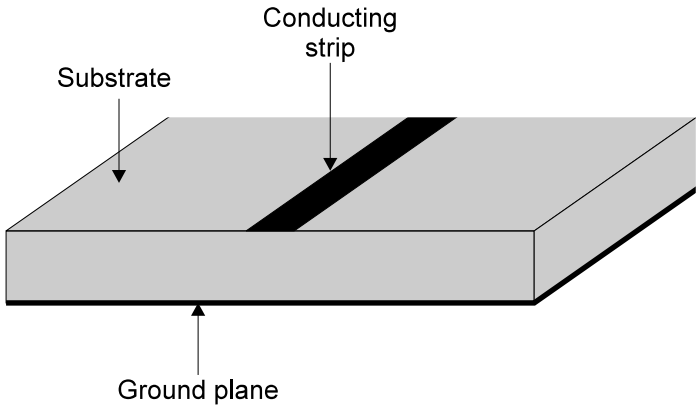

Figure 5.2: Microstrip transmission line.

In broad terms, the characteristic impedance of microstrip depends primarily upon the width of the strip conductor, while the propagation coefficient depends on the permittivity and thickness of the substrate and superstrate.

5.3.2 Coplanar Waveguide

There are several variants of the coplanar waveguide configuration, but all consist basically of a strip conductor on a substrate with a ground plane on either side, separated by a narrow slot. This is depicted in Figure 5.3.

The main differences in coplanar waveguide geometry which occur between authors concerns the ground plane (or absence thereof) on the other side of the substrate. Early workers in the field (Wen, 1969; Dupuis and Campbell, 1973; Davis et al., 1973; Hatsuda, 1975) treated coplanar waveguide as having no ground plane on the underside of the substrate. Instead, an infinite air dielectric was assumed to exist above and below the structure. More recently,

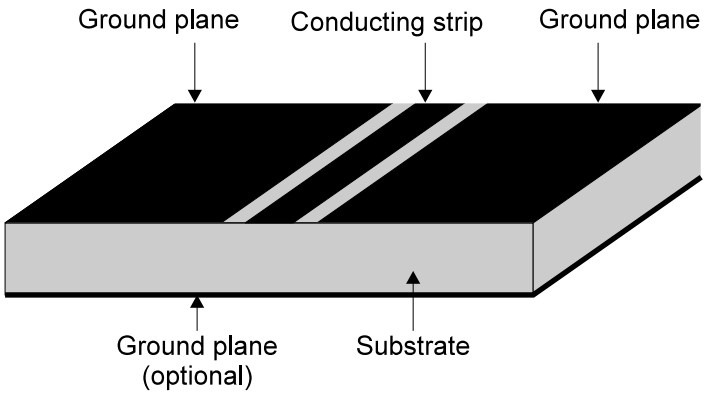

Figure 5.3: Coplanar waveguide transmission line.

workers have considered the case in which the underside of the structure is covered by a ground plane (Veyres and Hanna, 1980; Ghione and Naldi, 1983; Lin and Sheen, 1994).

5.4 Prototype Moisture Sensors

As part of the process of designing a sensor which was appropriate for the measurement of cheese curd moisture, six candidate sensors were fabricated. Three of these were microstrip, while the other three were coplanar waveguide. Each sensor could be used as either a reflection-based or transmission-based device.

In choosing the dimensions of each sensor a nominal operating frequency of 3 GHz was assumed, and methanol was selected as the material under test. As discussed in Chapter 2, methanol is a polar dielectric whose properties can be accurately described by a Cole-Cole function (Jordan et al., 1978). At a frequency of 3 GHz and a temperature of 25°C the permittivity of methanol is $20.6 - j14.1$, which is similar to that of cheese curd. For example, cream cheese with 45.5% moisture content has a permittivity of $21 - j5.3$ (at the production temperature of 80°C). The deterministic nature of the permittivity of methanol made it a convenient test dielectric, especially given the ease of handling compared to cheese curd.

The dimensions of each group of sensors were selected such that one sensor would have an impedance with a real part of 50Ω when covered by methanol, while the other two sensors would have impedances with real parts somewhat above and below 50Ω. In this way the field

surrounding each sensor would fringe into the methanol superstrate by a different amount, with the result that each sensor would have a different sensitivity.

In order to estimate the input impedance of each sensor when covered by methanol, a quasi-static spectral domain analysis was performed. It will be shown in Part II of this thesis that this technique can be rather inaccurate when applied to planar structures covered by high-permittivity materials. However, its relatively simple nature made it useful for providing a 'first approximation' of the characteristic impedance of each sensor. A detailed description of the quasi-static spectral domain method is provided in Chapter 6.

5.4.1 Microstrip Sensors

The three microstrip sensors were fabricated on a single sheet of $0.05''$ (1.27 mm) Rogers RT/duroid 6010 microwave substrate, having $\varepsilon_r' = 10.2 \pm 0.250$ and $\tan\delta = 0.0023$. A brass baseplate was machined to provide mechanical strength for the substrate, and the two were soldered together to ensure electrical continuity. Each sensor on the substrate was 63 mm in length and was terminated at either end in a female SMA microstrip launcher, enabling transmission measurements to be made by connecting one port of an Automatic Network Analyser to each connector and measuring the transmission coefficient of the sensor. Alternatively, reflection measurements could be made by terminating one of the SMA connectors in a matched load or short circuit, and measuring the input reflection coefficient at the other port.

As mentioned above, each sensor was designed assuming that the material under test was methanol at 25°C. A summary of the dimensions of each microstrip sensor is given below in Table 5.1.

Table 5.1: Details of microstrip moisture sensors. All characteristic impedances have been estimated by static spectral domain analysis (see Sections 6.3–6.5 for details).

Strip Width (mm)	Sensor Characteristic Impedance (Ω)	
	Methanol Superstrate	Air Superstrate
0.24	$58.9 + j10.1$	91.0
0.49	$47.7 + j7.8$	73.1
0.97	$37.1 + j5.8$	56.2

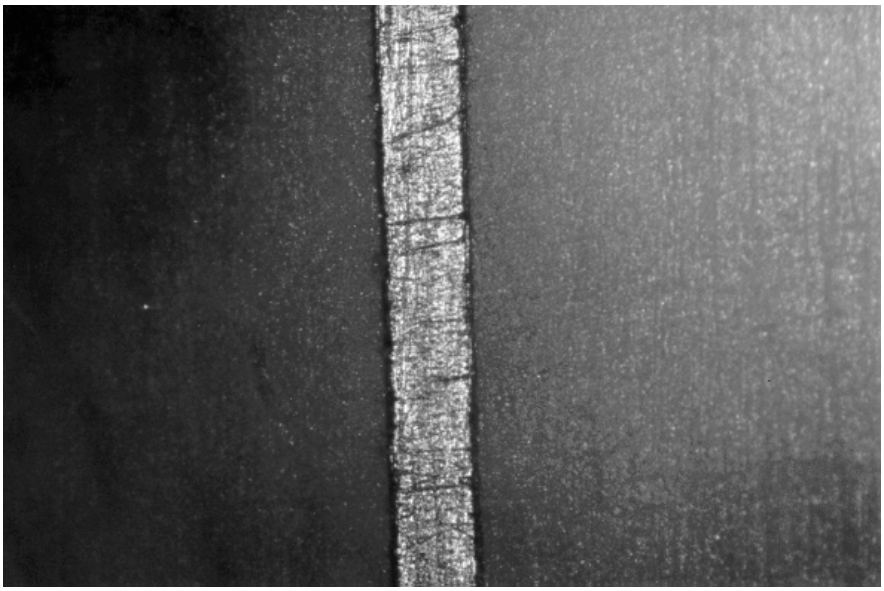

Figure 5.4: 91Ω microstrip moisture sensor. Scale of photograph is approximately 48 times true size. $2w = 0.24$ mm, $d = 1.27$ mm, $\varepsilon_1 = 10.2$.

The strip widths quoted in Table 5.1 were measured using a travelling microscope with a magnification factor of 60×. This enabled measurements to be made with an accuracy of ± 0.005 mm. By mounting a camera on the microscope it was possible to photograph the magnified images, one of which is shown in Figure 5.4. Note that the effective magnification factor of this photograph as it appears on the page is approximately 48×.

An added advantage of the travelling microscope is that it enables fabrication defects to be located which may not be obvious to the naked eye. This is clear in Figure 5.5, which shows a section of a sensor which has been slightly underetched, leaving an excess deposit of copper on the substrate. Imperfections such as this can cause performance to depart from theoretical predictions.

Also visible in Figures 5.4 and 5.5 are a large number of scratches on the surface of the strip conductor. Surface roughness can cause a significant increase in the ohmic loss of a microstrip transmission line (Pucel et al., 1968), and can be responsible for poor agreement between theory and experiment. Note also, however, that where a lossy dielectric like methanol is present, the effects of ohmic loss will probably not be significant by comparison.

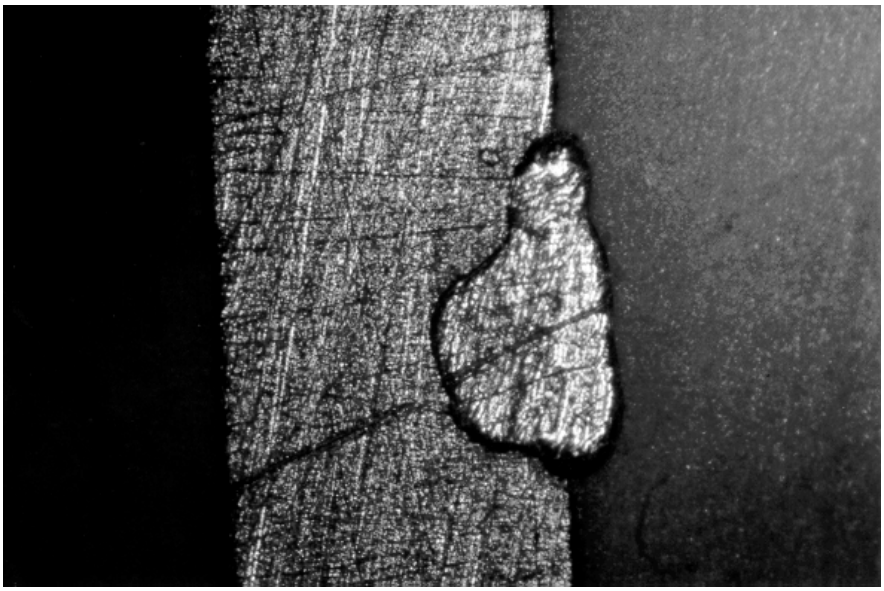

Figure 5.5: Underetched section of 56Ω microstrip moisture sensor. Scale of photograph is approximately 48 times true size. $2w = 0.97$ mm, $d = 1.27$ mm, $\varepsilon_1 = 10.2$.

5.4.2 Coplanar Waveguide Sensors

Like the microstrip sensors described above, three coplanar waveguide sensors were fabricated on a sheet of Rogers RT/duroid 6010 substrate (thickness = 1.27 mm, $\varepsilon_r' = 10.2 \pm 0.250$, $\tan\delta = 0.0023$). Once again each sensor was designed assuming that the material under test was methanol at 25°C. A summary of the dimensions of each coplanar waveguide sensor is given in Table 5.2.

Table 5.2: Details of coplanar waveguide moisture sensors. All characteristic impedances have been estimated using static spectral domain analysis.

Strip Width (mm)	Slot Width (mm)	Sensor Characteristic Impedance (Ω)	
		Methanol Superstrate	Air Superstrate
0.24	1.03	$47.0 + j10.0$	91.7
0.24	0.51	$41.2 + j8.9$	76.1
0.48	0.54	$34.0 + j7.3$	63.3

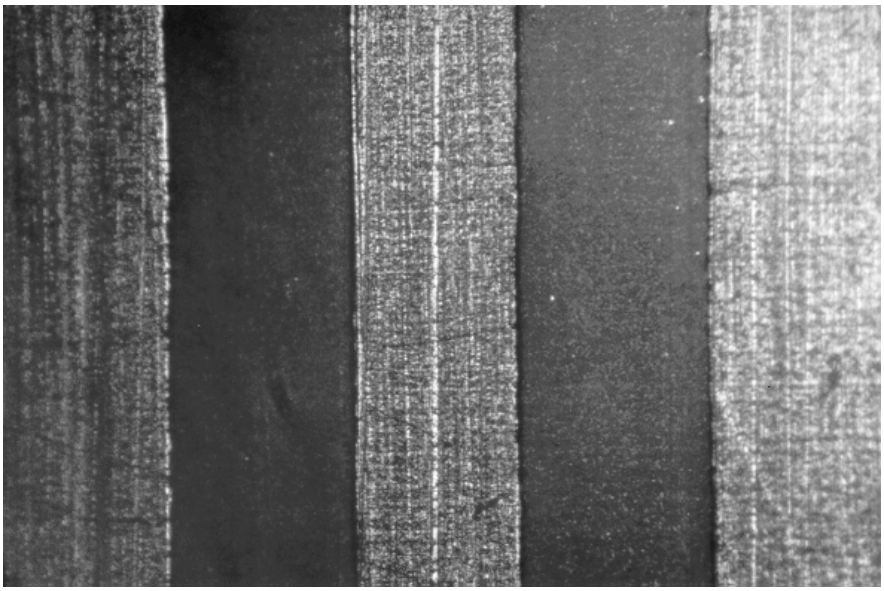

Figure 5.6: 63Ω coplanar waveguide moisture sensor. Scale of photograph is approximately 46 times true size. $2w = 0.48$ mm, $s_1 = s_2 = 0.54$ mm, $d = 1.27$ mm, $\varepsilon_1 = 10.2$.

As before, a brass baseplate provided mechanical strength. Each sensor was 63 mm in length with a female SMA launcher at either end. A photograph taken using the travelling microscope is shown in Figure 5.6 at a magnification of approximately 46 times true size.

The coplanar waveguide sensors proved more difficult to manufacture than the microstrip sensors. Part of the problem concerned the provision of a ground connection for the two ground planes on the top layer of the sensor. Where the ground plane on the underside of the sensor was grounded through the brass baseplate (which in turn was connected to the flange of the SMA launcher), no such arrangement existed for the ground strips on the top of the sensor. Ultimately this was solved by creating a solder joint between the flange of each SMA launcher and the top ground planes. These connections, while not very robust, proved satisfactory for the purposes of laboratory testing.

The other difficulty encountered in manufacturing coplanar waveguide sensors was that the strip conductors were very narrow and therefore particularly vulnerable to fabrication defects. A typical example of this is shown in Figure 5.7, where the centre conductor has been overetched in one place.

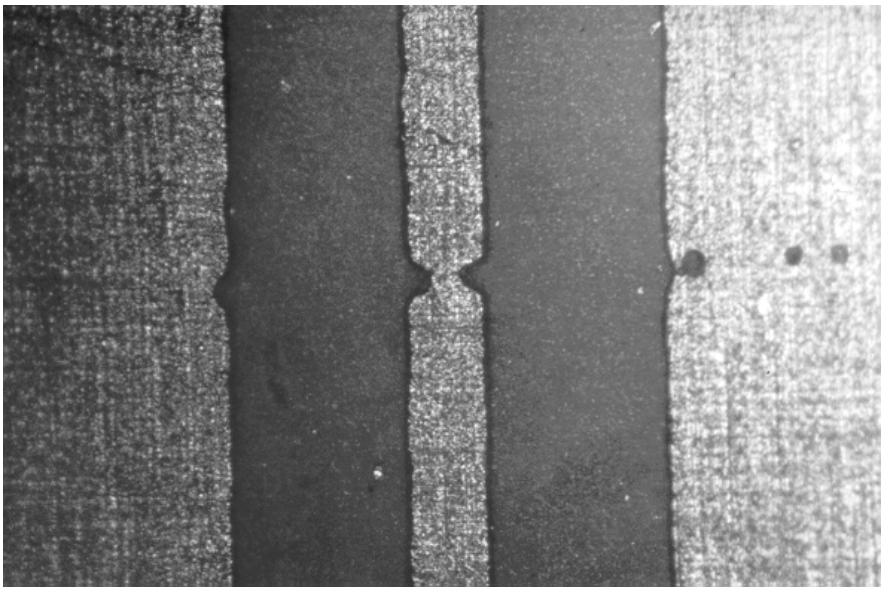

Figure 5.7: 76Ω coplanar waveguide moisture sensor with overetched section. Scale of photograph is approximately 46 times true size. $2w = 0.24$ mm, $s_1 = s_2 = 0.51$ mm, $d = 1.27$ mm, $\varepsilon_1 = 10.2$.

While overetching could be problematic, introducing impedance mismatches and causing disagreement between theory and experiment, the defect shown in Figure 5.8 was more serious. The centre conductor was completely severed, with disastrous consequences for the performance of the sensor. In this instance an attempt was made to salvage the sensor by bridging the gap with some silver paint; remnants of this can be seen in Figure 5.8 in the slots of the waveguide. Unfortunately this repair attempt was not successful, and the sensor could not be used.

5.5 Sensor Characterisation

In order for a sensor to be useful, its behaviour must be determined in advance by either empirical or theoretical means. There are pros and cons associated with each method, some of which are discussed below.

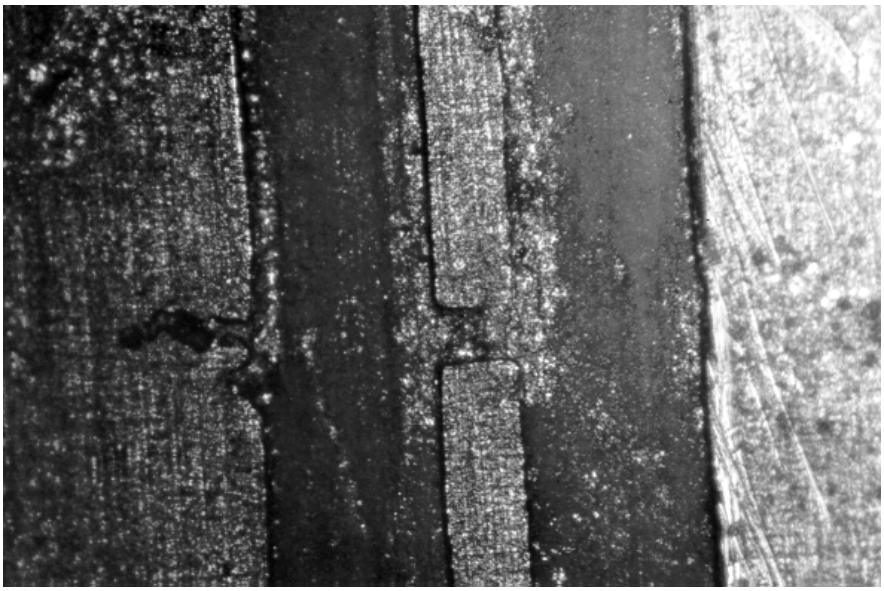

Figure 5.8: 76Ω coplanar waveguide moisture sensor with broken track. Scale of photograph is approximately 46 times true size. $2w = 0.24$ mm, $s_1 = s_2 = 0.51$ mm, $d = 1.27$ mm, $\varepsilon_1 = 10.2$.

5.5.1 Empirical Characterisation

The empirical characterisation of a sensor involves making measurements on a number of samples of the material under test, and then fitting a curve of best fit to the data. This approach has been used in practice by such workers as Kent (1972; 1973; 1979; 1993).

The disadvantage with this approach is that the sensor can only be used within the limits of the calibration curve. If a sample is encountered which has a moisture content greater than anything in the calibration data, then no reliable estimate can be obtained. The only option in such a situation would be to extrapolate the curve of best fit, a risky procedure in view of the fact that the curve is merely a convenient function which has no firm physical basis.

5.5.2 Theoretical Characterisation

The alternative to empirical calibration is to develop a theoretical model of the electromagnetic behaviour of the sensor. An accurate theoretical model can take a lot of the guesswork out of sensor design, and has the added advantage of enabling a variety of different sensor configura-

tions to be analysed prior to any prototyping work. This results in savings of time and money. Furthermore, a good general sensor model can in principle be used with *any* test material, and is not restricted to making measurements within the bounds of an empirical calibration curve.

The disadvantage of theoretical sensor characterisation is that it is extremely difficult to develop accurate models for any but the simplest structures. For this reason the candidate sensor designs investigated for this project were all very simple, consisting essentially of straight lengths of transmission line.

5.5.3 Commercial Analysis Software

A third option which is available to the designer is to use commercial electromagnetic (EM) simulation software. EM simulators model the behaviour of fields in and around high-frequency devices by direct numerical solution of Maxwell's equations. Until recently this option was only open to those with access to high-end engineering workstations. However, with the evolution of fast and cheap desktop PCs, commercial EM simulation software is becoming a serious alternative for those with quite modest computing resources.

A wide variety of simulators is available, with numerous optional add-ons to suit different applications. As a minimum, most packages include a graphical model editor, a numerical field solving engine, and a post-processor for viewing the results of simulations.

EM simulators are commonly classified as either full 3D or $2\frac{1}{2}$D. Full 3D simulators are generally the most powerful and expensive of the two, employing processor- and memory-intensive techniques like the Finite Element Method (FEM) or the Finite Difference Time Domain (FDTD) method. One of the main advantages of full 3D analysis tools is that the user can specify quite arbitrary structures comprised of many different materials, each of which may be lossy, nonlinear and/or anisotropic. Examples of commercially available full 3D simulators include Ansoft HFSS, CST Microwave Studio, Remcom XFDTD, APLAC Solutions EM module, and Zeland FIDELITY.

By contrast, $2\frac{1}{2}$D simulators are tailored for stratified structures, such as microstrip, coplanar waveguide, stripline, slotline and the like. Rather than discretising the entire volume around the

structure of interest, $2\frac{1}{2}$D simulators solve only for the currents or fields across each dielectric interface, using techniques like the Method of Lines or the Method of Moments. The fields throughout the entire volume of the device can then be obtained from the resulting current or field distributions. For this reason, $2\frac{1}{2}$D simulators are often referred to as 'planar 3D' simulators. Examples of commercial $2\frac{1}{2}$D simulators include Ansoft Ensemble, Eagleware EMPOWER, Sonnet Planar 3D Simulator, AWR EMSight, and Zeland IE3D.

While commercial software packages can be very powerful design tools, they cannot easily be adapted to an online industrial application. In the case of a microwave moisture meter, the sensor model is only part of a larger program which must perform a variety of tasks besides just analysing the sensor. It is not clear how a commercial EM simulator could be incorporated into the control software for the instrument. Even if this were possible, such software is overkill in an application where only a single structure (i.e. the sensing head) is ever going to be analysed.

Another disadvantage of commercial EM simulators is the high cost. Entry-level prices start at around A$10 000 for packages like Eagleware EMPOWER. At the top end of the market, full 3D software suites like CST Microwave Studio can retail for up to A$100 000. As such, the use of commercial EM software to characterise the sensing head of a microwave moisture meter would significantly increase the total cost of the final product, making it difficult to meet the low-cost objective of this project.

5.5.4 Summary of Characterisation Philosophies

Of the three approaches to sensor characterisation (empirical, theoretical, and via commercial software) no single approach is the best in all cases. However, for the application of a microwave moisture meter the preferred method was theoretical characterisation. This approach, if done properly, offers some of the flexibility of a commercial package, while at the same time lending itself to implementation as a subroutine in a larger program.

One question mark over a theoretical sensor model is: Can it be used in a real-time application? This depends largely on the nature of the model, the usual trade-off being between speed and accuracy.

The following chapters will cover the development of two theoretical models, both based on the powerful spectral domain method. One of these models is a static approximation, which is only exact at DC. The other is a full-wave model, which can account for frequency dependent phenomena such as dispersion, surface waves and radiation.

5.6 Conclusion

This chapter has discussed some of the considerations pertaining to the choice of an appropriate sensor for a microwave moisture sensing instrument. These included performance, cost, complexity and the ease of integration into a production process.

Three different classes of microwave sensor have been discussed: reflection, transmission and resonant sensors. Each has strengths and limitations.

Candidate reflection sensors included the open-ended coaxial probe and the free-space reflection sensor. The coaxial probe was considered unsuitable primarily due to its high sensitivity to contacting errors, and the low penetration into the material under test. Free-space sensors were rejected for many reasons, including high cost, large sample requirements, and high sensitivity to variations in the distance between the antenna and the sample.

Several types of transmission sensor were investigated, including waveguide-based and free-space sensors. While waveguide transmission sensors proved useful in the cheese curd permittivity survey, great care was needed in preparing samples. The need for a lengthy calibration procedure with expensive standards was also necessary, making this technique less than optimal for a factory environment. Free-space transmission sensors suffered from many of the same limitations as their reflection-based counterparts. Other problems arising from standing waves in the sample also hinder the practical implementation of these sensors.

Two different types of resonant sensor were examined. One was the cavity resonator, the other was the quasioptical resonator. Both offer superior permittivity measurement accuracy compared to other sensor types. Unfortunately both of these devices can be difficult and expensive to fabricate, and require complex support hardware. Moreover, due to the need for samples of

a precise geometry it is not obvious how these sensors could be integrated into a production environment.

A strong case has been presented in favour of planar contact sensors. These devices offer the advantages of low cost, ease of fabrication, broadband operation and a high degree of configurability.

Both microstrip and coplanar waveguide sensors were considered. Coplanar waveguide was eventually rejected as it proved more difficult to manufacture. Microstrip was therefore the final choice.

Three different approaches to sensor characterisation have been discussed. For the purposes of this project a theoretical model has been chosen as the preferred means of characterisation. This approach is justified on the grounds that it offers the most favourable combination of flexibility and accuracy. However, it has also been noted that such a model can require significant time and effort to develop.

5.7 Summary: End of Part I

This chapter marks the end of Part I of this thesis. So far the basic principles of microwave sensing have been explained, and the results of a cheese curd permittivity survey have been presented which demonstrate that a measurable correlation exists between curd dielectric behaviour and moisture content. An account has been given of the design and construction of a computer-controlled six-port reflectometer, proving that it is possible to make highly accurate vector reflection measurements using hardware built from relatively cheap, off the shelf components. Finally, a range of different microwave sensors has been reviewed, and a strong case has been made for microstrip contact sensors to be used for this application.

Part II of this thesis is concerned chiefly with the development of a theoretical model of a microstrip sensor in contact with a lossy, high-permittivity material like cheese curd. The treatment given to this work is more detailed, in-depth, and narrowly focused than the subject matter discussed in Part I. While this transition involves a somewhat abrupt change of style, it is nevertheless necessary in order to adequately describe the sensor model, without which the

microwave moisture meter would be totally dependent upon empirical calibration data for its operation.

Thus, where Part I has presented all the major building blocks required to build an accurate moisture sensing instrument, Part II will complete the picture by showing how the theoretical model was developed, thereby enabling meaningful dielectric information to be extracted from raw scattering parameter data.

Part II

Propagation on Microstrip Line in Contact with Lossy, High Permittivity Material

Chapter 6

The Spectral Domain Method I: Static Approximation

6.1 Introduction

The first step in developing a microstrip sensor model was to determine the propagation coefficient and characteristic impedance of the structure when in contact with cheese curd. This information would later enable the scattering parameters of the entire sensor to be predicted using classical transmission line theory.

Two different models were evaluated in the course of this project. Both were variants of the powerful Spectral Domain Method, which simplifies the analysis of planar structures by transforming the field equations into the Fourier domain.

This chapter describes the first of the two sensor models to be developed. The analysis was based on a DC approximation which, while not as accurate as a frequency-dependent solution, has nevertheless found popularity with other workers in this field due to its relative simplicity and computational speed.

The first section of this chapter provides an overview of the spectral domain method, and outlines the assumptions and limitations of the low-frequency approximation.

The second section derives the Fourier transformed field equations for a microstrip transmission line covered by a non-air dielectric.

The third section introduces the family of basis functions which were used to represent the charge distribution on the strip conductor.

The fourth section explains how the propagation coefficient and characteristic impedance of the sensor were calculated.

The fifth section verifies the accuracy of the static model by comparing results with examples from the literature.

The final section summarises a number of strategies through which the analysis software could be made faster without sacrificing accuracy.

6.2 Quasi-TEM Spectral Domain Method

The static spectral domain method is a Fourier transform-based technique which provides a relatively simple, non-iterative means of calculating the capacitance and characteristic impedance of microstrip and other planar transmission lines. The term 'static' refers to the assumption of a TEM mode of propagation. This is not true in reality, however it is a reasonable approximation to the dominant mode of propagation at low frequencies (Mirshekar-Syahkal, 1990, p. 76). For this reason the static spectral domain method is often referred to as a *quasi-TEM* technique.

Several previous workers in this field have used the quasi-TEM method to analyse microstrip sensors. Bahl and Stuchly (1980) have modelled a microstrip resonator covered by such materials as water, polyolefin and mica. Khalid et al. (1988) have used the same technique to develop an optimal microstrip transmission sensor for measuring the moisture content of hevea latex.

The following sections develop the quasi-TEM analysis in detail. The geometry of the sensor and orientation of the coordinate system are shown in Figure 6.1. The strip conductor is assumed to have zero thickness and is perfectly conducting. The permittivity of the covering medium may assume any complex value. Propagation is in the z-direction.

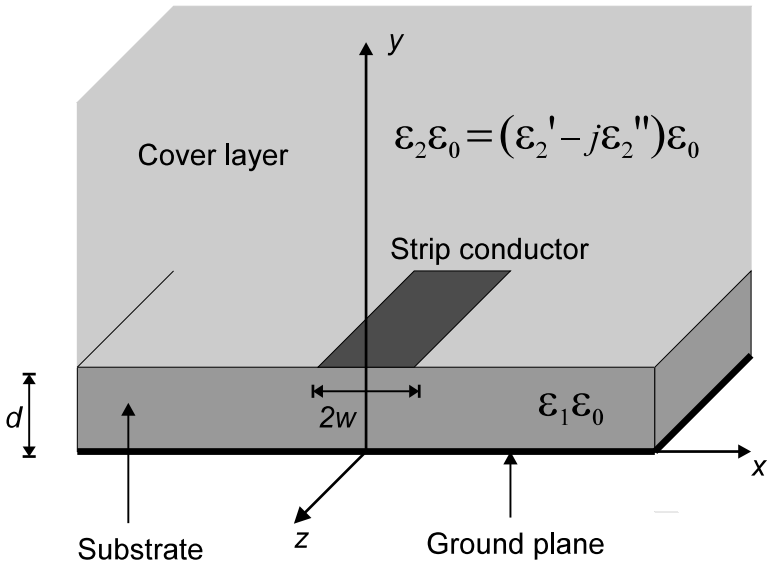

Figure 6.1: Microstrip transmission line covered by lossy medium of infinite extent.

6.3 Derivation of Fourier Transformed Field Equations

For a homogeneously-filled two-conductor transmission line with fields varying as $e^{j\omega t}$, Maxwell's curl equations can be written

$$\nabla \times \boldsymbol{E} = -j\omega\mu\boldsymbol{H} \tag{6.1}$$

$$\nabla \times \boldsymbol{H} = j\omega\varepsilon\boldsymbol{E} \tag{6.2}$$

where $\boldsymbol{E}$ and $\boldsymbol{H}$ are the vector electric and magnetic fields respectively, and ε and μ are the the absolute permittivity and permeability respectively of the medium filling the transmission line (Pozar, 1990, pp. 126–130).

Assuming wave propagation in the z-direction, and applying the condition that the z-directed components of $\boldsymbol{E}$ and $\boldsymbol{H}$ are equal to zero, it can be shown that:

$$\boldsymbol{E}_t = -\nabla_t u e^{-j\beta z} \tag{6.3}$$

$$\boldsymbol{H}_t = \sqrt{\frac{\varepsilon}{\mu}}\boldsymbol{E}_t \tag{6.4}$$

where $\boldsymbol{E}_t$ and $\boldsymbol{H}_t$ are the transverse components of $\boldsymbol{E}$ and $\boldsymbol{H}$ respectively, and β is the phase coefficient of the propagating wave (Mirshekar-Syahkal, 1990, pp. 75–80). $u(x, y)$ is a scalar potential function which is the solution of Laplace's equation in the transverse plane:

$$\nabla_t^2 u = 0 \tag{6.5}$$

In the case of microstrip there are two regions to consider, namely the substrate region and the region above the strip. If we let ϕ_i denote the scalar potential in the i^{th} region then this must be a solution of Laplace's equation in that region. Thus we have

$$\nabla_t^2 \phi_i = 0 \qquad i = 1,\, 2 \tag{6.6}$$

i.e.

$$\left(\frac{\partial^2}{\partial x^2} + \frac{\partial^2}{\partial y^2} \right) \phi_i = 0 \qquad i = 1,\, 2 \tag{6.7}$$

We now take the Fourier transform of both sides with respect to x and enforce the boundary conditions at the ground plane and at infinity (Yamashita and Mittra, 1968). These conditions can be written in the Fourier domain as:

$$\tilde{\phi}_1 = 0 \quad \text{at} \quad y = 0 \tag{6.8}$$

$$\tilde{\phi}_2 \to 0 \quad \text{as} \quad y \to \infty \tag{6.9}$$

Enforcing boundary conditions 6.8 and 6.9 on the Fourier transformed Laplace's equation yields

$$\tilde{\phi}_1 = A_1 \sinh(|\alpha| y) \tag{6.10}$$

$$\tilde{\phi}_2 = B_2 e^{-|\alpha| y} \tag{6.11}$$

where $\tilde{\phi}_i$ denotes the Fourier transform of ϕ_i in the i^{th} region and α is the Fourier parameter.

In order to determine the potentials $\tilde{\phi}_1$ and $\tilde{\phi}_2$, the constants A_1 and B_2 must be found. To do this we enforce the boundary conditions at the dielectric interface (i.e. $y = d$):

$$E_{x,2} - E_{x,1} = 0 \tag{6.12}$$

$$\varepsilon_2 E_{y,2} - \varepsilon_1 E_{y,1} = \begin{cases} \sigma(x) & |x| < w \\ 0 & w < |x| < \infty \end{cases} \tag{6.13}$$

$$\phi_1 = \phi_2 = \begin{cases} V_0 & |x| < w \\ V(x) & w < |x| < \infty \end{cases} \tag{6.14}$$

where $\sigma(x)$ is the surface charge density on the strip, $V(x)$ is the potential distribution at the dielectric interface excluding the strip, and V_0 is the potential of the strip itself.

In the Fourier domain Equations 6.12–6.14 become

$$\tilde{\phi}_2 - \tilde{\phi}_1 = 0 \tag{6.15}$$

$$\varepsilon_2 \frac{\partial \tilde{\phi}_2}{\partial y} - \varepsilon_1 \frac{\partial \tilde{\phi}_1}{\partial y} = \tilde{\sigma} \tag{6.16}$$

$$\tilde{\phi}_2 = \tilde{\phi}_1 = \tilde{V}_0 + \tilde{V} \tag{6.17}$$

By substituting Equations 6.10 and 6.11 into the above boundary conditions the following expression is obtained:

$$G(\alpha)\tilde{\sigma} = \tilde{V}_0 + \tilde{V} \tag{6.18}$$

where $G(\alpha)$ is the spectral domain Green's function for microstrip at DC, given by

$$G(\alpha) = \frac{1}{|\alpha| \left[\varepsilon_2 + \varepsilon_1 \coth\left(|\alpha| d\right)\right]} \tag{6.19}$$

Although Equations 6.18 and 6.19 have been developed to analyse microstrip, the same equations apply equally to any grounded two-layer planar structure, including coplanar waveguide. This was another reason the spectral domain method was chosen for this project—the same

sensor model (and hence computer program) could be adapted to a variety of sensor configurations, with only a few minor changes required for each new sensor. Unfortunately, as discussed in Chapter 5, coplanar waveguide sensors proved too difficult to fabricate and were eventually rejected in favour of microstrip.

At this stage Equation 6.18 contains two unknowns: the strip surface charge density $\sigma(x)$ and the potential distribution function $V(x)$. One of these must be specified in order to obtain a solution. The usual approach is to expand either $\sigma(x)$ or $V(x)$ as a set of trial functions of the form

$$f(x) = \sum_{p=1}^{P} a_p f_p(x) \tag{6.20}$$

where a_p are constants whose values must be obtained as part of the solution process. Taking the Fourier transform of $f(x)$ yields

$$\tilde{f}(\alpha) = \sum_{p=1}^{P} a_p \tilde{f}_p(\alpha) \tag{6.21}$$

The question of whether to expand $\sigma(x)$ or $V(x)$ in the manner described above depends on the distribution of copper on the dielectric interface (Mirshekar-Syahkal and Davies, 1979). The answer will usually be dictated by which approach provides the greatest computational advantage. Upon reviewing the literature in this field (see for example Pregla and Pintzos, 1974; Knorr and Kuchler, 1975; Mirshekar-Syahkal and Davies, 1979; Mirshekar-Syahkal, 1986; Ke et al., 1992) a convenient rule of thumb emerges which can be summarised as follows:

> If a planar transmission line has conducting strips which are narrower than the slots, then expand $\sigma(x)$ as a set of trial functions. If the strips are wider than the slots, expand $V(x)$.

For microstrip this implies that $\sigma(x)$ should be expanded in order to obtain the greatest rate of convergence.

In order to solve for the characteristics of a given structure, the popular Galerkin method can be used. The application of this method to microstrip is discussed in Section 6.5. Firstly, however, the important issue of the choice of trial functions shall be discussed.

6.4 Basis Functions

The choice of the functions used to represent the charge density on the strip conductor is a topic which has received exhaustive coverage in the literature. Consequently no attempt will be made here to present a definitive treatment of the subject. Rather, a broad overview shall be presented, followed by a discussion of the basis functions used for the analysis of the moisture sensors.

Although the exact nature of the charge or voltage distribution across the dielectric interface of a planar structure is generally not known, a high degree of accuracy can still be obtained if the basis functions capture the basic properties of the distribution of interest.

For microstrip this means that the basis functions should incorporate the edge singularity into their behaviour. The edge singularity refers to the unbounded nature of the charge density at the edge of the strip conductor (Meixner, 1972). In theory, for a perfectly conducting strip the charge density should approach infinity at the edges of the strip in a manner similar to Figure 6.2.

For this project the basis functions used to represent the charge density on microstrip were the of the same form as those suggested by Jansen (1978) for the longitudinal component of current on microstrip:

$$\sigma_1(x) = \frac{1}{\sqrt{1-\left(\frac{x}{w}\right)^2}} \tag{6.22}$$

$$\sigma_p(x) = \frac{\cos\left[(p-1)\pi\left(\frac{x}{w}\right)\right] - J_0\left[(p-1)\pi\right]}{\sqrt{1-\left(\frac{x}{w}\right)^2}} \qquad p = 2,\, 3,\, \ldots,\, P \tag{6.23}$$

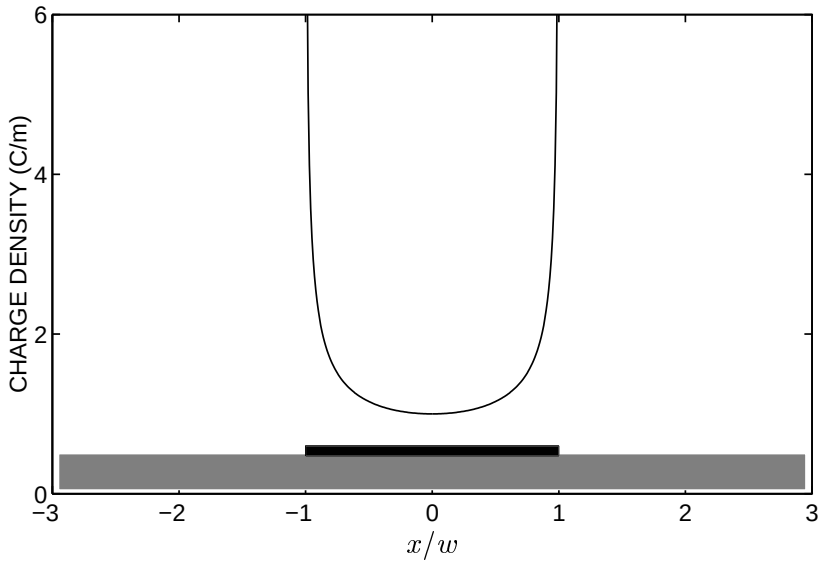

Figure 6.2: Theoretical charge distribution on microstrip conductor. Substrate and strip conductor included on plot for comparison.

In the Fourier domain these functions become

$$\tilde{\sigma}_1 = \frac{w}{2} J_0(\alpha w) \tag{6.24}$$

$$\tilde{\sigma}_p = \frac{w}{4} \{ J_0 [\alpha w - (p-1)\pi] + J_0 [\alpha w + (p-1)\pi] - 2 J_0 [(p-1)\pi] \, J_0(\alpha w) \} \qquad p = 2, 3, \ldots, P \tag{6.25}$$

A significant feature of Equations 6.24 and 6.25 is the presence of the Bessel function J_0. For large arguments J_0 can be approximated by a decaying sinusoid with an envelope that is inversely proportional to the square root of the argument (Kreyszig, 1993, p. 228). As such, J_0 is a function that decays to zero at a continually decreasing rate. It will be shown in the next section that this ultimately leads to a system of equations which is numerically very tedious to evaluate. Many authors have found that by relaxing the requirement to capture the edge condition, simpler basis functions with more rapidly decaying Fourier transforms can be used without significant loss of accuracy. This is due to the variational nature of the quasi-TEM method, which renders it relatively insensitive to the type of basis function used (Yamashita, 1968). For example, Khalid et al. (1988) have used a function of the form $\sigma(x) = 1 + |x/w|^3$ to represent the charge distribution on the strip. Similarly, Yamashita and Mittra (1968) have

used the simple piecewise-linear function $\sigma(x) = |x|$. Pozar (1990, pp. 187–189) has gone even further and used the function $\sigma(x) = 1$, which neglects the edge condition entirely yet still provides reasonable agreement with conventional formulas. The advantage of these trial functions is that they all have Fourier transforms which decay towards zero much more rapidly than Equations 6.24 and 6.25, leading to a final system of equations which can be evaluated with far greater speed.

Thus, where it is necessary to capture the edge condition with maximum accuracy, the basis functions of Equations 6.22 and 6.23 are recommended. However, if it becomes important to reduce computing time, one of the less computationally demanding alternatives should be used.

Additional speedup strategies are discussed in Section 6.7.

6.5 Solution Procedure

Expanding the surface charge density on the strip in terms of the trial functions $\sigma_p(x)$ we have

$$\sigma(x) = \sum_{p=1}^{P} a_p \sigma_p(x) \tag{6.26}$$

In the Fourier domain this becomes

$$\tilde{\sigma}(\alpha) = \sum_{p=1}^{P} a_p \tilde{\sigma}_p(\alpha) \tag{6.27}$$

Substitution of Equation 6.27 into Equation 6.18 yields

$$G(\alpha) \sum_{p=1}^{P} a_p \tilde{\sigma}_p(\alpha) = \widetilde{V}_0 + \widetilde{V} \tag{6.28}$$

The application of Galerkin's method entails taking the inner product of the voltage and charge distributions across the dielectric interface. For this project the inner product of two functions X and Y was defined as

$$< X, Y > \;\; = \;\; \frac{1}{2\pi} \int_{-\infty}^{\infty} X(x) Y^*(x)\, dx \tag{6.29}$$

where Y^* is the complex conjugate of Y. This is similar to the definition used by Mirshekar-Syahkal (1990, pp. 43–45), except that the sidewalls which are present in Mirshekar-Syahkal's analysis have been moved to infinity here. In the Fourier domain the inner product can be defined as follows:

$$< \widetilde{X}, \widetilde{Y} > \quad = \quad \int_{-\infty}^{\infty} \widetilde{X} \widetilde{Y}^* \, d\alpha \tag{6.30}$$

If X and Y are orthogonal to each other, then Equation 6.29 evaluates to zero. This is also true of Equation 6.30, as demonstrated by Parseval's identity:

$$\frac{1}{2\pi} \int_{-\infty}^{\infty} X(x) Y^*(x) \, dx \quad = \quad \int_{-\infty}^{\infty} \widetilde{X}(\alpha) \widetilde{Y}^*(\alpha) \, d\alpha \tag{6.31}$$

Applying these results to the microstrip problem, we take the following inner product:

$$< \left(\widetilde{V}_0 + \widetilde{V} \right), \tilde{\sigma} > \tag{6.32}$$

Expanding this expression we obtain

$$< \left(\widetilde{V}_0 + \widetilde{V} \right), \tilde{\sigma} > \quad = \quad < \widetilde{V}_0, \tilde{\sigma} > + < \widetilde{V}, \tilde{\sigma} > \tag{6.33}$$

By definition $V(x)$ is nonzero everywhere on the dielectric interface except on the strip conductor. By contrast, $\sigma(x)$ is nonzero on the strip and zero everywhere else. $V(x)$ and $\sigma(x)$ are therefore orthogonal to each other, implying that their inner product must equal zero. Using Parseval's identity in Equation 6.31, the above expression can be simplified to

$$< \left(\widetilde{V}_0 + \widetilde{V} \right), \tilde{\sigma} > \quad = \quad < \widetilde{V}_0, \tilde{\sigma} > \tag{6.34}$$

Substituting Equations 6.27 and 6.28 into this expression produces the following system of P linear equations in P unknowns:

$$\sum_{p=1}^{P} \left[a_p \int_{-\infty}^{\infty} G(\alpha) \tilde{\sigma}_{\acute{p}}^* \tilde{\sigma}_p \, d\alpha \right] = \int_{-\infty}^{\infty} \tilde{V}_0 \tilde{\sigma}_{\acute{p}}^* \, d\alpha \qquad \acute{p} = 1, \, 2, \, \ldots \, , \, P \tag{6.35}$$

These equations can then be solved to obtain the coefficients a_p. The integral expressions in Equation 6.35 were generally too complicated to evaluate analytically, requiring numerical integrations to be performed. The preferred method for this project was Simpson's $\frac{1}{3}$ rule. The limits of integration were chosen by graphing the integrands in Equation 6.35 against α and selecting an upper value $\alpha_{\max}$ at which the magnitudes of the integrands had decayed away to a negligible level. The symmetrical nature of $G(\alpha)$, $\tilde{\sigma}_p(\alpha)$ and $\tilde{V}_0(\alpha)$ meant that each integral did not need to be evaluated over the entire range $\alpha = -\alpha_{\max}$ to $\alpha = \alpha_{\max}$. Rather, the same result could be obtained by integrating from $\alpha = 0$ to $\alpha = \alpha_{\max}$ and then doubling the answer, thereby increasing the speed of the program considerably.

From inspection of Equation 6.35 it is evident that the rate of decay of the integrands with increasing α is a function of the rate of decay of the Fourier transformed basis functions $\tilde{\sigma}_p$. As discussed in Section 6.4, basis functions which accurately represented the edge condition on the strip conductor were generally found to have slowly decaying Fourier transforms. By contrast, basis functions which neglected the edge condition had Fourier transforms which decayed much more rapidly. Consequently the range over which the integrals in Equation 6.35 had to be evaluated varied with the choice of basis functions. This had a corresponding impact on the speed with which each integral could be evaluated.

In order to determine the effective permittivity ε_{eff} and the characteristic impedance Z_0 of the microstrip line, it is first necessary to calculate the static capacitance C with and without the substrate and superstrate present. The capacitance per unit length of the microstrip line is given by:

$$C = \frac{Q}{V_0} \tag{6.36}$$

where Q is the total charge per unit length on the centre strip. This can be calculated from Equation 6.37 (Pozar, 1990, pp. 187–189):

$$Q = \int_{-w}^{w} \sum_{p=1}^{P} a_p \sigma_p(x)\, dx \tag{6.37}$$

Depending on the type of trial functions chosen, Equation 6.37 may be evaluated either numerically or analytically. ε_{eff} can then be calculated via the equation

$$\varepsilon_{\text{eff}} = \frac{C_{\text{eff}}}{C_0} \tag{6.38}$$

where C_{eff} is the capacitance per unit length with the substrate and covering material present, and C_0 is the capacitance per unit length with $\varepsilon_1 = \varepsilon_2 = 1$. The phase coefficient β of the dominant propagating mode is

$$\beta = \frac{2\pi f \sqrt{\varepsilon_{\text{eff}}}}{c} \tag{6.39}$$

The characteristic impedance Z_0 for the line is given by

$$Z_0 = \frac{\sqrt{\varepsilon_{\text{eff}}}}{cC_{\text{eff}}} \tag{6.40}$$

where c is the speed of electromagnetic waves in free space.

The line is thus completely characterised. This information can be used in conjunction with classical transmission line formulas to calculate the reflection and transmission coefficients of a microstrip sensor having this geometry.

To demonstrate the use of this technique, consider the following example. A microstrip transmission line has a substrate with permittivity $\varepsilon_1 = 10.2 - j0$ and thickness $d = 1.27$ mm. The width of the strip conductor is $2w = 0.97$ mm, and the permittivity of the covering medium is $\varepsilon_2 = 75 - j0$. The potential of the strip V_0 is assumed to be 1 V.

The first step in solving for ε_{eff} and Z_0 is to calculate the capacitance of the structure with $\varepsilon_1 = \varepsilon_2 = 1$. For the sake of simplicity, only 2 basis functions will be used. (It will be shown later that this number is more than sufficient in most cases.) Substitution of these parameters into Equation 6.35 produces the following system of equations to be solved:

$$\begin{bmatrix} \int_0^{\alpha_{\max}} G|\tilde{\sigma}_1|^2 \, d\alpha & \int_0^{\alpha_{\max}} G\tilde{\sigma}_1^*\tilde{\sigma}_2 \, d\alpha \\ \int_0^{\alpha_{\max}} G\tilde{\sigma}_2^*\tilde{\sigma}_1 \, d\alpha & \int_0^{\alpha_{\max}} G|\tilde{\sigma}_2|^2 \, d\alpha \end{bmatrix} \begin{bmatrix} a_1 \\ a_2 \end{bmatrix} = \begin{bmatrix} \int_0^{\alpha_{\max}} \tilde{V}_0\tilde{\sigma}_1^* \, d\alpha \\ \int_0^{\alpha_{\max}} \tilde{V}_0\tilde{\sigma}_2^* \, d\alpha \end{bmatrix} \tag{6.41}$$

After plotting the six integrands in Equation 6.41, a value of $\alpha_{\max}$ of $150\,000$ is found to be sufficient. An interval size of $\alpha = 75$ will be used, corresponding to a total of 2000 intervals between $\alpha = 0$ and $\alpha = \alpha_{\max}$. Solving for a_1 and a_2 yields:

$$\begin{bmatrix} a_1 \\ a_2 \end{bmatrix} = \begin{bmatrix} 1.4805 \times 10^{-8} \\ 4.4565 \times 10^{-9} \end{bmatrix} \tag{6.42}$$

This result can be substituted into Equation 6.37 to obtain the total charge Q on the strip conductor with $\varepsilon_1 = \varepsilon_2 = 1$:

$$Q = \int_{-w}^{w} [a_1\sigma_1(x) + a_2\sigma_2(x)]\, dx \tag{6.43}$$

$$= \int_{-w}^{w} a_1\sigma_1(x)\, dx + \int_{-w}^{w} a_2\sigma_2(x)\, dx \tag{6.44}$$

Using the basis functions from Equation 6.23 it is possible to evaluate the above integrals analytically. Indeed, it can be shown that it is only necessary to evaluate the first term, as the second term evaluates to zero. This is due to a useful property of this family of trial functions whereby

$$\int_{-w}^{w} a_p\sigma_p(x)\, dx = \begin{cases} a_1 w\pi & p = 1 \\ 0 & p = 2,\, 3,\, \ldots,\, P \end{cases} \tag{6.45}$$

The total charge Q on the strip conductor is therefore given by

$$Q = a_1 w\pi = (1.4805 \times 10^{-8}) \times (0.485 \times 10^{-3}) \times \pi \tag{6.46}$$

$$= 22.56 \times 10^{-12}\ \text{C} \tag{6.47}$$

It is then a straightforward matter to calculate the capacitance of the microstrip line:

$$C_0 = \frac{Q}{V_0} = \frac{22.56 \times 10^{-12}}{1.0} \tag{6.48}$$

$$= 22.56\ \text{pF} \tag{6.49}$$

Repeating the above process with the substrate and superstrate present (i.e. with $\varepsilon_1 = 10.2$ and $\varepsilon_2 = 75$), a value of $C_{\text{eff}} = 656.42$ pF is obtained. ε_{eff} and Z_0 can then be obtained using Equations 6.38 and 6.40 respectively:

$$\varepsilon_{\text{eff}} = \frac{C_{\text{eff}}}{C_0} = 29.10 \tag{6.50}$$

$$Z_0 = \frac{\sqrt{\varepsilon_{\text{eff}}}}{cC_{\text{eff}}} = 27.41\ \Omega \tag{6.51}$$

It is interesting to compare these results with those obtained using more basis functions. If the number of basis functions is increased from 2 to 10, the calculated values of ε_{eff} and Z_0 are

$$\varepsilon_{\text{eff}} = 28.84 \tag{6.52}$$

$$Z_0 = 27.23\ \Omega \tag{6.53}$$

The relative change in each parameter is less than 1%. This is a rather surprising result, given that the first set of results took 98 seconds to generate on a Cyrix PR200 desktop PC, whereas the second set took several hours.

6.6 Verification of Technique

In order to verify that the quasi-TEM analysis software was functioning correctly, the output was checked against results from the literature. Three different sets of parameters were examined for various ratios of strip width to substrate height. These are summarised in Table 6.1.

Table 6.1: Details of microstrip simulations used to verify correct operation of quasi-TEM software.

ε_1	ε_2	Reference Publication
11.7	1	Yamashita and Mittra (1968)
2.32	75	Bahl and Stuchly (1980)
10.5	65	Khalid et al. (1988)

Some comparisons of calculated and published values of ε_{eff} and Z_0 are given in Figures 6.3 and 6.4 respectively. Agreement is generally good to within a couple of percent, except for small values of $2w/d$, where some of the simulated values differ significantly from the published values. This is almost certainly an artifact of the numerical integration techniques which were used. As $2w/d$ decreases, the static spectral domain formulation becomes more sensitive to the parameters of the numerical integration, such as the limits of integration and interval size. Indeed, it is quite likely that the results given here are more accurate than the published results, given the greater computing power of PCs today compared with those in use when the published data first appeared in the literature.

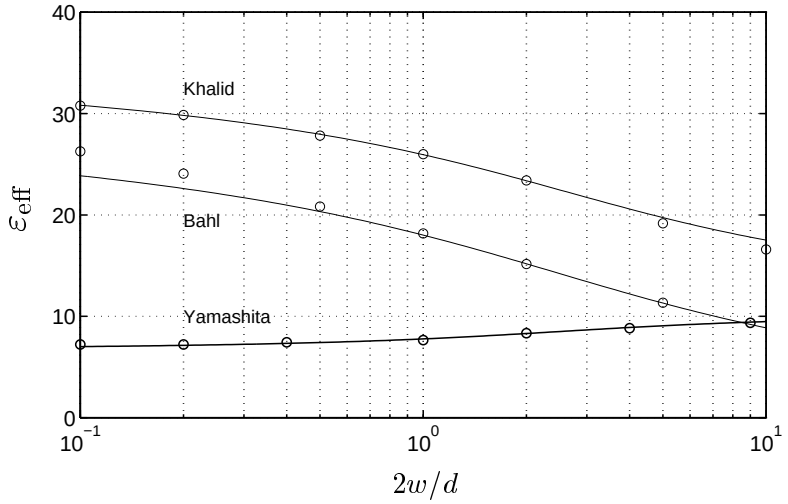

Figure 6.3: Comparison of microstrip ε_{eff} as predicted by quasi-TEM model with published data. (Published data denoted by small circles.)

Another possible reason for the disagreement between the simulated results and results from the literature is that the other authors used charge distributions which did not perfectly capture the edge condition on the strip. The computational advantages of neglecting the edge condition were discussed in Section 6.4, however the fact remains that this speedup comes at the expense of degraded accuracy.

One aspect of the quasi-TEM analysis software which could not be independently verified was the effect of loss in the covering material. This was due to a lack of published data in this area, which is surprising given that previous work has been carried out on microstrip sensors with a protective layer (Kent and Price, 1979; Khalid et al., 1988). Unfortunately nothing was found in the literature on the static analysis of simple microstrip sensors having no protective layer.

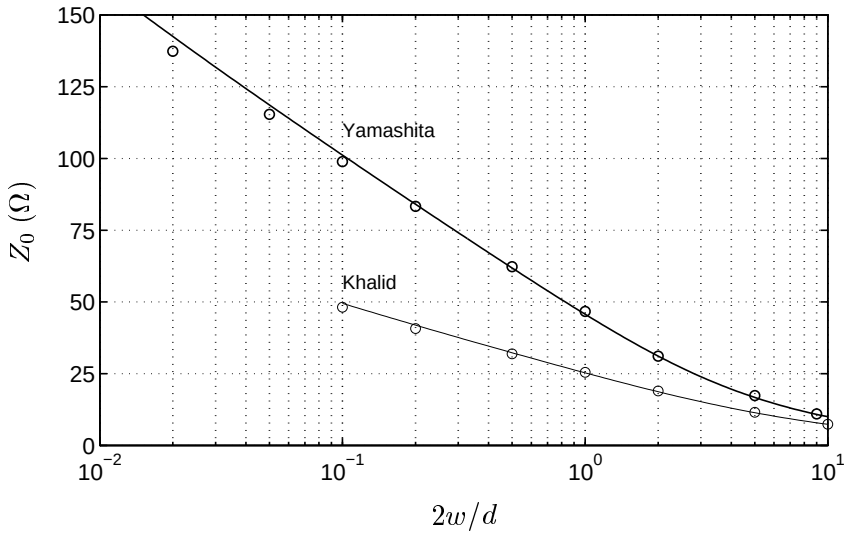

Figure 6.4: Comparison of microstrip Z_0 as predicted by quasi-TEM model with published data. (Published data denoted by small circles.)

The other issue to be resolved later in this thesis is whether the static approximation can be used to accurately model the real-life scattering parameters of a microstrip sensor covered by a lossy dielectric. This is addressed in Chapter 10, where experimental and theoretical results are compared and discussed.

6.7 Performance Improvement Strategies

Despite some minor discrepancies between simulated and published data, it is clear that the quasi-TEM analysis software written for this project functioned as required. However, execution speed will always be an issue if the software is ever to be embedded in an instrument required to operate in real time.

A number of speedup strategies are available which can improve performance without degrading accuracy significantly. Some of these have been mentioned in earlier sections. A summary of the available options is provided below:

- Reducing the number of trial functions. This can usually be done with confidence due to the variational nature of the static spectral domain method.

- Using trial functions which neglect the edge condition. Such functions often have rapidly decaying Fourier transforms, leading to systems of equations that can be solved relatively quickly.

- Shortening the limits of integration for numerical integrals. Every time the ratio of strip width to substrate height is changed, the limits of integration should be checked to determine whether they can be reduced.

- Using lower point densities when performing numerical integrations. This is a fairly safe strategy if the method of quadrature involves interpolation between data points using higher-order functions (e.g. Simpson's $\frac{1}{3}$ rule). Close to $\alpha = 0$, however, integrands can exhibit sharp changes in magnitude, requiring caution to be exercised when reducing the number of points in the integration.

- A factor of two speed increase can be obtained by performing single-sided integrations, permissible due to the symmetry of $G(\alpha)$, $\tilde{\sigma}_p(\alpha)$ and $\tilde{V}_p(\alpha)$ about $\alpha = 0$.

6.8 Conclusion

This chapter has described the development of a low-frequency spectral domain analysis of a microstrip transmission line covered by a lossy material of infinite extent.

Fourier transformed field equations have been derived for microstrip. A family of basis functions has been chosen to represent the charge distribution on the strip conductor, including the edge singularity at the extremes of the strip.

The Galerkin method has been employed to solve for the basis function coefficients, making possible the calculation of the effective permittivity and characteristic impedance of microstrip. These two parameters provide a complete characterisation of the microstrip sensor—at least at DC—which can be used with standard transmission line formulas to predict the scattering parameters of the sensor.

A computer program has been written to implement the above procedure. The correct operation of this program with lossless test materials has been verified by comparing with other (theo-

retical) results from the literature. The issue of whether the program can accurately model the properties of a real sensor covered by lossy cheese curd will be addressed later in this thesis.

Several techniques for increasing the speed of the program have been suggested. It has been shown that dramatic reductions in the run time of the program can be achieved without significant loss of accuracy. This suggests that real-time instrument performance is possible using a characterisation model based on the static spectral domain method.

Chapter 7

Surface Waves

7.1 Introduction

In Chapter 6 a low-frequency analysis of microstrip was presented in which it was assumed that the dominant—and indeed, only—propagating mode was a TEM wave. In reality, however, a variety of modes of propagation can be supported by microstrip in addition to the bound mode. Of particular interest to this project is the family of modes referred to as *surface waves*.

Surface waves are characterised by fields which are tightly bound to the dielectric interface, decaying exponentially away from the interface (Pozar, 1990, pp. 170–176). Unlike the bound microstrip modes, surface waves are not necessarily guided by the strip conductor. This can result in a leakage of energy from the transmission line, which contributes to the attenuation term α in the propagation coefficient of the line.

Surface wave leakage cannot be taken into account by simple static approximations like the one in Chapter 6. More sophisticated methods are available for this purpose. The approach favoured in this thesis is the full-wave spectral domain analysis, which is discussed in Chapter 8. In order for this technique to be highly accurate, it is important to identify in advance which surface wave modes can be supported by the background structure of the transmission line. Only then can the effects of leakage into surface wave modes be taken into account.

This chapter is divided into two main sections.

The first section investigates the conditions necessary for surface waves to propagate on a grounded dielectric slab covered by a lossy, high permittivity medium of infinite extent. This analysis has produced original results which have since been published in *IEEE Microwave and Guided Wave Letters* (Horsfield and Ball, 2000).

The second section presents an alternative formulation of the surface wave eigen equations, performed entirely in the Fourier domain. This effectively maps each of the surface wave modes on the slab to the spectral plane, thereby enabling the full-wave microstrip analysis to account for signal loss due to this phenomenon.

This chapter concludes with a brief overview of leaky (i.e. improper) surface wave modes. These are nonphysical solutions to the surface wave equations which may nevertheless need to be taken into account when analysing microstrip transmission lines.

7.2 Overview: Optical Analogy of Surface Waves

The structure under consideration is a grounded dielectric slab covered by a material of infinite extent, as depicted in Figure 7.1. The orientation of the coordinate system is as shown. The permittivity of the covering medium may assume any complex value.

In situations where $\varepsilon_2' > \varepsilon_1'$, a structure such as this would not normally be expected to support surface waves. This conclusion could be reached using a ray-tracing method (Balanis, 1989), which provides a simple (and, it will be shown, simplistic) physical insight into the problem. The ray-tracing approach treats surface wave modes as wave beams which enter the dielectric slab and are reflected between the ground plane and the dielectric interface, as shown in Figure 7.2. In order for total internal reflection to occur at the dielectric interface, the angle of incidence θ of the beam at the dielectric interface must be larger than the critical angle θ_c, where

$$\theta_c = \arcsin\left(\sqrt{\frac{\varepsilon_2}{\varepsilon_1}}\right) \tag{7.1}$$

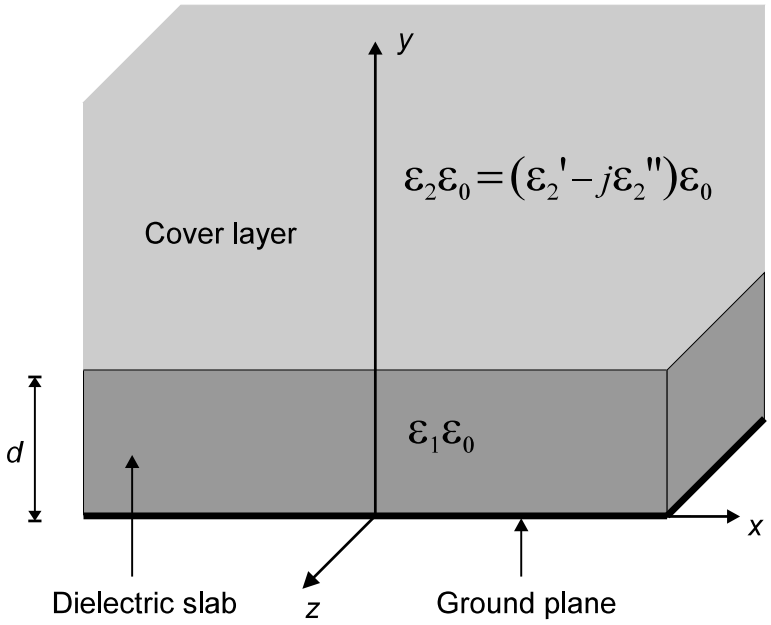

Figure 7.1: Grounded dielectric slab covered by superstrate of infinite extent.

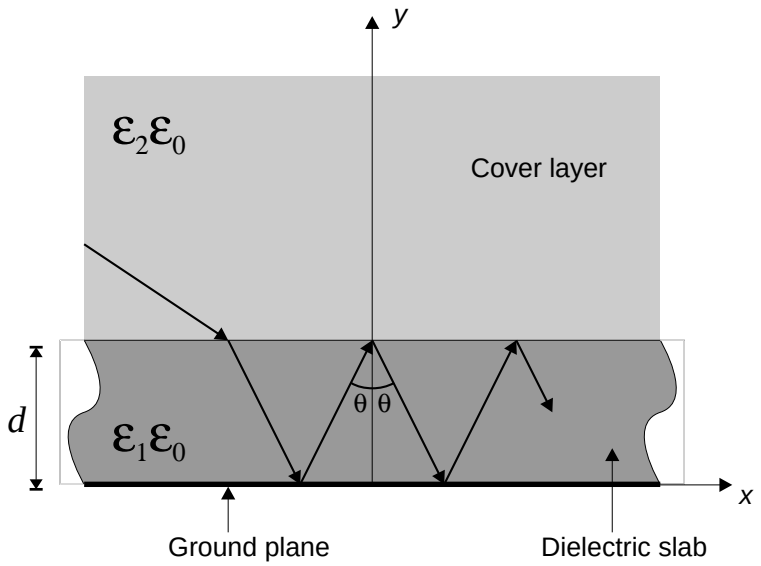

Figure 7.2: Propagation path of a wave beam incident on a grounded dielectric slab.

However, if ε_2' is greater than ε_1', the critical angle is undefined. This would seem to imply that total internal reflection cannot occur, and the wave beam exits from the slab. Therefore surface wave propagation would not be expected to occur.

However, the following sections will show that surface wave propagation *is* possible provided the covering medium contains some loss. Under these circumstances surface wave modes can propagate above cutoff frequencies which reduce as the loss factor increases, even when $\varepsilon_2' > \varepsilon_1'$.

7.3 Theory of Surface Waves

A concise derivation of the characteristic equations for the TM and TE surface wave modes is provided by Pozar (1990, pp. 170–176). A similar formulation is used here, the only difference being that the permittivity of the covering medium is not assumed to be air, but may assume any complex value.

For the TM family of surface wave modes the following familiar pair of equations must be solved:

$$hd = \frac{\varepsilon_2}{\varepsilon_1}(k_c d)\tan(k_c d) \tag{7.2}$$

$$(k_c d)^2 + (hd)^2 = (\varepsilon_1 - \varepsilon_2)(k_0 d)^2 \tag{7.3}$$

where d is the substrate thickness, ε_1 is the substrate permittivity, ε_2 is the complex permittivity of the medium above the slab, and k_0 is the free space wavenumber. The parameters h and k_c are the cutoff wavenumbers for the top and bottom regions respectively, and are defined as

$$h^2 = \beta^2 - k_2^2 \tag{7.4}$$

$$k_c^2 = k_1^2 - \beta^2 \tag{7.5}$$

where k_2 and k_1 are the wavenumbers in the top and bottom regions respectively, and β is the phase coefficient of the wave propagating in the z-direction. ε_1 and ε_2 may be complex (i.e. lossy), hence β, k_1 and k_2 may also be complex.

For the TE family of surface wave modes Equations 7.3 to 7.5 are still applicable and Equation 7.2 must be replaced by:

$$hd = -(k_c d)\cot(k_c d) \tag{7.6}$$

For the TM modes and TE modes respectively, simultaneous solution of Equations 7.2 and 7.3 or Equations 7.3 and 7.6 allows the propagation characteristics to be determined.

The nonlinear nature of the TM and TE eigen equations usually means an analytic solution cannot be obtained. However, an approximate solution can be obtained for the TM_0 mode if the substrate is assumed to be thin compared to a wavelength. This enables Equation 7.2 to be simplified to

$$h \approx \frac{\varepsilon_2}{\varepsilon_1} k_c^2 d \tag{7.7}$$

assuming $k_0 d \ll 1$. Substitution into Equation 7.3 yields a quadratic in h:

$$h^2 + \frac{\varepsilon_1}{\varepsilon_2 d} h + k_0^2(\varepsilon_2 - \varepsilon_1) = 0 \tag{7.8}$$

In order to satisfy the boundary conditions at infinity, the real part of h must be positive (Collin, 1991, pp. 725–734). Therefore the positive root of Equation 7.8 must be selected. In contrast to an air covered slab, it is found that the TM_0 mode may experience a low frequency cutoff. An approximate analytic expression for the cutoff frequency can be found by separating Equation 7.8 into real and imaginary parts and setting the real part of h to zero. Assuming that the slab is lossless ($\varepsilon_1'' = 0$) the result is:

$$f_c \approx \frac{c\varepsilon_1}{2\pi\varepsilon_2''|\varepsilon_2|^2 d}\sqrt{\varepsilon_2' \left[\varepsilon_2'(\varepsilon_2' - \varepsilon_1) - (\varepsilon_2'')^2\right]} \tag{7.9}$$

where c is the velocity of electromagnetic waves in free space. Propagation down to DC is only possible if no cutoff frequency is present, i.e. when:

$$(\varepsilon_2'')^2 > (\varepsilon_2' - \varepsilon_1')\varepsilon_2' \tag{7.10}$$

If $\varepsilon_2' > \varepsilon_1'$ then Equation 7.10 can only be satisfied if $\varepsilon_2'' \gg 0$. Hence, TM_0 surface wave propagation is possible if the covering material is sufficiently lossy (Horsfield and Ball, 2000).

7.4 Numerical Solution

Further insight into this phenomenon can be gained via a numerical solution of the TM and TE characteristic equations. This was achieved using Newton's method, implemented as a C++ program. The parameters of the slab used in the numerical solution were the same as those in Chapter 6, namely:

$$\varepsilon_1 = 10.2 - j0$$

$$d = 1.27\,\mathrm{mm}$$

Setting ε_2' equal to 15 and sweeping the loss factor ε_2'' over a wide range, the results shown in Figure 7.3 were obtained. These results verify that the existence of the TM_0 cutoff frequency is dependent on the amount of loss in the covering material. A comparison of computed cutoff frequencies and values estimated from Equation 7.9 is given in Table 7.1, showing good agreement.

Table 7.1: Comparison of numerical values for TM_0 cutoff frequency with estimates from Equation 7.9 for $\varepsilon_1 = 10.2$, $\varepsilon_2' = 15$, $d = 1.27$ mm.

ε_2''	Cutoff Frequency (GHz)	
	Estimate (Eq. 7.9)	Numerical
8.485	0	0
5	8.146	9.365
3	16.793	19.196
2	26.741	28.360

The numerical solution further suggests that all higher order TM modes and TE modes have cutoff frequencies which reduce as the amount of loss in the covering material increases. This is illustrated for the TM_1 and TE_1 modes in Figure 7.3.

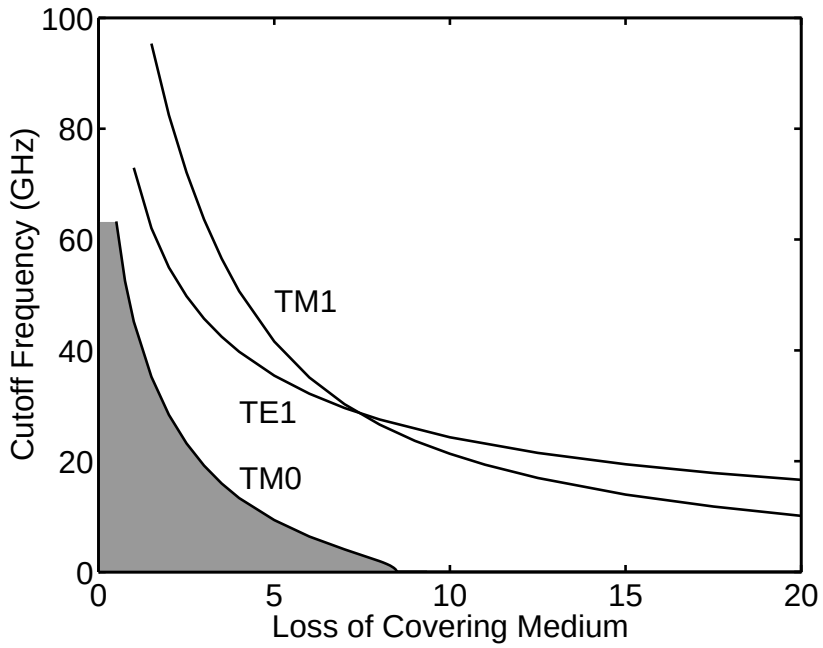

Figure 7.3: f_c vs ε_2'' for TM_0, TE_1 and TM_1 surface wave modes on grounded dielectric slab covered by lossy medium of infinite extent ($\varepsilon_1 = 10.2$, $\varepsilon_2' = 15$, $d = 1.27$ mm). No propagation is possible in shaded region.

These results have important consequences for the application of microstrip as a contact sensor for moist materials and other polar dielectrics such as methanol. As discussed in Chapter 2, the dielectric properties of these substances are highly frequency-dependent and can vary over a wide range. As such, leakage into surface wave modes may occur at some frequencies but not at others.

As an example, consider a microstrip sensor made out of the slab described above, and immersed in methanol at a temperature of 25°C. From Figure 2.2 in Chapter 2, it is clear that the permittivity of methanol has a real part greater than that of the slab for all frequencies below 6.96 GHz, and the loss factor of methanol is nonzero for all frequencies above DC. It is immediately obvious that this structure can support at least one surface wave mode at frequencies above 6.96 GHz. Less obvious is which modes, if any, can propagate *below* this frequency.

A numerical analysis of this structure enables the normalised attenuation and phase coefficients for the TM_0 mode to be calculated. These results, shown in Figure 7.4, indicate that a cutoff frequency exists at $f_c = 2.32$ GHz, below which the TM_0 mode cannot propagate. Above f_c a proper solution exists.

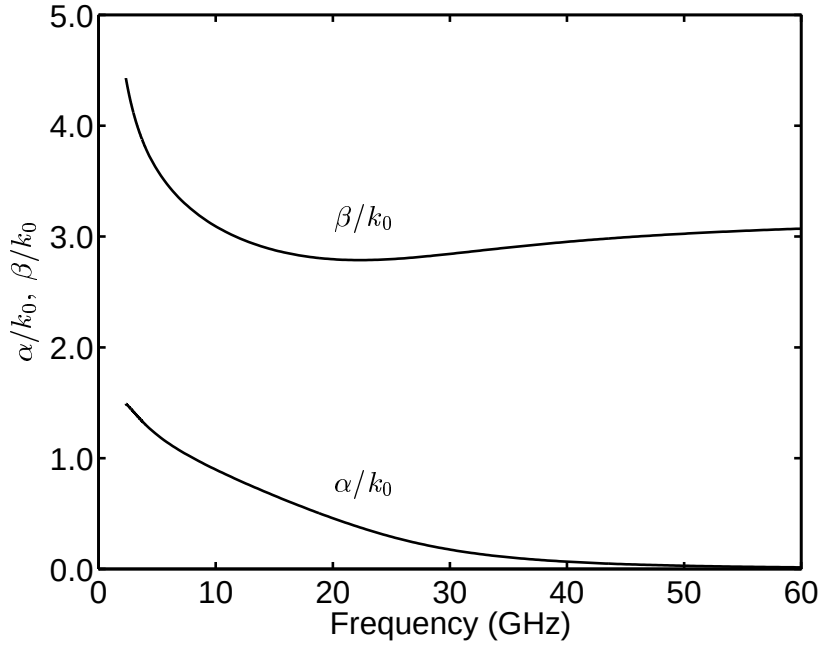

Figure 7.4: α/k_0 and β/k_0 vs frequency for TM_0 surface wave mode on grounded dielectric slab covered by methanol ($\varepsilon_1 = 10.2$, $d = 1.27$ mm, $T = 25°$C).

The implications of these results for full-wave analyses of microstrip are that there are frequencies at which leakage into surface wave modes must be taken into account, and frequencies at which surface waves cannot be supported by the structure and can therefore be neglected by the analysis software. In the preceding example, the development of microstrip analysis software would be somewhat simpler if it were restricted to frequencies below 2.32 GHz. Above this frequency the software would be significantly more complex, as it would need to contain a subroutine to solve the surface wave equations for all propagating modes at each frequency point of interest.

Another interesting feature of surface waves propagating on dielectric slab structures covered by lossy, high-permittivity dielectrics is faster-than-light phase velocity. This can be seen on a plot of effective permittivity ε_{eff} as a function of frequency. Figure 7.5 displays the effective permittivity of the TM_0 surface wave mode on a slab covered by a material with permittivity $\varepsilon_2 = 15 - j5$. It is evident from this figure that the TM_0 mode has a cutoff frequency at about 9.37 GHz. At frequencies just above cutoff the real part of ε_{eff} is between ε_1 and ε_2, and the loss factor is relatively high. This implies that the mode is bound only loosely to the slab. At higher frequencies the mode becomes more tightly bound to the slab. As shown

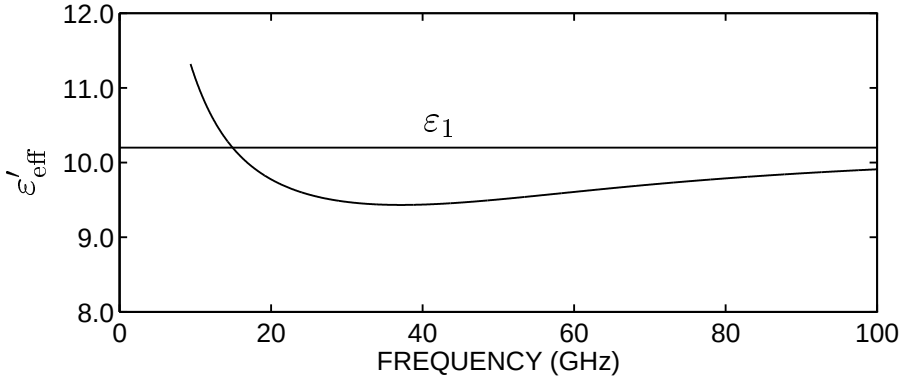

(a) Real part.

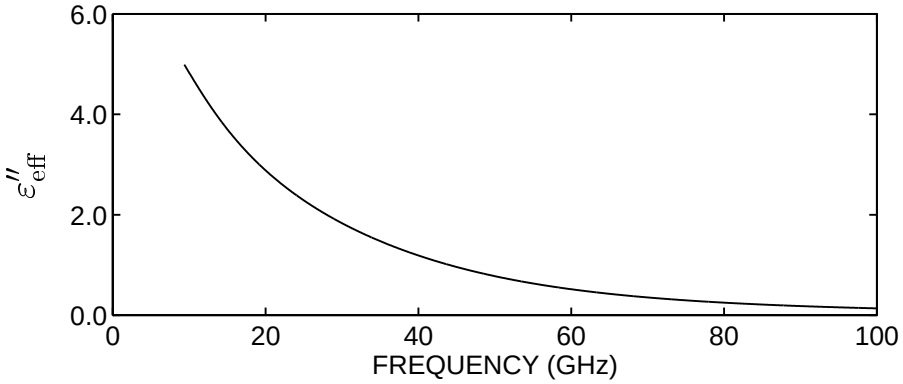

(b) Imaginary part.

Figure 7.5: Effective permittivity vs frequency for TM_0 surface wave mode on a grounded dielectric slab covered by a high-dielectric constant material ($\varepsilon_1 = 10.2$, $\varepsilon_2 = 15 - j5$, $d = 1.27$ mm).

in Figure 7.5(a), above 14.9 GHz the real part of ε_{eff} is less than the dielectric constant of the substrate. This implies that the phase velocity of the TM_0 mode is greater than that of a TEM wave in either medium, behaviour typical of a waveguide mode. As frequency increases further, $\varepsilon'_{\text{eff}}$ is asymptotic to ε_1, and $\varepsilon''_{\text{eff}}$ approaches zero, indicating that the mode is confined to the slab.

7.5 Spectral Domain Solution of Surface Wave Equations

While the results of Sections 7.3 and 7.4 are important and necessary milestones in developing an accurate model of microstrip, they are not particularly useful in their current form. This is because the analysis technique used in Chapter 8 is a full-wave spectral domain solution, in which the propagation characteristics of microstrip are determined entirely in the Fourier domain.

It will be shown in Chapter 8 that each surface wave mode manifests itself mathematically as a pole in the spectral domain Green's function for microstrip, which may have to be bypassed by the contour of integration when solving for the propagation coefficient of the line (Itoh, 1989). It is therefore necessary to map the solution for each surface wave mode to the Fourier domain. This can be achieved by transforming the original TM and TE field expressions into the spectral domain before solving. Instead of obtaining the cutoff wavenumbers h and k_c, the results of this analysis are the transverse wave numbers γ_1 and γ_2. It shall be shown in Chapter 8 that for open structures, γ_2 is a pole of the dyadic Green's function $[\boldsymbol{G}]$ and may have to be bypassed by the integration contour.

The following subsections present a derivation of the characteristic equations for the TM and TE surface wave modes in the spectral domain. This derivation does not usually appear in the literature, so its inclusion here is warranted in the interests of clarity. It will also serve as an introduction to the full-wave spectral domain analysis, which is covered in detail in Chapter 8.

7.5.1 TM Surface Wave Modes

The TM characteristic equations can be derived in much the same way in the spectral domain as in the space domain. The analysis involves matching the tangential field components across the dielectric interface.

Representing the longitudinal component of the electric field E_z using scalar potentials we can write

$$E_z = \phi(x, y)e^{-j\beta z} \tag{7.11}$$

where $\phi(x, y)$ satisfies the scalar wave equation in both regions:

$$\nabla_t^2 \phi_i + (k_i^2 - \beta^2)\phi_i = 0 \qquad i = 1,\ 2 \tag{7.12}$$

Taking the Fourier transform of Equation 7.12 and matching boundary conditions yields the spectral domain versions of the eigenvalue equations. The full derivation can be found in Appendix D. For the TM modes the resulting equations are:

$$(Kd)\tan(Kd) = \frac{\varepsilon_1}{\varepsilon_2}(\gamma_2 d) \tag{7.13}$$

$$(\gamma_2 d)^2 + (Kd)^2 = (\varepsilon_1 - \varepsilon_2)(k_0 d)^2 \tag{7.14}$$

where

$$\gamma_i^2 = \alpha^2 + \beta^2 - k_i^2 \qquad i = 1,\ 2 \tag{7.15}$$

$$\alpha = \text{Fourier parameter} \tag{7.16}$$

$$k_i = \text{wavenumber of a plane wave in the } i^{\text{th}} \text{ region} \tag{7.17}$$

$$K = -j\gamma_1 \tag{7.18}$$

It is obvious that Equations 7.13 and 7.14 are identical in form to Equations 7.2 and 7.3 respectively. As such, the solution procedure (and hence computer software) for obtaining the transverse wavenumbers γ_1 ($= jK$) and γ_2 in the spectral domain is identical to that for obtaining k_c and h in the space domain.

7.5.2 TE Surface Wave Modes

The solution of the TE surface wave equation is performed in a very similar fashion to the TM case. In an analogous manner we represent the longitudinal component of the magnetic field H_z as

$$H_z = \psi(x, y)e^{-j\beta z} \tag{7.19}$$

where $\psi(x, y)$ satisfies the scalar wave equation in both regions. Taking the Fourier transform of the wave equation and matching boundary conditions in a similar fashion to the TM case yields another pair of eigen equations which must be solved numerically for γ_1 and γ_2.

$$(\gamma_2 d) = -(Kd)\cot(Kd) \tag{7.20}$$

$$(\gamma_2 d)^2 + (Kd)^2 = (\varepsilon_1 - \varepsilon_2)(k_0 d)^2 \tag{7.21}$$

It is obvious that Equations 7.20 and 7.21 are identical in form to Equations 7.6 and 7.3 respectively. As such, the solution procedure for obtaining the transverse wavenumbers γ_1 $(= jK)$ and γ_2 in the spectral domain is identical to that for obtaining k_c and h in the space domain.

7.6 Leaky Wave Modes

The results presented in Sections 7.2 to 7.4 pertain only to *proper* surface wave modes; that is, solutions of the surface wave eigen equations which satisfy the boundary conditions at infinity and are therefore physically meaningful. However, proper surface wave modes are not the only solutions to these equations. There also exists an infinite number of improper, nonphysical solutions commonly referred to as *leaky wave modes* (Collin, 1991, pp. 732–744).

Although leaky wave modes do not correspond directly to physical propagating modes, they nevertheless constitute mathematical solutions to the surface wave equations which may have an impact on the full-wave spectral domain analysis of microstrip. Despite this, many authors do not check for the presence of leaky modes before carrying out an analysis of microstrip, yet still obtain results which agree well with experimental data (for a recent example see McMillan, 1998).

In view of this, it was decided not to make any allowances for leaky wave modes in this project. Although this introduced a possible (if improbable) source of error into the subsequent analysis of microstrip, it made the development of the analysis software much simpler.

7.7 Conclusion

This chapter has explored the propagation characteristics of surface waves on a lossless planar dielectric slab, for the unconventional case where the dielectric slab is covered by a non-air medium of infinite extent.

It has been shown that if the dielectric constant of the covering medium is greater than that of the slab, then TM and TE surface wave propagation is only possible if the covering medium contains some loss. Each surface wave mode exhibits a cutoff frequency which varies according to the loss of the covering medium. Even the TM_0 mode, which can propagate down to DC on air-covered substrates, may have a nonzero cutoff frequency, depending on the value of loss. Any surface wave modes which can be supported by the slab under these conditions must be taken into account when analysing a microstrip transmission line made from this background structure, as energy may be lost due to surface wave leakage.

This chapter also demonstrated that surface waves on such structures can exhibit propagation characteristics reminiscent of waves in rectangular waveguide, namely faster-than-light phase velocity.

An alternative formulation of the surface wave problem has been presented, the relevance of which will become obvious in Chapter 8. This approach involved the derivation of the TM and TE eigen equations in the spectral domain. The resulting equations were identical in form to those derived in the space domain, making it possible to solve these equations using the same solution procedures.

Finally, the existence of leaky wave modes has been discussed. These are nonphysical solutions to the surface wave equations which may nevertheless impact on the analysis of open microstrip transmission lines. Based on the experience of previous workers in this field, contributions from leaky waves were thought to be unlikely to occur. As a result, leaky wave modes will not be given any further consideration in this thesis.

Chapter 8

The Spectral Domain Method II: Full-Wave Analysis

8.1 Introduction

While quasi-TEM models of microstrip may provide reasonable accuracy at low frequencies, there are several frequency-dependent phenomena which cannot be taken into account using this method. One of these—surface waves—was discussed in Chapter 7. Other effects include dispersion, radiation, leaky dominant modes and higher order modes.

In order for a microstrip sensor model to be as accurate as possible, it is important to account for these effects. The preferred technique for this project was the full-wave spectral domain method. Like the static model described in Chapter 6, this method entails the transformation of the field equations into the Fourier domain, thereby simplifying the solution procedure considerably. Unlike the static model, however, the full-wave model makes no assumptions about the nature of the fields on the transmission line, and is therefore entirely general.

This chapter describes the development of a full-wave model of microstrip to enable the propagation coefficient of the line to be calculated. This is presented in three main parts.

The first part provides a brief outline of the high-frequency effects mentioned above. This is

followed by a derivation of the Fourier transformed field equations, and a description of the solution procedure for determining the propagation coefficient of the transmission line.

The second part of this chapter is concerned with the details of precisely how to account for the effects of surface waves and radiation. This entails an analysis of the migration of poles and branch points in the complex plane to ensure that the solution obtained is physically correct. In addition to this, surface wave and radiation leakage conditions are derived which make it possible to tell at a glance whether energy is lost to these mechanisms.

The final part of this chapter investigates the impact of the dielectric properties of the covering medium on the propagation characteristics of microstrip. It will be shown that this leads to several significant and original results. Indeed, one of the principal outcomes of this thesis arises out of this investigation: namely, that the propagation characteristics of microstrip covered by a material other than air are much more complex than previously thought. Simple quasi-TEM approximations like the one presented in Chapter 6 are simply not capable of capturing this complexity. This provides a justification for the time and effort which have been expended on this analysis.

8.2 Overview of Frequency-Dependent Phenomena

The following subsections introduce the principal mechanisms which cause the true behaviour of microstrip to depart from the static case.

8.2.1 Dispersion

Dispersion arises as a consequence of the heterogeneous nature of microstrip. The presence of two dielectric regions means that the phase velocity is different on either side of the dielectric interface. This gives rise to a hybrid mode of propagation comprised of one or more TE and TM modes which are coupled by the presence of the strip conductor (Itoh and Mittra, 1973). As a result, the effective permittivity of the structure departs from the static value and can vary significantly with frequency.

8.2.2 Surface Waves

As discussed in Chapter 7, surface waves are modes which propagate parallel to the dielectric interface, attenuating rapidly away from the interface. Unlike the bound propagating modes of microstrip, surface waves do not necessarily propagate along the strip conductor. This can result in a leakage of energy from the transmission line, which contributes to the attenuation coefficient of the line.

8.2.3 Radiation

Radiation from microstrip can occur into the infinite half-space above the transmission line. The energy lost in this way manifests itself as a contribution to the attenuation coefficient of the transmission line.

8.2.4 Leaky Dominant Modes

In addition to the conventional dominant mode of microstrip (or 'EH_0' mode, as it is commonly referred to), it is possible under certain conditions for a so-called leaky dominant mode to be excited. Discovered only recently, this is a propagating mode which has a field pattern and surface current distribution that are very similar to the traditional EH_0 mode (Nghiem et al., 1996). Depending on the excitation frequency and material parameters, the leaky dominant mode can leak energy to either or both of the radiation field and the surface wave modes. Propagation can occur independently of and simultaneously with the conventional dominant mode.

8.2.5 Higher Order Modes

At sufficiently high frequencies it is possible for one or more higher order modes to propagate in addition to the EH_0 mode. These modes can interfere with the dominant mode, causing the theoretical model of microstrip to depart from measured results.

Notwithstanding this potential for error, the propagation of higher order modes on microstrip sensors was not investigated in the course of this project. Interference from higher order modes was thought to be unlikely to occur for two main reasons.

Firstly, the frequency band of interest was in the low gigahertz range. Previous work on higher order modes suggests that the EH_1, EH_2, EH_3 modes etc can only propagate down to the low gigahertz region when the ratio of strip width to substrate thickness is large. Typical values of $2w/d$ which have appeared in the literature are: 14.3 (Jansen, 1978); 4.7 (Oliner and Lee, 1986; Bagby et al., 1993); and 18.9 (Lin and Sheen, 1997). By contrast, the three microstrip sensors which were fabricated for this project had $2w/d$ ratios of 0.19, 0.39 and 0.76. This suggests that the cutoff frequencies of the higher order modes for these sensors were likely to occur well above the frequency range of interest for this project.

Secondly, there is the issue of coupling mechanisms. Most commercially available microstrip launchers are designed to excite the EH_0 mode. As such, it is doubtful whether any of the higher modes would be excited by such a structure, even if the source frequency was above the cutoff for the mode.

Of course, until a proper analysis is carried out to determine what effects a lossy, high-permittivity covering medium has on the propagation of higher order modes, it is unknown whether these modes are likely to introduce an error into the microstrip sensor model. Such a study is beyond the scope of this project, but would be a suitable topic for a future project.

8.3 Derivation of Fourier Transformed Field Equations

The full-wave spectral domain analysis of microstrip is rather more involved than the static approximation due to the hybrid nature of the field on the line. This gives rise to field components in the direction of propagation, as well as transverse to the direction of propagation. Consequently, the surface currents excited on the strip will have both a longitudinal (z-directed) component and a transverse (x-directed) component. The resulting Green's function is therefore dyadic in nature.

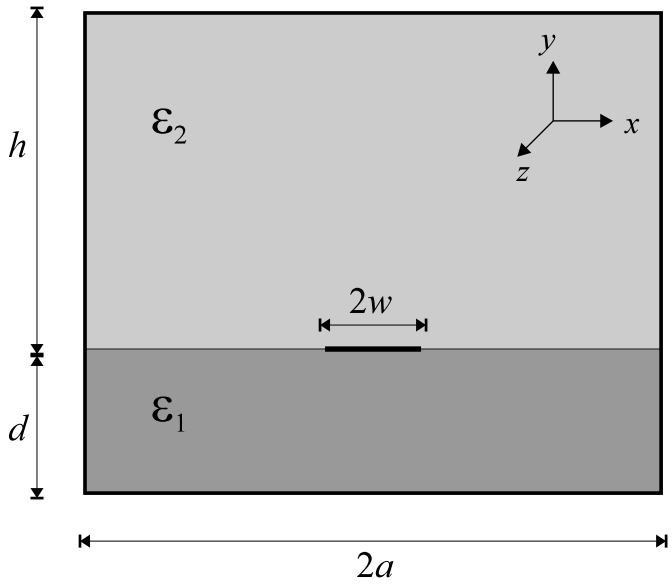

Figure 8.1: Cross section of shielded microstrip transmission line.

The spectral domain formulation presented below is essentially the same as that of Mirshekar-Syahkal (1990, pp. 23–49), which was developed for shielded planar structures like the one shown in Figure 8.1. The main departure from the original analysis by Mirshekar-Syahkal is that the side walls and roof have been located at infinity in the final equations, thereby enabling a solution to be obtained for open microstrip.

The static analysis presented in Chapter 6 involved determination of the potential function $\phi(x, y)$ which was the solution to Laplace's equation. By contrast, the full-wave analysis involves the determination of two scalar potential functions $\phi(x, y)$ and $\psi(x, y)$, which are the solutions of the scalar wave equation

$$\nabla_t^2 u_i + (k_i^2 - \beta^2) u_i = 0 \qquad i = 1,\ 2 \tag{8.1}$$

where k_i is the wavenumber in the i^{th} region and β is the phase coefficient of the wave propagating in the z-direction. In the Fourier domain Equation 8.1 becomes

$$\frac{\partial^2 \tilde{u}_i}{\partial y^2} - \gamma_i^2 \tilde{u}_i = 0 \tag{8.2}$$

where

$$\tilde{u}_i(\alpha_n, y) = \frac{1}{2a}\int_{-a}^{+a} -u_i(x,y)e^{j\alpha_n x}\,dx \tag{8.3}$$

$$\gamma_i^2 = \alpha_n^2 + \beta^2 - k_i^2 \tag{8.4}$$

α_n is the Fourier parameter, given by $(n+\frac{1}{2})\frac{\pi}{a}$ for even microstrip modes, and $\frac{n\pi}{a}$ for odd modes. All other variables presented so far may be complex.

By enforcing the appropriate boundary conditions at the ground plane ($y = 0$) and at the roof of the enclosure ($y = h + d$) it can be shown that the solution to Equation 8.2 is

$$\left.\begin{aligned}\tilde{\phi}_1(\alpha_n, y) &= A_1 \sinh(\gamma_1 y)\\ \tilde{\psi}_1(\alpha_n, y) &= C_1 \cosh(\gamma_1 y)\end{aligned}\right\} \quad 0 < y < d$$

$$\left.\begin{aligned}\tilde{\phi}_2(\alpha_n, y) &= B_2 \sinh\left(\gamma_2(h+d-y)\right)\\ \tilde{\psi}_2(\alpha_n, y) &= D_2 \cosh\left(\gamma_2(h+d-y)\right)\end{aligned}\right\} \quad d < y < h + d \tag{8.5}$$

where $A_1(\alpha)$, $B_2(\alpha)$, $C_1(\alpha)$ and $D_2(\alpha)$ are constants to be determined at each value of α_n by the solution process. In order to obtain these coefficients it is necessary to match the tangential components of the fields at the dielectric interface. The boundary conditions at the interface are

$$E_{z,2} - E_{z,1} = 0 \tag{8.6}$$

$$E_{x,2} - E_{x,1} = 0 \tag{8.7}$$

$$H_{z,2} - H_{z,1} = J_x(x)e^{-j\beta z} \tag{8.8}$$

$$H_{x,2} - H_{x,1} = -J_z(x)e^{-j\beta z} \tag{8.9}$$

where $J_x(x)$ and $J_z(x)$ are the transverse and longitudinal components of the surface current

density on the strip. In the Fourier domain the above boundary conditions become

$$\widetilde{E}_{z,2} - \widetilde{E}_{z,1} = 0 \tag{8.10}$$

$$\widetilde{E}_{x,2} - \widetilde{E}_{x,1} = 0 \tag{8.11}$$

$$\widetilde{H}_{z,2} - \widetilde{H}_{z,1} = \widetilde{J}_x(\alpha_n)e^{-j\beta z} \tag{8.12}$$

$$\widetilde{H}_{x,2} - \widetilde{H}_{x,1} = -\widetilde{J}_z(\alpha_n)e^{-j\beta z} \tag{8.13}$$

Substituting the spectral domain expressions for the E and H fields into the above boundary conditions yields a system of equations of the form

$$\begin{bmatrix} a_{11} & a_{12} & a_{13} & a_{14} \\ a_{21} & a_{22} & a_{23} & a_{24} \\ a_{31} & a_{32} & a_{33} & a_{34} \\ a_{41} & a_{42} & a_{43} & a_{44} \end{bmatrix} \begin{bmatrix} A_1 \\ B_2 \\ C_1 \\ D_2 \end{bmatrix} = \begin{bmatrix} 0 \\ 0 \\ -\widetilde{J}_z \\ \widetilde{J}_x \end{bmatrix} \tag{8.14}$$

where coefficients a_{ij} are given by the substitution process. Solution of Equation 8.14 produces expressions for $A_1(\alpha_n)$, $B_2(\alpha_n)$, $C_1(\alpha_n)$ and $D_2(\alpha_n)$ in terms of $\widetilde{J}_x$ and $\widetilde{J}_z$. Therefore at the dielectric interface (i.e. $y = d$) the following equations apply:

$$\widetilde{E}_z = G_{11}(\alpha_n, \beta)\widetilde{J}_x + G_{12}(\alpha_n, \beta)\widetilde{J}_z \tag{8.15}$$

$$\widetilde{E}_x = G_{21}(\alpha_n, \beta)\widetilde{J}_x + G_{22}(\alpha_n, \beta)\widetilde{J}_z \tag{8.16}$$

where $G_{11}(\alpha_n, \beta)$, $G_{12}(\alpha_n, \beta)$, $G_{21}(\alpha_n, \beta)$ and $G_{22}(\alpha_n, \beta)$ are referred to as the spectral domain Green's functions of microstrip/coplanar waveguide type problems (Mirshekar-Syahkal, 1990, p. 34). For shielded structures these functions are defined as follows:

$$G_{11}(\alpha_n,\beta) = G_{22}(\alpha_n,\beta) = \frac{j\omega}{k_2^2}\{\alpha_n\beta[\mu_1\gamma_1\tanh(\gamma_1 d) + \mu_2\gamma_2\tanh(\gamma_2 h)]\}/\Delta \tag{8.17}$$

$$G_{12}(\alpha_n,\beta) = -\frac{j\omega}{k_2^2}\left[\mu_1\gamma_1(k_2^2-\beta^2)\tanh(\gamma_1 d) + \mu_2\gamma_2(k_1^2-\beta^2)\tanh(\gamma_2 h)\right]/\Delta \tag{8.18}$$

$$G_{21}(\alpha_n,\beta) = -\frac{j\omega}{k_2^2}\left[\mu_1\gamma_1(k_2^2-\alpha_n^2)\tanh(\gamma_1 d) + \mu_2\gamma_2(k_1^2-\alpha_n^2)\tanh(\gamma_2 h)\right]/\Delta \tag{8.19}$$

where

$$\Delta = \left[\gamma_1\tanh(\gamma_1 d) + \frac{\varepsilon_1}{\varepsilon_2}\gamma_2\tanh(\gamma_2 h)\right]\left[\gamma_1\coth(\gamma_1 d) + \frac{\mu_1}{\mu_2}\gamma_2\coth(\gamma_2 h)\right] \tag{8.20}$$

For the case of open microstrip the roof and side walls of the shield are allowed to recede to infinity (Mirshekar-Syahkal, 1990, p. 24). Assuming that the dielectrics above and below the strip are nonmagnetic (i.e. $\mu_1 = \mu_2 = \mu_0$), Equations 8.17–8.20 reduce to

$$G_{11}(\alpha,\beta) = G_{22}(\alpha,\beta) = \frac{j\omega}{k_2^2}\{\alpha\beta\mu_0[\gamma_1\tanh(\gamma_1 d) + \gamma_2]\}/\Delta \tag{8.21}$$

$$G_{12}(\alpha,\beta) = -\frac{j\omega\mu_0}{k_2^2}\left[\gamma_1(k_2^2-\beta^2)\tanh(\gamma_1 d) + \gamma_2(k_1^2-\beta^2)\right]/\Delta \tag{8.22}$$

$$G_{21}(\alpha,\beta) = -\frac{j\omega\mu_0}{k_2^2}\left[\gamma_1(k_2^2-\alpha^2)\tanh(\gamma_1 d) + \gamma_2(k_1^2-\alpha^2)\right]/\Delta \tag{8.23}$$

where

$$\Delta = [\gamma_1\tanh(\gamma_1 d) + \frac{\varepsilon_1}{\varepsilon_2}\gamma_2][\gamma_1\coth(\gamma_1 d) + \gamma_2] \tag{8.24}$$

The discrete Fourier parameter α_n has been replaced by the continuous parameter α, which may be complex depending on the path of integration. Similarly, the Fourier transform expression in Equation 8.3 must be replaced by

$$\tilde{u}_i(\alpha, y) = \frac{1}{2\pi} \int_{-\infty}^{+\infty} -u_i(x, y) e^{j\alpha x}\, dx \tag{8.25}$$

A crucial assumption which has been made in recasting this problem for open microstrip is that the real part of γ_2 is greater than zero. This ensures that the boundary conditions at infinity—namely, that all fields must approach zero—are satisfied. This issue also has implications for the calculation of the radiation field, and is discussed in more detail in Section 8.8.

The final form of Equations 8.15 and 8.16 can be expressed in matrix notation:

$$\begin{bmatrix} G_{11}(\alpha,\beta) & G_{12}(\alpha,\beta) \\ G_{21}(\alpha,\beta) & G_{22}(\alpha,\beta) \end{bmatrix} \begin{bmatrix} \widetilde{J}_x \\ \widetilde{J}_z \end{bmatrix} = \begin{bmatrix} \widetilde{E}_z \\ \widetilde{E}_x \end{bmatrix} \tag{8.26}$$

$$[\boldsymbol{G}(\alpha,\beta)] \left[\widetilde{\boldsymbol{J}}\right] = \left[\widetilde{\boldsymbol{E}}\right] \tag{8.27}$$

where the matrix $[\boldsymbol{G}(\alpha, \beta)]$ is referred to as a dyadic Green's function.

The system of equations represented by Equation 8.27 are the final equations in the Fourier domain. They are quite general, the only assumptions being that the strip conductor has zero thickness, the substrate is infinitely wide and the covering layer is infinitely high. Equation 8.27 applies equally to microstrip, coplanar waveguide, and any other uniform planar transmission line.

However, it is not yet possible to solve for β because $\left[\widetilde{\boldsymbol{E}}\right]$ and $\left[\widetilde{\boldsymbol{J}}\right]$ are unknown. The procedure for calculating β is covered in Section 8.5. Firstly, however, a brief discussion about basis functions is required.

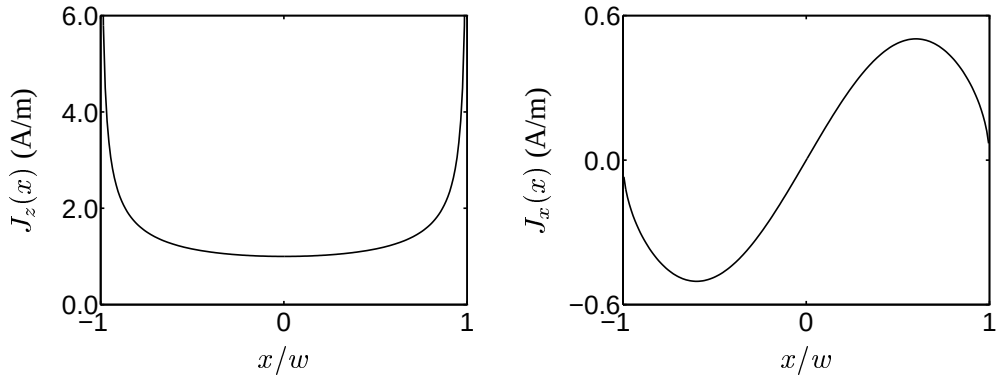

(a) Longitudinal component.

(b) Transverse component.

Figure 8.2: Approximate distributions of longitudinal and transverse current components on a perfectly conducting strip.

8.4 Basis Functions

The topic of basis functions has already been addressed in Section 6.4 in the context of a static spectral domain analysis of microstrip. Much of that discussion is also relevant to the full-wave analysis, except that instead of expanding the surface *charge* distribution as a family of basis functions, it is the surface *current* distribution that is of interest. As was the case with the static analysis, it is important to choose a set of basis functions that adequately represents the current distribution on the strip.

An added complication with the full-wave model is that the strip current has two components: a longitudinal component J_z, and a transverse component J_x. The former contains an edge singularity very similar to the charge distribution in the DC analysis. The latter, however, approaches zero at the edges of the strip. Consequently, a totally different set of basis functions is required for the transverse current component. The approximate behaviour of J_z and J_x across the strip conductor is depicted in Figure 8.2.

The basis functions selected for this project were almost identical to those suggested by Jansen (1978). For the longitudinal current component the following expansion was used:

$$J_{z,1}(x) = \frac{1}{\sqrt{1-\left(\frac{x}{w}\right)^2}} \tag{8.28}$$

$$J_{z,q}(x) = \frac{\cos\left[(q-1)\pi\left(\frac{x}{w}\right)\right] - J_0\left[(q-1)\pi\right]}{\sqrt{1-\left(\frac{x}{w}\right)^2}} \qquad q = 2,\, 3,\, \ldots,\, Q \tag{8.29}$$

where J_0 denotes a zero order Bessel function of the first kind. In the Fourier domain these functions become

$$\widetilde{J}_{z,1} = \frac{w}{2} J_0(\alpha w) \tag{8.30}$$

$$\widetilde{J}_{z,q} = \frac{w}{4}\left\{J_0\left[\alpha w - (q-1)\pi\right] + J_0\left[\alpha w + (q-1)\pi\right] - 2J_0\left[(q-1)\pi\right] J_0(\alpha w)\right\} \qquad q = 2,\, 3,\, \ldots,\, Q \tag{8.31}$$

The transverse current component is related to the longitudinal component via the following integral expression:

$$J_{x,p}(x) = \int_0^X J_{z,p+1}(X')\, dX' \qquad p = 1,\, 2,\, \ldots,\, P \tag{8.32}$$

where $X = x/w$. The above expression is slightly different to that of Jansen, who used $J_{x,1} = 0$. Otherwise the equation is the same. The Fourier transform of Equation 8.32 is

$$\widetilde{J}_{x,p} = \frac{\widetilde{J}_{z,p+1}}{\alpha w} \tag{8.33}$$

The advantage of the above families of basis functions is that the behaviour of J_x and J_z near the edge of the strip is captured explicitly. However, there is a slight drawback in that each of the Fourier transform expressions contains the Bessel function J_0. It was noted in Chapter 6 that this tends to produce inner products which are computationally demanding to evaluate. This is undesirable if the algorithm is to be used in a real time instrument.

Like the quasi-TEM analysis, the full-wave analysis software can be made to run significantly faster by neglecting the edge condition. This allows basis functions with more rapidly decaying

Fourier transforms to be used, often with only minimal loss of accuracy (Mirshekar-Syahkal, 1990, p. 54). Indeed, in the course of this project a wide variety of basis functions were implemented, including a uniform distribution, Legendre polynomials, sinusoidal functions and a simple cubic polynomial. It was typically found that solutions differed by only 1–2%, and program execution times were much shorter.

Despite the advantages offered by these alternative basis functions, it was decided that it would be unwise to neglect the edge condition, at least during the developmental phase of the sensor model. This was due to the fact that no previous work has ever been reported in the literature on the full-wave analysis of microstrip covered by a lossy, high-permittivity material. As a result there was concern that failure to capture the edge condition could have unforeseen consequences. For this reason, the basis functions of Jansen were used in the majority of cases.

8.5 Solution Procedure

In Chapter 6 the Galerkin method was applied to microstrip by expanding the surface charge density $\sigma(x)$ on the strip as a set of trial functions, and then calculating the inner products

$$< \left(\tilde{V}_0 + \tilde{V} \right), \tilde{\sigma}_p > \qquad p = 1,\ 2,\ \ldots,\ P$$

This produced a linear system of equations which was solved for the basis function coefficients and, ultimately, the propagation characteristics of the transmission line.

In a similar fashion, the application of Galerkin's method to the full-wave analysis of microstrip involves expanding the surface *current* density on the strip as a set of basis functions. As mentioned earlier, the current density has two components, J_x and J_z. Expanding each component yields

$$J_x(x) = \sum_{p=1}^{P} a_p J_{x,p}(x) \tag{8.34}$$

$$J_z(x) = \sum_{q=1}^{Q} b_q J_{z,q}(x) \tag{8.35}$$

These trial functions are then Fourier transformed and substituted into Equations 8.15 and 8.16.

The next step is to take the inner products of the tangential electric field components at the dielectric interface and the strip surface current. Using the definition of the inner product given in Section 6.5, the following expressions are obtained:

$$< \widetilde{E}_x, \widetilde{J}_{x,p} > \;=\; \int_{-\infty}^{\infty} \widetilde{E}_x \widetilde{J}^*_{x,p}\, d\alpha \qquad p = 1,\ 2,\ \ldots\ ,\ P \tag{8.36}$$

$$< \widetilde{E}_z, \widetilde{J}_{z,q} > \;=\; \int_{-\infty}^{\infty} \widetilde{E}_z \widetilde{J}^*_{z,q}\, d\alpha \qquad q = 1,\ 2,\ \ldots\ ,\ Q \tag{8.37}$$

Because the strip has been assumed to be a perfect conductor, the tangential electric field on the strip must be zero. Elsewhere the electric field is nonzero. By contrast, the current density on the dielectric interface is zero everywhere except on the strip. The tangential electric field and the current density at $y = d$ are therefore orthogonal to each other, implying that their inner product must evaluate to zero, i.e.

$$< \widetilde{E}_x, \widetilde{J}_{x,p} > \;=\; 0 \qquad p = 1,\ 2,\ \ldots\ ,\ P \tag{8.38}$$

$$< \widetilde{E}_z, \widetilde{J}_{z,q} > \;=\; 0 \qquad q = 1,\ 2,\ \ldots\ ,\ Q \tag{8.39}$$

Substituting Equations 8.15 and 8.16 into the above expressions produces a system of linear homogeneous equations of the form

$$\sum_{p=1}^{P} \left[a_p \int_{-\infty}^{\infty} G_{11} \widetilde{J}_{x,p} \widetilde{J}^*_{z,\acute{q}}\, d\alpha \right] + \sum_{q=1}^{Q} \left[b_q \int_{-\infty}^{\infty} G_{12} \widetilde{J}_{z,q} \widetilde{J}^*_{z,\acute{q}}\, d\alpha \right] \;=\; 0$$

$$\acute{q} = 1,\ 2,\ \ \ldots\ ,\ \ Q \tag{8.40}$$

$$\sum_{p=1}^{P} \left[a_p \int_{-\infty}^{\infty} G_{21} \widetilde{J}_{x,p} \widetilde{J}^*_{x,\acute{p}}\, d\alpha \right] + \sum_{q=1}^{Q} \left[b_q \int_{-\infty}^{\infty} G_{22} \widetilde{J}_{z,q} \widetilde{J}^*_{x,\acute{p}}\, d\alpha \right] \;=\; 0$$

$$\acute{p} = 1,\ 2,\ \ \ldots\ ,\ \ P \tag{8.41}$$

The integral expressions in these equations must be evaluated numerically. For this project the preferred method was Simpson's $\frac{1}{3}$ rule. Due to the symmetrical nature of the integrands, it was only necessary to perform single-sided integrations. It then remained to find an appropriate upper limit of integration $\alpha_{\max}$. This was achieved by graphing the magnitude of each

integrand against α and identifying the point where the magnitudes had all decayed away to very small levels. Any increase in the upper limit of integration beyond this point caused a negligible change in the results.

Equations 8.40 and 8.41 have a nontrivial solution only when the determinant of the coefficient matrix is zero. That is, the eigenvalue of the coefficient matrix is the phase coefficient β, and the eigenvector associated with β contains the coefficients a_p and b_q. This eigenvalue must be located using a numerical root-finding algorithm. The secant method was found to be the most robust and reliable algorithm for this purpose. Choosing a starting estimate for β, the determinant of Equations 8.40 and 8.41 was evaluated by reducing the coefficient matrix to upper-triangular form and calculating the product of the diagonal elements (Anton and Rorres, 1987). The starting estimate was refined iteratively until the magnitude of the change in successive estimates of β was less than 10^{-4}.

In previous chapters it has been the practice to present an example at this point, to illustrate the use of each technique as it was introduced. In this case, however, there still remains a number of issues which must be resolved before the spectral domain method can be applied to a microstrip sensor immersed in a material like cheese curd. Specifically, the question of how to incorporate the effects of surface waves and radiation into the analysis has yet to be answered.

It will be shown in the following sections that although these phenomena are diverse in origin, they all impact on the one remaining degree of freedom in the spectral domain formulation: the path of integration.

8.6 Dependence of Solution on Path of Integration

This section marks the beginning of the second part of this chapter. Much of the material presented so far has been based upon traditional spectral domain formulations: Fourier transformed expressions have been derived for the fields across the dielectric interface of microstrip; some of the considerations pertaining to the choice of basis functions have been discussed; and the Galerkin method has been presented as a means of solving for the propagation coefficient of the line.

However, there are some subtle yet very important issues which have yet to be addressed concerning the evaluation of the integrals in the inner product expressions $< \widetilde{E}_x, \widetilde{J}_{x,p} >$ and $< \widetilde{E}_z, \widetilde{J}_{z,q} >$. The manner in which these integrals are calculated enables the effects of leakage into surface wave modes and radiation to be taken into account.

The most common means of evaluating the integral expressions in Equations 8.40 and 8.41 is to integrate along the real axis from $\alpha = -\infty$ to $\alpha = +\infty$. In a lossless system with an isotropic substrate this always results in an attenuation coefficient of zero, implying that the propagating mode is purely bound. For the dominant mode of an air-covered microstrip line this is absolutely correct, and the literature is replete with authors who have adopted this approach and achieved excellent agreement between theoretical and experimental results (see e.g. Itoh and Mittra, 1973; Hashimoto, 1985; Mirshekar-Syahkal, 1990). However, when a microstrip transmission line is immersed in a lossy medium with a high dielectric constant, integrating along the real axis may not necessarily provide the correct answer. Indeed, it is possible that the spectral domain method may not converge at all under these circumstances.

In such situations the only solution is to deform the path of integration off the real axis into the complex α-plane. It will be shown in the following sections that there is a sound physical basis for this strategy. Firstly, however, it is helpful to consider the spectral domain formulation from a purely mathematical perspective.

Given that the Fourier parameter α can assume any complex value, the integral expressions in Equations 8.40 and 8.41 can be regarded as line integrals in the complex α-plane. As such, their value is dependent not only upon the endpoints of the path of integration, but also upon the path itself (Kreyszig, 1993, p. 755).

If the endpoints of the path of integration are joined by a semicircle of infinite radius—such that the contribution to the total line integral is zero—each integral expression becomes a contour integral, and must therefore obey Cauchy's integral theorem. Other laws of complex analysis also apply, including those governing branch points and branch cuts.

In the event that the integrands in Equations 8.40 and 8.41 contain singular points (or 'poles'), it is possible that one or more of these points could lie inside the integration contour. The decision must then be made as to whether or not the contour should be deformed around these poles.

The same situation can arise with branch points; if a branch point lies inside the boundary of the integration contour, it may be necessary to deform the integration contour around it to avoid intersecting the associated branch cut.

The following two sections shall show how the poles and branch points in Equations 8.40 and 8.41 can be identified and mapped to the complex plane. Subsequent to this a simple technique will be presented to determine which, if any, of these points should be bypassed by the contour of integration, thereby preserving the continuity of the physical situation.

8.7 Surface Wave Poles

To determine whether the integrals associated with $< \widetilde{E}_x, \widetilde{J}_{x,p} >$ and $< \widetilde{E}_z, \widetilde{J}_{z,q} >$ contain singular points, it is necessary to examine each term in the integrands.

Inspection of the Fourier transformed basis functions $\widetilde{J}_{x,p}$ and $\widetilde{J}_{z,q}$ quickly reveals that these functions are analytic for all α. This leaves the dyadic Green's function as the only possible source of any singularities.

By examining each of the Green's dyad components, it becomes evident that any propagating surface wave mode will manifest itself as a pole in the dyadic Green's function. To demonstrate that this is so, the TE and TM surface wave eigen equations from Chapter 7 must be rewritten in a slightly different form. Using the substitution $\gamma_1 = jK$ from Section 7.5.1, Equations 7.13 and 7.20 can be expressed as:

$$\gamma_1 \tanh(\gamma_1 d) + \frac{\varepsilon_1}{\varepsilon_2}\gamma_2 = 0 \tag{8.42}$$

$$\gamma_1 \coth(\gamma_1 d) + \gamma_2 = 0 \tag{8.43}$$

From Section 8.3 it is known that the denominator of each component of the dyadic Green's function is given by

$$\Delta = [\gamma_1 \tanh(\gamma_1 d) + \frac{\varepsilon_1}{\varepsilon_2}\gamma_2][\gamma_1 \coth(\gamma_1 d) + \gamma_2] \tag{8.44}$$

It is evident that Δ is simply the product of Equations 8.42 and 8.43. Therefore the roots of the surface wave eigen equations are also roots of Δ, and hence poles of the spectral domain Green's function $[\boldsymbol{G}(\alpha, \beta)]$.

To determine the location of a surface wave pole in the complex plane, it is first necessary to solve for the wavenumber γ_2 of the mode. (The C++ program described in Section 7.4 can be used for this purpose.) Substitution of γ_2 and the current estimate of the microstrip phase coefficient β into Equation 8.4 enables the location of the Green's function pole α_p to be calculated:

$$\begin{aligned} \gamma_2^2 &= \alpha_p^2 + \beta^2 - k_2^2 \\ \therefore\ \alpha_p^2 &= \gamma_2^2 - \beta^2 + k_2^2 \\ \alpha_p &= \sqrt{\gamma_2^2 - \beta^2 + k_2^2} \end{aligned} \tag{8.45}$$

The means of determining whether or not the integration contour should be deformed around the surface wave poles is covered in Section 8.9. Firstly, however, some comments on radiation loss are necessary.

8.8 Radiation Loss and the Cutting of the Complex Plane

8.8.1 Dual-Valued Parameters

The analysis of radiation from open microstrip centres around the branch points associated with wavenumbers γ_1 and γ_2. These parameters both appear numerous times in each component of the dyadic Green's function, and are significant because each is a square root function of the form

$$\gamma_i = \pm\sqrt{\alpha^2 + \beta^2 - k_i^2} \qquad\qquad i = 1,\ 2 \tag{8.46}$$

It is clear from the above equation that γ_1 and γ_2 are dual-valued functions of the Fourier parameter α. In complex analysis these functions are described as having two 'branches'. The

correct branches must be chosen such that the fields on the structure attenuate away from the strip (Collin, 1991, pp. 728–732).

For planar structures with a ground plane γ_1 always appears in the form $\gamma_1 \tanh(\gamma_1 d)$ or $\gamma_1 \coth(\gamma_1 d)$, as shown in Equations 8.21–8.24. These are both even functions of γ_1, hence the sign of γ_1 is unimportant.

However, the sign of γ_2 is of *paramount* importance, as this parameter appears by itself in Equations 8.21–8.24. Consequently, the value of the dyadic Green's function will be different depending on which branch of γ_2 is chosen. The incorrect choice can lead to the nonphysical case of fields which increase away from the strip.

8.8.2 Spectral and Non-Spectral Regions of the Complex Plane

In order to make the correct decision about which branch of γ_2 to choose, it is helpful to refer back to the original spectral domain formulation presented in Section 8.3. This involved deriving the Fourier transformed field equations for shielded microstrip, and then allowing the roof and side walls of the shield to recede to infinity.

In order to satisfy the boundary conditions at infinity, it was stipulated that the real part of γ_2 had to be positive. As a result, when evaluating the integrals associated with the inner products $< \widetilde{E}_x, \widetilde{J}_{x,p} >$ and $< \widetilde{E}_z, \widetilde{J}_{z,q} >$, a decision must be made at every point on the integration contour as to whether the sign of Equation 8.46 should be positive or negative. Fortunately it is possible to derive a relatively simple relation which makes this a straightforward process:

Let $\alpha_b = \alpha_b' + j\alpha_b''$ be a point on the boundary dividing that part of the complex plane where the positive root must be chosen from that where the negative root must be chosen. (By convention, these areas are referred to as the *spectral* and *nonspectral* regions respectively.) The point α_b must satisfy the relation

$$\Re\{\gamma_2\} = 0 \tag{8.47}$$

Substituting Equation 8.46 into this relation and expanding yields

$$\begin{aligned}
\Re\left\{\left(\alpha_b^2+\beta^2-k_2^2\right)^{\frac{1}{2}}\right\} &= 0 \\
\Re\left\{\left[(\alpha_b'+j\alpha_b'')^2+(\beta'-j\beta'')^2-(k_2'-jk_2'')^2\right]^{\frac{1}{2}}\right\} &= 0 \\
\Re\left\{\left[(\alpha_b')^2-(\alpha_b'')^2+2j\alpha_b'\alpha_b''+(\beta')^2-(\beta'')^2\right.\right. & \\
\left.\left.-2j\beta'\beta''-(k_2')^2+(k_2'')^2+2jk_2'k_2''\right]^{\frac{1}{2}}\right\} &= 0
\end{aligned} \tag{8.48}$$

Equation 8.48 cannot be satisfied unless the imaginary component is greater than or equal to zero. Therefore on the boundary between the two regions we have

$$2j\alpha_b'\alpha_b''-2j\beta'\beta''+2jk_2'k_2'' = 0 \tag{8.49}$$

Simplifying this expression gives

$$\begin{aligned}
\alpha_b'\alpha_b''-\beta'\beta''+k_2'k_2'' &= 0 \\
\alpha_b'\alpha_b'' &= \beta'\beta''-k_2'k_2'' \\
\alpha_b'' &= \frac{\beta'\beta''-k_2'k_2''}{\alpha_b'}
\end{aligned} \tag{8.50}$$

Equation 8.50 defines a hyperbolic curve which divides the spectral and nonspectral regions of the complex α-plane from one another, as shown in Figure 8.3. As the path of integration traverses the complex plane, this relation can be used to determine whether the contour is in a spectral or nonspectral part of the plane, thereby enabling the correct branch of γ_2 to be selected.

8.8.3 Branch Cut Selection

An undesirable consequence of the dual-valued nature of γ_2 is that the integrals which must be evaluated as part of Galerkin's method may not be single-valued. This makes it impossible to employ such techniques as Cauchy's integral theorem in the solution procedure (Grimm and Nyquist, 1993).

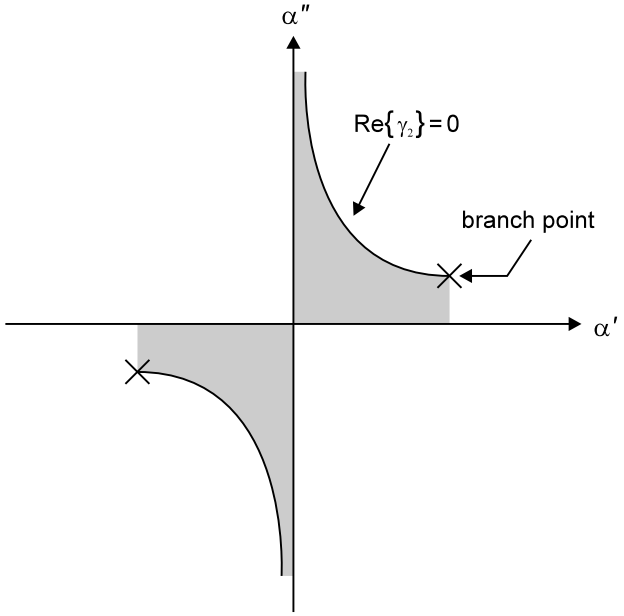

Figure 8.3: Plot showing the boundary between the spectral and nonspectral regions of the complex α-plane. Shaded areas denote nonspectral regions.

To ensure that all integrals remain single-valued, it is necessary to specify a branch cut in the complex plane which may not be crossed by the path of integration. Generally speaking, the choice of branch cut is arbitrary. However, evaluation of integrals can be performed more efficiently if the branch cut is chosen with care (Collin, 1991, pp. 728–732).

Different authors have suggested a variety of branch cuts. Two options were evaluated for this project. A brief discussion of each is provided below.

8.8.3.1 The Sommerfeld Branch Cut

The first type of branch cut to be considered was the Sommerfeld branch cut. While ultimately rejected for this project, this type of branch cut still warrants a brief mention here due to its frequent use in the literature.

The Sommerfeld branch cut lies on the boundary between the spectral and nonspectral regions of the α-plane. As such, it can be described using Equation 8.50. When used as the branch cut associated with the branch point γ_2, it must be bypassed by the integration contour in the manner shown in Figure 8.4.

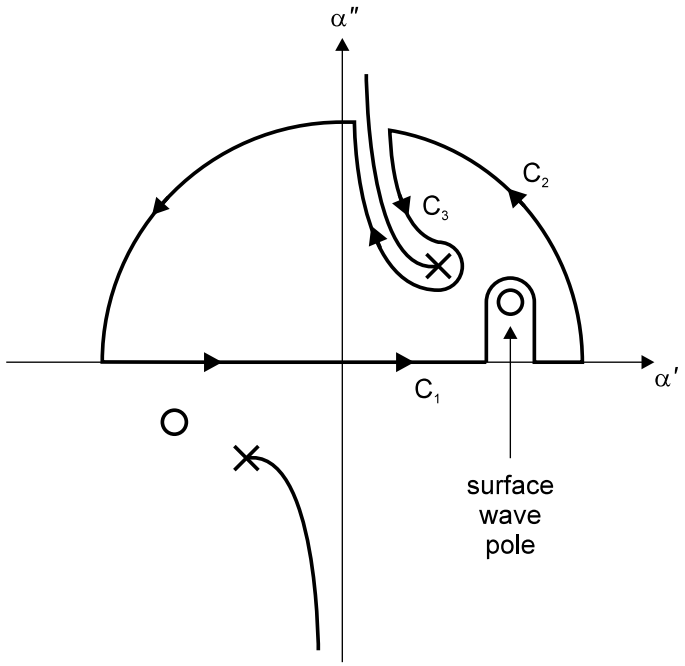

Figure 8.4: Path of integration taken when bypassing surface wave pole and branch point with Sommerfeld branch cut.

The advantage of using this branch cut is that the integral around the segment of the contour labelled C_2 vanishes altogether (Collin, 1991, pp. 728–732). The contour integral due to segment C_1 will also vanish except for the residues associated with the surface wave poles. The branch cut integral performed along segment C_3 represents the radiation field and has a continuous eigenvalue spectrum (Collin, 1991, pp. 728–732). If we let the total contour due to C_1, C_2 and C_3 be denoted by C, then the contour integral for the structure is given by

$$\int_C \;=\; -\int_{C_3} - 2\pi j \sum \text{residues} \tag{8.51}$$

The disadvantage of the Sommerfeld branch cut is that the contour C_3 is inconvenient to evaluate numerically. This is due to the presence of Bessel functions in the expressions for $\widetilde{J}_x$ and $\widetilde{J}_z$. These functions are evaluated using an asymptotic series expansion, which can cause the computer to overflow for arguments with large imaginary parts. This led to the Sommerfeld branch cut eventually being rejected.

It is interesting to note that some authors have avoided this problem by allowing the path of integration to simply pass *through* the Sommerfeld branch cut as shown in Figure 8.5. Exam-

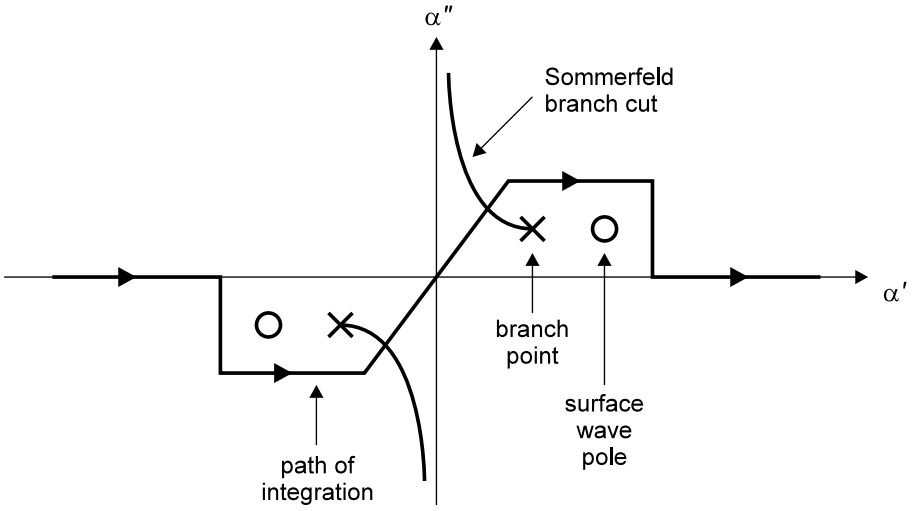

Figure 8.5: Alternative path of integration which bypasses branch point by crossing branch cut.

ples include Michalski and Zheng (1989), Das and Pozar (1991), and Nghiem et al. (1996). As mentioned at the beginning of this section, it is supposed to be forbidden for the integration contour to cross a branch cut. However, this does not seem to prevent the above authors from obtaining theoretical results which agree well with experimental data. Despite this, it was decided to adopt a more mathematically rigorous approach for this project, and select a path of integration which did not cross the branch cut. In order to avoid the numerical problems discussed earlier, this entailed the choice of a different branch cut.

8.8.3.2 The Grimm-Nyquist Branch Cut

The branch cut which was finally chosen was based on that described by Grimm and Nyquist (1993). This type of branch cut is frequently referred to in the literature, however it does not appear to have its own name. For the sake of convenience it shall hereafter be referred to as the Grimm-Nyquist branch cut, although it is not certain whether these authors were the first to propose this type of branch cut.

The Grimm-Nyquist branch cut does not have an explicit function to describe its path in the complex plane. Instead, it is usually described in qualitative terms. In order for a branch cut to be classified as a Grimm-Nyquist type, it must always be asymptotic to the negative

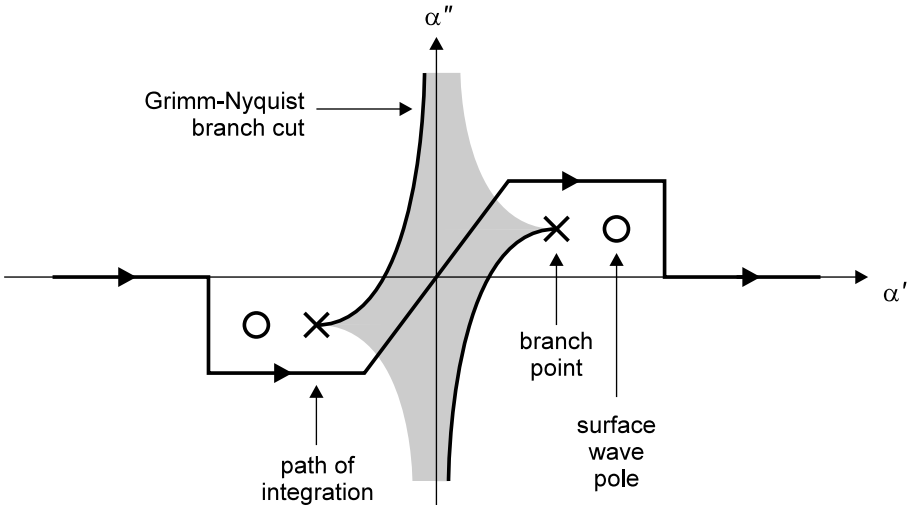

Figure 8.6: Graphic representation of the Grimm-Nyquist branch cut and the deformed integration contour. Shaded area denotes nonspectral region of complex plane.

imaginary axis, as illustrated in Figure 8.6. This criterion must be satisfied irrespective of where the branch point lies in the complex plane. The Grimm-Nyquist branch cut offers three main advantages.

Firstly, it enables the path of integration to lie entirely on the top Riemann sheet of the complex plane. At no point is there a need for the path to cross the branch cut. As a result all integrands remain analytic.

Secondly, it ensures that the continuity of the physical problem is maintained at all times. This is due to the fact that the branch cut does not change direction if the branch point migrates from one quadrant to another. By contrast, the Sommerfeld branch cut will be asymptotic to the negative imaginary axis only when the branch point resides in the fourth quadrant. If the branch point migrates to the first quadrant, the Sommerfeld branch cut reverses direction and becomes asymptotic to the positive imaginary axis, as is clear from Equation 8.50.

Finally, the Grimm-Nyquist branch cut ensures that the contour of integration is not violated if the branch point migrates from the fourth quadrant to the first. Instead, the contour can be deformed in a simple and consistent manner as the branch point progresses into the first quadrant. The same cannot be said of the Sommerfeld branch cut, which requires the contour

to be altered from a simple path along the real axis to the inconvenient path which was shown in Figure 8.4.

In the absence of a standard function to describe the Grimm-Nyquist branch cut, it falls to each worker to provide their own definition. For this project the approach of Lin and Sheen (1997) was adopted. These workers have used a simple vertical line originating at the branch point and progressing downwards. Although this type of branch cut does not asymptote towards the negative imaginary axis as stipulated by Grimm and Nyquist, it is easier to incorporate into numerical integrations and does not have a noticeable impact on the accuracy of the solution.

8.8.4 Closing Remarks

Before leaving the topic of branch cuts, some final comments are necessary to put the issue in perspective.

Much of the preceding discussion about branch cuts is somewhat academic, having little practical impact on the solution procedure or indeed the solution itself. As discussed in Section 8.8.3.1, numerous authors have chosen integration contours which intersect the branch cut, without apparent loss of accuracy in the final result. That this should be the case is not surprising, despite the fact that the rules of complex analysis appear to have been violated. After all, a branch cut is simply an arbitrary boundary designed to ensure that complex integrals remain analytic by preventing integration contours from completely encircling branch points.

Consequently, the only circumstances in which the choice of branch cut would become a serious consideration is if the contour of integration were required to completely encircle the branch point. Under these conditions the contour would move from the top Riemann sheet to the bottom Riemann sheet, or vice versa. To accurately model this behaviour a more sophisticated computer program would be needed than that which has already been developed.

Fortunately this situation is not likely to arise with the spectral domain formulation presented here. However, other formulations have been presented in which multiple encirclements of the branch point can occur. For example, Mesa et al. (1999) have presented a spectral domain analysis of open microstrip in which the Fourier transform is taken with respect to the *longitudinal*

(i.e. z-directed) coordinate, instead of the transverse (x-directed) coordinate. In solving for the current on the line, the branch point is encircled twice.

Thus, in certain circumstances the choice of branch cut is an important matter which warrants careful consideration. For the purposes of this thesis, however, it is covered only for the sake of mathematical rigour, and does not affect the outcome of the analysis in any practical sense.

A matter of far greater significance is the question of how to determine whether or not the branch point needs to be bypassed by the integration contour. As is the case with surface wave poles, it can be shown that it is not necessary to deform the contour around the branch point in all cases. This is discussed in more detail in the following section.

8.9 Considerations in the Deformation of the Integration Contour

8.9.1 Pole and Branch Point Migration

The deformation of the integration contour in the spectral plane is a topic that has received a great deal of attention over the last two decades. One of the most important outcomes of this work has been the realisation that it is not always necessary to deform the contour around the branch point and the surface wave poles. This has been discussed by such workers as Boukamp and Jansen (1983), and more recently by Bagby et al. (1993) and Lin and Sheen (1997).

The decision as to how the integration contour should be deformed is based on the migration of the branch point and surface wave poles as the loss of the covering material varies. The most commonly used approach is to start by assuming the covering medium is highly lossy, and noting the location of the branch point and poles in the complex α-plane, as shown in Figure 8.7(a). The loss of the covering medium is then reduced to zero, and the migration path of these points is monitored. If the branch point or poles cross the real axis on the way to their final location, then the integration contour must be deformed such that these points lie on the same side as before, as shown in Figure 8.7(b). This maintains the continuity of the physical situation (Grimm and Nyquist, 1993). Depending on the parameters of the structure, it may be necessary to deform the integration contour around the surface wave poles, and/or the branch point, or it may not be necessary to deform the contour at all.

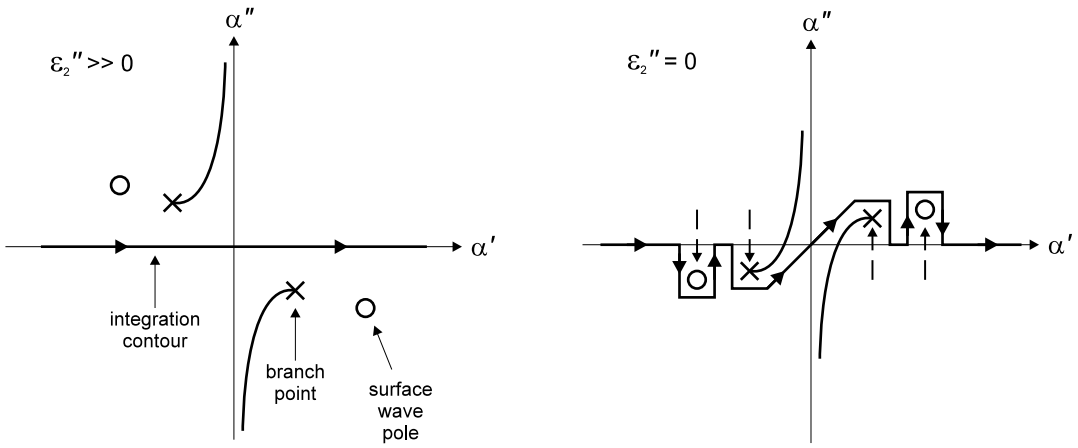

(a) Branch point and surface wave pole location for $\varepsilon_2'' \gg 0$.

(b) Branch point and surface wave pole location for $\varepsilon_2'' \to 0$.

Figure 8.7: Migration of branch point and surface wave poles as ε_2'' changes from high loss to low loss.

The migration of poles and branch points in the complex plane—and hence the conditions required for leakage to the surface wave modes and radiation field—can be described more precisely by examining the transverse wavenumber γ_2 in more detail. This is covered in the following two sections.

8.9.2 Surface Wave Leakage Condition

As discussed in Section 8.9.1, it is only necessary to deform the integration contour around a surface wave pole if the pole migrates across the integration contour as the loss of the covering medium varies. If the contour has to be deformed, then energy leakage due to surface waves is implicated.

A more detailed examination of the transverse wavenumber γ_2 enables a surface wave leakage condition to be derived for microstrip. This takes the form of an upper and lower bound for the phase coefficient β of microstrip, between which the propagating mode leaks energy to surface wave modes. To derive these upper and lower threshold values it is necessary to return to the standard definition of γ_2, namely

$$\gamma_2 \quad = \quad \sqrt{\alpha^2 + \beta^2 - k_2^2} \tag{8.52}$$

If $\gamma_{2,p}$ is the transverse wavenumber of the surface wave mode (obtained using the solution procedure described in Section 7.4), the location of the corresponding pole α_p in the spectral plane can be calculated as follows:

$$\begin{aligned} \gamma_{2,p}^2 &= \alpha_p^2 + \beta^2 - k_2^2 \\ \alpha_p^2 &= \gamma_{2,p}^2 + k_2^2 - \beta^2 \\ \alpha_p &= \sqrt{\gamma_{2,p}^2 + k_2^2 - \beta^2} \end{aligned} \tag{8.53}$$

All of the above parameters may be complex, i.e.

$$\begin{aligned} \alpha_p &= \alpha_p' + j\alpha_p'' \\ \gamma_{2,p} &= \gamma_{2,p}' + j\gamma_{2,p}'' \\ k_2 &= k_2' - jk_2'' \\ \beta &= \beta - j\alpha \end{aligned}$$

Substitution into Equation 8.53 yields

$$\begin{aligned} \alpha_p' + j\alpha_p'' &= \sqrt{(\gamma_{2,p}' + j\gamma_{2,p}'')^2 + (k_2' - jk_2'')^2 - (\beta - j\alpha)^2} \\ &= \sqrt{A + jB} \end{aligned} \tag{8.54}$$

where

$$A = (\gamma_{2,p}')^2 - (\gamma_{2,p}'')^2 + (k_2')^2 - (k_2'')^2 - \beta^2 + \alpha^2 \tag{8.55}$$

$$B = 2\gamma_{2,p}'\gamma_{2,p}'' - 2k_2'k_2'' + 2\alpha\beta \tag{8.56}$$

For the surface wave pole α_p to be able to migrate between the first and fourth quadrants, the real part of the expression under the square root sign, A, must always be positive, i.e.

$$A > 0 \tag{8.57}$$

Substituting Equation 8.55 into this relation and solving for β produces the following result:

$$\beta_{\max} \quad < \quad \sqrt{(\gamma'_{2,p})^2 - (\gamma''_{2,p})^2 + (k'_2)^2 - (k''_2)^2 + \alpha^2} \tag{8.58}$$

Equation 8.58 is the upper boundary of β. The phase coefficient of the propagating microstrip mode must be less than this value in order for leakage into the surface wave mode corresponding to $\gamma_{2,p}$ to occur.

The lower boundary of β can be obtained by requiring B in Equation 8.54 to be greater than zero. If this condition is satisfied the surface wave pole α_b will reside in the first quadrant, implicating surface wave leakage. Mathematically this condition can be written as:

$$B \quad > \quad 0 \tag{8.59}$$

Substituting Equation 8.56 into this relation and solving for β yields

$$\beta_{\min} \quad > \quad \frac{k'_2 k''_2 - \gamma'_{2,p}\gamma''_{2,p}}{\alpha} \tag{8.60}$$

Equation 8.60 is the lower boundary of β. The phase coefficient of the propagating microstrip mode must be greater than this value in order for leakage into the surface wave mode corresponding to $\gamma_{2,p}$ to occur.

8.9.3 Radiation Leakage Condition

Similar reasoning can be used to determine whether the transmission line mode of microstrip loses energy due to radiation. As before, an upper and lower boundary can be derived for β, within which radiation leakage occurs. The starting point is again the expression for the transverse wavenumber γ_2:

$$\gamma_2 = \sqrt{\alpha^2 + \beta^2 - k_2^2}$$

At the location of the branch point α_b in the complex plane, the value of γ_2 is zero. Substituting this into the above expression and solving for α_b we obtain

$$\alpha_b = \sqrt{k_2^2 - \beta^2} \tag{8.61}$$

The parameters α_b, k_2 and β may all be complex, i.e.

$$\begin{aligned} \alpha_b &= \alpha_b' + j\alpha_b'' \\ k_2 &= k_2' - jk_2'' \\ \beta &= \beta - j\alpha \end{aligned}$$

Substitution into Equation 8.61 yields

$$\alpha_b' + j\alpha_b'' = \sqrt{(k_2')^2 - (k_2'')^2 - \beta^2 + \alpha^2 - 2jk_2'k_2'' + 2j\alpha\beta} \tag{8.62}$$

Restrictions similar to those of Section 8.9.2 are then placed on Equation 8.62, namely

- For the branch point α_b to migrate between the first and fourth quadrants, the real part of the expression under the square root sign must always be positive; and
- For α_b to reside in the first quadrant—implying radiation leakage—the imaginary part of the expression under the square root sign must be positive

These conditions produce the following limiting values of β:

$$\beta_{\max} < \sqrt{(k_2')^2 - (k_2'')^2 + \alpha^2} \tag{8.63}$$

$$\beta_{\min} > \frac{k_2'k_2''}{\alpha} \tag{8.64}$$

Thus, if the phase coefficient of the transmission line mode lies within these limits, then leakage to the radiation field is implicated.

8.10 Impact of Material Properties on Propagation

This chapter has hitherto been concerned with the fundamental theoretical considerations of the spectral domain analysis of microstrip. The first part of this chapter introduced the basic equations and described the solution procedure. The second part focused on contour deformation, with a view to capturing the effects of energy loss due to surface waves and radiation.

The third and final part will now draw upon the above results to investigate an issue of great importance to this thesis: the effects of the dielectric properties of the covering material on the propagation characteristics of a microstrip sensor. In the process, an original and surprising result shall be presented; namely, that under certain conditions it is possible for the 'bound' dominant mode of microstrip to radiate. This conclusion directly contradicts the claims of several previous workers in this field, yet is entirely consistent with the reasoning of those same workers.

This chapter concludes with an examination of leaky dominant modes. This is a recently discovered phenomenon which has the potential to impact on measurement situations that may be encountered in practice, especially where the test material has a very high moisture content.

8.11 Propagation Regimes of the EH_0 Microstrip Mode

8.11.1 Bound Regime

Before investigating the propagation characteristics of microstrip covered by a material like cheese curd, it is instructive to look at the classic problem of air-covered microstrip. This will provide a simple illustration of the use of the techniques which were covered earlier in this chapter. It will also enable some comparisons to be made with published results, thereby verifying that the analysis software is functioning correctly.

The sensor of interest is an air-covered microstrip transmission line made from a substrate with dielectric constant $\varepsilon_1 = 10.2 - j0$ and thickness $d = 1.27$ mm. The centre conductor width is $2w = 0.97$ mm, and the source frequency is 4 GHz. Representing the x- and z-directed

components of the surface current by one basis function each, the following pair of equations is obtained:

$$< \widetilde{E}_x, \widetilde{J}_{x,1} > \;=\; 0 \tag{8.65}$$

$$< \widetilde{E}_z, \widetilde{J}_{z,1} > \;=\; 0 \tag{8.66}$$

Substituting the expressions for $\widetilde{E}_x$ and $\widetilde{E}_z$ from Equation 8.26 into the above inner products creates a homogeneous system of linear equations:

$$\begin{bmatrix} \int_{-\infty}^{+\infty} G_{11}\widetilde{J}_{x,1}\widetilde{J}^*_{z,1}\,d\alpha & \int_{-\infty}^{+\infty} G_{12}\widetilde{J}_{z,1}\widetilde{J}^*_{z,1}\,d\alpha \\ \int_{-\infty}^{+\infty} G_{21}\widetilde{J}_{x,1}\widetilde{J}^*_{x,1}\,d\alpha & \int_{-\infty}^{+\infty} G_{22}\widetilde{J}_{z,1}\widetilde{J}^*_{x,1}\,d\alpha \end{bmatrix} \begin{bmatrix} a_1 \\ b_1 \end{bmatrix} = \begin{bmatrix} 0 \\ 0 \end{bmatrix} \tag{8.67}$$

As discussed in Section 8.5, the integral expressions in the above matrix must be evaluated numerically. Due to the symmetrical nature of the integrands, it is only necessary to perform single-sided integrations. It then remains to find an appropriate upper limit of integration $\alpha_{\max}$. This is achieved by graphing the magnitude of each integrand against α and identifying the point where the magnitudes have all decayed away to negligible levels. The magnitudes of the integrands in Equation 8.67 are plotted in Figure 8.8, from which it is evident that $\alpha_{\max} = 70\,000$ is a suitable upper limit of integration. A step size of $\Delta\alpha = 35$ is chosen by trial and error, in order to provide sufficient point density to ensure that the numerical integrations are accurately evaluated.

An arbitrary starting estimate of $\beta = 223 - j10$ is chosen. In solving for β we must decide whether or not to deform the integration contour around the surface wave pole(s) (if any exist) and the branch point. Using the C++ program described in Section 7.4, it is found that only the TM_0 surface wave mode can be supported by the background structure at this frequency. Sweeping the loss factor of the covering medium over a wide range and solving for β at each point, the TM_0 surface wave pole and branch point follow the locus shown in Figure 8.9. It is clear that the migration path lies entirely in the fourth quadrant. The path never crosses the real axis, so it is not necessary to deform the contour of integration. Consequently, no leakage to the surface or space waves is expected, i.e. the microstrip mode is totally bound. In general this will *always* be the case for the EH_0 mode of air-covered microstrip with an isotropic substrate (Boukamp and Jansen, 1983).

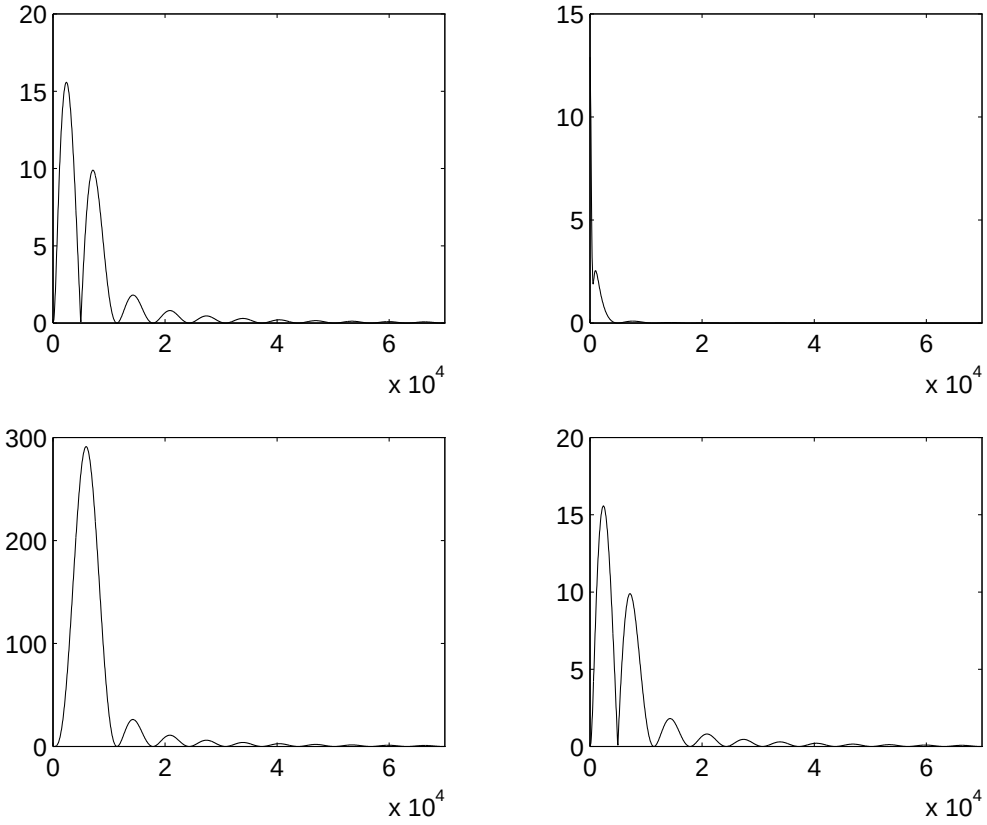

Figure 8.8: Plot of magnitudes of integrands as a function of α for microstrip having $\varepsilon_1 = 10.2$, $\varepsilon_2 = 1$, $d = 1.27$ mm, $2w = 0.97$ mm and $f = 4$ GHz.

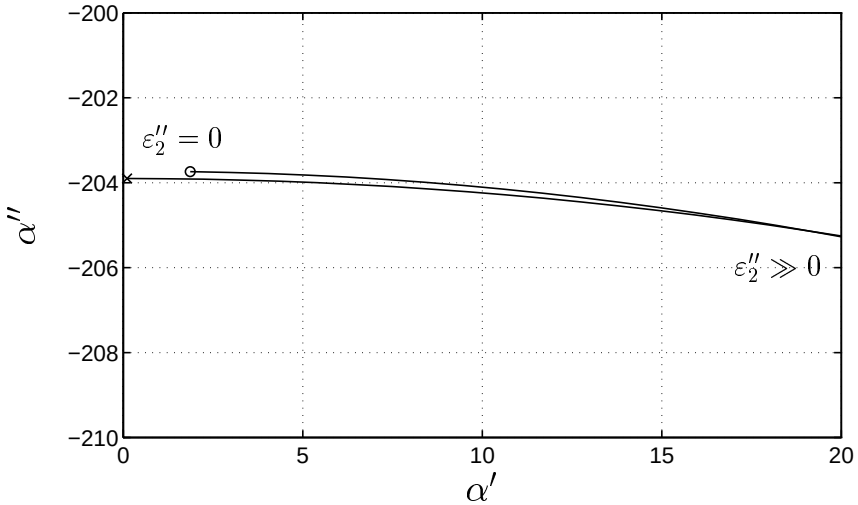

Figure 8.9: Path of migration of TM_0 surface wave pole and branch point for air-covered microstrip as loss of covering medium varies. Circle and cross denote pole and branch point respectively when $\varepsilon_2'' = 0$.

For this example the final value of β is $220.46 - j0$. This was returned by the program after 5 iterations, during which the determinant of the coefficient matrix decreased from 10^9 to 10^{-2}. The time taken to calculate this value was 83 seconds on a Cyrix PR200 desktop PC.

To verify that the analysis software functioned correctly, the output was compared with published results from the literature. The details of the simulation are summarised in Table 8.1. Computed and published results are plotted together in Figure 8.10, with good agreement.

Table 8.1: Details of microstrip simulation used to verify correct operation of full-wave software.

ε_1	ε_2	d (mm)	$2w$ (mm)	Reference Publication
11.7	1	3.17	3.0432	Denlinger (1971)

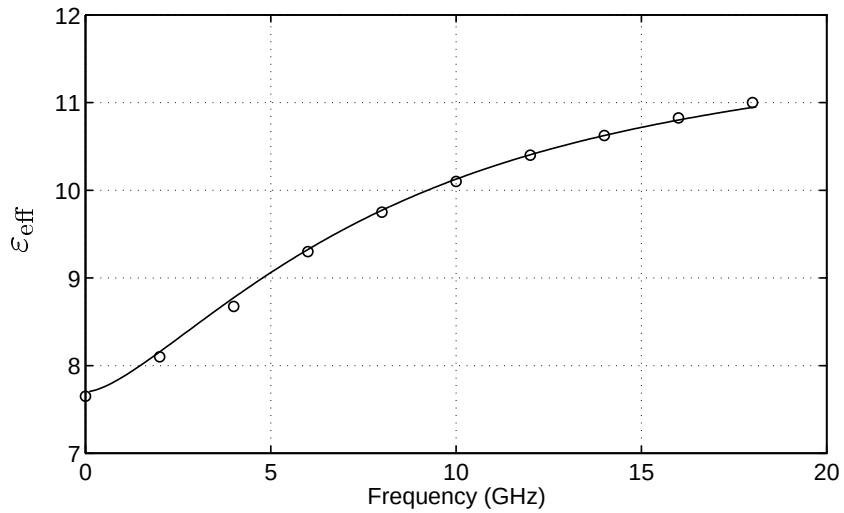

Figure 8.10: Comparison of microstrip ε_{eff} as predicted by full-wave software with results published by Denlinger (1971). (Published data denoted by small circles.)

8.11.2 Surface Wave Regime

To determine whether surface wave leakage occurs on microstrip covered by a high-permittivity superstrate, it is first necessary to establish whether or not any modes can be supported by the background structure.

While it is well known that the TM_0 mode can propagate down to DC on air-covered microstrip, it was shown in Chapter 7 that with a high-permittivity covering medium present, the TM_0 mode has a nonzero cutoff frequency which varies inversely with the loss factor of the covering medium.

Consider a microstrip transmission line with $\varepsilon_1 = 10.2 - j0$, $\varepsilon_2' = 15$, $d = 1.27$ mm and $2w = 0.97$ mm. At a frequency of 4 GHz, the locus of the TM_0 surface wave pole in the complex plane as the loss factor of the covering material varies is as shown in Figure 8.11. It is evident that the pole approaches the real axis as the loss factor decreases, however the TM_0 mode enters its cutoff region before it can cross the real axis. This implies that no leakage into the TM_0 surface wave mode occurs at this frequency.

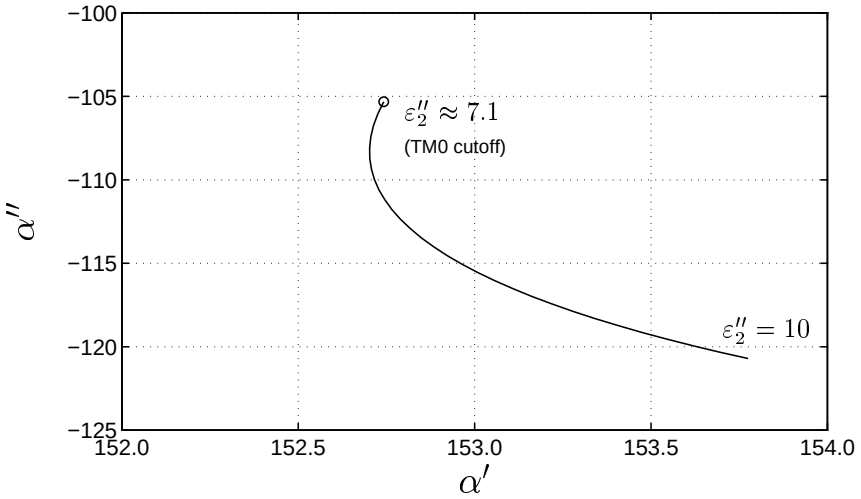

Figure 8.11: Migration of TM_0 surface wave pole with respect to superstrate loss for microstrip covered by a high-permittivity material. ($\varepsilon_1 = 10.2 - j0$, $\varepsilon_2' = 15$, $d = 1.27$ mm, $2w = 0.97$ mm, $f = 4$ GHz. Circle denotes pole location where TM_0 mode is cutoff.)

Setting the permittivity of the covering material to $\varepsilon_2' = 15 - j7$ and calculating the propagation coefficient over the frequency range 0.1–54 GHz, the results in Figure 8.12 are obtained. The migration paths of the TM_0 surface wave pole and branch point as a function of frequency are plotted in Figure 8.13. Both points remain in the fourth quadrant over the entire frequency range. At low frequencies the TM_0 pole approaches the real axis, but becomes cutoff before it can cross it. Consequently, no surface wave leakage is expected to occur.

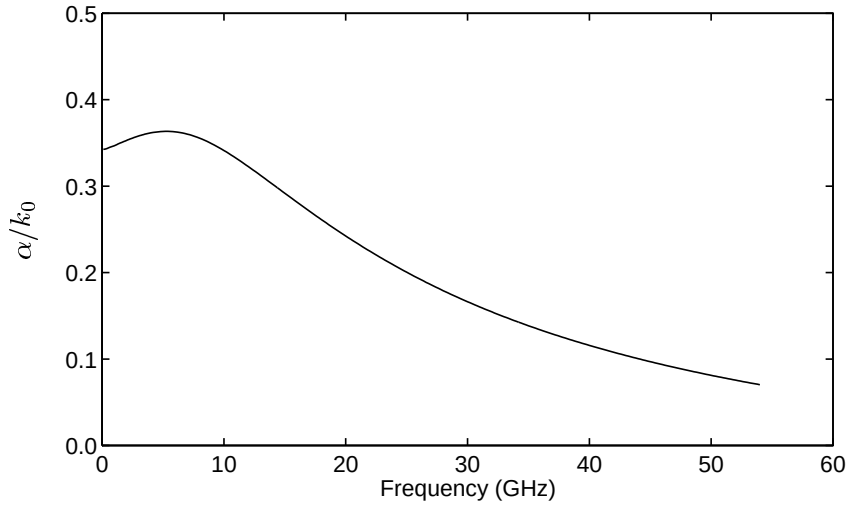

(a) Normalised attenuation coefficient.

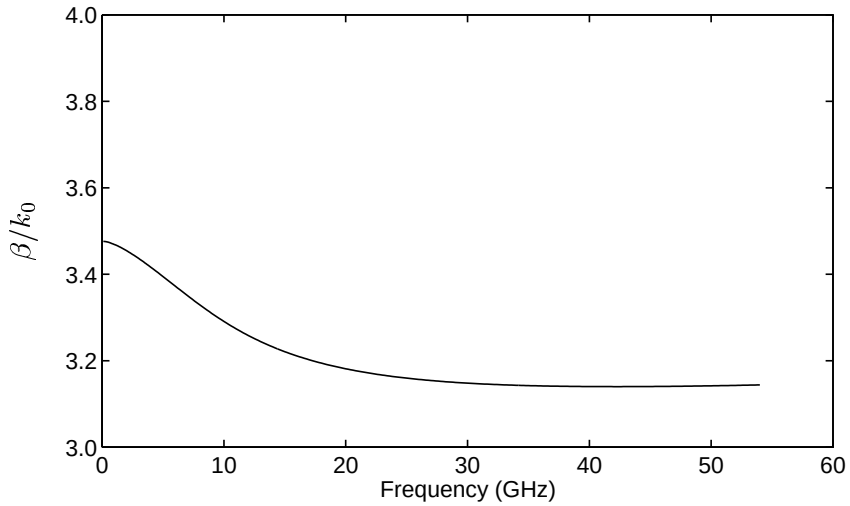

(b) Normalised phase coefficient.

Figure 8.12: Normalised attenuation and phase coefficients of microstrip covered by a lossy, high-permittivity material. ($\varepsilon_1 = 10.2 - j0$, $\varepsilon_2 = 15 - j7$, $d = 1.27$ mm, $2w = 0.97$ mm.)

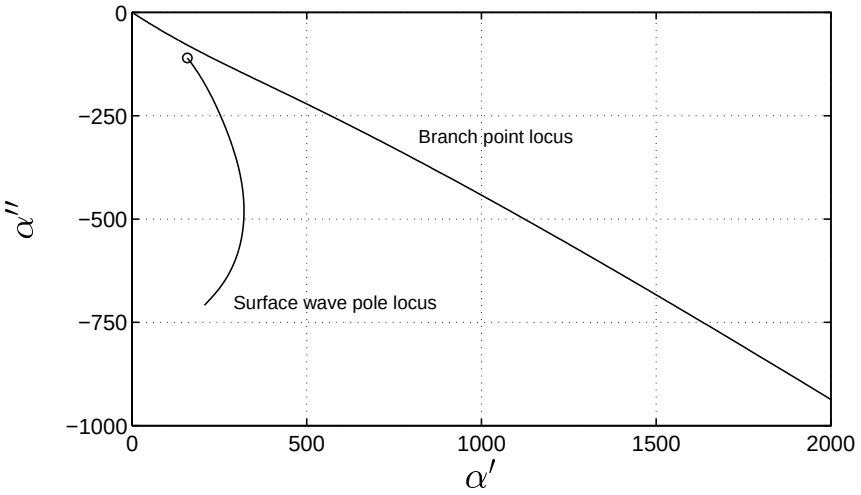

Figure 8.13: Migration of TM_0 surface wave pole and branch point with respect to frequency for microstrip covered by a lossy, high-permittivity material. ($\varepsilon_1 = 10.2 - j0$, $\varepsilon_2 = 15 - j7$, $d = 1.27$ mm, $2w = 0.97$ mm. Circle denotes pole location where TM_0 mode is cutoff.)

In the course of this project it was found that surface wave leakage never occurred for microstrip covered by a lossy, high-permittivity medium. The reason for this was that a relatively high level of loss was required in most cases for surface waves to be able to propagate; however, this same high loss caused the surface wave poles to remain deep in the fourth quadrant of the complex plane. Thus, while it may have been possible in some cases for one or more surface wave modes to propagate, the EH_0 microstrip mode was never able to couple to these modes.

8.11.3 Radiation Regime

There is a common claim in the literature that the EH_0 mode of microstrip never leaks to the surface or space waves. For example, Boukamp and Jansen (1983) have stated categorically that ‘ ... the fundamental mode [of microstrip] never radiates because its phase velocity is always less than that of the slowest surface wave mode.’

A host of subsequent authors have based their own work on the reasoning of Boukamp and Jansen. However, several counterexamples have since been published which show the above statement to be false in certain cases. For instance, Shigesawa et al. (1995) have shown that the EH_0 mode can become leaky if the substrate is anisotropic.

Of considerably greater relevance to this project is the work of Das and Pozar (1991), who have performed a spectral domain analysis of a thin metal strip sandwiched between two lossless isotropic half-spaces of infinite extent. The results of this analysis have shown that the strip always leaks energy into the medium with the larger dielectric constant. This is highly pertinent to the analysis of microstrip sensors, and is explored in the following sections.

Not discussed by Das and Pozar are the effects of dielectric loss on leakage. This is also analysed below, and is believed to be an original result.

Case 1: Lossless High-Permittivity Superstrate

The most dramatic example of leakage from the EH_0 mode into the radiation field occurs from microstrip covered by a lossless half-space with a dielectric constant greater than that of the substrate. The transmission line under consideration is as before, i.e. $\varepsilon_1 = 10.2 - j0$, $d = 1.27$ mm, $2w = 0.97$ mm, $f = 4$ GHz. The permittivity of the covering material is $\varepsilon_2 = 15 - j0$.

As before, we start by making the covering material highly lossy, and then decreasing the loss factor to zero. The resulting branch point locus is shown in Figure 8.14. It is clear that the branch point crosses the real axis, requiring the contour of integration to be deformed around the branch point to preserve the continuity of the physical situation. No surface wave poles are shown on Figure 8.14, as all modes are cutoff in this example.

A slight discontinuity can be seen where the branch point locus crosses the real axis. This is an artefact of the buffer zone which was created around all poles and branch points, to prevent the contour of integration from getting too close to these points. The motivation for this practice stemmed from the fact that all contour integrals had to be evaluated numerically, and were therefore sensitive to the finite accuracy of the computer. In the event that the contour of integration passed too close to a singular point like a surface wave pole, there was a risk that the large magnitudes of the integrands in this part of the complex plane could obliterate the contributions from other parts of the integration. Consequently, a limit was placed on how close the contour could approach such points. However, if the pole and branch points moved into the fourth quadrant of the complex plane, the contour of integration was performed along the real axis without any consideration to the proximity of the pole and branch points to the

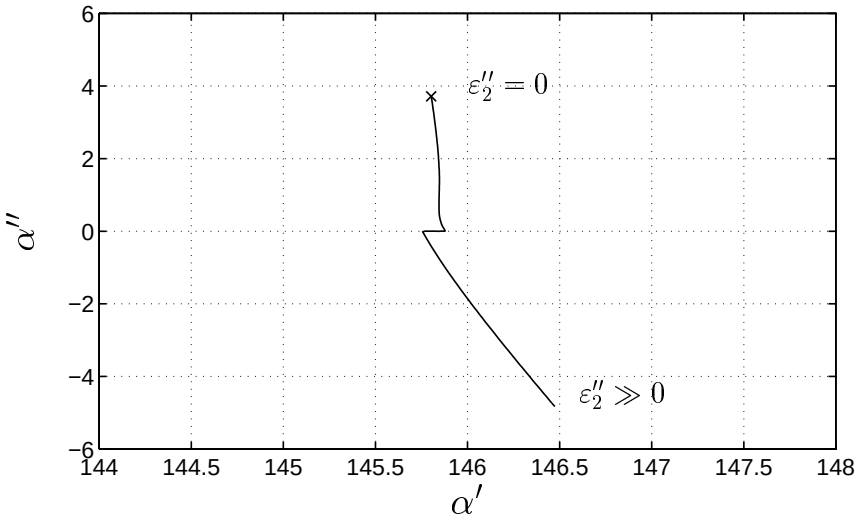

Figure 8.14: Migration of branch point with respect to superstrate loss for microstrip covered by a material with a dielectric constant greater than that of the substrate. ($\varepsilon_1 = 10.2 - j0$, $\varepsilon_2' = 15$, $d = 1.27$ mm, $2w = 0.97$ mm, $f = 4$ GHz. Cross denotes branch point location when $\varepsilon_2'' = 0$.)

contour. The result is a discontinuity like the one in Figure 8.14. It could be argued that this is a potential source of error for situations where the poles and/or branch point lie just below the real axis. However, it was decided that the risk did of this happening was not high enough to justify the necessary programming effort, so no attempt was made to rectify this quirk.

Plots of the normalised attenuation and phase coefficients of this mode are depicted in Figure 8.15. The dashed curve labelled $\beta_{\max}$ on Figure 8.15(b) is a plot of Equation 8.63, which is the upper boundary of β for radiation leakage to occur. The lower boundary—given by Equation 8.64—is not shown, as it is equal to zero at all frequencies due to the fact that $\varepsilon_2'' = k_2'' = 0$. Therefore it is clear that in this example the EH_0 mode radiates at *all* frequencies above DC. This is consistent with the results of Das and Pozar (1991).

Case 2: High-Permittivity Superstrate with Moderate Loss

The presence of a small amount of loss in the covering medium can cause the EH_0 mode of microstrip to radiate at some frequencies, and remain bound at others. This is demonstrated by the following example, and is believed to be an original result. A paper on this topic is currently being prepared for submission to *IEEE Microwave and Guided Wave Letters*.

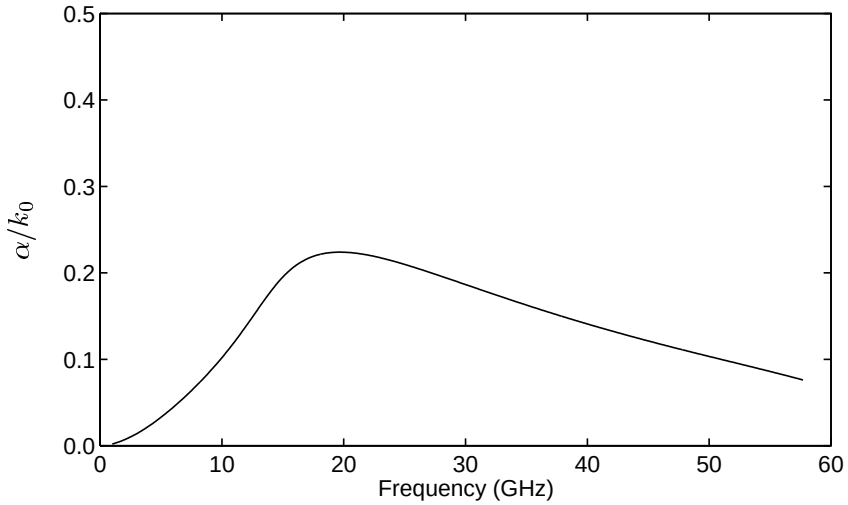

(a) Normalised attenuation coefficient.

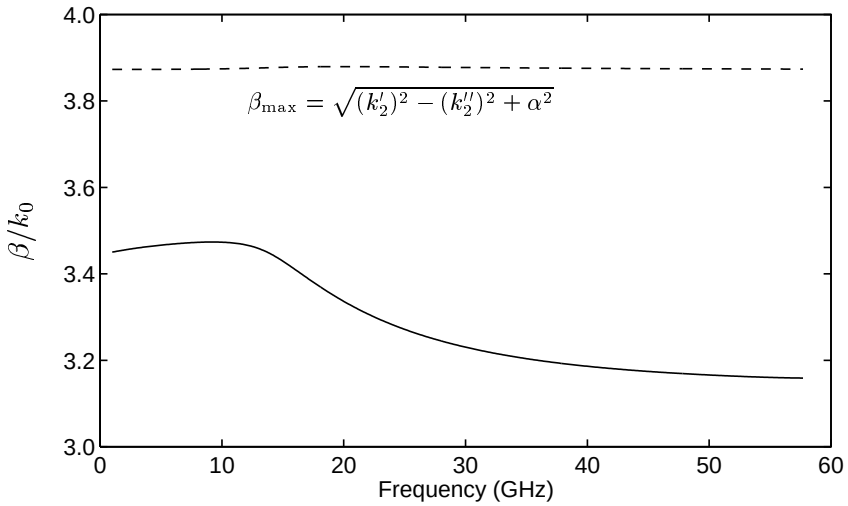

(b) Normalised phase coefficient. $\beta_{\max}$ is the upper bound of β for radiation leakage to occur.

Figure 8.15: Normalised attenuation and phase coefficients of microstrip covered by a lossless, high-permittivity material. ($\varepsilon_1 = 10.2 - j0$, $\varepsilon_2 = 15 - j0$, $d = 1.27$ mm, $2w = 0.97$ mm.)

Using the same parameters as Case 1, but setting $\varepsilon_2'' = 1$, the curves in Figure 8.16 are obtained. This time both the upper and lower bounds of β are plotted on Figure 8.16(b). It is evident that the EH_0 mode radiates between 9.5 GHz and 33.5 GHz, and is bound elsewhere.

No surface wave leakage occurs in this example, as the first surface wave mode is cutoff below 45 GHz and lies in the fourth quadrant of the complex plane above 45 GHz.

Case 3: High-Permittivity Superstrate with High Loss

The final case to explore is microstrip covered by a high-permittivity medium with a large loss factor. Repeating the previous example with a superstrate permittivity of $\varepsilon_2 = 15 - j2$, the graphs in Figure 8.17 are obtained. Under these circumstances the EH_0 mode is bound at all frequencies. The cutoff frequency of the TM_0 surface wave mode is 28.36 GHz. Above this frequency the pole due to the TM_0 mode resides entirely in the fourth quadrant of the complex plane, implying that no surface wave leakage occurs.

The branch point loci associated with Cases 1, 2 and 3 are plotted in Figure 8.18. As expected, the branch point for the lossless case (i.e. $\varepsilon_2'' = 0$) remains in the first quadrant, implying radiation leakage at all frequencies. For the case where $\varepsilon_2'' = 1$, the branch point migrates from the fourth to the first quadrants and then back to the fourth again, indicating that radiation leakage occurs over a limited bandwidth. The branch point locus for the high-loss case (i.e. $\varepsilon_2'' = 2$) lies entirely in the fourth quadrant, implying that the mode is bound at all frequencies.

8.12 Leaky Dominant Microstrip Modes

A surprising development which has been reported in the literature in recent years is the discovery of a number of new dominant microstrip modes. Commonly referred to as *leaky dominant modes*, these modes propagate in addition to, and independently of, the conventional EH_0 mode, and are characterised by their tendency to leak power into surface wave modes and/or the radiation field (Nghiem et al., 1996).

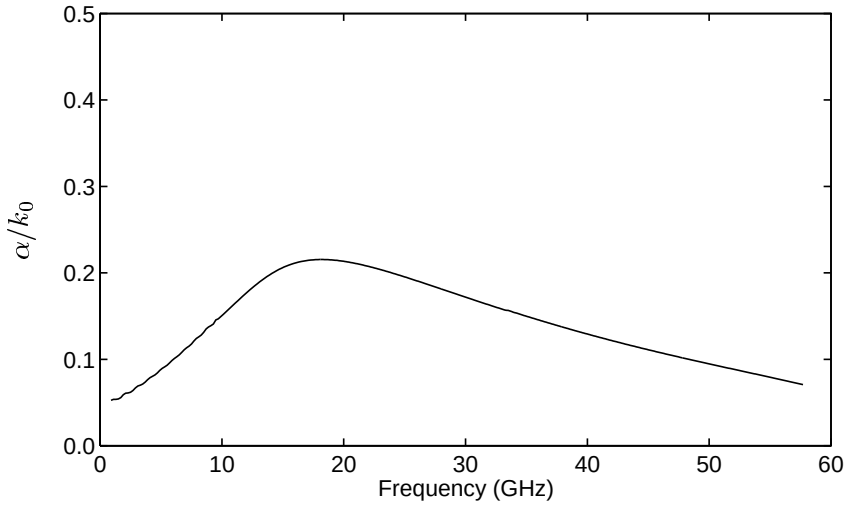

(a) Normalised attenuation coefficient.

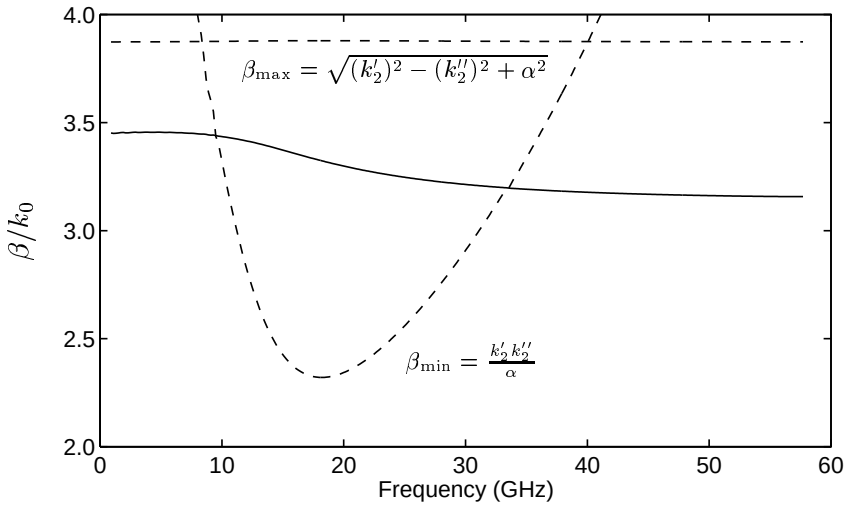

(b) Normalised phase coefficient. $\beta_{\max}$ and $\beta_{\min}$ are the upper and lower bounds of β respectively for radiation leakage to occur.

Figure 8.16: Normalised attenuation and phase coefficients of microstrip covered by a high-permittivity material with moderate loss. ($\varepsilon_1 = 10.2 - j0$, $\varepsilon_2 = 15 - j1$, $d = 1.27$ mm, $2w = 0.97$ mm.)

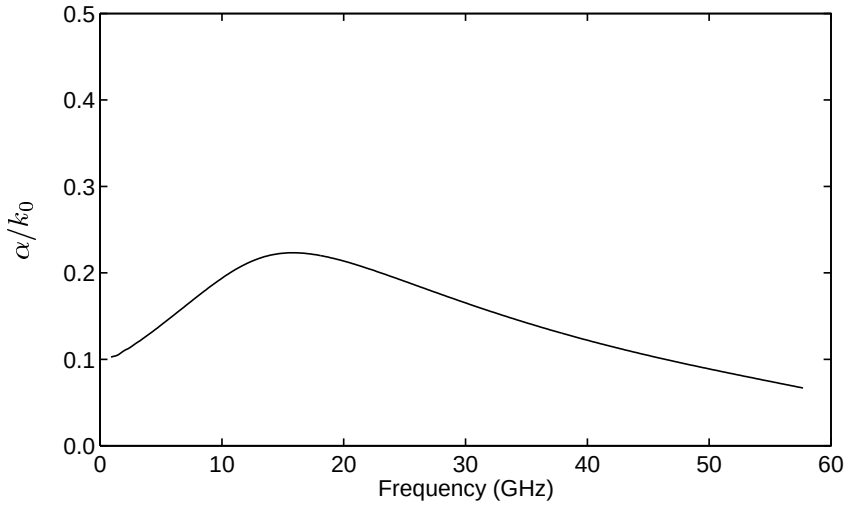

(a) Normalised attenuation coefficient.

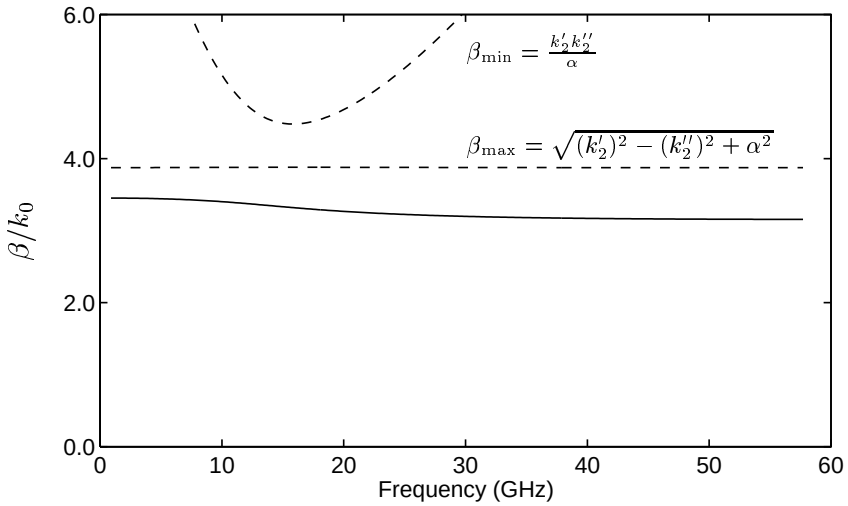

(b) Normalised phase coefficient. $\beta_{\max}$ and $\beta_{\min}$ are the upper and lower bounds of β respectively for radiation leakage to occur.

Figure 8.17: Normalised attenuation and phase coefficients of microstrip covered by a high-permittivity material with high loss. ($\varepsilon_1 = 10.2 - j0$, $\varepsilon_2 = 15 - j2$, $d = 1.27$ mm, $2w = 0.97$ mm.)

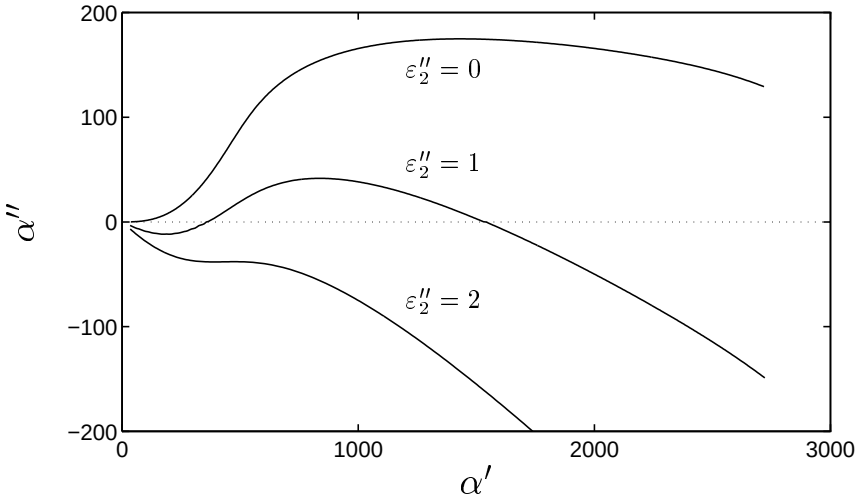

Figure 8.18: Plot of branch point locus for different values of superstrate loss as frequency varies from DC to 60 GHz. ($\varepsilon_1 = 10.2 - j0,\ \varepsilon_2' = 15,\ d = 1.27$ mm, $2w = 0.97$ mm.)

In contrast to the higher order modes of microstrip such as the EH_1, EH_2 and EH_3 modes, leaky dominant modes have current distributions that are very similar to the conventional EH_0 mode. The E-fields of these modes are likewise very similar close to the dielectric interface, becoming less so at large distances from the transmission line. As such, the same set of basis functions that would be used to analyse the conventional dominant mode can be used for leaky dominant modes. Furthermore, because both modes have very similar current distributions and field patterns, both modes are likely to be strongly excited by the same type of microstrip launcher.

A diverse range of structures are capable of supporting these modes. Examples from the literature include conductor-backed coplanar strips (Tsuji and Shigesawa, 1993), microstrip on a lossy, anisotropic substrate (Shigesawa et al., 1993), stripline with an air gap (Nghiem et al., 1993; Nghiem et al., 1995), slotline (Zehentner et al., 1998), and microstrip on an isotropic substrate (Nghiem et al., 1996). As such, leaky dominant modes appear to be a phenomenon applicable to all planar transmission lines.

A significant difference between leaky dominant modes and the conventional EH_0 mode is that the former may not necessarily propagate down to DC. Instead, each mode can have a cutoff frequency whose value depends upon the geometry of the line and the dielectric properties of the covering medium. For air-covered structures there is often a band of frequencies between

the cutoff frequency of the leaky mode and the frequency where the leaky mode becomes physically meaningful. This band of frequencies is commonly referred to as the *spectral gap*, and can be regarded as a transitional region where the leaky EH_0 mode gradually asserts itself (Shigesawa et al., 1993).

For this project, the leaky dominant mode(s) on each microstrip sensor were located by simply running the analysis software with different starting estimates until a new solution was found. In deciding whether or not to deform the integration contour around poles and branch points, the same rules were applied as for the conventional EH_0 mode. This approach was somewhat different from that presented by Nghiem et al. (1996), who used a variety of different integration contours as a means of locating different dominant mode solutions, as depicted in Figure 8.19. However, it is doubtful whether the approach of Nghiem et al. is consistent with

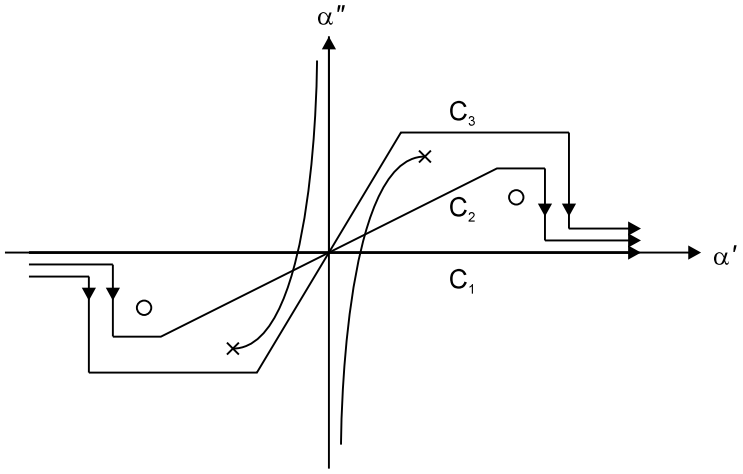

Figure 8.19: Paths of integration yielding alternative dominant microstrip modes.

the reasoning of authors such as Boukamp and Jansen (1983) and Bagby et al. (1993). After all, simply choosing arbitrarily to bypass some points but not others does not necessarily mean that the end result will be a new microstrip mode—more likely, it will mean that a physically meaningless answer has been produced. For this project, the deformation of the integration contour was always performed on the basis of pole and branch point migration, as described in Section 8.9. This ensured that all modal solutions were obtained in a consistent and physically meaningful fashion.

The problem still remains, however, as to how to identify whether a leaky dominant mode is a physical propagating mode, or merely a mathematical anomaly. Numerous papers on this subject have appeared in the literature in recent years. However, most authors have concentrated on leaky modes which couple only to the TM_0 surface wave mode; no work appears to have been carried out on leaky modes that couple to the space wave. This is clearly a major deficiency in the state of the art, especially where this project is concerned, given that radiation leakage is a real possibility. A detailed analysis of this subject is beyond the scope of this project, but would be an excellent area for future work.

Before leaving the topic of leaky dominant modes, a brief example is in order to illustrate this phenomenon in the context of microstrip covered by a high-permittivity superstrate. Due to the lack of prior work in the literature on this subject, the following discussion and example are—to the best of the author's knowledge—original work.

The sensor under consideration is the microstrip transmission line from Section 8.11.3. The superstrate permittivity is higher than previous examples, having a value of $\varepsilon_2 = 30 - j0$. Using a variety of starting estimates, two dominant mode solutions are found. These are plotted in Figure 8.20.

From the plot of α/k_0 in Figure 8.20, it is clear that both the conventional and leaky EH_0 modes on this transmission line experience considerable attenuation. The conventional mode radiates from DC upwards, while the leaky mode radiates at all frequencies down to 0.8 GHz, where it becomes cutoff. No surface waves can be supported by this structure, so the attenuation on the line is due entirely to radiation.

It is also interesting to examine how variations in material parameters affect the propagation characteristics of the leaky mode in the above example. For example, if the loss factor of the superstrate is increased beyond $\varepsilon_2'' = 19.7$ at a frequency of 2 GHz, the leaky EH_0 mode enters its cutoff region and no longer propagates. Similarly, if the real part of the superstrate permittivity is decreased below $\varepsilon_2' = 20.8$ at 2 GHz, the leaky EH_0 mode is again at cutoff.

If this example appears somewhat contrived—given that ε_2 has been deliberately chosen to produce more than one EH_0 mode solution—then consider the real-life example in Figure 8.21. This is a simulation of the same sensor immersed in distilled water. A leaky EH_0 mode solution

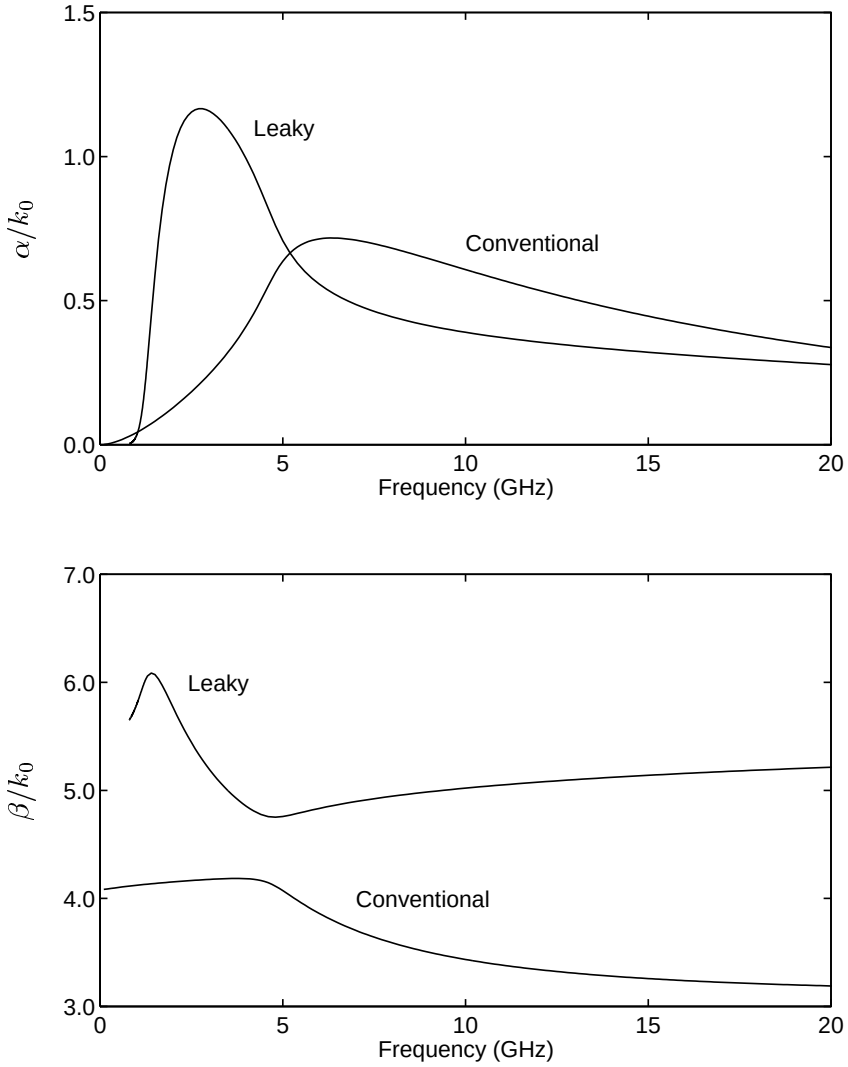

Figure 8.20: Normalised attenuation and phase coefficients of conventional and leaky EH_0 modes of microstrip covered by a lossless, high-permittivity material. ($\varepsilon_1 = 10.2 - j0$, $\varepsilon_2 = 30 - j0$, $d = 1.27$ mm, $2w = 0.97$ mm.)

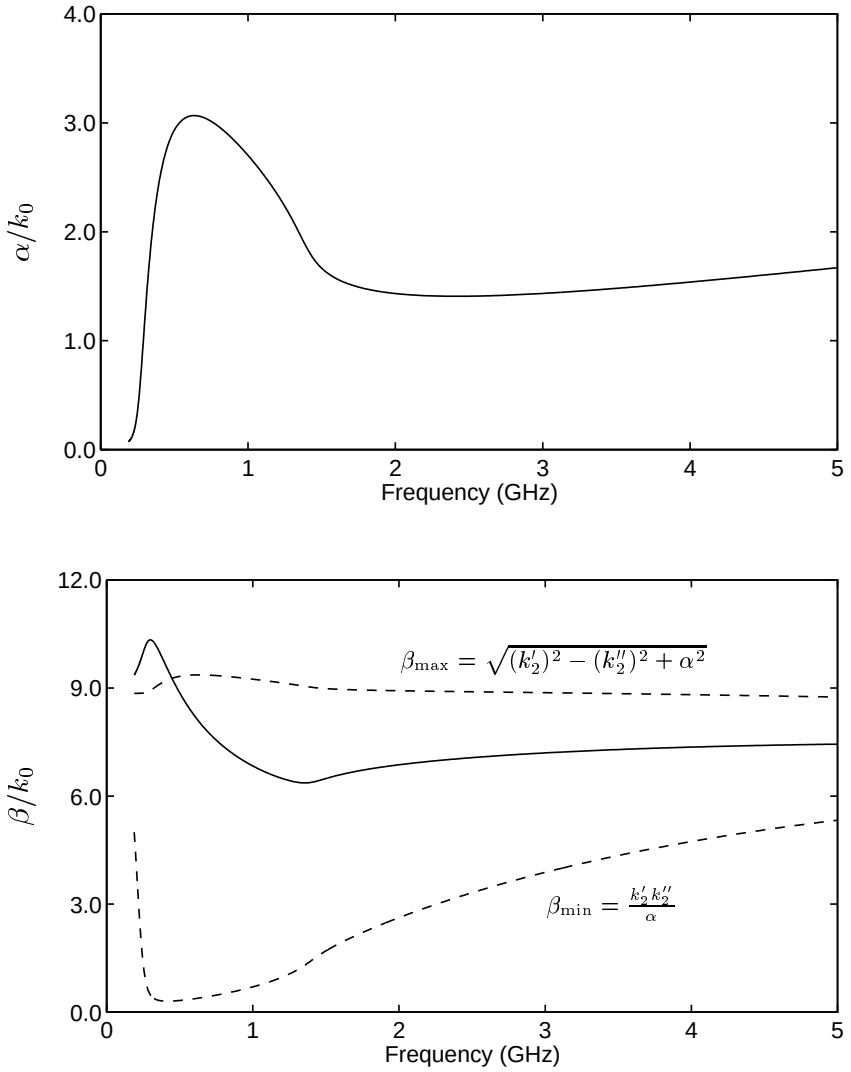

Figure 8.21: Normalised attenuation and phase coefficients of leaky EH_0 mode of microstrip covered by distilled water. ($\varepsilon_1 = 10.2 - j0$, $d = 1.27$ mm, $2w = 0.97$ mm, $T_{\text{water}} = 25°$C.)

exists above 0.19 GHz, with radiation leakage implicated above 0.45 GHz. That is not to say that this solution represents a *physical* mode across the entire frequency band. Rather, it simply demonstrates that multiple EH_0 solutions can arise when making measurements on real-life measurands.

Clearly the conditions for the propagation of leaky dominant microstrip modes on microstrip depend upon a number of parameters. Very little has been published in the literature on this topic, rendering it a suitable area for future research.

8.13 Conclusion

This chapter has described the main stages in the development of a full-wave spectral domain model of a microstrip sensor covered by a lossy, high-permittivity material. This has been presented in three major parts.

The first part of this chapter introduced the full-wave spectral domain method. Topics included the derivation of the Fourier transformed field equations, choice of basis functions, and the use of Galerkin's method to solve for the propagation coefficient of the EH_0 microstrip mode.

The second part of this chapter was concerned with the deformation of the integration contour in the complex plane. This was shown to be dependent upon several factors, including the locations of surface wave poles and branch points in the complex plane, and the choice of branch cut. For this project the branch cut suggested by Grimm and Nyquist (1993) was the preferred option, as it resulted in a simple path of integration, and ensured that all integrands remained analytic. Also discussed in the second part of this chapter was the migration of surface wave poles and branch points through the complex plane as the loss factor of the superstrate varied. This is one of the prime considerations in deciding whether or not the integration contour should bypass these points. To that end, a surface wave leakage condition and a radiation leakage condition have been derived. Each consists of two equations, which provide an upper and lower bound for the phase coefficient of the EH_0 mode. If the phase coefficient is within these limits, energy loss to the corresponding leakage mechanism is expected.

The third and final part of this chapter has explored the relationship between the propagation characteristics of a microstrip sensor, and the dielectric properties of the covering medium. In the process some significant and original results have been obtained.

Firstly, it has been shown that if the dielectric constant of the covering medium is greater than that of the substrate, then leakage to surface wave modes is unlikely to occur. This is due to the fact that such a structure can only support surface wave modes if the superstrate is lossy; however, this same loss acts to prevent the EH_0 mode from coupling to the surface wave modes by keeping the corresponding poles in the fourth quadrant of the complex plane.

Secondly, it has been shown that the presence of a high-permittivity covering medium can cause the EH_0 microstrip to leak energy to the radiation field. This result contradicts the statements of several previous workers in this field, but is nevertheless entirely consistent with their own reasoning. It has further been shown that as the loss factor of the superstrate increases, the EH_0 mode radiates over a smaller frequency range. If the superstrate loss increases past a certain point, radiation leakage is suppressed completely, and the attenuation on the line is due entirely to dielectric loss.

Finally, it has been shown that under certain conditions a second EH_0 mode can propagate in addition to the conventional EH_0 mode. This so-called leaky dominant mode has a similar current distribution and field pattern to the conventional mode, and loses significant energy to the radiation field. Unlike the conventional mode, however, the leaky EH_0 mode cannot propagate down to DC; rather, it experiences a cutoff frequency which is dependent upon the dielectric properties of the covering material. Another unique feature of this type of mode is that it does not necessarily become a physical mode immediately above cutoff. Instead, it must pass through a transitional region known as the spectral gap, wherein it gradually asserts itself as a physically meaningful propagating mode.

This chapter has identified three topics which are suitable areas for future research.

Firstly, the conditions necessary for the propagation of higher-order modes on microstrip covered by a lossy, high-permittivity material like cheese curd have yet to be established. Traditionally these modes only propagate at high frequencies, or when the ratio of strip width to substrate thickness is large. However, whether this remains true with a lossy, non-air half-space above the transmission line is unknown.

Secondly, more work is needed on the subject of leaky dominant modes which lose energy to radiation. Previous authors have concentrated mainly on those modes which leak to the TM_0 surface wave mode, but leakage to the space wave has never been thoroughly investigated. A particular requirement that was identified in this project was a ‘physicality condition’; that is, a means of determining when a leaky dominant mode ceases to be merely a spurious mathematical solution, and starts to become a physically propagating mode.

Finally, a more thorough investigation of the different propagation regimes of leaky dominant modes on microstrip sensors is warranted. For example, it is not yet known whether such modes can leak to surface waves. Similarly, it is not clear precisely how the cutoff frequencies of each leaky mode are affected by changes in the dielectric properties of the superstrate.

Chapter 9

Simulation of Sensor Scattering Parameters

9.1 Introduction

So far the main focus of Part II of this thesis has been the determination of the propagation characteristics of microstrip. The results of this work have been shown to be significant in their own right, however they are not sufficient to achieve the ultimate objective: the simulation of the scattering parameters of the entire sensor.

The analysis techniques presented in Chapters 6–8 have assumed that the transmission line under consideration is infinite in extent. That is, the substrate was assumed to be infinitely wide, the source of the signal on the line was located at $z = -\infty$, the line was terminated at $z = +\infty$, and the thickness of the covering dielectric was infinite. However, in any practical implementation of a microstrip sensor these parameters will all be finite. Consequently the properties of the sensor will deviate from the ideal case.

Another practical consideration which has been neglected to this point is the means of coupling energy onto the transmission line. The type and number of modes which are excited on the microstrip line are dependent on the launching structure. Problems which may be encountered in this area include impedance mismatch between the launcher and the microstrip sensor, and

variation in the properties of the launcher depending on the dielectric behaviour of the covering medium.

Finally, there is the more immediate problem of how to determine the characteristic impedance of the microstrip sensor itself. Any transmission line representation of the sensor will require this parameter to be defined and calculated at every frequency of interest.

This chapter will address the above issues. The first section describes how the characteristic impedance of the sensor was calculated. This is followed by an analysis of the launching structure which was used. The last section of this chapter puts the results of the first two sections together in order to model the performance of the whole sensor.

9.2 Calculation of Microstrip Characteristic Impedance

A crucial step in modelling microstrip using conventional transmission line formulas is to define the characteristic impedance Z_0 of the line. However, this is problematic due to the fact that the mode of propagation on microstrip is not TEM. As such, there is no unambiguous definition of the voltage or current on the line (Collin, 1991, pp. 316–319).

9.2.1 Definition of Microstrip Characteristic Impedance

Numerous definitions of microstrip characteristic impedance have been proposed in the literature. Many express Z_0 in terms of the complex power on the line and the current on the strip (Denlinger, 1971). Unfortunately, these approaches require power to be determined by integrating the z-component of the Poynting vector $\boldsymbol{S} = \boldsymbol{E} \times \boldsymbol{H}$ over the cross-section of the transmission line (Denlinger, 1971; Lin and Sheen, 1997). Computationally, this is a very expensive exercise, especially when used with the spectral domain method. This is due to the fact that $\boldsymbol{E}$ and $\boldsymbol{H}$ must be obtained by inverse Fourier transform at every point in the integral.

For this project a more economical approach was chosen in determining microstrip Z_0. Using a method similar to that described by Collin (1991, pp. 316–319), Z_0 is expressed in terms of the voltage and current on the line. As mentioned above, these parameters have no unique

definitions. However by assuming that the transverse components of the electric field are much greater than the longitudinal component, and that the longitudinal strip current is much greater than the transverse component, the following definition is valid to a good approximation:

$$\begin{aligned} Z_0 &= \frac{V}{I_{\mathrm{TOT}}} \\ &= \frac{-\int_0^d E_y \, dy}{I_{\mathrm{TOT}}} \end{aligned} \tag{9.1}$$

where Z_0 is the characteristic impedance of the line, V is the voltage on the strip conductor, E_y is the y-directed component of the electric field evaluated at $x = 0$ (i.e. the centre of the strip conductor), d is the substrate thickness, and I_{TOT} is the total z-directed current on the strip.

9.2.2 Calculation of Voltage on Strip Conductor

The evaluation of the integral in the numerator of Equation 9.1 was performed numerically, using Simpson's $\frac{1}{3}$ Rule over 20 intervals. This was found to be more than adequate for the microstrip transmission lines under consideration. In order to calculate E_y at each point in the substrate, it was necessary to perform an inverse Fourier transform of $\widetilde{E}_y$:

$$E_y = \int_{-\infty}^{\infty} \widetilde{E}_y e^{-j\alpha y} \, dx \tag{9.2}$$

where the contour chosen for α is the same as that used in finding the propagation coefficient β. In practice the limits of integration were set to suitably large values which were selected by inspecting the integrand for a range of values of α. $\widetilde{E}_y$ was defined using the following expression from Mirshekar-Syahkal (1990, p. 31):

$$\widetilde{E}_y = -j(\gamma_1 \beta A + j\omega\mu_0 \alpha C)\cosh(\gamma_1 y) \qquad (e^{-j\beta z} \text{ assumed}) \tag{9.3}$$

where A and C are constants obtained from the spectral domain analysis of the structure.

9.2.3 Calculation of Total Strip Current

The total z-directed current on the strip was determined by integrating Equation 8.35 across the strip conductor:

$$I_{\mathrm{TOT}} = \int_{-w}^{w} \sum_{q=1}^{Q} b_q J_{z,q}(x)\, dx \tag{9.4}$$

Both numerical and analytical approaches were used in evaluating the integral in Equation 9.4, depending on the type of basis functions which had been chosen. For most families of basis functions it was more convenient to integrate numerically, using the Trapezoidal Rule over 1000 intervals. While computationally demanding, this method involved a minimum of analytical preprocessing. However, problems did arise with this technique due to the edge singularity, which returned a longitudinal current density of infinity at $\pm w$. To avoid this problem, the limits of integration were set to $\pm 0.9999w$, thereby capturing the edge condition (at least, partially) without causing the computer to overflow.

For the basis functions suggested by Jansen (1978) it was preferable to perform the integral analytically. As discussed in Chapters 6 and 8, this family of functions is defined as follows:

$$J_{z,1}(x) = \frac{1}{\sqrt{1-\left(\frac{x}{w}\right)^2}} \tag{9.5}$$

$$J_{z,q}(x) = \frac{\cos\left[(q-1)\pi\left(\frac{x}{w}\right)\right] - J_0\left[(q-1)\pi\right]}{\sqrt{1-\left(\frac{x}{w}\right)^2}} \qquad q = 2, 3, \ldots, Q \tag{9.6}$$

Jansen's basis functions have an attractive property whereby

$$\int_{-w}^{w} J_{z,q}(x)\, dx = \begin{cases} w\pi & \text{if } q = 1 \\ 0 & \text{otherwise} \end{cases} \tag{9.7}$$

This result can only be obtained via a somewhat complicated by-parts integration, however it provides a significant computational advantage over numerical integration, especially in view of the fact that the Bessel function in Equation 9.6 has been eliminated from the expres-

sion. Furthermore, the contribution of the edge singularity is captured in its entirety, providing greater accuracy than the numerical approach.

9.2.4 Verification of Characteristic Impedance Formulation

The validity of the characteristic impedance calculations was determined by comparison with published data from the literature. To select an example, consider an open, air-covered microstrip transmission line comprised of a lossless substrate with a dielectric constant of $\varepsilon_1 = 10.2$. Let the thickness of the substrate equal 1.27 mm and the width of the strip conductor equal 0.97 mm. The stimulus frequency is 4 GHz.

Using the spectral domain method with one basis function for the z-directed current and one basis function for the x-directed current, the propagation coefficient is found to be $\beta = 220.46$ rad/m. The vector of coefficients giving a_1 and b_1 indicates that the longitudinal current is larger than the transverse current by a factor of approximately 7300. Hence, the conditions described in Section 9.2.1 have been met, and Equation 9.1 can be used to calculate Z_0.

Substituting the above results into Equation 9.1 gives $Z_0 = 56.56\ \Omega$, which is within 0.2% of the result quoted by Bahl and Trivedi (1977).

Published data for the Z_0 of microstrip covered by a non-air medium is somewhat difficult to come by. While previous researchers have investigated microstrip contact sensors, most work to date has involved microstrip transmission lines covered by a thin protective layer. Examples include Kent (1972; 1973; 1979), Bahl and Stuchly (1980) and Khalid et al. (1988). This is used to provide protection against corrosion and to reduce signal loss on the line. Unfortunately, the presence of the protective layer also causes dramatic perturbations to the properties of the transmission line, making comparison with unprotected microstrip difficult. Added to this is the fact that the majority of analytical models of microstrip sensors are quasi-TEM, which become less accurate as frequency and superstrate permittivity increase. A comparison of static and full-wave models is presented in Chapter 10.

9.3 Modelling of Coaxial to Microstrip Launchers

9.3.1 Launcher Impedance Mismatch

The launching structures which were used to couple energy into and out of each microstrip sensor were standard 50Ω SMA-type microstrip launchers. While these components are designed to provide a reasonably good match between coaxial and microstrip transmission lines, in practice they inevitably introduce a finite impedance mismatch into the system which can cause the measured S-parameters of the sensor to depart from the ideal case.

To complicate matters further, it was soon discovered that the presence of a test material on the sensor measurement surface, as illustrated in Figure 9.1, perturbed the fields at the aperture of the launcher. As a result the S-parameters of the launchers were not constant at a given frequency as originally assumed. Rather, they proved to be highly dependent upon the dielectric properties of the material under test.

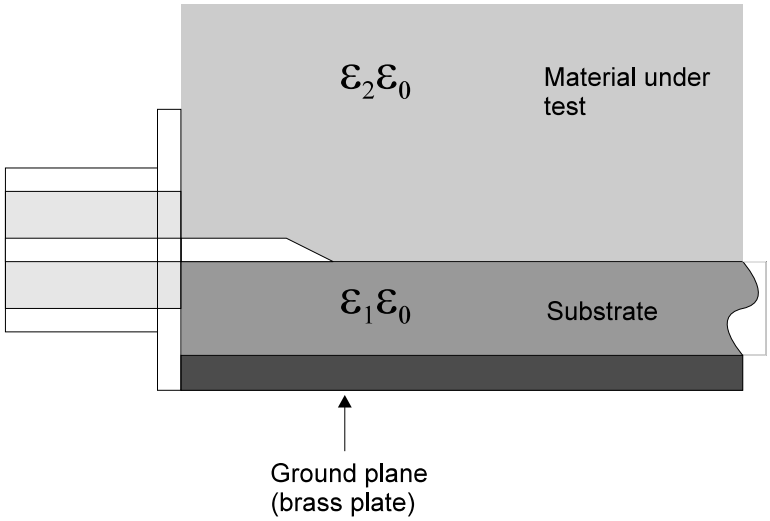

Figure 9.1: Coaxial-to-microstrip launcher attached to sensor covered by test liquid.

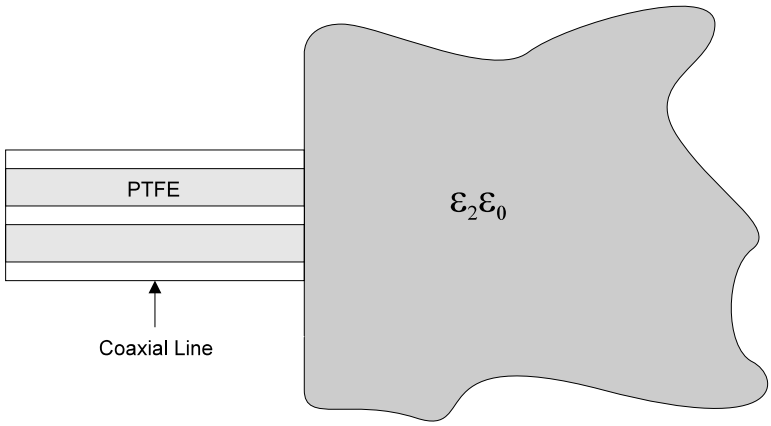

(a) Open-ended coaxial line.

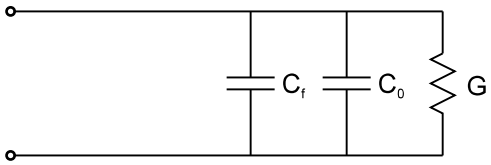

(b) Equivalent circuit.

Figure 9.2: Open-ended coaxial line immersed in an unknown dielectric, and its equivalent circuit representation.

9.3.2 Equivalent Circuit Representation

In order to account for the impedance mismatches caused by the coaxial to microstrip launchers, an equivalent circuit was developed whose properties mirrored those of the launchers. This approach was preferable to performing a rigorous field analysis of the launchers, due to the complicated nature of the fields near the interface between the coaxial and microstrip sections.

The equivalent circuit representation which proved most useful was the same as that used to model an open-circuited coaxial probe immersed in a lossy dielectric medium. A large body of work exists in the literature for such structures, particularly for permittivity measurement applications. The geometry and corresponding equivalent circuit of an open-ended coaxial probe is shown in Figures 9.2(a) and 9.2(b) respectively (Stuchly et al., 1982).

The shunt capacitance C_f in Figure 9.2(b) represents the electric field in the coaxial line, and is independent of the permittivity of the medium beyond the probe aperture. The shunt capac-

itance C_0 represents the field which fringes into the dielectric at the end of the line, while the conductance G represents the energy loss due to radiation, ionic conductivity and dielectric loss. Both C_0 and G are dependent upon the permittivity of the external medium.

9.3.3 Calculation of Equivalent Circuit Component Values

Several authors have presented approximate closed form expressions for probe input impedance in terms of the lumped elements C_f, C_0, G, and the permittivity of the surrounding medium (Stuchly et al., 1982; Gajda and Stuchly, 1983; Marsland and Evans, 1987). Other authors have developed simplified numerical solutions with the same intention (Mosig et al., 1981; Xu et al., 1991).

In the case of the microstrip launchers, however, no simple relationship is likely to exist between these parameters. This is due to the presence of the microstrip substrate and ground plane, which, combined with the test material, create an inhomogeneous medium at the end of the coaxial line. Consequently, existing closed-form approximations and numerical solutions which attempt to define C_0 and G in terms of the permittivity of the material under test will not generally be applicable.

The ideal solution to this problem would have been to redesign the sensor in such a way that the launchers were located outside the test chamber, as shown in Figure 9.3. By ensuring that the microstrip launchers were isolated from the test material, the values of C_0 and G could be made independent of the test material. Unfortunately this was not an option, as the time and expense involved in fabricating another sensor were prohibitive.

Ultimately the decision was made to take an 'educated guess' as to what the equivalent circuit parameters C and G should be. (For the sake of simplicity the two capacitive terms C_f and C_0 were combined into one term, C.) This guess was based upon what was known of the material under test. For example, when making measurements on a polar liquid like methanol, it was known *a priori* that the permittivity of the liquid could be described by a Debye function. Therefore it would seem reasonable to assume that the equivalent shunt capacitance C and conductance G of the microstrip launchers would also exhibit a Debye-like characteristic. Pro-

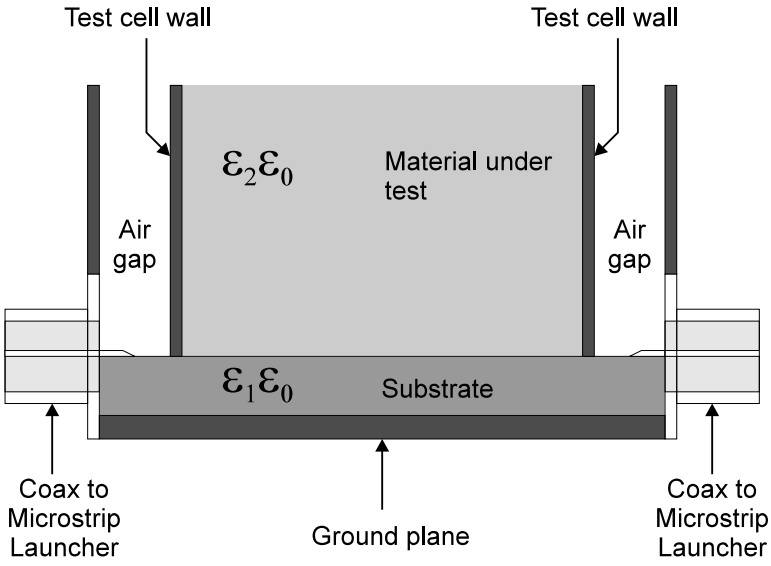

Figure 9.3: Cross-section of microstrip sensor with partitions inserted to isolate launchers from material under test.

ceeding from this assumption it is possible to derive expressions for C and G in the following manner:

Let the transition between the coaxial and microstrip sections of the launcher be represented by a purely capacitive term C_{T}. If the launcher was a parallel plate capacitor, C_{T} could be described by the following well-known expression:

$$C_{\mathrm{T}} \quad = \quad \frac{\varepsilon_0 \varepsilon_{\mathrm{r}} A}{d} \tag{9.8}$$

where ε_0 is the permittivity of free space, ε_{r} is the relative permittivity of the material between the plates of the capacitor, and A and d are the plate area and separation respectively. While this expression is by no means an accurate characterisation of the launcher capacitance, it does enable the following generalisation to be made:

$$C_{\mathrm{T}} \quad \propto \quad \varepsilon_{\mathrm{r}} \tag{9.9}$$

If the material under test is a polar substance like water, methanol or cheese curd, then the

relative permittivity of the material ε_{r} can be described by a Debye function:

$$\begin{aligned} \varepsilon_{\mathrm{r}} &= \varepsilon_{\infty} + \frac{\varepsilon_{\mathrm{s}} - \varepsilon_{\infty}}{1 + j\omega\tau} \\ &= \left[\varepsilon_{\infty} + \frac{\varepsilon_{\mathrm{s}} - \varepsilon_{\infty}}{1 + \omega^2\tau^2}\right] - j\left[\frac{(\varepsilon_{\mathrm{s}} - \varepsilon_{\infty})\omega\tau}{1 + \omega^2\tau^2}\right] \end{aligned} \tag{9.10}$$

Substituting Equation 9.10 into Equation 9.9 yields:

$$C_{\mathrm{T}} \propto \left[\varepsilon_{\infty} + \frac{\varepsilon_{\mathrm{s}} - \varepsilon_{\infty}}{1 + \omega^2\tau^2}\right] - j\left[\frac{(\varepsilon_{\mathrm{s}} - \varepsilon_{\infty})\omega\tau}{1 + \omega^2\tau^2}\right] \tag{9.11}$$

The shunt admittance Y due to C_{T} is given by

$$Y = j\omega C_{\mathrm{T}} \tag{9.12}$$

Substituting Equation 9.11 into this expression we obtain:

$$Y \propto (j\omega)\left[\varepsilon_{\infty} + \frac{\varepsilon_{\mathrm{s}} - \varepsilon_{\infty}}{1 + \omega^2\tau^2}\right] - (j\omega)j\left[\frac{(\varepsilon_{\mathrm{s}} - \varepsilon_{\infty})\omega\tau}{1 + \omega^2\tau^2}\right] \tag{9.13}$$

This equation has a real part and an imaginary part. It can therefore be rewritten as

$$Y \propto G + j\omega C \tag{9.14}$$

where

$$G \propto \frac{(\varepsilon_{\mathrm{s}} - \varepsilon_{\infty})\omega^2\tau}{1 + \omega^2\tau^2} \tag{9.15}$$

$$C \propto \varepsilon_{\infty} + \frac{\varepsilon_{\mathrm{s}} - \varepsilon_{\infty}}{1 + \omega^2\tau^2} \tag{9.16}$$

In practice the relaxation period τ was chosen to be the same as that of the material under test. The parameters ε_{s} and ε_{∞}, however, were chosen empirically to minimise the difference between theory and experiment.

To some extent this constitutes a circular argument—that is, in order to choose the coefficients of the launcher admittance function, experimental data is required. As a result the sensor model has no predictive capability, since it requires experimental data as one of its inputs. Nevertheless, it will be shown in Chapter 10 that this approach still leads to some compelling results, due to the fact that by adjusting only two degrees of freedom—namely, the shunt capacitance C and conductance G of the launcher model—it is possible obtain agreement between *four* variables: S_{11} magnitude, S_{11} phase, S_{21} magnitude and S_{21} phase. This is a valuable outcome, as it provides evidence supporting the veracity of the spectral domain model. In the absence of a sensor with isolated launchers, this is the next best verification technique.

9.4 Calculation of Scattering Parameters

The scattering parameters of each microstrip sensor were simulated by reducing the sensors to a series of two-port networks in cascade. In general, five such networks were required in order to accurately simulate a sensor: one for the microstrip test chamber, two for the shunt admittances presented by the launching structures at either end of the sensor, and two for the phase shifts through the launchers.

Each two-port was defined in terms of an *ABCD* matrix based on one of the well-known standard forms (Pozar, 1990, pp. 231–237). Thus, the *ABCD* matrices for the launchers were based on the standard form for a shunt admittance Y:

$$\begin{bmatrix} A & B \\ C & D \end{bmatrix} = \begin{bmatrix} 1 & 0 \\ Y & 1 \end{bmatrix} \tag{9.17}$$

where $Y = G + j\omega C$. Both launchers were assumed to have identical *ABCD* matrices, so that only one pair of values for C and G had to be determined.

Each launcher also had a short (~ 9.5 mm) PTFE-filled coaxial connector built into it, which caused a small phase shift at each end of the sensor. This was accounted for by a separate

ABCD matrix based on the standard form for a transmission line:

$$\begin{bmatrix} A & B \\ C & D \end{bmatrix} = \begin{bmatrix} \cos(\beta l) & jZ_0 \sin(\beta l) \\ jY_0 \sin(\beta l) & \cos(\beta l) \end{bmatrix} \tag{9.18}$$

where $\beta = \frac{2\pi\sqrt{\varepsilon_r}}{\lambda_0}$, $l = 9.5$ mm, $Z_0 = 50\Omega$, and $Y_0 = 1/Z_0$. The relative permittivity ε_{r} of the PTFE in the connector was assumed to be 2.08.

The same standard form was used to derive the *ABCD* matrix for the microstrip test cell. Of course, Z_0 and β had to be determined at every frequency of interest using the spectral domain method coupled with the procedure discussed in Section 9.2, making this a more time consuming exercise.

Having derived an *ABCD* matrix for each section of the sensor, it was possible to obtain the *ABCD* matrix of these components in cascade by multiplication:

$$\begin{aligned} [ABCD_{\mathrm{TOTAL}}] \;=\; & [ABCD_{\mathrm{COAX}}]\,[ABCD_{\mathrm{LAUNCHER}}] \\ & [ABCD_{\mathrm{MICROSTRIP}}]\,[ABCD_{\mathrm{LAUNCHER}}] \\ & [ABCD_{\mathrm{COAX}}] \end{aligned} \tag{9.19}$$

To obtain the S-parameters corresponding to the *ABCD* matrix in Equation 9.19 it was necessary to perform a transformation. This can be achieved by considering the voltage and current at each port of the network in terms of incident and reflected waves, as depicted Figure 9.4.

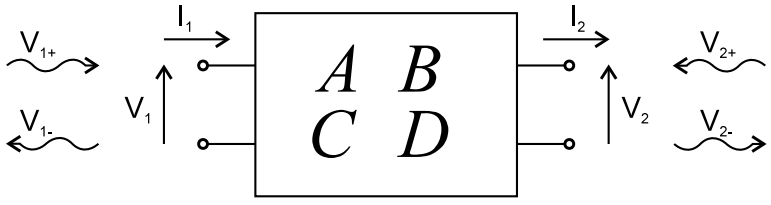

Figure 9.4: Two-port network with voltages and currents at each port.

The voltage at the measurement plane of Port 1 can be regarded as the sum of the incident and reflected waves at the port:

$$V_1 = V_{1+} + V_{1-} \tag{9.20}$$

where V_1 is the voltage at Port 1, and V_{1+} and V_{1-} are the incident and reflected waves respectively at Port 1. Similarly, the current flowing into Port 1 can be expressed in terms of V_{1+} and V_{1-}:

$$I_1 = \frac{V_{1+}}{Z_0} - \frac{V_{1-}}{Z_0} \tag{9.21}$$

where Z_0 is the reference impedance at Port 1. Following the same procedure for Port 2 yields two similar equations. These can then be substituted into the *ABCD* representation of the network:

$$\begin{bmatrix} V_1 \\ I_1 \end{bmatrix} = \begin{bmatrix} A & B \\ C & D \end{bmatrix} \begin{bmatrix} V_2 \\ I_2 \end{bmatrix} \tag{9.22}$$

$$\begin{bmatrix} V_{1+} + V_{1-} \\ (V_{1+} - V_{1-})/Z_0 \end{bmatrix} = \begin{bmatrix} A & B \\ C & D \end{bmatrix} \begin{bmatrix} V_{2+} + V_{2-} \\ (V_{2-} - V_{2+})/Z_0 \end{bmatrix} \tag{9.23}$$

Assuming Port 2 is terminated in a matched load (i.e. $V_{2+} = 0$) and dividing all terms in Equation 9.23 by V_{1+}, the following pair of equations is obtained:

$$1 + S_{11} = AS_{21} + \frac{B}{Z_0} S_{21} \tag{9.24}$$

$$1 - S_{11} = CZ_0 S_{21} + DS_{21} \tag{9.25}$$

Solving for S_{21} yields

$$S_{21} = \frac{2}{A + B/Z_0 + Z_0 C + D} \tag{9.26}$$

The same approach can be used to derive the transformations for S_{11}, S_{12} and S_{22}. The complete set of these expressions is provided below in Equations 9.27–9.30.

$$S_{11} = \frac{A + B/Z_0 - Z_0C - D}{A + B/Z_0 + Z_0C + D} \tag{9.27}$$

$$S_{12} = \frac{2(AD - BC)}{A + B/Z_0 + Z_0C + D} \tag{9.28}$$

$$S_{21} = \frac{2}{A + B/Z_0 + Z_0C + D} \tag{9.29}$$

$$S_{22} = -\frac{A - B/Z_0 + Z_0C - D}{A + B/Z_0 + Z_0C + D} \tag{9.30}$$

9.5 Conclusion

This chapter has described the steps involved in simulating the S-parameters of a microstrip sensor.

An appropriate definition of microstrip characteristic impedance Z_0 has been chosen and implemented in software. The calculated value of Z_0 has been shown to agree well with published results.

An equivalent circuit model of the coaxial to microstrip adaptors at each end of the sensor has been developed. This model consists of a short length of PTFE-filled transmission line driving a shunt capacitance C and conductance G, whose values are dependent upon frequency, launcher geometry, and the dielectric properties of the material under test. In the event that the material under test is a polar substance, a semi-empirical pair of functions based on the Debye equation has been proposed to describe C and G.

An *ABCD* matrix representation of each part of the sensor has been developed. This has enabled the *ABCD* parameters for the entire sensor to be obtained by simple matrix multiplication. A process has been outlined for converting the sensor *ABCD* matrix to a matrix of scattering parameters.

Chapter 10

Results

10.1 Introduction

The static and full-wave models of microstrip presented in Chapters 6 and 8 have been shown to agree well with results from the literature. However, the ultimate test of a sensor model is not how well it agrees with other theoretical models; rather, it is the extent to which it can reproduce real-life measurements.

To that end, a series of Automatic Network Analyser measurements were performed on a microstrip sensor using methanol as the test material. The resulting data was compared with S-parameters predicted by the static and full-wave models. This chapter summarises the results of that investigation, with a view to determining which of the two sensor models is the most accurate.

The first section describes a set of permittivity measurements which were carried out on samples of methanol using a Dielectric Probe, in order to confirm that the Debye parameters of the methanol sample agreed with previously published values.

The remaining sections of this chapter compare the measured and predicted scattering parameters of the sensor when covered by methanol. To improve the agreement between the two sets

of results, equivalent circuit parameters are selected to model the phase shift and impedance mismatch due to the microstrip launchers at either end of the sensor.

10.2 Dielectric Probe Measurements of Methanol Permittivity

The usefulness of methanol as a test liquid with known dielectric properties was discussed in Chapter 2. A 2.5 litre bottle of Analytical Grade methanol (99.8% minimum assay) was purchased for this purpose.

In order to use methanol as a test liquid, it was first necessary to determine its Debye parameters. Although such data has previously been published by other workers (see e.g. Jordan et al., 1978), a check on this information was nevertheless carried out using an HP85070M Dielectric Probe.

The first step in this process was to measure the complex permittivity of methanol over a wide frequency band. Several sets of measurements were performed, with the Dielectric Probe being recalibrated before each measurement to mitigate against experimentally induced errors. The results of these measurements are shown in Figure 10.1.

The second step was to estimate the relaxation period τ of the liquid. This was obtained by plotting the measured ε'' against frequency. The turning point of this curve occurs at the relaxation frequency f_{rel} for methanol, which is related to τ by

$$\tau = \frac{1}{2\pi f_{\mathrm{rel}}} \tag{10.1}$$

where τ has units of seconds and f_{rel} has units of hertz. From the loss curve in Figure 10.1(b) it is evident that f_{rel} is approximately 3.2 GHz, giving a relaxation period of $\tau = 49.74$ ps.

The final step is to estimate the static permittivity ε_{s} and infinite frequency permittivity ε_{∞} from the measured data. This involved simultaneous solution of the Debye functions introduced in Chapter 2:

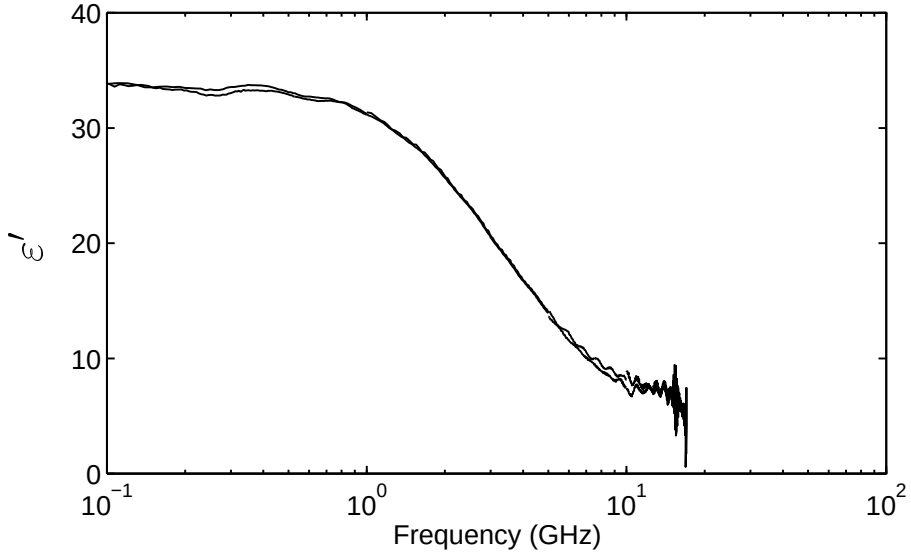

(a) Real part.

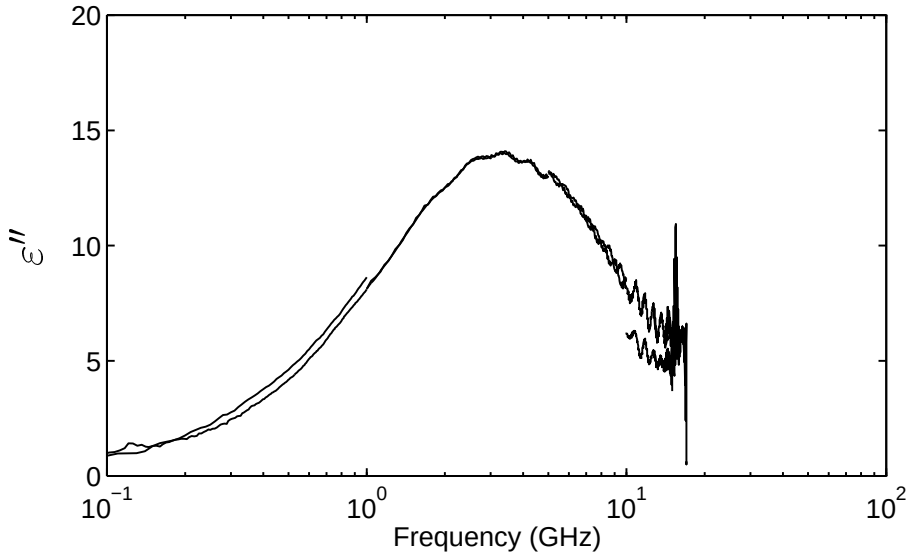

(b) Imaginary part.

Figure 10.1: Permittivity of methanol at 25°C as measured by HP8510 Automatic Network Analyser equipped with Dielectric Probe Kit.

$$\varepsilon' = \varepsilon_\infty + \frac{\varepsilon_s - \varepsilon_\infty}{1 + \omega^2\tau^2} \tag{10.2}$$

$$\varepsilon'' = \frac{(\varepsilon_s - \varepsilon_\infty)\omega\tau}{1 + \omega^2\tau^2} \tag{10.3}$$

For the sake of simplicity the spreading factor α was assumed to be zero for this analysis. Substituting the value of τ which was estimated earlier into Equations 10.2 and 10.3 and solving simultaneously for ε_s and ε_∞ yields

$$\varepsilon_\mathrm{s} = \varepsilon' + \omega\tau\varepsilon'' \tag{10.4}$$

$$\varepsilon_\infty = \varepsilon' - \frac{\varepsilon''}{\omega\tau} \tag{10.5}$$

Theoretically the value obtained for ε_s and ε_∞ should be constant for every measured point. However, the imperfect nature of the measured data meant that a range of values was obtained for each parameter, as shown in Figure 10.2. Thus, ε_s and ε_∞ had to be chosen by averaging each of the data sets in Figures 10.2(a) and 10.2(b). The estimated values in this case were $\varepsilon_\mathrm{s} = 33.8$ and $\varepsilon_\infty = 5.6$.

A comparison of the experimentally determined Debye parameters with values published by Jordan et al. (1978) is given in Table 10.1, with good agreement. A graph of the Debye function corresponding to these parameters is plotted alongside the measured permittivity data in Figure 10.3.

Table 10.1: Comparison of Debye parameters estimated from experimental data with the results of Jordan et al. (1978).

Debye Parameter	Calculated Value	Published Value
τ (ps)	49.74	49.69
ε_s	33.8	33.7
ε_∞	5.6	4.5

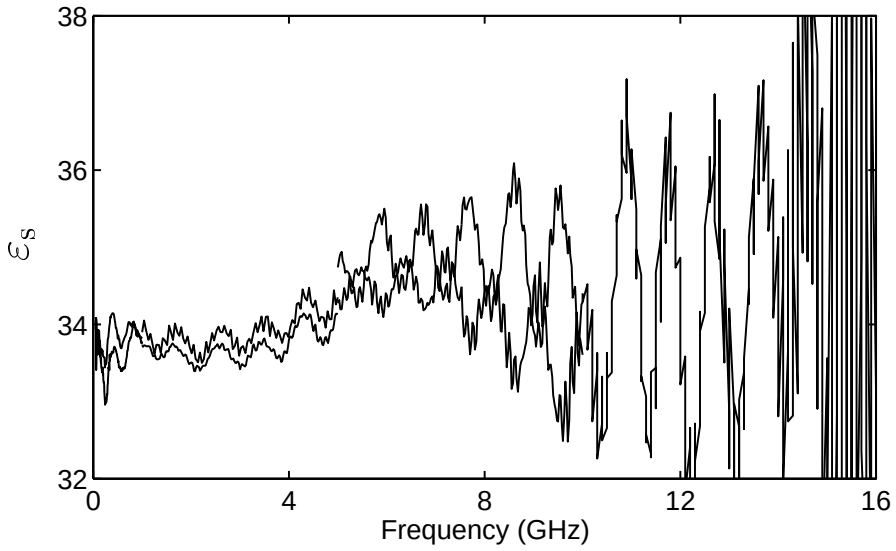

(a) Static permittivity.

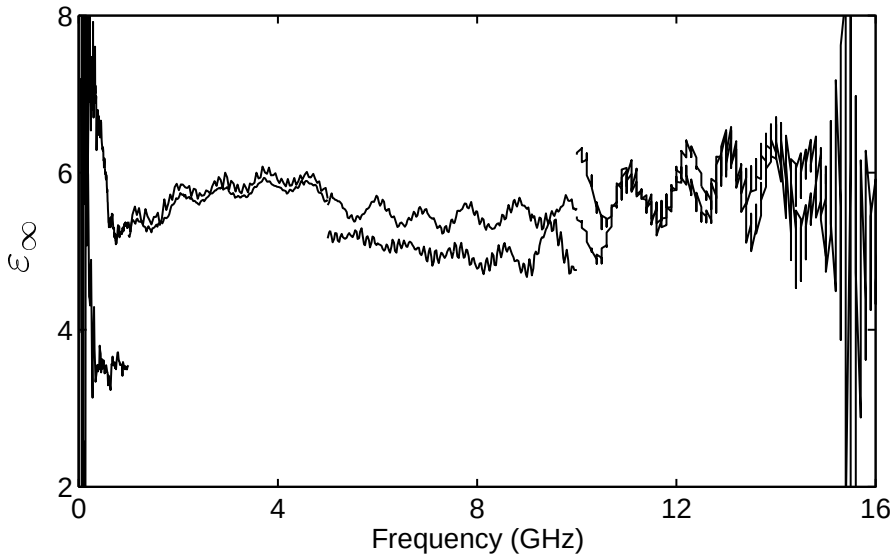

(b) Infinite frequency permittivity.

Figure 10.2: Static and infinite frequency permittivity of methanol vs frequency as calculated from data from HP Dielectric Probe.

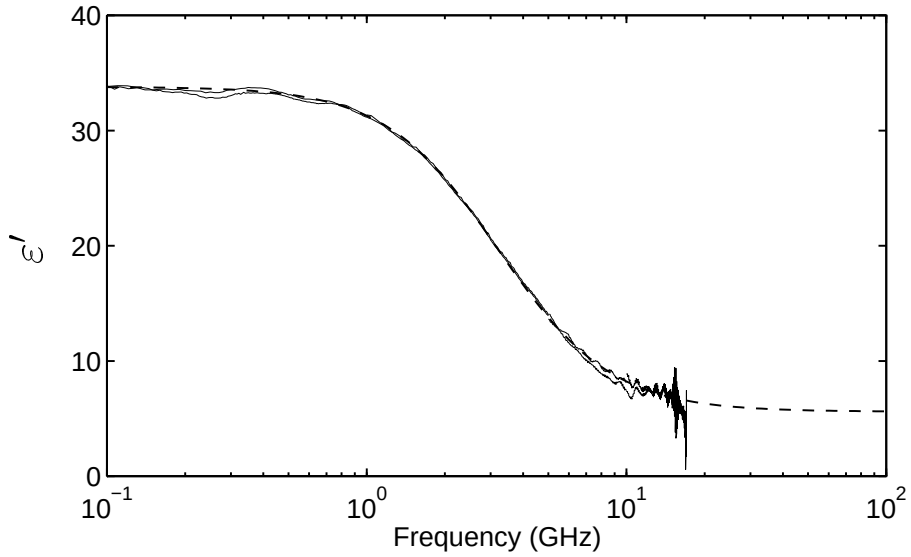

(a) Real part.

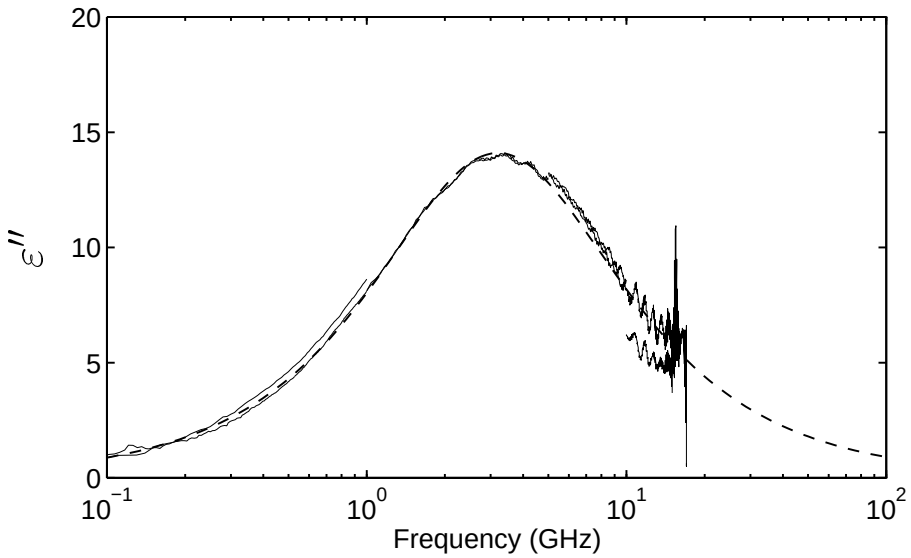

(b) Imaginary part.

Figure 10.3: Permittivity of methanol at 25°C as measured by HP Dielectric Probe Kit. Dashed curves denote Debye functions generated using constants estimated from measured data.

10.3 Comparison of Static and Full-Wave Models

Before comparing the two sensor models with experimental data, the models were first compared with each other. This was to demonstrate that the static and full-wave models actually produced different results, thereby justifying the time and effort expended on the full-wave analysis.

A methanol-covered sensor was analysed by both models. The parameters of the simulation were: $\varepsilon_1 = 10.2 - j0$, $d = 1.27$ mm, $2w = 0.97$ mm. The temperature of the methanol sample was 21.1°C. Figure 10.4 shows the predicted attenuation and phase coefficients of the line.

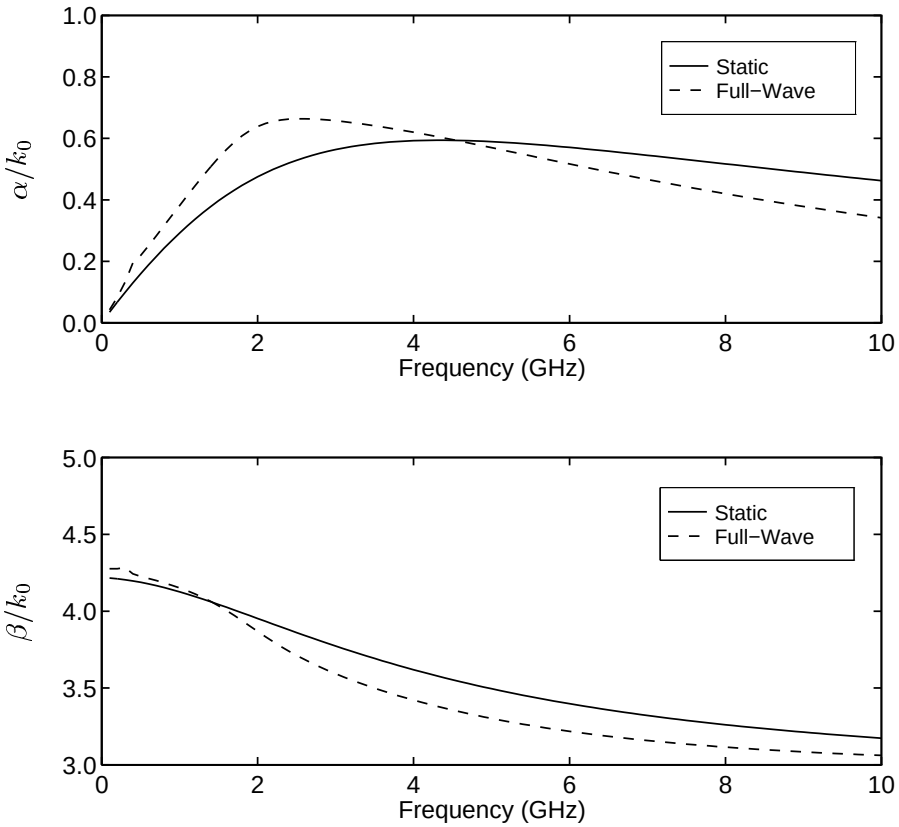

Figure 10.4: Normalised attenuation and phase coefficients of methanol-covered microstrip as predicted by static and full-wave models. ($\varepsilon_1 = 10.2 - j0$, $d = 1.27$ mm, $2w = 0.97$ mm, $T_{\mathrm{meth}} = 21.1$°C.)

There are a number of significant differences between the propagation characteristics predicted by the two models. The normalised attenuation coefficient as calculated by the full-wave model peaks earlier and at a higher value than the static model. At first it was suspected that radiation or surface wave leakage may have been the reason for this difference, given that the static model cannot account for these effects. However, as shown in Figure 10.5, both the branch point and TM_0 surface wave pole remained in the fourth quadrant of the complex plane at every point in the full-wave simulation. Consequently, no leakage to either of the space wave or TM_0 surface wave mode was implicated, suggesting that the difference between the propagation coefficients calculated by the two models was due to dispersion.

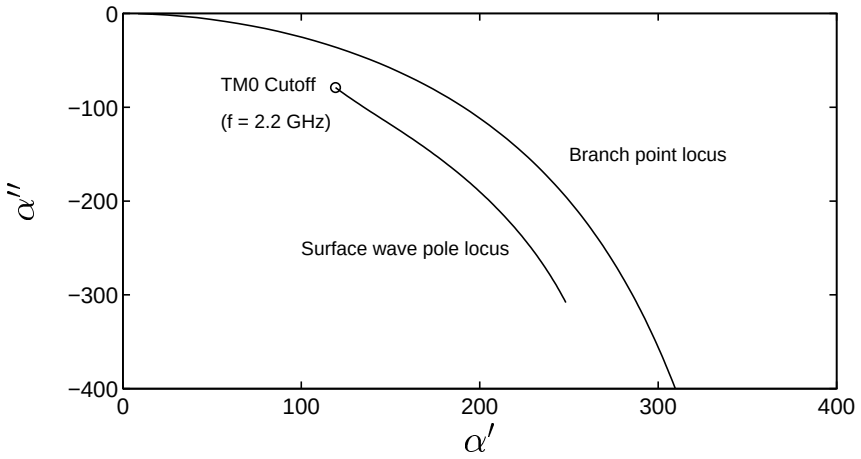

Figure 10.5: Migration of TM_0 surface wave pole and branch point with respect to frequency for microstrip covered by methanol. ($\varepsilon_1 = 10.2 - j0$, $d = 1.27$ mm, $2w = 0.97$ mm, $T_{\mathrm{meth}} = 21.1$°C. Circle denotes pole location where TM_0 mode is cutoff.)

The simulated characteristic impedance of the sensor is plotted in Figure 10.6. The difference between the two sensor models was relatively large. Of particular concern were the results for the real part of Z_0 at low frequencies. Theoretically the static and full-wave curves should have converged towards each other as frequency decreased towards DC. However, in this case the curves for the real part of Z_0 crossed over at about 3.1 GHz, and diverged to a peak difference of 2.83Ω (or a relative difference of 8.8%) below this frequency. Upon investigating this discrepancy it was found that the numerical integrals associated with each model had been truncated at values that were somewhat too low. These integrals were subsequently recomputed using wider limits of integration, with the result that the peak difference between the static

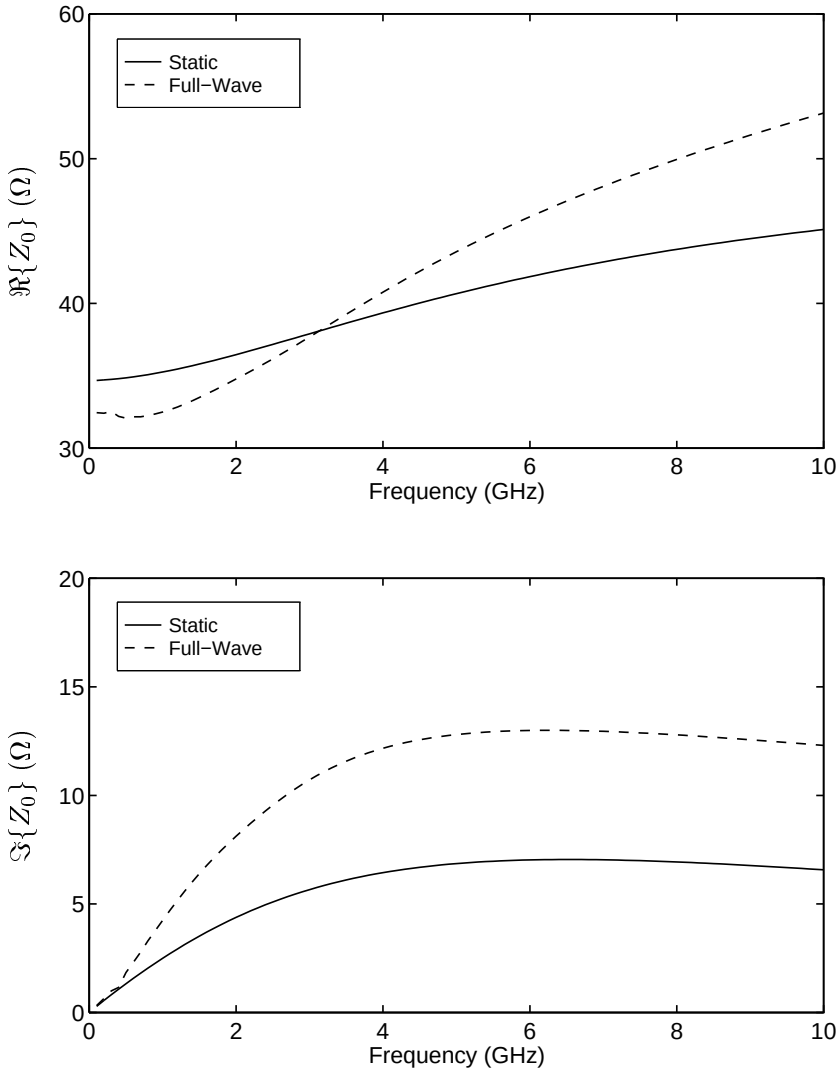

Figure 10.6: Characteristic impedance of methanol-covered microstrip as predicted by static and full-wave models. ($\varepsilon_1 = 10.2 - j0$, $d = 1.27$ mm, $2w = 0.97$ mm, $T_{\mathrm{meth}} = 21.1°$C.)

and full-wave solutions decreased to 0.37Ω (a relative difference of 1.1%) at a frequency of 0.7 GHz.

At frequencies above 3.1 GHz the relative difference between the static and full-wave solutions of Z_0 increased considerably. At 10 GHz the difference was 15.1% and 46.6% respectively for the real and imaginary parts of Z_0. Again it was suspected that premature truncation of the numerical integrals had contributed to these large differences. However, after recalculating Z_0 using wider limits of integration, the relative differences between the static and full-wave solutions were found to change only slightly, to 17.1% and 42.3% for the real and imaginary parts of Z_0 respectively.

Figures 10.7 and 10.8 compare the predicted reflection and transmission coefficients respectively of the sensor. No allowance has been made for the impedance mismatch or phase shift introduced by the microstrip launchers. As would be expected, the S_{11} and S_{21} curves calculated by the static and full-wave models are in reasonably good agreement at low frequencies, however this deteriorates above 2 GHz.

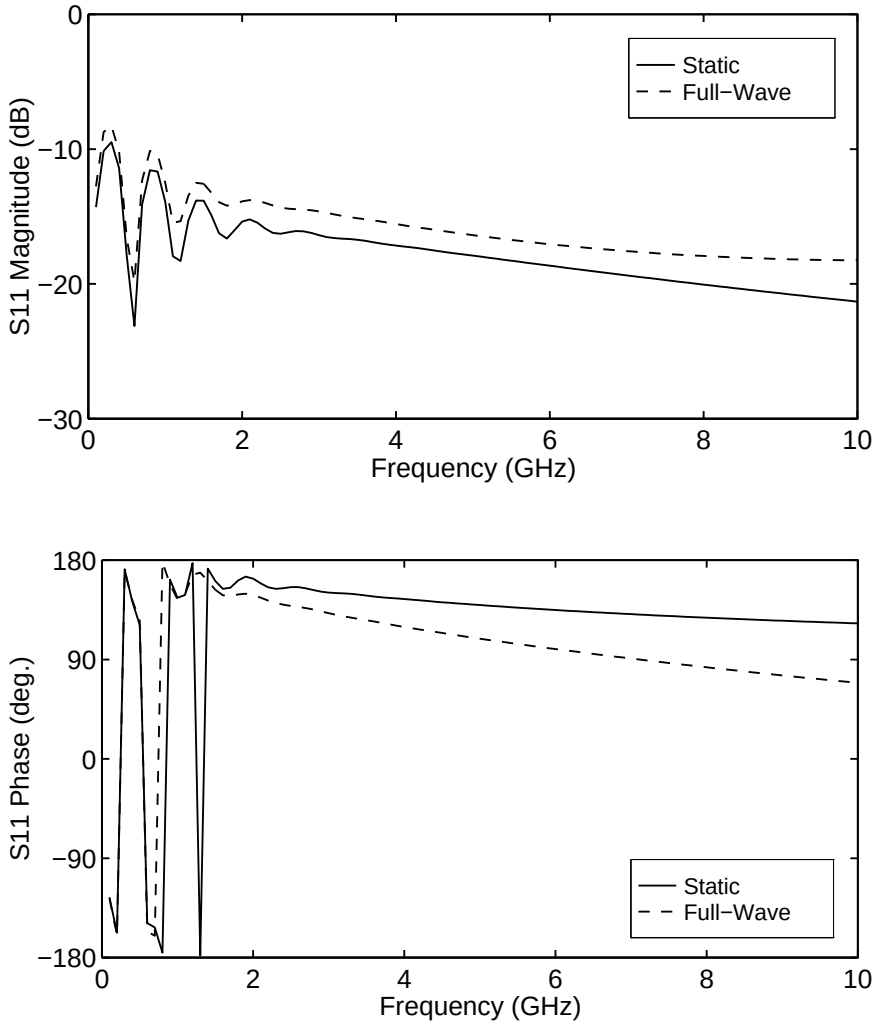

Figure 10.7: S_{11} of methanol-covered microstrip as predicted by static and full-wave models. Temperature of methanol assumed to be 21.1°C. No correction is made for mismatch caused by launchers.

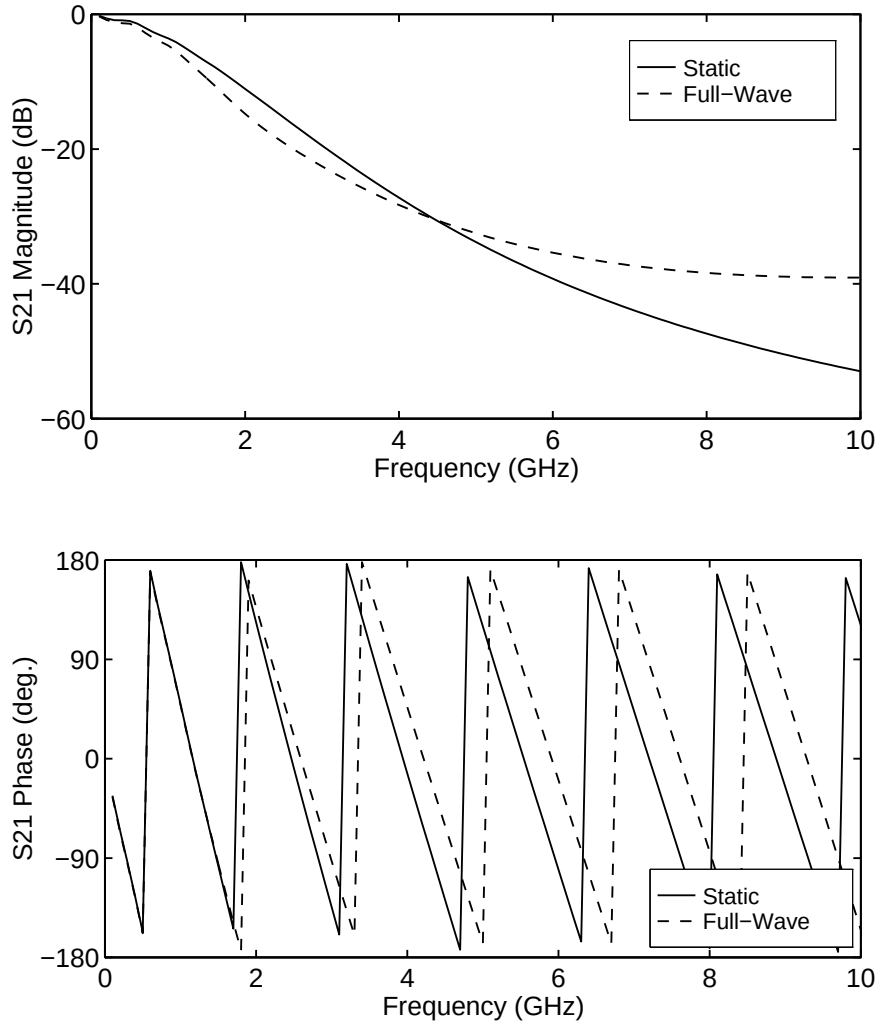

Figure 10.8: S_{21} of methanol-covered microstrip as predicted by static and full-wave models. Temperature of methanol assumed to be 21.1°C. No correction is made for mismatch caused by launchers.

10.4 Comparison of Theory and Experiment (Launcher Mismatch Neglected)

10.4.1 Static Model

A comparison of the measured S-parameters of a methanol-covered microstrip sensor with those predicted by the quasi-TEM sensor model are presented in Figures 10.9 and 10.10. No correction has been made for the phase shift and mismatch introduced by the launchers at either end of the sensor.

In general agreement is poor across the entire frequency band. In the case of the S_{11} results, the measured and predicted magnitudes differed by up to 12.5 dB. The results for S_{21} differed by up to 10 dB at some frequencies. The phase curves likewise exhibited significant discrepancies, which grew larger with increasing frequency.

Despite these differences, there were several encouraging aspects to the results obtained using the static model. For example, the agreement between theory and experiment was relatively good at low frequencies, which is to be expected given that that the TEM approximation is most valid towards DC. Another positive feature of the results in Figures 10.9 and 10.10 is that the *pattern* of peaks and nulls in the simulated and measured magnitude curves have very similar profiles, despite the large differences in their absolute values.

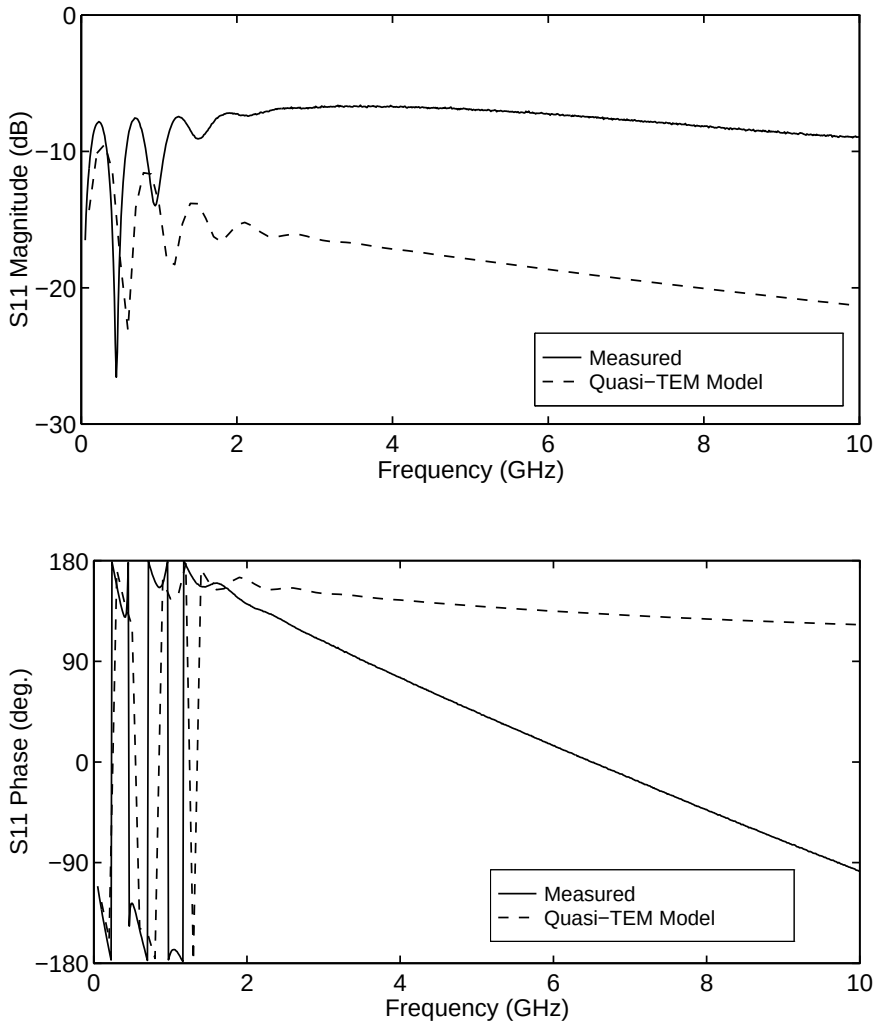

Figure 10.9: Comparison of measured S_{11} of methanol-covered microstrip with value predicted by quasi-TEM theoretical model. Temperature of methanol is 21.1°C. Model makes no correction for mismatch caused by launchers.

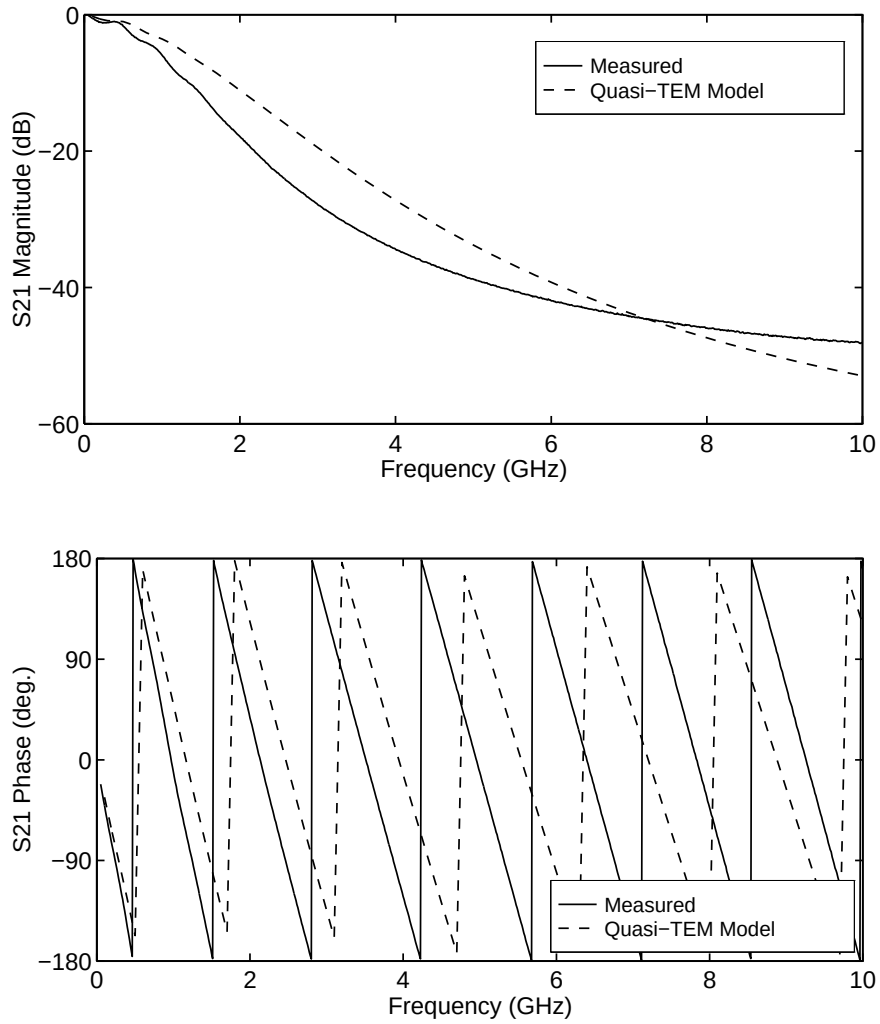

Figure 10.10: Comparison of measured S_{21} of methanol-covered microstrip with value predicted by quasi-TEM theoretical model. Temperature of methanol is 21.1°C. Model makes no correction for mismatch caused by launchers.

10.4.2 Full-Wave Model

The agreement between measurement and theory for the uncorrected full-wave model was slightly better compared to the static model, but overall the results were still poor.

As shown in Figure 10.11, the error in the magnitude of S_{11} peaked at almost 10 dB (compared with 12.5 dB for the static model). The error in the phase of S_{11} was small below 2 GHz, but grew steadily larger above this frequency.

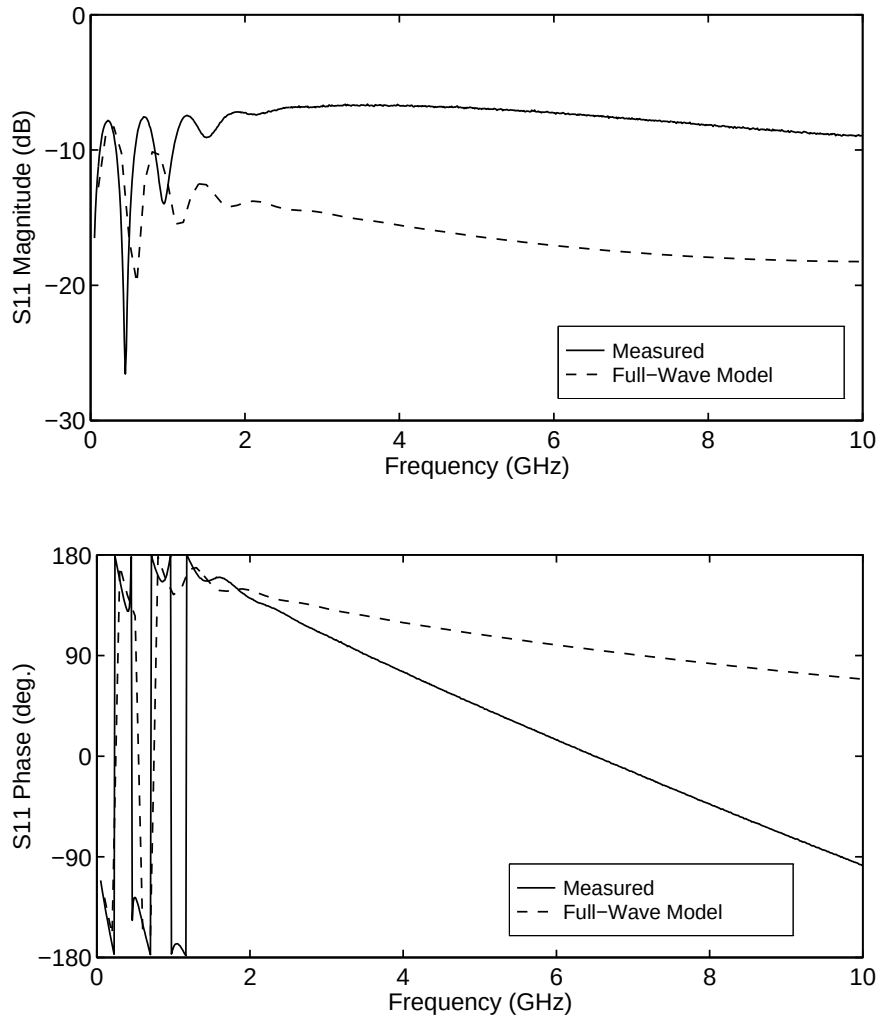

Figure 10.11: Comparison of measured S_{11} of methanol-covered microstrip with value predicted by full-wave theoretical model. Temperature of methanol is 21.1°C. Model makes no correction for mismatch caused by launchers.

The results for S_{21}, plotted in Figure 10.12, also displayed large differences between measurement and theory. Magnitude error was around 9 dB, compared with 10 dB for the static model. The measured phase rolled off more rapidly with frequency than the simulated phase, although this was to be expected given that the full-wave model neglected the electrical length of the microstrip launchers.

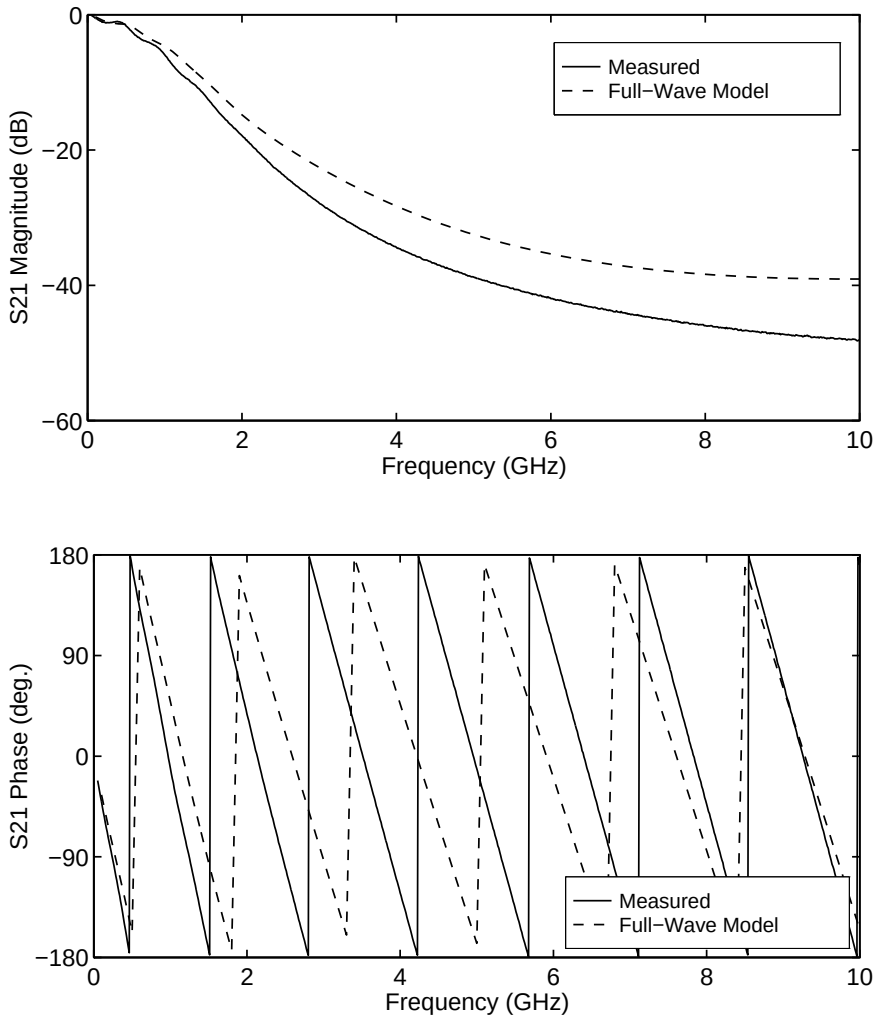

Figure 10.12: Comparison of measured S_{21} of methanol-covered microstrip with value predicted by full-wave theoretical model. Temperature of methanol is 21.1°C. Model makes no correction for mismatch caused by launchers.

As was the case with the uncorrected static model, there are encouraging aspects to the full-wave results. The agreement at low frequencies (i.e. below about 1 GHz) is good, and the general profiles of the simulated and measured magnitude curves are very similar, despite the large differences in the absolute values.

10.5 Comparison of Theory and Experiment (Launcher Mismatch Corrected)

10.5.1 Launcher Admittance Function

The agreement between theoretical and experimental results was improved by taking into account the mismatch and phase shift due to the microstrip launchers. As outlined in Chapter 9, the launcher model consisted of a 9.5 mm length of PTFE-filled coaxial line in cascade with a shunt admittance. A range of admittance functions based on the Debye equation were investigated. This produced the following functions for the shunt components C and G:

$$C = \left[0.8 + \frac{2.9}{1+\omega^2\tau^2}\right] \cdot K(F) \qquad \text{pF} \tag{10.6}$$

$$G = \frac{2.9\omega^2\tau}{1+\omega^2\tau^2} \cdot K(F) \qquad \text{pS} \tag{10.7}$$

where τ is the relaxation period of methanol, F is the stimulus frequency in gigahertz, and $K(F)$ is an empirical correction function of the form

$$K(F) = \frac{1}{1+0.15F+0.01F^2} \tag{10.8}$$

Plots of Equations 10.6 and 10.7 are shown in Figures 10.13(a) and 10.13(b) respectively.

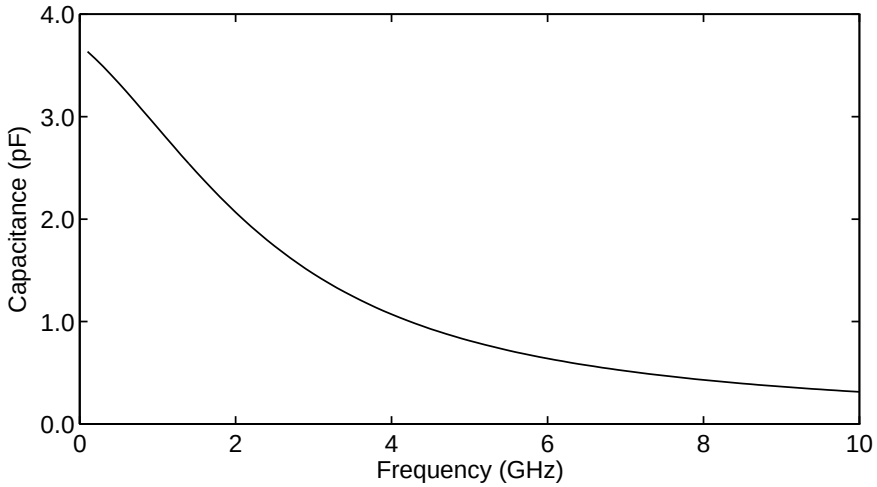

(a) Equivalent shunt capacitance.

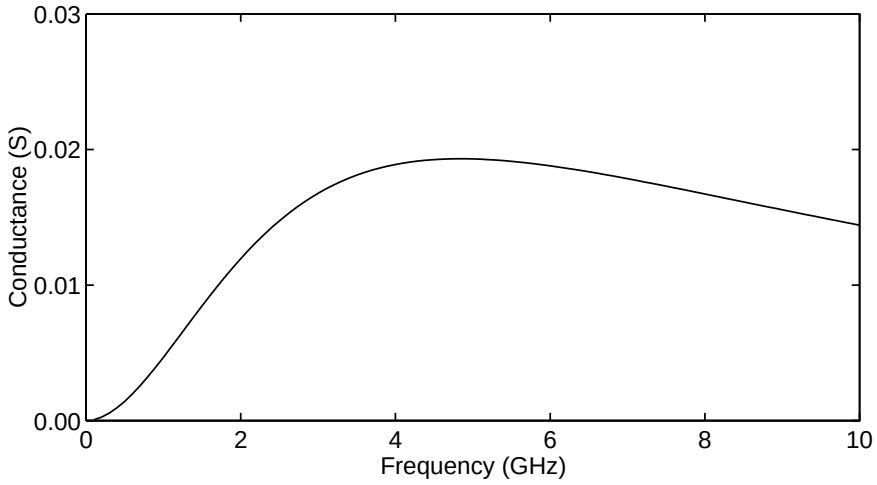

(b) Equivalent shunt conductance.

Figure 10.13: Equivalent shunt components required to minimise the difference between measured and simulated scattering parameters of microstrip sensor. Temperature of methanol sample is 21.1°C.

10.5.2 Static Model

Substituting Equations 10.6 and 10.7 into the equivalent circuit model of the microstrip launchers produced the corrected S-parameters shown in Figures 10.14 and 10.15. Agreement between measured and theoretical results has improved considerably compared with the uncorrected case.

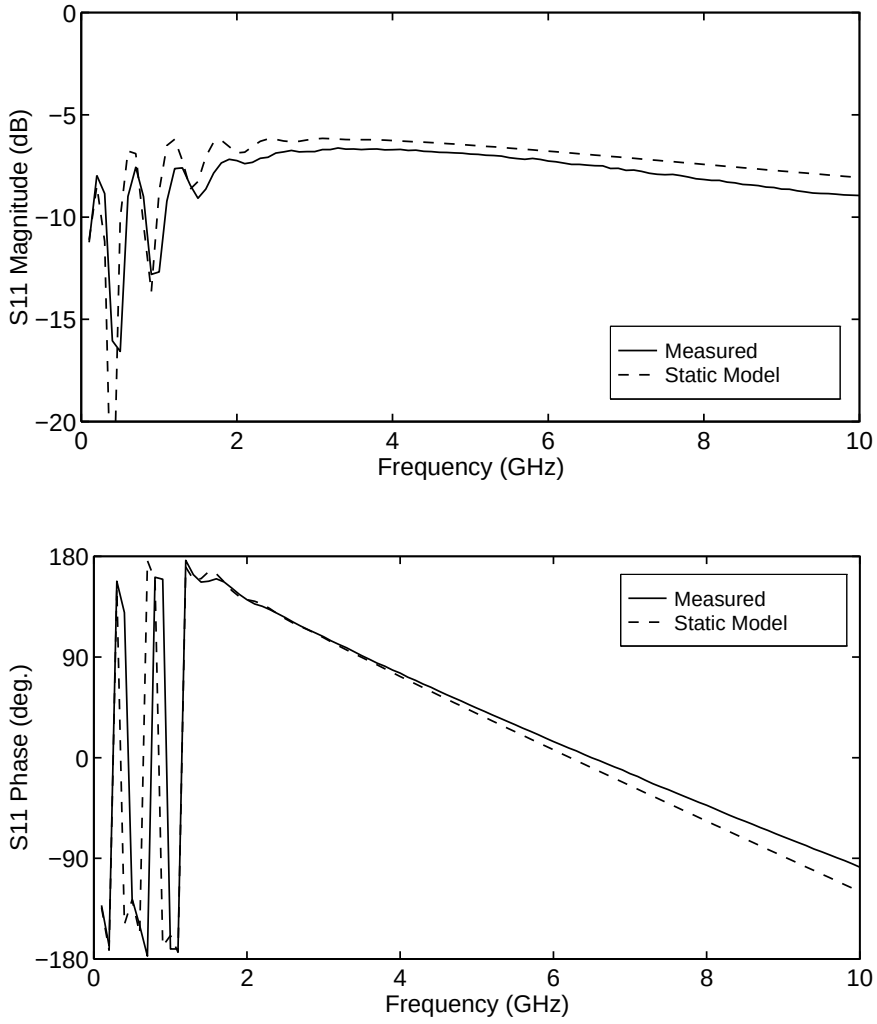

Figure 10.14: Comparison of measured S_{11} of methanol-covered microstrip with quasi-TEM model, with equivalent circuit parameters chosen to minimise the difference between measured and simulated S-parameters. Temperature of methanol sample is 21.1°C.

However, large differences still exist between the measured and theoretical S_{21} at high frequencies. These could not be eliminated without sacrificing the relatively good agreement which was achieved for S_{11}. This was an inherent feature of the static model; any attempt to improve the agreement between measurement and theory for one S-parameter invariably came at the expense of the other S-parameter.

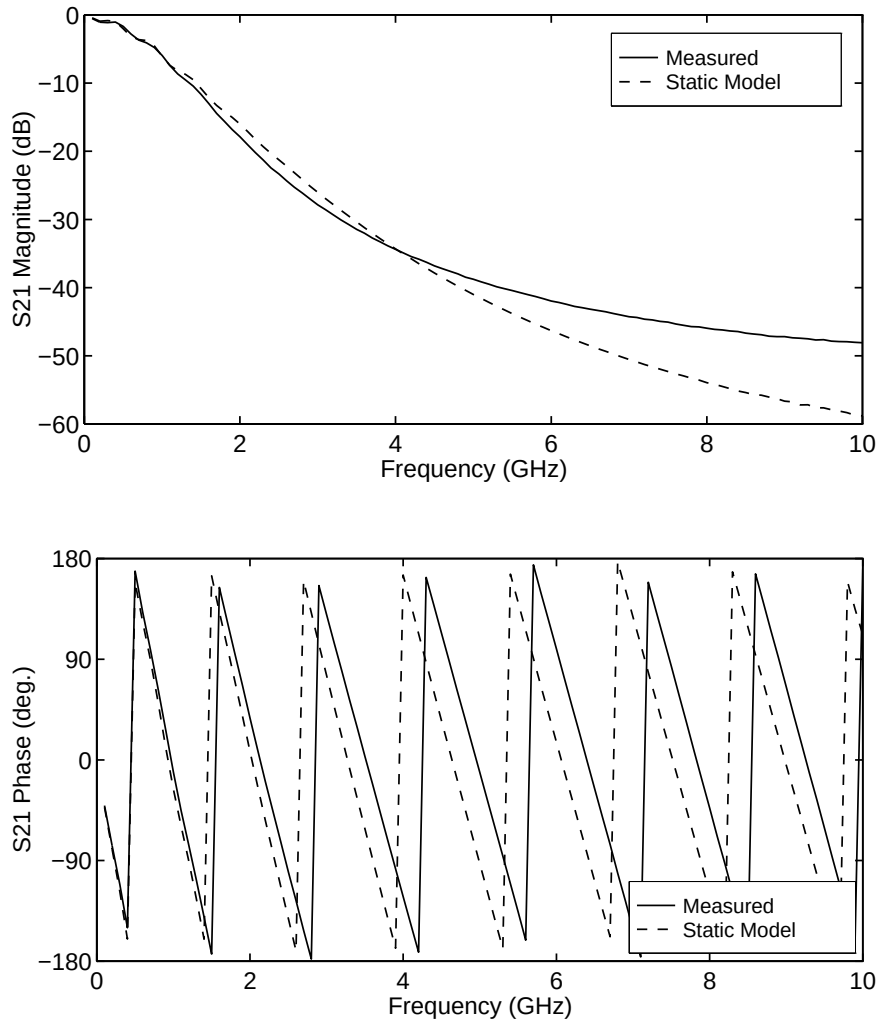

Figure 10.15: Comparison of measured S_{21} of methanol-covered microstrip with quasi-TEM model, with equivalent circuit parameters chosen to minimise the difference between measured and simulated S-parameters. Temperature of methanol sample is 21.1°C.

10.5.3 Full-Wave Model

The corrected S-parameters for the full-wave model are shown in Figures 10.16 and 10.17. As was the case with the static model, the agreement between measurement and theory has been greatly improved.

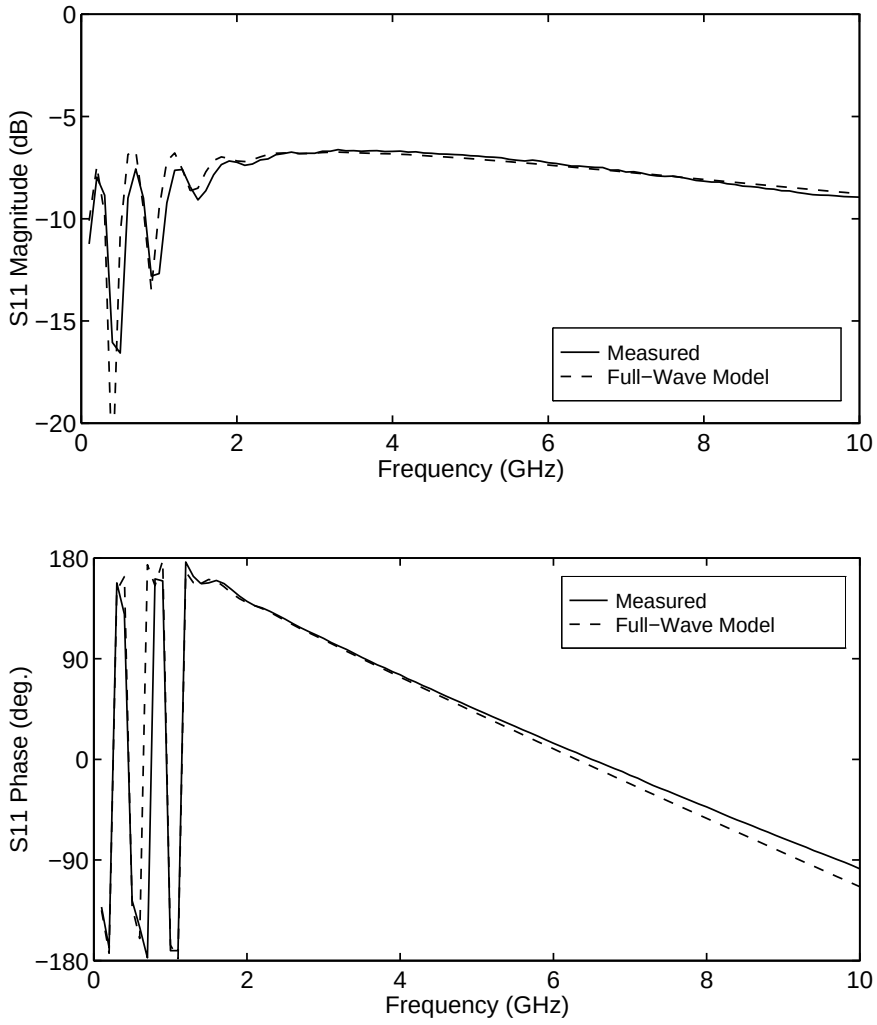

Figure 10.16: Comparison of measured S_{11} of methanol-covered microstrip with full-wave model, with equivalent circuit parameters chosen to minimise the difference between measured and simulated S-parameters. Temperature of methanol sample is 21.1°C.

In general it was found that better agreement with experiment was achieved with the full-wave model than with the static model. Unlike the static model, it was possible to adjust the parameters of the launcher model to improve one of the S-parameters without sacrificing the other.

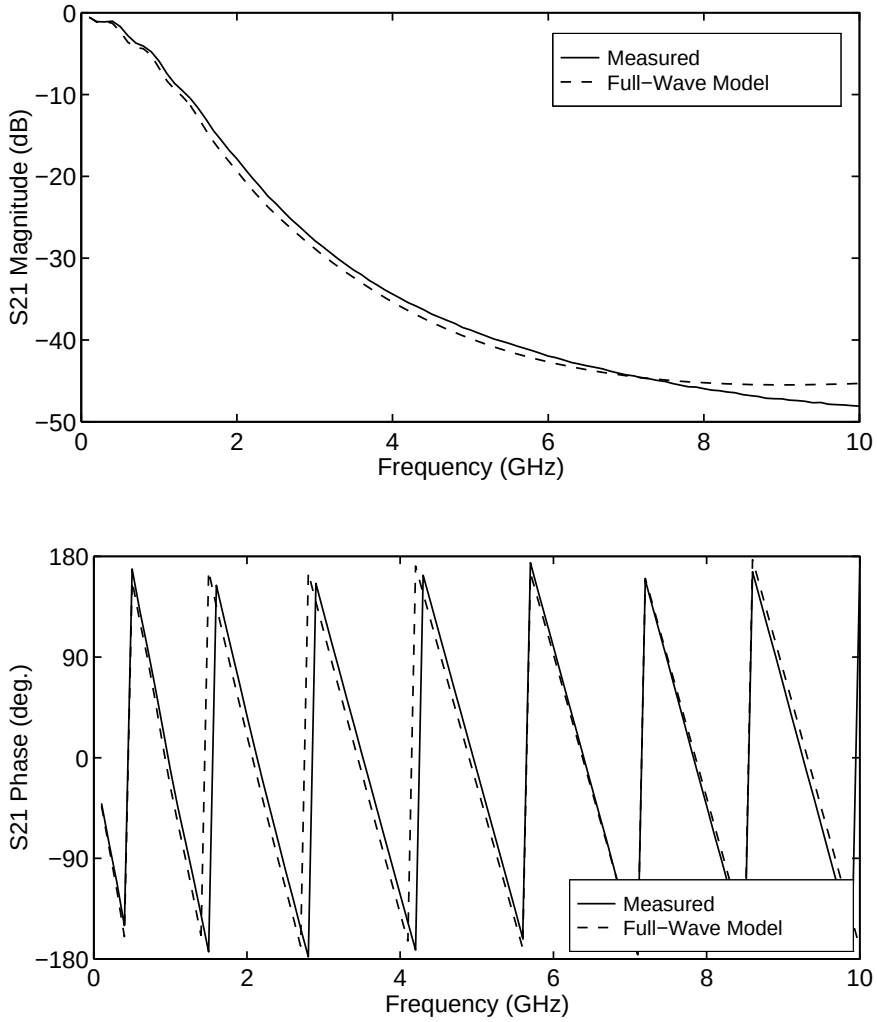

Figure 10.17: Comparison of measured S_{21} of methanol-covered microstrip with full-wave model, with equivalent circuit parameters chosen to minimise the difference between measured and simulated S-parameters. Temperature of methanol sample is 21.1°C.

10.6 Conclusion

This chapter has presented the results of a series of laboratory measurements which were performed on a methanol-covered microstrip sensor, the intention being to verify which of the two theoretical models could best predict the real-life S-parameters of the sensor.

The permittivity of methanol has been measured with a Dielectric Probe. The results have enabled the Debye parameters of methanol to be estimated and compared with published data. Good agreement was obtained, which suggested that the published Debye parameters could be used with confidence in subsequent simulations of microstrip immersed in methanol.

A comparison has been made between the output from the quasi-TEM and full-wave sensor models. This has demonstrated that some substantial differences exist between the propagation coefficient and characteristic impedance (and hence S-parameters) predicted by each model. Interestingly, these differences were *not* caused by surface waves and radiation, but by dispersion. The lack of agreement between the two models vindicates the time and effort expended on the full-wave spectral analysis, as it demonstrates some of the limitations of the static models which have previously been so popular with other workers in this field.

The S-parameters of a microstrip sensor immersed in methanol have been measured with an Automatic Network Analyser. This data has been compared with both the static and full-wave sensor models. Initially the mismatch due to the microstrip launchers was neglected. As a result neither model was in close agreement with the measured data, although the full-wave model was arguably slightly better than the static model.

The use of an equivalent circuit model of the microstrip launchers has greatly improved the agreement between theory and experiment. The parameters of the equivalent circuit model C and G were defined using two semi-empirical functions based on the Debye equation. Using this approach it has been shown that the static model can be made to agree quite well with either the measured S_{11} or S_{21}, but not both. In the case of the full-wave model, however, it was possible to obtain close agreement between both S_{11} and S_{21}.

Chapter 11

Discussion and Conclusions

11.1 Introduction

The main proposition of this thesis was that it is possible to measure the moisture content of cheese curd accurately, cheaply and quickly by microwave sensing, given intelligent instrument design. The broad aim of this project was to develop tools and techniques which demonstrated the validity of this proposition.

As set out in Section 1.3, the specific objectives of the project were threefold, namely: to establish the extent to which the dielectric properties of cheese curd are affected by moisture content; to develop hardware to measure the scattering parameters of a sensor immersed in samples of cheese curd; and to develop a sensor model to map measured S-parameters to a corresponding value of permittivity. Moisture content could then be determined from an empirical calibration curve or a dielectric mixing model.

This chapter summarises the major findings of this thesis and their significance to the wider body of knowledge in the field. The chapter concludes with a summary of suggested areas for future work.

11.2 Dielectric Properties of Cheese Curd

The extensive series of measurements performed on cream cheese curd and low-fat cheddar cheese curd has demonstrated that cheese curd permittivity is a parameter whose value depends on moisture content, frequency and salt content. Temperature is also likely to be an influencing factor, but this was not investigated in detail as the curd temperature was assumed to be fixed by the production process.

As shown in Section 3.8, the impact of moisture content on permittivity was significant. Both the real and imaginary parts of permittivity increased as the amount of water in the samples increased. For the range of moisture contents surveyed, this relationship was found to be approximately linear. These results provide compelling evidence for the proposition that microwave sensing is an appropriate technique to use in this application.

The variation of permittivity with frequency was found to be consistent with a Debye characteristic. This was to be expected given the high proportion of water in most of the samples measured.

At low frequencies the presence of salt in the curd samples was found to account for most of the measured loss. Above 6 GHz ionic conductivity was overtaken by polar loss as the dominant contributor to the loss factor of the cheese curd.

In the course of this work a novel algorithm has been developed which resolves the ambiguity inherent in many waveguide permittivity measurement techniques. This approach is extremely reliable when used with dispersive dielectrics, less so when used with low permittivity materials having large loss factors.

11.3 Prototype Measurement Hardware

As described in Chapter 4, the computer-controlled six-port reflectometer which was developed for this project demonstrated that the vector reflection coefficient can be measured with a high degree of accuracy using relatively cheap off-the-shelf components. In evaluating the

performance of the six-port under laboratory conditions it was found that the instrument could measure its own calibration standards with an accuracy of better than 1% magnitude error and 1° phase error. This level of performance was contingent on three factors, namely:

- Availability of a stable frequency source. For this project the stimulus frequency was required to be within 0.25% of the nominal value.
- Four of the five calibration standards to be equispaced around the perimeter of the Smith chart (assuming the fifth standard is a matched load).
- Diode detectors to be characterised using recently measured voltage vs power data, preferably at the frequency of interest.

It has been noted that transmission-based measurement techniques can potentially provide superior results to reflection-based approaches. Furthermore, the concept of the Dual Six-Port, examined in Section 4.4, suggests that such techniques may be implemented at relatively low-cost. However, the resources for this project did not allow this possibility to be explored in depth.

11.4 Sensor Geometry

A diverse range of sensor types was investigated before microstrip was selected. Three classes of sensing geometry were examined: reflection, transmission and resonant. The final decision entailed a tradeoff between accuracy, cost and ease of use.

Planar contact sensors were favoured because they are relatively cheap and easy to manufacture. Furthermore, a diverse range of sensor types can be implemented by simply modifying the distribution of copper on the substrate. The limitation of this type of sensor is that analytical models are difficult to develop due to the complicated nature of the fields close to the dielectric interface.

11.5 Quasi-TEM Spectral Domain Analysis of Microstrip

The quasi-TEM spectral domain analysis of microstrip covered by a high-permittivity half-space has been shown to have a number of attractive features. Of the two models developed for this project, the quasi-TEM model was the fastest and the simplest. Furthermore, due to the popularity of the quasi-TEM approach with other workers in the field, a substantial body of knowledge on this technique is available in the literature. This is a valuable resource for the designer who does not necessarily wish to go back to first principles in developing a new sensor.

The fact remains, however, that the static spectral domain analysis is only exact at DC. At all frequencies above DC it is an approximation, and is therefore unable to account for a host of frequency-dependent phenomena. While this was not found to be significant at low frequencies, large differences emerged between the static and full-wave models as frequency increased, as discussed in Section 10.3.

Therefore despite the popularity of quasi-TEM models of microstrip with previous workers in the field, the conclusion must be made that this type of model should be used with caution. This is especially the case with microstrip immersed in a high-permittivity medium, where—as shown in Chapters 7 and 8—the propagation characteristics of the line can be much more complex than would be encountered on air-covered lines.

11.6 Full-Wave Spectral Domain Analysis of Microstrip

The full-wave spectral domain analysis of microstrip has yielded three new features of the propagation characteristics of this type of transmission line when covered by a lossy, high-permittivity material. These properties have been shown to be significant in the design of sensors for the cheese industry. The results of this analysis are also applicable to the study of planar contact sensors in general.

11.6.1 Surface Wave Propagation on Microstrip Sensors

The analysis of the background structure of microstrip presented in Chapter 7 has shown that surface waves can be supported by a grounded dielectric slab even when the covering medium has a higher dielectric constant than the slab. However, this is only possible if the covering medium contains some loss (Horsfield and Ball, 2000). Furthermore, all surface wave modes—including the TM_0 mode—have been shown to possess non-zero cutoff frequencies which decrease as the loss of the covering medium increases. As far as the author is aware, these results have not previously been deduced and appear to be fundamental contributions to the field of microstrip sensor analysis.

The implications of these results for the study of propagation on microstrip are that energy may be leaked from the EH_0 microstrip mode to one or more surface wave modes. While this did not occur in any of the cases considered in the course of this project, the potential for surface wave leakage to occur in other cases could not be completely ruled out. Consequently the spectral domain model of microstrip had to be designed to track the location of the corresponding poles in the spectral plane, so that any attenuation due to surface wave leakage could be captured by the model.

11.6.2 Radiation Leakage

A mathematically rigorous analysis of microstrip (presented in Chapter 8) has shown that the EH_0 mode can leak energy to the space wave if the medium above the line has a permittivity with a real part greater than that of the substrate. Indeed, if the covering medium is lossless, the EH_0 mode radiates at *all* frequencies above DC.

This phenomenon has previously been described by at least two other authors. What does not appear to have been previously explored is the effect of loss in the covering medium on radiation leakage from the EH_0 mode. It has been shown in Section 8.11.3—apparently for the first time—that as the loss factor of the superstrate increases, the EH_0 mode radiates over a diminishing band of frequencies. If the loss factor increases beyond a certain point, all radiation is suppressed and the EH_0 mode becomes completely bound to the substrate.

Simulations of a microstrip sensor covered by methanol revealed that the loss factor of methanol was always large enough to suppress any radiation. In view of this it may seem tempting to suggest that the analysis software could be made simpler and faster by simply integrating along the real axis in all cases, instead of devoting processing time to the monitoring of branch point and pole migrations in the spectral plane. However, this is not recommended as it is not possible to rule out radiation leakage with measurands other than methanol. As a result the analysis software was left unchanged so that the effects of radiation leakage could be captured if necessary.

11.6.3 Leaky Dominant Modes

Leaky dominant microstrip modes were covered briefly in this thesis. It has been demonstrated in Section 8.12 that the cutoff frequencies of these modes depend not only upon the geometry of the sensor, but also upon the dielectric properties of the covering material. It is believed that these insights into the propagation characteristics of leaky dominant modes are original results.

While no such modes were found in simulations with a methanol test liquid, a leaky dominant mode was discovered in a simulation with distilled water. This mode leaked only to the space wave, and was cutoff below 0.19 GHz. The possibility clearly exists for leaky EH_0 modes to propagate when making measurements on cheese curd, if only when the moisture content is high. However, this was not explored in detail during this project, due to the fact that there is not yet any way of knowing precisely when these modes become physically propagating modes. Although previous workers have focused their attention on leaky EH_0 modes which couple to the TM_0 surface wave mode, no work appears to have been performed on leaky EH_0 modes which couple to the space wave.

11.7 Simulation of Sensor S-Parameters

As discussed in Chapter 9, accurate simulation of the S-parameters of a microstrip sensor proved to be a significant challenge. This was largely due to the way in which the sensor was fabricated: the aperture of each microstrip launcher formed part of the test chamber wall, hence the impedance mismatch due to the launchers was not fixed, but instead was a strong function

of the dielectric properties of the material in the test chamber. As a result, initial attempts to simulate the S-parameters of a sensor immersed in methanol did not produce good agreement with experiment. This problem was present in both the static and full-wave sensor models, as evidenced by the results presented in Section 10.4.

The use of an equivalent circuit model to correct for the launcher mismatch improved the agreement considerably. The values of the components in the equivalent circuit model were generally chosen empirically. The exception to this practice was the methanol measurements, where a function based on the Debye equation for polar liquids was used to characterise C and G.

The best agreement between theory and experiment was obtained with the full-wave model of microstrip. By adjusting the coefficients of the launcher admittance function, both S_{11} and S_{21} could be made to agree with the measured values. This was not found to be possible with the static model, where improvements in one set of S-parameters and could only be achieved at the expense of the other set. That said, there was not a great deal to distinguish one sensor model from the other at low frequencies; it was only at frequencies above 2 GHz that the two models began to differ significantly.

11.8 Recommendations for Future Work

A considerable body of evidence has been gathered in support of the underlying proposition of this thesis. The permittivity of cheese curd has been shown to vary significantly with moisture content; a low-cost reflection coefficient measurement system has been built and tested in the laboratory; a simple, easy-to-fabricate sensing head has been chosen; and two different models of this sensor have been developed and compared with measured data, with good agreement.

In carrying out this work, four topics have been identified as suitable areas for future research. These are outlined in the following subsections.

11.8.1 Six-Port Reflectometer

The six-port reflectometer performed well under laboratory conditions. However, a considerable amount of extra work would be needed if this instrument were to be installed in a factory environment.

Firstly, electronic and microwave components should be mounted in a robust enclosure and sealed against the ingress of moisture. Furthermore, this enclosure, along with the microstrip sensor and any exposed cables, must be Clean in Place (CIP); i.e. they must be able to withstand the factory's cleaning and sterilisation process, which usually involves large amounts of water and caustic cleaning agents.

Secondly, the instrument would be more likely to find widespread acceptance if it could be made self-calibrating, obviating the need for factory staff to attach five calibration standards in the correct sequence prior to making measurements. One possible configuration has been outlined in Section 4.15.3, however the practical implementation of this is likely to be a considerable challenge.

Finally, the six-port would be greatly enhanced by the addition of a temperature sensor to either the sensing head or the amplifier board. For the purposes of this project it was assumed that the temperature of the curd was fixed by the production equipment. However, in practice there are likely to be daily or seasonal variations in the mean production temperature. The inclusion of a temperature sensor would enable this variable to be taken into account when calculating the moisture content of the cheese curd.

11.8.2 Propagation on Microstrip Covered by a High-Permittivity Half-Space

The full-wave analysis of microstrip was originally undertaken purely as a means of mapping measured S-parameters to a corresponding value of permittivity. Due to the unusual nature of the problem, however, this became a very complex and time-consuming exercise. At the completion of this project there remain several salient issues which are appropriate subjects for future research.

An analysis should be carried out to determine the extent to which the propagation characteristics of the higher-order modes of microstrip are influenced by the presence of a non-air covering medium.

Leaky dominant modes on microstrip is a current research topic, as discussed in Section 8.12. Due to the tendency of these modes to lose energy to the radiation field, there is a need for a 'physicality condition' which defines precisely where a *radiative* leaky EH_0 mode (as distinct from one which leaks to the TM_0 surface wave mode) begins to assert itself as a physical, propagating mode. Indeed, it is not even clear whether or not a spectral gap exists for these modes on a sensor immersed in a test material.

Similarly, little is known of the dependence of leaky dominant modes on frequency, sensor geometry, and the dielectric properties of the material under test. Further work in this area is warranted for two reasons: one, because it will aid in the accurate characterisation of microstrip sensors; and two, because it will contribute to the basic understanding of propagation on planar transmission lines.

On a less esoteric front, the spectral domain analysis software is too slow in its present form to be used in a real-time environment. This is to be expected, given that the main priority of the full-wave analysis was to maximise the accuracy of the sensor model. Hence, no attention was paid to the program's execution speed. Numerous speedup strategies have been suggested in Chapters 6 and 8 of this thesis. Anyone attempting to incorporate the full-wave software into a real-time instrument would be well advised to revisit the relevant sections in these chapters.

Finally, the sensor model requires a small but important modification before it can be incorporated into a moisture sensing instrument. At present the model can predict the S-parameters of a sensor given the permittivity of the test material (and frequency, sensor geometry etc). In practice, however, the inverse procedure is required; that is, the calculation of sample permittivity from measured S-parameters. Using a solution procedure like the secant method it would be possible to obtain convergence in a small number of iterations.

11.8.3 Sensor Design and Characterisation

The microstrip sensors which were fabricated for this project were not intended to be optimal in any sense. Indeed, the length of the sensors, the width of the strip conductor, and the permittivity and thickness of the substrate were all chosen in a somewhat arbitrary fashion. Consequently there are several potential avenues for future work in this area.

Firstly, the microstrip sensors should be redesigned in such a way that the launching structures are isolated from the material under test. This will make the sensor modelling process simpler and more accurate, as any remaining impedance mismatch due to the launchers will be independent of the material in the test chamber. The selection of the equivalent circuit parameters C and G would still need to be done empirically, but only once. Having determined these parameters at every frequency of interest, all subsequent simulations could be corrected with the same values of C and G.

Secondly, a proper study should be conducted into how the sensor could be optimised for maximum sensitivity. Such a study could not be performed in isolation—some knowledge would be required of the instrument for which the sensor was intended, to ensure that the optimised sensor did not operate beyond the dynamic range of the instrument. Several of the sensor-related publications cited in this thesis contain design curves for microstrip sensors, albeit based on quasi-TEM models. These publications would provide a useful starting point in the design of a sensor optimised for the measurement of cheese curd moisture.

Finally, there is the non-trivial task of preparing the sensor for factory use. Issues to consider include: where to locate the sensor in the production process; how to ensure that the sensor maintains good contact with the curd; and how to ruggedise the sensor to withstand the factory's CIP process.

11.8.4 Cheese Curd Dielectric Model

The two sensor models discussed in Part II of this thesis were both developed with the same objective in mind: to enable the measured S-parameters of a sensor immersed in a test material

to be mapped to a corresponding value of material permittivity. However, little mention has been made of the final step; namely, the mapping of permittivity to a value of moisture content.

To be sure, passing reference has been made to empirical calibration curves which relate permittivity to moisture content, and the results presented in Chapter 3 (in particular the plot of ε_{r} vs moisture content in Figure 3.8) may well be adequate for this purpose. However, generally speaking it has been tacitly assumed that in practice, sufficient calibration data would be available for the instrument to predict moisture content from permittivity.

Thus, one of the key steps in adapting the instrument for commercial use would be to compile a more comprehensive database of cheese curd permittivity data for a wide range of moisture contents (and temperatures, salt contents, frequencies etc). This would entail further rounds of laboratory measurements using the waveguide test cells described in Chapter 3. Alternatively, measurements could be carried out using a microstrip sensor, assuming that the problems with the launcher mismatch discussed in Chapters 9 and 10 could be resolved first.

While the idea of an empirical calibration curve has its merits, there is another way of calculating curd moisture content from permittivity: a dielectric mixing model. This type of model attempts to predict the bulk dielectric properties of a material based on the permittivity of its individual constituents, the relative proportions of those constituents, the microstructure of the material, and density. Obviously this requires a very detailed understanding of the material of interest in order to succeed; hence, the development of a mixing model for cheese curd would require research into the composition and microstructure of the product. Complicating the modelling process is the question of how to account for the presence of bound water, which occurs where the molecules of water are physically restricted by a matrix of other constituents, or are chemically bonded to other molecules of the material (Kraszewski, 1996, pp. 14–17). As a result, bound water has dielectric properties quite different from those of free water.

If the reports of previous workers in this field are anything to go by, the development of an accurate mixing model of cheese curd is likely to be a very challenging task, requiring a number of variables to be taken into account. However, if successful, this model would transform the existing measurement system from a general-purpose permittivity measuring device into a dedicated cheese curd moisture sensing instrument.

References

Abdulnour, J., Akyel, C. and Wu, K. (1995). A generic approach for permittivity measurement of dielectric materials using a discontinuity in a rectangular waveguide or a microstrip line, *IEEE Transactions on Microwave Theory and Techniques* **43**(5): 1060–1066.

Altman, J. L. (1964). *Microwave Circuits*, D. van Nostrand Co., Inc.

Anton, H. and Rorres, C. (1987). *Elementary Linear Algebra with Applications*, John Wiley & Sons, Inc., chapter 2, pp. 72–78.

Baek, K.-H., Sung, H.-Y. and Park, W. S. (1995). A 3-position Transmission/Reflection method for measuring the permittivity of low loss materials, *IEEE Microwave and Guided Wave Letters* **5**(1): 3–5.

Bagby, J. S., Lee, C.-H., Nyquist, D. P. and Yuan, Y. (1993). Identification of propagation regimes on integrated microstrip transmission lines, *IEEE Transactions on Microwave Theory and Techniques* **41**(11): 1887–1894.

Bahl, I. J. and Stuchly, S. S. (1980). Analysis of a microstrip covered with a lossy dielectric, *IEEE Transactions on Microwave Theory and Techniques* **28**(2): 104–109.

Bahl, I. J. and Trivedi, D. K. (1977). A designer's guide to microstrip line, *Microwaves* p. 174.

Baker-Jarvis, J., Vanzura, E. J. and Kissick, W. A. (1990). Improved technique for determining complex permittivity with the Transmission/Reflection method, *IEEE Transactions on Microwave Theory and Techniques* **38**(8): 1096–1103.

Balanis, C. A. (1989). *Advanced Engineering Electromagnetics*, John Wiley & Sons, chapter 8, pp. 414–444.

Ball, J. A. R. and Horsfield, B. (1998). Resolving ambiguity in broadband waveguide permittivity measurements on moist materials, *IEEE Transactions on Instrumentation and Measurement* **47**(2): 390–392.

Ball, J. A. R., Horsfield, B., Holdem, J. R., Keam, R. B., Holmes, W. S. and Green, A. (1996a). Cheese curd permittivity and moisture measurement using a 6-port reflectometer, *Proceedings of the 1996 Asia-Pacific Microwave Conference, New Delhi, India*. (Session B5, Paper No. INV1).

Ball, J. A. R., Horsfield, B., Holdem, J. R., Keam, R. B., Holmes, W. S. and Green, A. (1996b). On-line moisture measurement during cheese production, *Proceedings of the 1996 Conference on Scientific and Industrial RF & Microwave Applications, Melbourne, Australia*.

Berman, M., Somlo, P. I. and Buckley, M. J. (1987). A comparative statistical study of some proposed six-port junction designs, *IEEE Transactions on Microwave Theory and Techniques* **MTT-35**(11): 971–977.

Bialkowski, M. E. and Dimitrios, A. P. (1993). A step-frequency six-port network analyser with a real-time display, *AEÜ* **47**(3).

Bois, K. J., Handjojo, L. F., Benally, A. D., Mubarak, K. and Zoughi, R. (1999). Dielectric plug-loaded two-port transmission line measurement technique for dielectric property characterization of granular and liquid materials, *IEEE Transactions on Instrumentation and Measurement* **48**(6): 1141–1148.

Boughriet, A.-H., Legrand, C. and Chapoton, A. (1997). Noniterative stable Transmission/Reflection method for low-loss material complex permittivity determination, *IEEE Transactions on Microwave Theory and Techniques* **45**(1): 52–57.

Boukamp, J. and Jansen, R. H. (1983). Spectral domain investigation of surface wave excitation and radiation by microstrip lines and microstrip disk resonators, *Proceedings of the 13th European Microwave Conference*, pp. 721–726.

Brunetti, L. (1991). Six-port reflectometer: Some geometric Γ-estimators, *IEEE Transactions on Instrumentation and Measurement* **40**(5): 866–869.

Chan, W. F. P. and Chambers, B. (1987). Measurement of nonplanar dielectric samples using an open resonator, *IEEE Transactions on Microwave Theory and Techniques* **MTT-35**(12): 1429–1434.

Colef, G., Karmel, P. R. and Ettenberg, M. (1990). New *in-situ* calibration of diode detectors used in six-port network analyzers, *IEEE Transactions on Instrumentation and Measurement* **39**(1): 201–204.

Collin, R. E. (1991). *Field Theory of Guided Waves*, 2nd edn, IEEE Press.

Cook, R. J., Jones, R. G. and Rosenberg, C. B. (1974). Comparison of cavity and open-resonator measurements of permittivity and loss angle at 35 GHz, *IEEE Transactions on Instrumentation and Measurement* **IM-23**(4): 438–442.

Cullen, A. L. and Yu, P. K. (1971). The accurate measurement of permittivity by means of an open resonator, *Proc. R. Soc. Lond.* **325**: 493–509.

Das, N. K. and Pozar, D. M. (1991). Full-wave spectral-domain computation of material, radiation, and guided wave losses in infinite multilayered printed transmission lines, *IEEE Transactions on Microwave Theory and Techniques* **39**(1): 54–63.

Davis, M. E., Williams, E. W. and Celestini, A. C. (1973). Finite-boundary corrections to the coplanar waveguide analysis, *IEEE Transactions on Microwave Theory and Techniques* **MTT-21**: 594–596.

Denlinger, E. J. (1971). A frequency dependent solution for microstrip transmission lines, *IEEE Transactions on Microwave Theory and Techniques* **MTT-19**(1): 30–39.

Deshpande, M. D., Reddy, C. J., Tiemsin, P. I. and Cravey, R. (1997). A new approach to estimate complex permittivity of dielectric materials at microwave frequencies using waveguide measurements, *IEEE Transactions on Microwave Theory and Techniques* **45**(3): 359–366.

Dupuis, P. A. J. and Campbell, C. K. (1973). Characteristic impedance of surface-strip coplanar waveguides, *Electronics Letters* **9**(16): 354–355.

Enders, A. (1989). An accurate measurement technique for line properties, junction effects, and dielectric and magnetic material parameters, *IEEE Transactions on Microwave Theory and Techniques* **37**(3): 598–605.

Engen, G. F. (1976). Determination of microwave phase and amplitude from power measurements, *IEEE Transactions on Instrumentation and Measurement* **IM-25**(4): 414–418.

Engen, G. F. (1977a). An improved circuit for implementing the six-port technique of microwave measurements, *IEEE Transactions on Microwave Theory and Techniques* **MTT-25**: 1080–1083.

Engen, G. F. (1977b). The six-port reflectometer: An alternative network analyzer, *IEEE Transactions on Microwave Theory and Techniques* **MTT-25**(12): 1075–1080.

Engen, G. F. (1978a). Calibrating the six-port reflectometer by means of sliding terminations, *IEEE Transactions on Microwave Theory and Techniques* **MTT-26**: 951–957.

Engen, G. F. (1978b). The six-port measurement technique – a status report, *Microwave Journal* **21**: 18–89.

Engen, G. F. and Hoer, C. A. (1972). Application of an arbitrary six-port junction to power measurement problems, *IEEE Transactions on Instrumentation and Measurement* **IM-21**: 470–474.

Gajda, G. and Stuchly, S. S. (1983). An equivalent circuit of an open-ended coaxial line, *IEEE Transactions on Instrumentation and Measurement* **IM-32**(4): 506–508.

Ghannouchi, F. M. and Bosisio, R. G. (1989). Measurement of microwave permittivity using a six-port reflectometer with an open-ended coaxial line, *IEEE Transactions on Instrumentation and Measurement* **38**(2).

Ghannouchi, F. M. and Bosisio, R. G. (1991). A wideband millimeter wave six-port reflectometer using four diode detectors calibrated without a power ratio standard, *IEEE Transactions on Instrumentation and Measurement* **40**(6): 1043–1046.

Ghione, G. and Naldi, C. (1983). Parameters of coplanar waveguides with lower ground plane, *Electronics Letters* **19**(18): 734–735.

Grimm, J. M. and Nyquist, D. P. (1993). Spectral analysis considerations relevant to radiation and leaky modes of open-boundary microstrip transmission line, *IEEE Transactions on Microwave Theory and Techniques* **41**(1): 150–153.

Hallikainen, M. T., Ulaby, F. T. and Abdelrazik, M. (1986). Dielectric properties of snow in the 3 to 37 GHz range, *IEEE Transactions on Antennas and Propagation* **AP-34**(11): 1329–1340.

Hallikainen, M. T., Ulaby, F. T., Dobson, M. C., El-Rayes, M. A. and Wu, L.-K. (1985). Microwave dielectric behaviour of wet soil—Part I: Empirical models and experimental observations, *IEEE Trans. Geosci. Remote Sensing* **23**: 25–34.

Hashimoto, M. (1985). A rigorous solution for dispersive microstrip, *IEEE Transactions on Microwave Theory and Techniques* **MTT-33**(11): 1131–1137.

Hasted, J. B. (1973). *Aqueous Dielectrics*, Chapman and Hall, London.

Hatsuda, T. (1975). Computation of coplanar-type strip-line characteristics by relaxation method and its application to microwave circuits, *IEEE Transactions on Microwave Theory and Techniques* **MTT-23**(10): 795–802.

Hewlett-Packard Corporation (1985). Measuring the dielectric constant of solids with the HP 8510 network analyzer, *Hewlett-Packard Product Note 8510-3* .

Hewlett-Packard Corporation (1992). *HP 8719C, HP 8720C, HP 8722A/C Network Analyser Operating Manual*, 2nd edn, Hewlett-Packard Corporation, 1400 Fountaingrove Parkway, Santa Rosa, CA 95403, U.S.A.

Hewlett-Packard Corporation (1993). *HP 85070M Dielectric Probe Measurement System / HP 85070B High-Temperature Dielectric Probe Kit : Technical Data*, Hewlett-Packard Corporation.

Holdem, J. and Tuck, D. L. (1992). Improvement to microwave measurement of carcass fat thickness, *Proceedings of AIM '92 Conference*, Auckland, New Zealand.

Horsfield, B. and Ball, J. A. R. (2000). Surface wave propagation on a grounded dielectric slab covered by a high-permittivity material, *IEEE Microwave and Guided Wave Letters* **10**(5): 171–173.

Horsfield, B., Ball, J. A. R., Holmes, W. S., Green, A., Holdem, J. R. and Keam, R. B. (1996). A technique for measuring cheese curd moisture in real time, *Proceedings of the 1996 Conference on Engineering in Agriculture and Food Processing, Gatton, Australia*. (Paper No. SEAg 96/065).

Huang, J., Wu, K., Morin, P. and Akyel, C. (1996). Characterization of highly dispersive materials using composite coaxial cells: Electromagnetic analysis and wideband measurement, *IEEE Transactions on Microwave Theory and Techniques* **44**(5): 770–777.

Hunter, J. D. and Somlo, P. I. (1985). An explicit six-port calibration method using five standards, *IEEE Transactions on Microwave Theory and Techniques* **MTT-33**(1): 69–72.

Itoh, T. (1989). *Numerical Techniques for Microwave and Millimeter-Wave Passive Structures*, John Wiley & Sons, chapter 4, pp. 355–356.

Itoh, T. and Mittra, R. (1973). Spectral-domain approach for calculating the dispersion characteristics of microstrip lines, *IEEE Transactions on Microwave Theory and Techniques* pp. 496–499.

Janezic, M. D. and Jargon, J. A. (1999). Complex permittivity determination from propagation constant measurements, *IEEE Microwave and Guided Wave Letters* **9**(2): 76–78.

Jansen, R. H. (1978). High speed computation of single and coupled microstrip parameters including dispersion, higher order modes, loss and finite strip thickness, *IEEE Transactions on Microwave Theory and Techniques* **MTT-26**: 75–87.

Jarem, J. M., Johnson, J. B. and Albritton, W. S. (1995). Measuring the permittivity and permeability of a sample at K_a band using a partially filled waveguide, *IEEE Transactions on Microwave Theory and Techniques* **43**(12): 2654–2667.

Jordan, B. P., Sheppard, R. J. and Szwarnowski, S. (1978). The dielectric properties of formamide, ethanediol and methanol, *Journal of Physics D: Applied Physics* **11**: 695–701.

Kaatze, U. (1989). Complex permittivity of water as a function of frequency and temperature, *Journal of Chemical and Engineering Data* **34**: 371–374.

Ke, J.-Y., Tsai, I.-S. and Chen, C. H. (1992). Dispersion and leakage characteristics of coplanar waveguides, *IEEE Transactions on Microwave Theory and Techniques* **40**(10): 1970–1973.

Kent, M. (1972). The use of strip-line configurations in microwave moisture measurement, *Journal of Microwave Power* **7**(3): 185–193.

Kent, M. (1973). The use of strip-line configuration in microwave moisture measurements II, *Journal of Microwave Power* **8**(2): 189–194.

Kent, M., Elder, B., Leonard, C., Lees, A. and Christie, R. H. (1993). An On-line microwave instrument to monitor the solids contents of milk products during processing, *Journal of the Society of Dairy Technology* **46**(3): 96–99.

Kent, M. and Price, T. E. (1979). Compact microstrip sensor for high moisture content materials, *Journal of Microwave Power* **14**(4): 363–365.

Khalid, K. B., Maclean, T. S. M., Razaz, M. and Webb, P. W. (1988). Analysis and optimal design of microstrip sensors, *IEE Proceedings* **135, Part H**(3): 187–195.

Knorr, J. B. and Kuchler, K.-D. (1975). Analysis of coupled slots and coplanar strips on dielectric substrate, *IEEE Transactions on Microwave Theory and Techniques* **MTT-23**(7): 541–548.

Kraszewski, A. (ed.) (1996). *Microwave Aquametry: Electromagnetic Wave Interaction with Water-Containing Materials*, IEEE Press.

Kraszewski, A. W. and Nelson, S. O. (1992). Observations on resonant cavity perturbation by dielectric objects, *IEEE Transactions on Microwave Theory and Techniques* **40**(1): 151–155.

Kraszewski, A. W. and Nelson, S. O. (1993). Nondestructive microwave measurement of moisture content and mass of single peanut kernels, *Transactions of the ASAE* **36**(1): 127–134.

Kraszewski, A. W. and Nelson, S. O. (1994). Microwave resonator technique for moisture content and mass determination in single soybean seeds, *IEEE Transactions on Instrumentation and Measurement* **43**(3): 487–489.

Kraszewski, A. W., Nelson, S. O. and You, T.-S. (1989). Sensing dielectric properties of arbitrarily shaped biological objects with a microwave resonator, *IEEE MTT-S International Microwave Symposium Digest* **1**: 187–190.

Kraszewski, A. W., Nelson, S. O. and You, T.-S. (1990). Use of a microwave cavity for sensing dielectric properties of arbitrarily shaped biological objects, *IEEE Transactions on Microwave Theory and Techniques* **38**(7): 858–863.

Kraszewski, A. W., You, T.-S. and Nelson, S. O. (1989). Microwave resonator technique for moisture content determination in single soybean seeds, *IEEE Transactions on Instrumentation and Measurement* **IM-38**(1): 79–84.

Kraus, J. D. (1984). *Electromagnetics*, 3rd edn, McGraw-Hill.

Kress-Rogers, E. (1993). *Instrumentation and Sensors for the Food Industry*, Butterworth-Heinemann Ltd, chapter 7, pp. 191–193.

Kreyszig, E. (1993). *Advanced Engineering Mathematics*, 7th edn, John Wiley & Sons.

Ku, H. S., Ball, J. A. R., Siores, E. and Horsfield, B. (1999). Microwave processing and permittivity measurement of thermoplastic composites at elevated temperature, *Journal of Materials Processing Technology* **89-90**: 419–424.

Ku, H. S., Horsfield, B., Ball, J. A. R. and Siores, E. (2001). Permittivity measurement of thermoplastic composites at elevated temperature, *Journal of Microwave Power and Electromagnetic Energy* **36**(2): 101–111.

Ku, H. S., Siores, E., Ball, J. A. R. and Horsfield, B. (1998). An important step in microwave processing of materials: Permittivity measurements of thermoplastic composites at elevated temperatures, *Proceedings of the 1998 Pacific Conference on Manufacturing, Brisbane, Australia*, pp. 68–73.

Kudra, T., Raghavan, V., Akyel, C., Bosisio, R. and van de Voort, F. (1992). Electromagnetic properties of milk and Its constituents at 2.45 GHz, *Journal of Microwave Power and Electromagnetic Energy* **27**(4): 199–204.

Labaar, F. (1984). The exact solution to the six-port equations, *Microwave Journal* pp. 219–228.

Lin, Y.-D. and Sheen, J.-W. (1994). Surface wave leakage of coplanar waveguide with nearby back conductor plane, *IEEE MTT-S International Microwave Symposium Digest*, pp. 1701–1704.

Lin, Y.-D. and Sheen, J.-W. (1997). Mode distinction and radiation-efficiency analysis of planar leaky-wave line source, *IEEE Transactions on Microwave Theory and Techniques* **45**(10): 1672–1680.

Lynch, A. C. (1983). Measurement of permittivity using an open resonator, *IEE Proceedings* **130**(7): 365–368.

Marsland, T. P. and Evans, S. (1987). Dielectric measurements with an open-ended coaxial probe, *IEE Proceedings–H* **134**(4): 341–349.

McMillan, L. O. (1998). *Microstrip Leaky Wave Antennas: Half Spaces and Focusing Applicators*, PhD thesis, University of Queensland Department of Computer Science and Electrical Engineering.

Meixner, J. (1972). The behaviour of electromagnetic fields at edges, *IEEE Transactions on Antennas and Propagation* **AP-20**(4): 442–446.

Mesa, F., Di Nallo, C. and Jackson, D. R. (1999). The theory of surface-wave and space-wave leaky-mode excitation on microstrip lines, *IEEE Transactions on Microwave Theory and Techniques* **47**(2): 207–215.

Meyer, W. and Schilz, W. (1980). A microwave method for density independent determination of the moisture content of solids, *Journal of Physics D: Applied Physics* **13**: 1823–1830.

Michalski, K. A. and Zheng, D. (1989). Rigorous analysis of open microstrip lines of arbitrary cross section in bound and leaky regimes, *IEEE Transactions on Microwave Theory and Techniques* **37**(12): 2005–2010.

Mirshekar-Syahkal, D. (1986). Dispersion in shielded coupled coplanar waveguides, *Electronics Letters* **22**(7): 358–360.

Mirshekar-Syahkal, D. (1990). *Spectral Domain Method for Microwave Integrated Circuits*, Research Studies Press.

Mirshekar-Syahkal, D. and Davies, J. B. (1979). Accurate solution of microstrip and coplanar structures for dispersion and for dielectric and conductor losses, *IEEE Transactions on Microwave Theory and Techniques* **MTT-27**(7): 694–699.

Moreau, J.-M., Idriss, A. E. and Tibaudo, C. (1994). Permittivity measurements of materials during heating by microwaves, *Measurement Science and Technology* **5**.

Mosig, J. R., Besson, J.-C. E., Gex-Fabry, M. and Gardiol, F. E. (1981). Reflection of an open-ended coaxial line and application to nondestructive measurement of materials, *IEEE Transactions on Instrumentation and Measurement* **IM-30**(1): 46–51.

Ness, J. (1983). Broadband permittivity measurements at microwave frequencies, *IREE Conference Digest*, pp. 330–332.

Ness, J. (1985). Broadband permittivity measurements using the semi-automatic network analyser, *IEEE Transactions on Microwave Theory and Techniques* **33**(11): 1222–1226.

Neumayer, B. (1990). A new analytical method for complete six-port reflectometer calibration, *IEEE Transactions on Instrumentation and Measurement* **39**(2).

Nghiem, D., Williams, J. T. and Jackson, D. R. (1993). Proper and improper dominant mode solutions for a stripline with an air gap, *Radio Science* **28**(6): 1163–1180.

Nghiem, D., Williams, J. T., Jackson, D. R. and Oliner, A. A. (1995). Leakage of the dominant mode on stripline with a small air gap, *IEEE Transactions on Microwave Theory and Techniques* **43**(11): 2549–2556.

Nghiem, D., Williams, J. T., Jackson, D. R. and Oliner, A. A. (1996). Existence of a leaky dominant mode on microstrip line with an isotropic substrate: Theory and measurements, *IEEE Transactions on Microwave Theory and Techniques* **44**(10): 1710–1715.

Nicolson, A. M. and Ross, G. F. (1970). Measurement of the intrinsic properties of materials by time-domain techniques, *IEEE Transactions on Instrumentation and Measurement* **IM-19**(4): 377–382.

Nyfors, E. and Vainikainen, P. (1989). *Industrial Microwave Sensors*, Artech House, Inc.

Oliner, A. A. and Lee, K. S. (1986). The nature of the leakage from higher order modes on microstrip line, *IEEE MTT-S International Microwave Symposium Digest*, Institute of Electrical and Electronic Engineers, New York, pp. 57–60.

Potter, C. M. (n.d.). *Six-Port Principles and the Architecture of the 6210 Reflection Analyzer*, Marconi Instruments Limited. Publication No. 46889-468.

Pozar, D. M. (1990). *Microwave Engineering*, Addison-Wesley.

Pregla, R. and Pintzos, S. G. (1974). Determination of the propagation constants in coupled microslots by a variational method, *Proceedings of the Fifth Colloquium on Microwave Communication, Budapest*, pp. 491–500.

Pucel, R. A., Massé, D. J. and Hartwig, C. P. (1968). Losses in microstrip, *IEEE Transactions on Microwave Theory and Techniques* **MTT-16**(6): 342–350.

Robinson, A. W. and Bialkowski, M. E. (1992). An investigation into microwave moisture measurements, *1992 Asia-Pacific Microwave Conference, Adelaide*, pp. 571–574.

Sabburg, J., Ball, J. A. R. and Ness, J. B. (1992). Broadband permittivity measurements of wet soils, *1992 Asia-Pacific Microwave Conference*, pp. 607–610.

Shigesawa, H., Tsuji, M. and Oliner, A. A. (1993). The nature of the spectral gap between bound and leaky solutions when dielectric loss is present in printed-circuit lines, *Radio Science* **28**(6): 1235–1243.

Shigesawa, H., Tsuji, M. and Oliner, A. A. (1995). Simultaneous propagation of bound and leaky dominant modes on printed-circuit lines: A new general effect, *IEEE Transactions on Microwave Theory and Techniques* **43**(12): 3007–3019.

Somlo, P. I. (1996). Brief outline of six-port impedance measurements, *Proceedings of the 1996 Conference on Scientific and Industrial RF & Microwave Applications, Melbourne*.

Somlo, P. I. and Hunter, J. D. (1982). A six-port reflectometer and its complete characterization by convenient calibration procedures, *IEEE Transactions on Microwave Theory and Techniques* **MTT-30**(2): 186–192.

Somlo, P. I. and Hunter, J. D. (1985). *Microwave Impedance Measurement*, Peter Peregrinus Ltd.

Stuchly, M. A., Brady, M. M., Stuchly, S. S. and Gajda, G. (1982). Equivalent circuit of an open-ended coaxial line in a lossy dielectric, *IEEE Transactions on Instrumentation and Measurement* **IM-31**(2): 116–119.

Stuchly, M. A. and Stuchly, S. S. (1980). Coaxial line reflection methods for measuring dielectric properties of biological substances at radio and microwave frequencies – a review, *IEEE Transactions on Instrumentation and Measurement* **IM-29**(3): 176–183.

Sydenham, P. H., Hancock, N. H. and Thorn, R. (1989). *Introduction to Measurement Science and Engineering*, John Wiley & Sons.

Tarr, L. W. (1983). An automated six-port for 2-18 GHz power and complex reflection coefficient measurements, *IEEE Transactions on Instrumentation and Measurement* **IM-32**(1): 162–164.

Tsuji, M. and Shigesawa, H. (1993). Simultaneous propagation of both bound and leaky dominant modes on conductor-backed coplanar strips, *IEEE MTT-S International Microwave Symposium Digest* **V**: 1295–1298.

Veyres, C. and Hanna, V. F. (1980). Extension of the application of conformal mapping techniques to coplanar lines with finite dimensions, *International Journal of Electronics* **48**(1): 47–56.

Wan, C., Nauwelaers, B., De Raedt, W. and Van Rossum, M. (1998). Two new measurement methods for explicit determination of complex permittivity, *IEEE Transactions on Microwave Theory and Techniques* **46**(11): 1614–1619.

Weir, W. B. (1974). Automatic measurement of complex dielectric constant and permeability at microwave frequencies, *Proceedings of the IEEE* **62**(1): 33–36.

Wen, C. P. (1969). Coplanar waveguide: A surface strip transmission line suitable for nonreciprocal gyromagnetic device applications, *IEEE Transactions on Microwave Theory and Techniques* **MTT-17**(12): 1087–1090.

Woods, D. (1979). Analysis and calibration theory of the general 6-port reflectometer employing four amplitude detectors, *Proceedings of the IEE* **126**(2).

Xu, Y., Bosisio, R. G. and Bose, T. K. (1991). Some calculation methods and universal diagrams for measurement of dielectric constants using open-ended coaxial probes, *IEE Proceedings–H* **138**(4): 356–360.

Yakabe, T., Kinoshita, M. and Yabe, H. (1994). Complete calibration of a six-port reflectometer with one sliding load and one short, *IEEE Transactions on Microwave Theory and Techniques* **42**(11).

Yamashita, E. (1968). Variational method for the analysis of microstrip-like transmission lines, *IEEE Transactions on Microwave Theory and Techniques* **MTT-16**(8): 529–535.

Yamashita, E. and Mittra, R. (1968). Variational method for the analysis of microstrip lines, *IEEE Transactions on Microwave Theory and Techniques* **MTT-16**(4): 251–256.

Zehentner, J., Macháč, J. and Migliozzi, M. (1998). Upper cutoff frequency of the bound wave and new leaky wave on the slotline, *IEEE Transactions on Microwave Theory and Techniques* **46**(4): 378–386.

Appendix A

Guide to Thesis Companion Disk

The following is a guide to the companion CD-ROM for this thesis, containing the most important computer programs from each phase of the project. Both the source code and executable files are included. Where appropriate, files containing input data for each program are also provided. Auxiliary software such as GPIB control programs and hardware diagnostic routines have been omitted.

All programs will run under Windows 95/98. Hardware requirements are modest: a Pentium 166 with 16 MB of RAM should be more than sufficient for most of the programs on the CD-ROM, although the full-wave spectral domain software would benefit from a faster processor.

To run a program it is recommended that the entire directory containing the executable file be copied to the user's hard drive. This will ensure that all the necessary input files are available for the program, and that the program can save results to disk if required.

NOTE: When files are copied from CD-ROM to hard disk, each file is marked 'read-only' by default. *It is strongly recommended that all files be changed to 'read-write' before attempting run any of the programs from the companion CD-ROM.*

Throughout the project all programs underwent a constant process of modification and augmentation; very few reached a stage where they could be said to be 'finished'. As such, most of the programs on the companion CD-ROM do not have much in the way of a user interface.

Indeed, in many cases the simulation parameters can only be changed by editing the source code and recompiling the program.

A.1 Chapter 3 Software

S-Parameter to Permittivity Converter

Program Name: newton3.exe

Location: \Chapter3\newton3

Source Files: newton3.ide, newton3.cpp

Compiler: Borland C++ ver. 4.52

Description: Converts measured S-parameters of waveguide test cells to complex permittivity. For more information see the file 'readme.txt' in the above directory.

Simulation of S_{21} of Rectangular Waveguide

Program Name: s21.exe

Location: \Chapter3\s21

Source Files: s21.ide, s21.cpp, egavga.bgi

Compiler: Borland C++ ver. 4.52

Description: Plots S_{21} of rectangular waveguide filled with an arbitrary dielectric. Program requires a tab-delimited text file containing frequency and permittivity data as one of its inputs. Results are stored to a .sim file of the same name as the input file. For more information refer to the file 'readme.txt' in the above directory.

Distilled Water Permittivity Calculator

Program Name: consts.exe

Location: \Chapter3\consts

Source Files: consts.ide, consts.cpp, h2oconsts.cpp, egavga.bgi

Compiler: Borland C++ ver. 4.52

Description: Plots permittivity of deionised distilled water against frequency using Debye parameters from Hasted (1973). User can specify any temperature from 0–75°C. Program stores results to file if desired.

A.2 Chapter 4 Software

Six-Port Reflectometer Control & Data Acquisition Program

Program Name: caldata.exe (Note: exe file not included on CD-ROM as it requires the prototype six-port hardware, and the PC30AT board and drivers.)

Location: \Chapter4\caldata

Source Files: caldata.mak, caldata.c, find_min.c, yigfreq.c, pc30at.c, pc30at.h, yig.h

Compiler: Microsoft QuickC ver. 2.5

Description: Control program for prototype six-port reflectometer. Allows user to 'dial up' desired oscillator frequency and measure diode voltages. Program will also read in diode linearisation data from file and convert measured voltages to power levels. To account for the effects of drift, the program will recalibrate itself at the user's request by relocating the standing wave nulls on the frequency stabilisation circuit.

Simulation of Hybrid-Based Six-Port

Program Name: hybrid1.exe

Location: \Chapter4\hybrid1

Source Files: hybrid1.ide, hybrid1.cpp

Compiler: Borland C++ ver. 4.52

Description: Simulate performance of six-port reflectometer with topology based on that of Engen (1977a). Program requires input file 'refco.dat', containing complex reflection coefficients of calibration standards at frequency of interest. Simulated diode power outputs stored to the file 'stdpower.dat'.

Calibration Software

Program Name: calib1.exe

Location: \Chapter4\calib1

Source Files: calib1.ide, calib1.cpp

Compiler: Borland C++ ver. 4.52

Description: Calculate calibration constants for six-port reflectometer. Program requires the input files 'refco.dat' and 'stdpower.dat'. These files contain the complex reflection coefficients of the calibration standards, and the power levels measured by the diode detectors. Calibration constants are stored to the file 'calcnsts.dat'. Program also creates a file called 'graph.dat', containing 15 constants for creating a plot of the three six-port circles in the Γ-plane.

Plot Six-Port Circles in the Complex Γ-Plane

Program Name: circles2.exe

Location: \Chapter4\circles2

Source Files: circles2.ide, circles2.cpp, egavga.bgi

Compiler: Borland C++ ver. 4.52

Description: Performs graphical check of calibration procedure by plotting the three six-port circles in the complex plane for each of the five calibration standards. Calculated value of Γ for each standard is printed at the bottom of the screen and compared with the true value. Program requires the input files 'refco.dat', 'stdpower.dat', 'graph.dat' and 'calcnsts.dat'.

A.3 Chapter 6 Software

Program Name: static.exe

Location: \Chapter6

Source Files: static.ide, static.cpp, basispak.cpp, mathpack.cpp, mstrip.h, basispak.h, mathpack.h

Compiler: Borland C++ ver. 4.52

Description: Quasi-TEM spectral domain analysis of microstrip covered by an arbitrary dielectric. Calculates propagation coefficient, characteristic impedance, effective permittivity, capacitance and S-parameters. Program can sweep frequency, superstrate permittivity, $2w/d$ ratio, or any combination thereof. Eleven output files are created by this program; see the file 'readme.txt' in the above directory for details.

A.4 Chapter 7 Software

TM Surface Wave Solver

Program Name: surface4.exe

Location: \Chapter7\surface4

Source Files: surface4.ide, surface4.cpp

Compiler: Borland C++ ver. 4.52

Description: Solves for the TM surface wave modes on a grounded dielectric slab covered by an arbitrary dielectric. Program calculates propagation coefficient, effective permittivity and cutoff wavenumbers in the top and bottom regions. Possible to sweep frequency, substrate permittivity, superstrate permittivity, or any combination thereof. Output stored to 'dump.dat'. The last value calculated is stored to the file 'kcinit.dat', to be used as the starting estimate for the next program run.

TE Surface Wave Solver

Program Name: surface5.exe

Location: \Chapter7\surface5

Source Files: surface5.ide, surface5.cpp

Compiler: Borland C++ ver. 4.52

Description: Solves for the TE surface wave modes on a grounded dielectric slab covered by an arbitrary dielectric. Program calculates propagation coefficient, effective permittivity and cutoff wavenumbers in the top and bottom regions. Possible to sweep frequency, substrate permittivity, superstrate permittivity, or any combination thereof. Output stored to 'out.dat'. The last value calculated is stored to the file 'kcinit.dat', to be used as the starting estimate for the next program run.

A.5 Chapter 8 Software

Full-Wave Spectral Domain Analysis of Microstrip

Program Name: open4.exe

Location: \Chapter8

Source Files: open4.ide, open4.cpp, spectral.cpp, mathpack.cpp, basispak.cpp, surface.cpp, open4.h, spectral.h, mathpack.h, basispak.h, surface.h, mstrip.h

Compiler: Borland C++ ver. 4.52

Description: Full-wave spectral domain analysis of microstrip covered by an arbitrary dielectric. Able to account for the effects of dispersion, leakage to the TM_0 surface wave mode, radiation and dielectric loss. Calculates propagation coefficient, effective permittivity, characteristic impedance, S-parameters, *ABCD* parameters and the E-field around the sensor. Program can sweep frequency, superstrate permittivity, substrate permittivity, or any combination thereof. Depending on the options selected, this program may

produce as many as 16 output files. See the file 'readme.txt' in the above directory for details.

A.6 Chapter 9 Software

MATLAB Script to Simulate Sensor S-Parameters

Main Script: sensor3.m

Associated Scripts: debye.m, probe5.m, getSraw.m, getdata.m, stot2.m, ABCD2S.m, cmplx2db.m

Location: \Chapter9

Platform: MATLAB for Windows ver. 4.2c.1

Description: Simulation of S-parameters of a microstrip sensor immersed in methanol, taking into account mismatch due to microstrip launchers at either end of sensor. Script reads in ABCD parameters of methanol-covered section of sensor as calculated by full-wave spectral domain model. Microstrip launchers are modelled as 9.5 mm lengths of coax in series with shunt components C and G. Values of C and G are determined from a semi-empirical function based on the Debye equation for polar liquids. Script produces six graphs: C, G, S_{11} magnitude, S_{11} phase, S_{21} magnitude, and S_{21} phase. Measured S-parameters are plotted for comparison.

A.7 Softcopy of Dissertation

File Name: thesis.ps

File Format: PostScript

Location: \Dissertation

Description: This thesis is available in electronic form on the companion CD-ROM. The file format used is **PostScript**, so special viewing software must be installed on the user's PC in order to read and/or print the file. One of the better viewers available (for Windows 95/98) is GSview32. This program can be downloaded free from the Internet. A copy has been included on the companion CD-ROM in the directory \Dissertation\Viewer. Simply run the programs **gs601w32.exe** and **gsv34w32.exe** (in that order), and follow the on-screen instructions.

Appendix B

Cheddar Cheese Permittivity Measurements

The following graphs display the results of permittivity measurements which were performed on samples of low-fat cheddar cheese curd. The same measurement setup was used as that described in Chapter 3. All curd samples were obtained from the Dairy Farmers factory in Toowoomba. Samples were taken before and after the addition of salt to the curd, to demonstrate the impact of this ingredient on the bulk dielectric properties of cheddar cheese curd.

The measurements presented here are not as extensive as those performed on cream cheese curd. Indeed, no measurements at all were conducted in the WR159 band. This was because the intention of the cheddar cheese measurements was simply to establish whether this curd type exhibited similar dielectric properties to cream cheese curd.

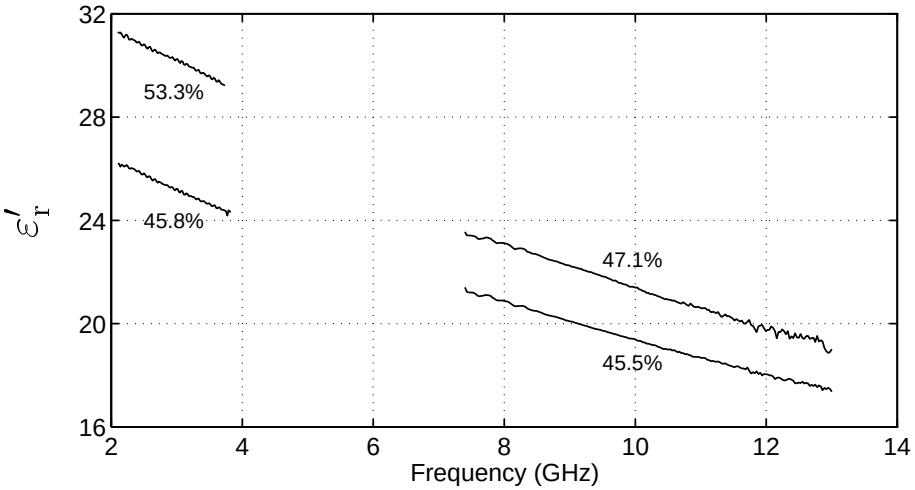

(a) Real part.

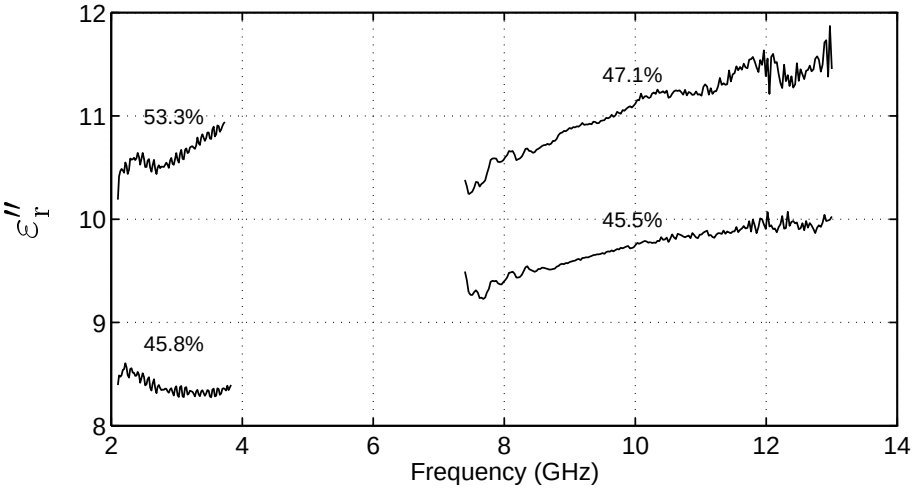

(b) Imaginary part.

Figure B.1: Permittivity of low-fat cheddar cheese curd with no additional salt added. Measurements were performed at the production temperature of 36°C.

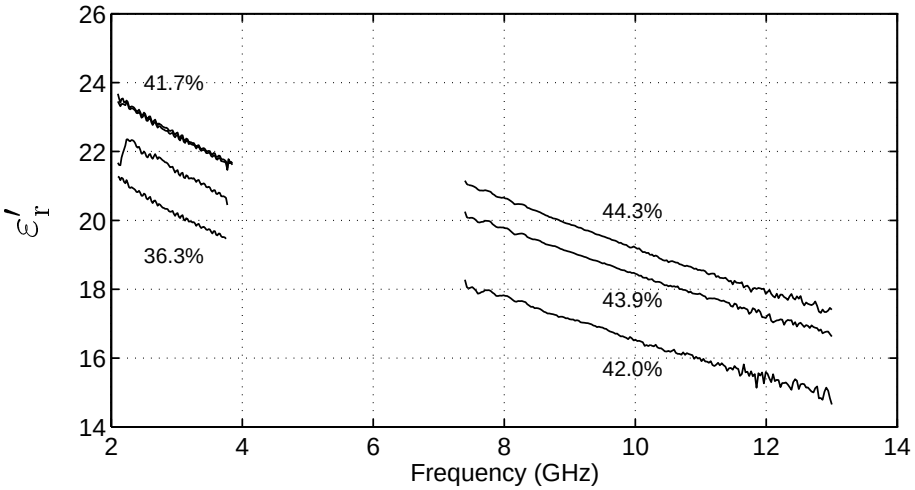

(a) Real part.

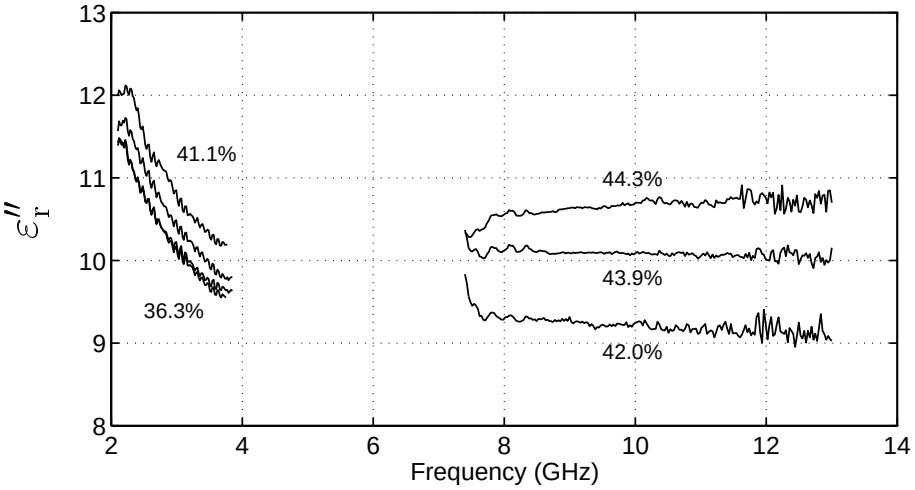

(b) Imaginary part.

Figure B.2: Permittivity of low-fat cheddar cheese curd after the addition of extra salt. Measurements were performed at the production temperature of 32–34°C.

Appendix C

Circuit Schematics and PCB Artwork

C.1 Six-Port Reflectometer Power Supply Schematic

The circuit diagram for the six-port reflectometer power supply is given in Figure C.1 on the following page. This diagram illustrates how the power rails from the PC30AT card in the PC controller were utilised to obtain the required voltage levels for the YIG-tuned oscillator and detector amplifiers.

The detector amplifiers themselves are not depicted in Figure C.1. Instead, these circuit elements were inserted directly into the PCB artwork for the amplifier board using a stock circuit design from Industrial Research Limited in Auckland, New Zealand. Consequently, the five A/D converter pins on the amplifier board are also omitted from the diagram.

The power supply schematic was designed in collaboration with John Holdem at Industrial Research Limited.

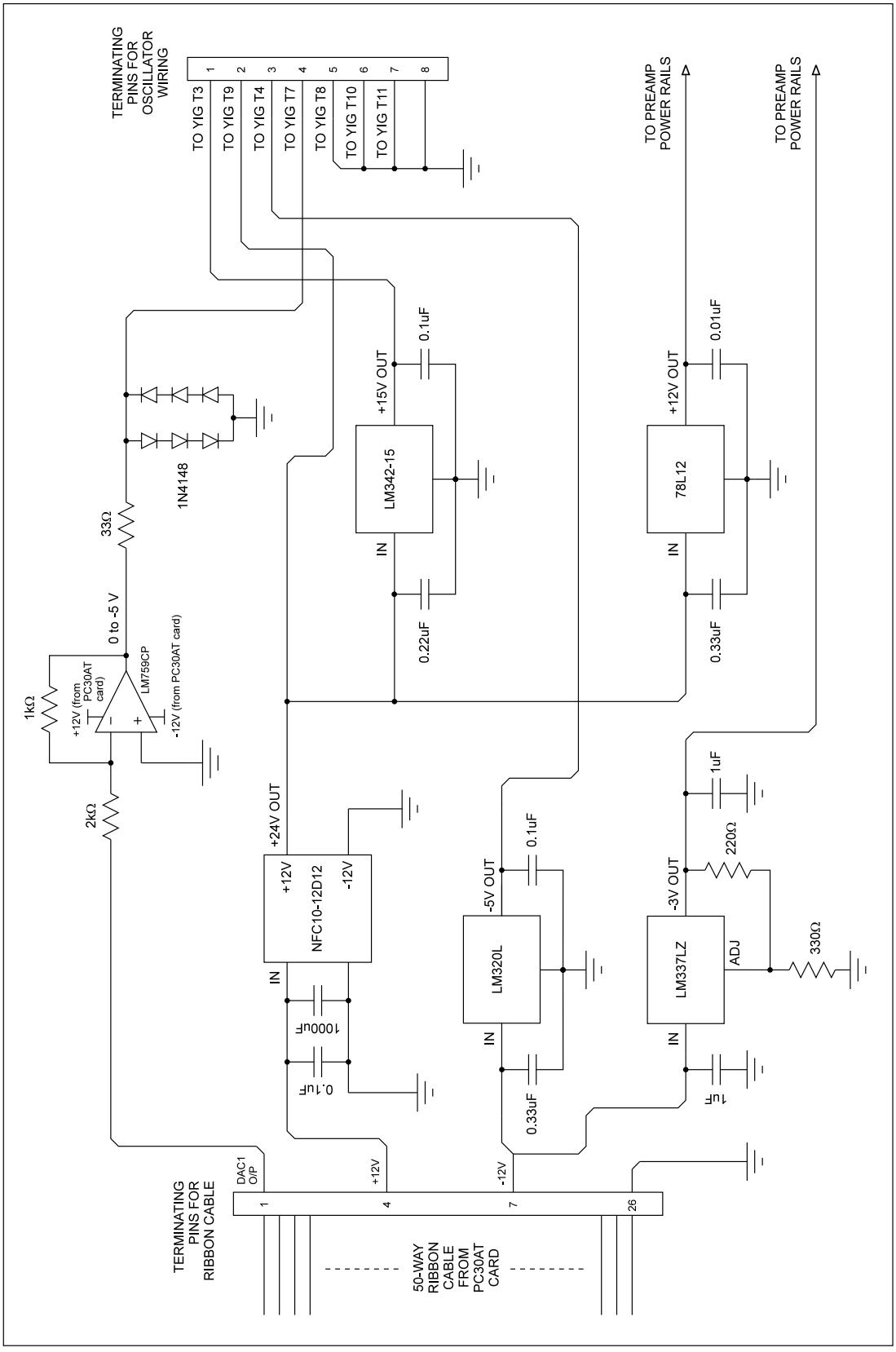

Figure C.1: Schematic of power supply on six-port reflectometer amplifier board.

C.2 PCB Artwork

Detector Amplifier Board

The PCB artwork for the six-port reflectometer amplifier board is presented in Figures C.2–C.4. These were drawn up by technical support staff at Industrial Research Limited in Auckland, New Zealand. The author gratefully acknowledges their assistance with this work.

During the manufacture of the PCB, an error occurred which resulted in the final board being a mirror image of what it should have been. Fortunately it proved possible to populate the board regardless, avoiding the need to have a new board fabricated and shipped from New Zealand.

Frequency Stabilisation Circuit

The PCB artwork for the oscillator frequency stabilisation circuit is shown in Figure C.5. This was drawn up by the author using Puff ver. 2.0.

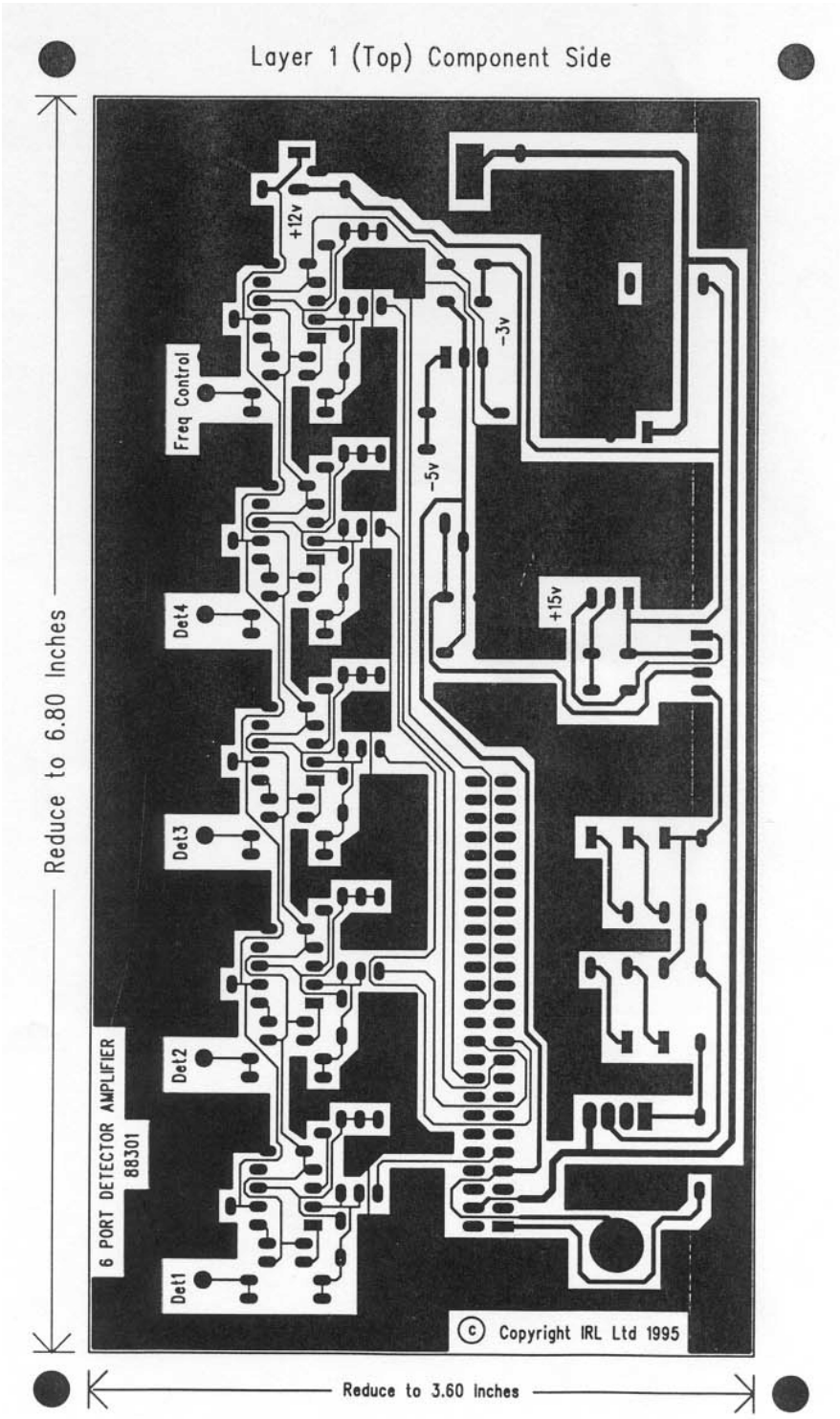

Figure C.2: PCB artwork for amplifier board (copper layer).

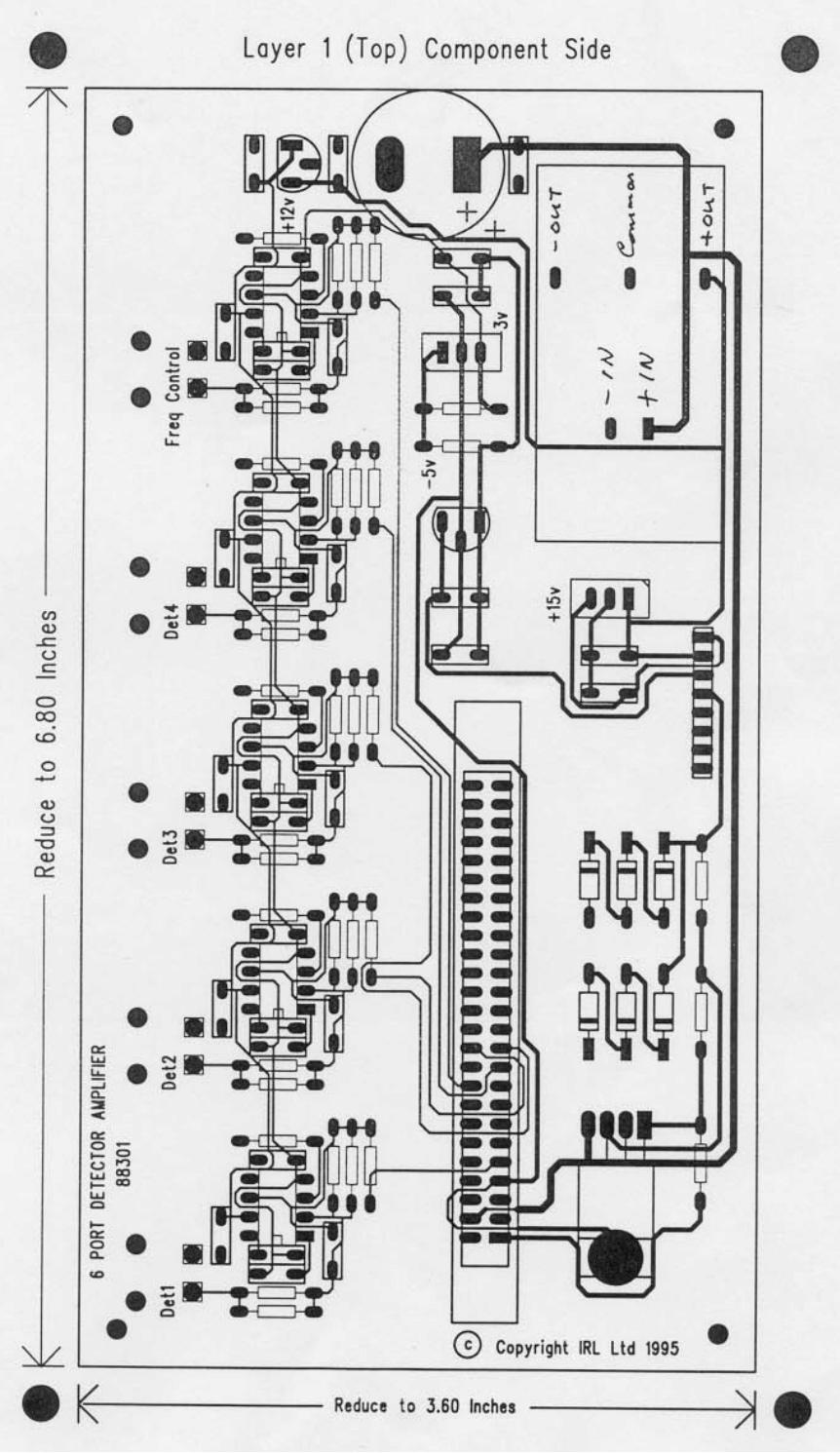

Figure C.3: PCB artwork for amplifier board (component layer).

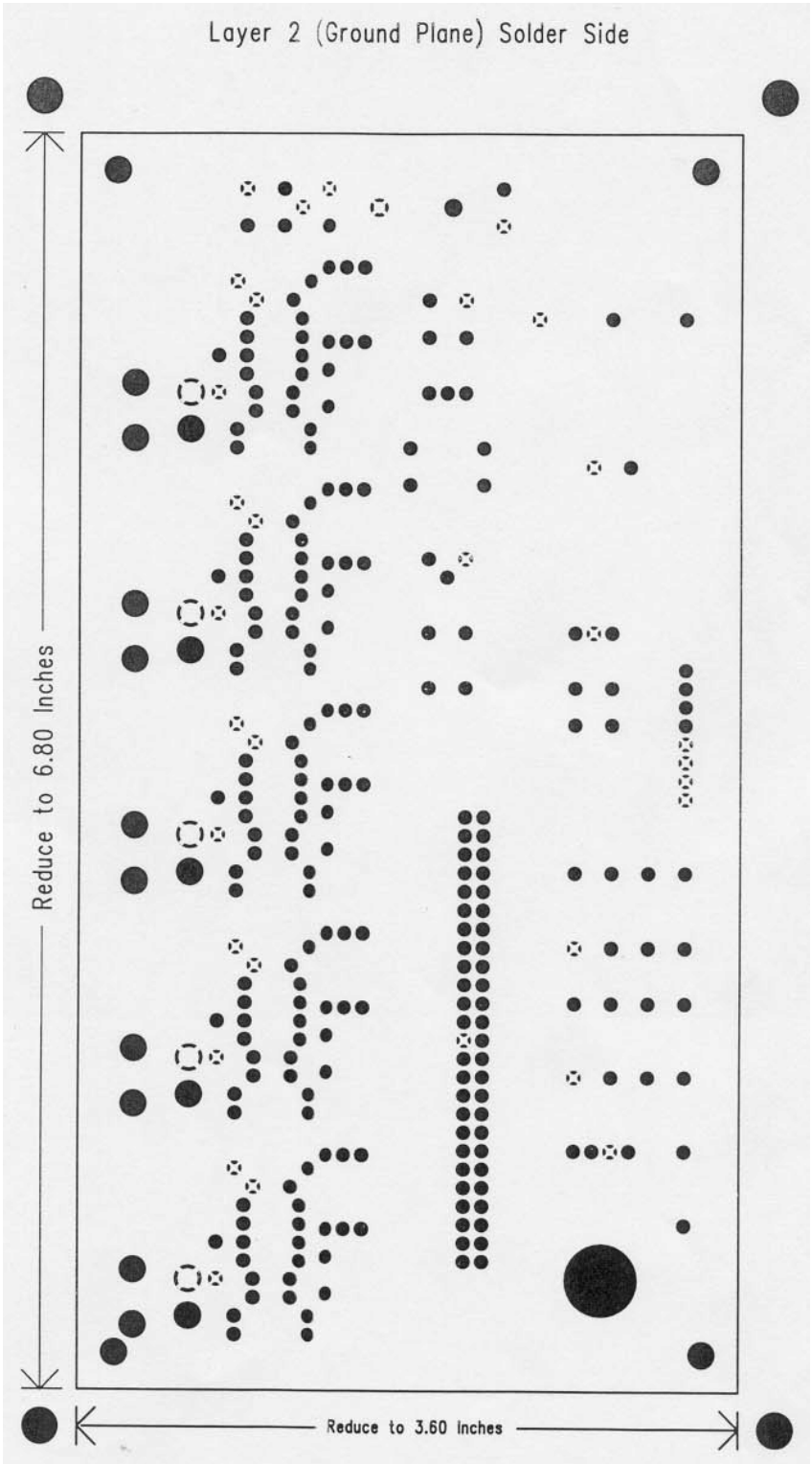

Figure C.4: PCB artwork for amplifier board (solder layer).

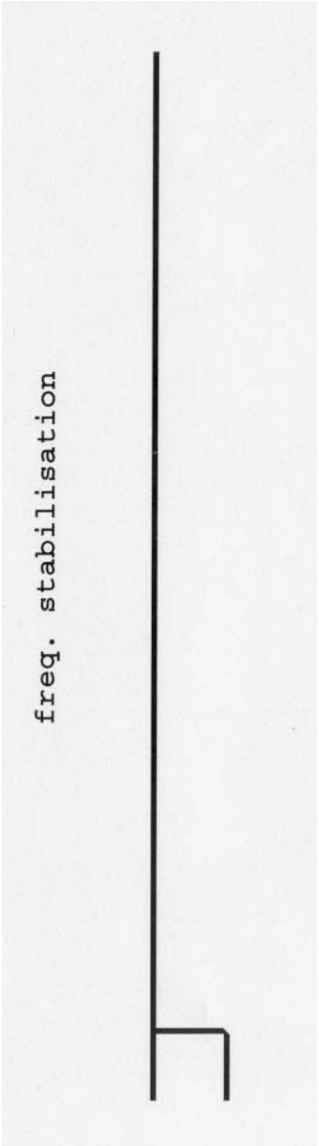

Figure C.5: PCB artwork for frequency stabilisation circuit.

Appendix D

Derivation of TM Surface Wave Equations in the Spectral Domain

The TM characteristic equations can be derived in much the same way in the spectral domain as in the space domain. The analysis involves matching the tangential field components across the dielectric interface.

Representing the longitudinal component of the electric field E_z using scalar potentials we can write

$$E_z = \phi(x,y)e^{-j\beta z} \tag{D.1}$$

where $\phi(x,y)$ satisfies the scalar wave equation in both regions

$$\nabla_t^2\phi_i + (k_i^2 - \beta^2)\phi_i \quad = \quad 0 \qquad i = 1,\ 2 \tag{D.2}$$

Expanding the scalar potential function ϕ_i as a Fourier transform yields

$$\phi_i(x,y) = \int_{-\infty}^{\infty} -\widetilde{\phi}_i(\alpha,y)e^{-j\alpha x}d\alpha \tag{D.3}$$

where

$$\widetilde{\phi}_i(\alpha, y) = \frac{1}{2\pi}\int_{-\infty}^{\infty} -\phi_i(x, y)e^{j\alpha x}dx \tag{D.4}$$

Applying the Fourier transform to the scalar wave equation yields

$$\frac{\partial^2}{\partial y^2}\widetilde{\phi}_i - \gamma_i^2\widetilde{\phi}_i = 0 \tag{D.5}$$

where

$$\gamma_i^2 = \alpha^2 + \beta^2 - k_i^2 \tag{D.6}$$

Solving Equation D.5 gives

$$\widetilde{\phi}_1 = Ae^{\gamma_1 y} + Be^{-\gamma_1 y} \tag{D.7}$$

$$\widetilde{\phi}_2 = Ce^{\gamma_2 y} + De^{-\gamma_2 y} \tag{D.8}$$

These equations can be solved for A, B, C and D by enforcing the appropriate boundary conditions. The first boundary condition is that all components of the electric field must be zero at infinity ($y = \infty$). This means we can write

$$\lim_{y\to\infty} E_{z,2} = 0 \tag{D.9}$$

Substitution of Equation D.9 into the scalar wave equation (Equation D.2 above) gives

$$\lim_{y\to\infty} \left(k_2^2 - \beta^2\right)\phi_2 e^{-j\beta z} = 0 \tag{D.10}$$

Taking the Fourier transform of Equation D.10 and substituting the solution for $\widetilde{\phi}_2$ from Equation D.8 produces

$$\begin{aligned} \lim_{y\to\infty} \left(k_2^2 - \beta^2\right)\widetilde{\phi}_2 e^{-j\beta z} &= 0 \\ \lim_{y\to\infty} \left(k_2^2 - \beta^2\right) e^{-j\beta z}\left(Ce^{\gamma_2 y} + De^{-\gamma_2 y}\right) &= 0 \end{aligned} \tag{D.11}$$

Assuming that $\Re(\gamma_2) > 0$, Equation D.11 can only be satisfied if $C = 0$. This results in

$$\widetilde{\phi}_2 = De^{-\gamma_2 y} \tag{D.12}$$

The second boundary condition is that the tangential components of the electric field must be zero at the ground plane ($y = 0$). This means we can write

$$\lim_{y\to 0} E_{z,1} = 0 \tag{D.13}$$

Performing similar substitutions to before we get

$$\begin{aligned}
\lim_{y\to 0} \left(k_1^2 - \beta^2\right) e^{-j\beta z} \left(Ae^{\gamma_1 y} + Be^{-\gamma_1 y}\right) &= 0 \\
\left(k_1^2 - \beta^2\right) e^{-j\beta z} \left(A + B\right) &= 0 \\
A + B &= 0 \\
A &= -B
\end{aligned} \tag{D.14}$$

so that

$$\begin{aligned}
\widetilde{\phi}_1 &= Ae^{\gamma_1 y} - Ae^{-\gamma_1 y} \\
&= 2A\left[\frac{e^{\gamma_1 y} - e^{-\gamma_1 y}}{2}\right] \\
&= 2A\sinh(\gamma_1 y)
\end{aligned}$$

The coefficient A is just an arbitrary constant, so we can make the substitution $2A = A$, giving:

$$\widetilde{\phi}_1 = A\sinh(\gamma_1 y) \tag{D.15}$$

The third boundary condition is that tangential electrical field components in each region must be equal at the dielectric interface. Thus

$$\begin{aligned}
E_{z,1} &= E_{z,2} \qquad (y = d) \\
\widetilde{E}_{z,1} &= \widetilde{E}_{z,2}
\end{aligned} \tag{D.16}$$

Assuming there is no variation in the x-direction (i.e. $\partial/\partial x = 0$) we can say that

$$\begin{aligned}
\widetilde{E}_z &= -\widetilde{\nabla}_t^2 \widetilde{\phi} e^{-j\beta z} \qquad (y = d) \\
&= -\left(0 + \frac{\partial^2}{\partial y^2}\right) \widetilde{\phi} e^{-j\beta z} \\
&= -\frac{\partial^2}{\partial y^2} \widetilde{\phi} e^{-j\beta z}
\end{aligned} \tag{D.17}$$

Substituting Equation D.17 into Equation D.16 we get

$$\begin{aligned}
-\frac{\partial^2}{\partial y^2} A \sinh(\gamma_1 y) e^{-j\beta z} &= -\frac{\partial^2}{\partial y^2} D e^{-\gamma_2 y} e^{-j\beta z} \qquad (y = d) \\
A\gamma_1^2 \sinh(\gamma_1 d) &= D\gamma_2^2 e^{-\gamma_2 d} \\
A\gamma_1^2 \sinh(\gamma_1 d) - D e^{-\gamma_2 d} &= 0
\end{aligned} \tag{D.18}$$

The fourth and final boundary condition is that tangential magnetic field components in each region must be equal at the dielectric interface. Thus

$$\begin{aligned}
H_{z,1} &= H_{z,2} \qquad (y = d) \\
\widetilde{H}_{z,1} &= \widetilde{H}_{z,2}
\end{aligned} \tag{D.19}$$

Given

$$H_t = j\omega\varepsilon \hat{k} \times \nabla_t \phi e^{-j\beta z} \tag{D.20}$$

it can be shown that

$$H_x = j\omega\varepsilon \frac{\partial}{\partial y} \phi e^{-j\beta z} \tag{D.21}$$

In the Fourier domain this becomes

$$\widetilde{H}_x = j\omega\varepsilon \frac{\partial}{\partial y} \widetilde{\phi} e^{-j\beta z} \tag{D.22}$$

Thus, at the dielectric interface ($y = d$) we have

$$\begin{aligned} j\omega\varepsilon_1 \frac{\partial}{\partial y}\widetilde{\phi}_1 e^{-j\beta z} &= j\omega\varepsilon_2 \frac{\partial}{\partial y}\widetilde{\phi}_2 e^{-j\beta z} \\ \varepsilon_1 \frac{\partial}{\partial y}\left[A\sinh(\gamma_1 y)\right] - \varepsilon_2 \frac{\partial}{\partial y}\left[De^{-\gamma_2 y}\right] &= 0 \\ A\varepsilon_1\gamma_1\cosh(\gamma_1 y) + D\varepsilon_2\gamma_2 e^{-\gamma_2 y} &= 0 \\ A\varepsilon_1\gamma_1\cosh(\gamma_1 d) + D\varepsilon_2\gamma_2 e^{-\gamma_2 d} &= 0 \end{aligned} \tag{D.23}$$

Equations D.18 and D.23 together form the following system of linear homogeneous equations:

$$\begin{bmatrix} \gamma_1^2\sinh(\gamma_1 d) & -\gamma_2^2 e^{-\gamma_2 d} \\ \varepsilon_1\gamma_1\cosh(\gamma_1 d) & \varepsilon_2\gamma_2 e^{-\gamma_2 d} \end{bmatrix} \begin{bmatrix} A \\ D \end{bmatrix} = \begin{bmatrix} 0 \\ 0 \end{bmatrix} \tag{D.24}$$

In order to obtain the nontrivial solutions of this system the determinant must be set to zero:

$$\gamma_1^2\gamma_2\varepsilon_2 e^{-\gamma_2 d}\sinh(\gamma_1 d) + \gamma_2^2\gamma_1\varepsilon_1 e^{-\gamma_2 d}\cosh(\gamma_1 d) = 0 \tag{D.25}$$

$$\frac{\varepsilon_2}{\gamma_2}\tanh(\gamma_1 d) + \frac{\varepsilon_1}{\gamma_1} = 0 \tag{D.26}$$

$$\tanh(\gamma_1 d) = -\frac{\varepsilon_1}{\varepsilon_2}\frac{\gamma_2}{\gamma_1} \tag{D.27}$$

Letting $\gamma_1 = jK$ we obtain

$$\begin{aligned} \tanh(jKd) &= -\frac{\varepsilon_1}{\varepsilon_2}\frac{\gamma_2}{jK} \\ j\tan(Kd) &= j\frac{\varepsilon_1}{\varepsilon_2}\frac{\gamma_2}{K} \\ \tan(Kd) &= \frac{\varepsilon_1}{\varepsilon_2}\frac{\gamma_2}{K} \end{aligned} \tag{D.28}$$

Equation D.28 is one of the eigen equations in the spectral domain which are required to characterise the slab structure. The other eigen equation may be derived as follows:

Recall that

$$\begin{aligned}\gamma_1^2 &= \alpha^2 + \beta^2 - k_1^2 \\ \gamma_2^2 &= \alpha^2 + \beta^2 - k_2^2\end{aligned}$$

Eliminating β^2 we get

$$\gamma_2^2 - \gamma_1^2 = k_1^2 - k_2^2 \tag{D.29}$$

Substituting $\gamma_1 = jK$ as before:

$$\begin{aligned}\gamma_2^2 - (jK)^2 &= \varepsilon_1 k_0^2 - \varepsilon_2 k_0^2 \\ \gamma_2^2 + K^2 &= (\varepsilon_1 - \varepsilon_2) k_0^2 \qquad \text{(D.30)}\end{aligned}$$

Equations D.28 and D.30 must now be solved simultaneously for γ_1 and γ_2 (where $\gamma_1 = jK$). Due to the nonlinear nature of these equations, a numerical method is needed. This is more easily achieved by multiplying Equation D.28 by d and Equation D.30 by d^2. The final equations in the spectral domain are thus

$$(Kd)\tan(Kd) = \frac{\varepsilon_1}{\varepsilon_2}(\gamma_2 d) \tag{D.31}$$

$$(\gamma_2 d)^2 + (Kd)^2 = (\varepsilon_1 - \varepsilon_2)(k_0 d)^2 \tag{D.32}$$